Domain Wall Transition Structures and Their Influence on Magnetization Reversals

Dissertation

zur Erlangung des Grades
des Doktors der Naturwissenschaften
der Naturwissenschaftlich-Technischen Fakultät
der Universität des Saarlandes

von

Sukhvinder Singh

Saarbrücken
2019

Tag des Kolloquiums:	February 20, 2020
Dekan:	Prof. Dr. Guido Kickelbick
Berichterstatter:	Prof. Dr. Uwe Hartmann
	Prof. Dr. Rainer Birringer
Vorsitz:	Prof. Dr. Frank Wilhelm-Mauch
Akad. Mitarbeiter:	Dr. Thomas John

Declaration of Authorship

I hereby certify that this thesis has been composed by me and is based on my own work, unless stated otherwise. All references and verbatim extracts have been quoted, and all sources of information, including graphs and data sets, have been identified.

Hiermit versichere ich, die vorliegende Arbeit selbstständig verfasst und keine anderen als die angegebenen Quellen und Hilfsmittel benutzt sowie die Zitate deutlich kenntlich gemacht zu haben.

Saarbrücken, September 16, 2019

Sukhvinder Singh

Acknowledgments

First and foremost, I would like to thank Prof. Dr. Uwe Hartmann for giving me an opportunity to work in the group and for his excellent guidance and confidence in my investigations.

I would also like to thank Dr. Haibin Gao for his constant discussions and fruitful inputs in my work. Next, I thank to all my other colleagues (both present and past) especially Gregor Büttel, Xian-Lin Zeng, Dr. Michael Koblischka, Thomas Karwoth and Stefan Griesing for introducing different techniques and all sort of helps during my work.

Furthermore, I would like to thank all the other people for their support in the characterizations of the samples, namely Mr. Jörg Schmauch (AG Birringer) for EDX and TEM investigations and Mr. Rudolf Karos (Leibniz Institute for New Materials, Saarbrücken) for XRD of my samples. In this regard, I would like to especially thank Prof. Dr. Leon Abelmann for VSM measurements and fruitful discussions and suggestions during our group-seminars.

Apart from my work, I am also grateful to my Saarbrücken "family-like" friends Aman, Varun, Anahita, Mansi and Nimba for their constant encouragements and beautiful time spent at lunches, coffees, dinners and other special occasions. This list of friends will be incomplete without naming Somnath, Melanie, Ettore, Selda, Kapil and Debajit for our weekend-dinner meetings in the city with cheerful moments and "philosophical conversations" over life.

In the last but not least, I express my gratitudes to my family for their support throughout my life.

Abstract

Properties of magnetic materials are determined by their internal structures. In this work, magnetic domains and domain walls were analyzed with the change of film deposition-conditions, an externally applied field and a perpendicular anisotropy. The influences of the transition structures (TSs) of the walls, such as vortices and antivortices, on the domain configurations and magnetization reversals were investigated. Different types of domains, domain walls and their TSs in permalloy (Py) patterned films were imaged with Magnetic Force Microscopy (MFM). The corresponding micromagnetic simulations were performed using Object-Oriented MicroMagnetic Framework (OOMMF) software.

On increasing the argon (Ar) sputtering pressure, pinning of the TSs and domain walls due to the increase of porosity in the films resulted in the formation of complex domain configurations with irregularly arranged magnetizations. Technically relevant domain configurations, with magnetizations well-defined by the shapes and dimensions of the films, were obtained by depositing films at $\sim$1 µbar Ar pressure.

By investigating the TSs during magnetization reversals, it was found that their nucleation created segments of reversed magnetizations inside the walls. These segments expanded with the increase of the applied field to form the domains of reversed magnetizations. In this process, domain walls also reversed their internal magnetizations with the displacement of a resulting single vortex along their wall-axes, as a consequence of the nucleation and annihilation of the TSs inside the walls.

Moreover, on observing the internal structures of the walls inside a film of a certain thickness and containing a perpendicular anisotropy, alternate upwards and downwards split magnetization segments were found. These segments expanded inside the domains with the increase of the film thickness and formed stripe domains. Hence, a fifty years old domain-phase diagram was refined by finding a premature formation of stripe domains inside the domain walls.

Zusammenfassung

Eigenschaften magnetischer Materialien sind bestimmt durch ihre interne Struktur. In dieser Arbeit wurden magnetische Domänen und Domänenwände mittels Änderung der Dünnschicht-Depositionsbedingungen, eines externen magnetischen Feldes sowie einer senkrechten Anisotropie untersucht. Der Einfluss von Übergangsstrukturen der Domänenwände, wie Wirbel und Antiwirbel, auf die Domänenkonfigurationen und Magnetisierungsumkehrung wurde untersucht. Verschiedene Arten von Domänen, Domänenwänden und deren Übergangsstrukturen in Permalloy strukturierten Filmen wurden mit einem Magnetkraftmikroskopie abgebildet. Die entsprechenden mikromagnetischen Simulationen wurden mit Hilfe der Object-Oriented MicroMagnetic Framework Software durchgeführt.

Bei Erhöhung des Argon-Gasdrucks in der Sputterkammer ergab sich eine Fixierung der Übergangsstrukturen und Domänenwände aufgrund der Erhöhung der Porösität der Filme, die zu einer Formation von komplexen Domänen-Konfigurationen mit irregulär ausgerichteten Magnetisierungen führte. Technisch relevante Domänenkonfigurationen, mit Magnetisierungen die durch die Form und Größe des Films definiert sind, wurden durch Sputter-Deposition bei einem Argon-Gasdruck von ca. 1 µbar erhalten.

Mittels Untersuchungen der Übergangsstrukturen während Magnetisierungsumkehrungen konnte herausgefunden werden, dass ihre Entstehung Segmente invertierter Magnetisierung innerhalb der Domänenwand erzeugte. Diese Segmente vergrößerten sich bei Erhöhung des externen Magentfeldes, um Domänen mit invertierter Magnetisierung zu bilden. In diesem Prozess invertierten Domänenwände ihre internen Magnetisierungen mit der Verschiebung eines resultierenden einzelnen Wirbel entlang der Wandachse als Folge der Nukleierung und Annihilation der Übergangsstrukturen innerhalb der Wände.

Des Weiteren wurden bei der Untersuchung der internen Strukturen der Domänenwände in einem Film bestimmter Dicke und Anisotropie sich abwechselnde auf- und abwärtsgeteilte Magnetisierungsbereiche gefunden. Diese Bereiche vergrößerten sich innerhalb der Domänen mit der Zunahme der Filmdicke und bildeten Streifendomänen. Infolgedessen konnte ein 50 Jahre altes Phasendiagram für magnetische Domänen aufgrund der Beobachtung einer vorzeitigen Formierung von Streifendomänen innerhalb

von Domänenwänden revidiert werden.

List of Acronyms

ABW	Asymmetric Bloch wall
ADW	Asymmetric domain wall
AFM	Atomic force microscope/microscopy
ANW	Asymmetric Néel wall
Ar	Argon
bcc	Body-centered cubic
BP	Bloch point
BS	Bloch switch
CTW	Cross-tie wall
EAS	Easy axis switching
EBL	Electron-beam lithography
EDX	Energy-dispersive X-ray spectroscopy
fcc	Face-centered cubic
FIB	Focused ion beam
HAS	Hard axis switching
LLG	Landau-Lifshitz-Gilbert
MFM	Magnetic force microscope/microscopy
NC	Néel cap
OOMMF	Object-oriented micromagnetic framework
PMMA	Poly methyl methacrylate
Py	Permalloy
sc	Simple cubic
SEM	Scanning electron microscope
SNW	Symmetric Néel wall
STEM	Scanning transmission electron microscope
TEM	Transmission electron microscope
TS	Transition structure
VAVP	Vortex-antivortex pair
VSM	Vibrating sample magnetometer
XRD	X-ray diffraction

List of Figures

Contents

1 Introduction

Today, magnetism and thus magnetic materials have become indispensable parts of our daily life. Some examples include their use in credit cards, mobile phones, hard disk drives, audio speakers and motorized household appliances [1]. The versatility of their impact on life demands a deeper understanding of their magnetic properties owing to their internal structures. Inside a magnetic material, a variety of extended and localized spatial magnetic configurations are formed [2]. These configurations have a hierarchical order. A magnetic material is divided into domains by domain walls, while within the domain walls there may exist localized TSs which further split the domain walls into segments of different magnetic configurations, as shown in Fig. 1.1. These TSs have dimensions of the order of a few tens of nanometers and consist of vortices, antivortices and magnetic singularities (see section 2.4) [2–9].

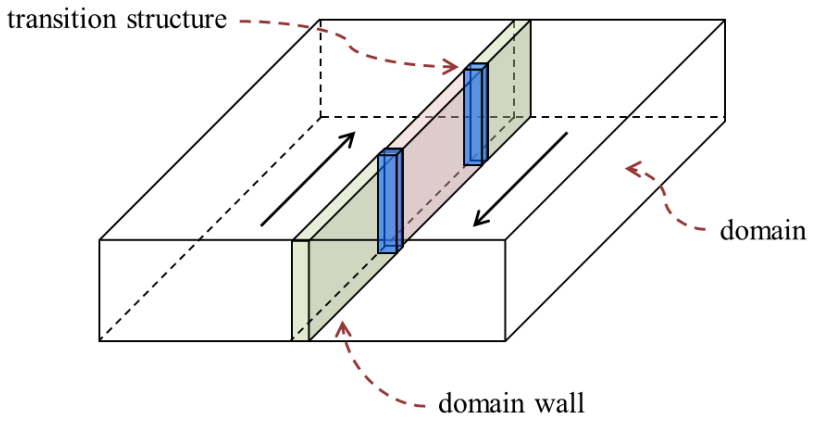

Figure 1.1: A simplified schematic depicting transition structures inside a domain wall.

A variety of domain walls exist in magnetic materials [2]. In thin films of soft magnetic materials such as Py, internal structures of the domain walls change from one-dimensional to two-dimensional magnetization configurations above a certain film-thickness [2]. Inside one-dimensional domain walls, the magnetization is oriented only in the plane of the film. However, inside two-dimensional domain walls, the magnetization

is oriented in the plane of the film at the surfaces and out of the plane of the film in the interiors of the walls [2]. In one-dimensional domain walls vortices and antivortices exist as TSs (see Fig. 2.15 in chapter 2) [3–5]. Whereas, inside two-dimensional domain walls, different combinations of vortices and antivortices at the surfaces and singularities in the interior of the walls form various types of complex three-dimensional TSs (see Figs. 2.16 to 2.19 in chapter 2) [6–9].

A magnetic anisotropy inside the material influences both the overall domain configurations (i.e., the overall arrangement of the magnetization inside the material) and the internal structures of the domains [2, 10]. In thin films, the internal structures of the domains change with the increase of the perpendicular (or out-of-plane of the film) anisotropy [2, 11, 12]. Homogeneously in-plane magnetized domains are superimposed by an alternate upwards and downwards tilted magnetization configuration, known as stripe domains [11]. According to the domain-phase diagram [12] (see Fig. 2.22 in chapter 2), stripe domains are formed abruptly above a perpendicular-anisotropy-dependent critical thickness of the film. In films with a larger perpendicular anisotropy, parallel- and maze-shaped band and cylinder-shaped bubble domains are formed, which possess the magnetization oriented completely out of the plane of the films [2].

The technically important properties of magnetic materials depend on both their structural characteristics (such as grain morphology, stress and elemental composition etc.) [13–17] and the types of their internal magnetic configurations (i.e., the types of domains, domain walls and TSs) formed inside them [18–24]. Over the past few decades, the analysis and manipulation of the internal magnetic configurations inside patterned thin films has become a subject of an intense interest to enable various new applications in the field of magnetic data storage and sensor devices [22, 24–28]. Internal structures of the domain walls and their various type of TSs within and without applied magnetic fields [29–31] or current pulses [23, 32, 33] are investigated in detail in this context. It is found that the TSs significantly influence the static and dynamic properties of the walls [22, 26, 31, 34] and also control the evolution of the domain configurations (i.e., the rearrangement of the domains) within an applied field [35–38]. Since the domain configurations determine the characteristics of the hysteresis loops [39–41], magnetoresistance [42–44], magnetoimpedance [45, 46] and numerous other magnetic effects [10, 47–49] of the materials, it is crucial to understand the role of the TSs in the basic magnetization processes such as the formation of the domains and magnetization reversals in the patterned thin films.

In this work, the role of the TSs in the formation of different types of domain configurations and their internal structures, manipulation of the internal structure

of the domain walls and the magnetization reversal of Py patterned thin films is investigated. Due to the soft magnetic properties of Py [50], it is one of the most widely used magnetic materials for both basic research and various technical applications [51]. Micro-patterned Py films of various shapes and thicknesses were prepared using electron-beam lithography (EBL) and sputter deposition. Different types of domain configurations, domain walls and their TSs within and without an externally applied magnetic field were analyzed with MFM. Moreover, in order to better understand the three-dimensional magnetic configurations and to evaluate the contributions of different magnetic energies, micromagnetic simulations were also performed using OOMMF software [52].

This thesis is organized as follows:

In chapter 2, the basic concepts of micromagnetism, different types of domain walls, their TSs and stripe domains are discussed.

In chapter 3, a brief description of the structural and magnetic properties of Py and different techniques used in this work is presented.

In chapter 4, the formation of different types of zero-field domain configurations with the change of the Ar sputtering pressure is explained. It is shown that the grain morphology influences the domain configurations. The formation of well-defined and repeatable domain configurations in micro-patterned Py films is explained.

In chapter 5, the role of the TSs in magnetization reversals of the micro-patterned Py films is explained. The nucleation and annihilation of the TSs and an interplay of the different magnetic energies are analyzed to understand the evolution of the domain configurations within an applied magnetic field.

In chapter 6, the role of the TSs in the reversal of the internal magnetization configurations of the one-dimensional and two-dimensional domain walls within an externally applied magnetic field are investigated and compared, respectively.

In chapter 7, the influence of the perpendicular anisotropy on the domain wall internal structures and the consequent formation of the stripe domains is investigated. A refined domain-phase diagram for the formation of the stripe domains is presented.

In chapter 8, finally the results are concluded and a brief outlook of the future investigations is presented.

2 Basics of micromagnetism, domain walls, their transition structures and stripe domains

2.1 Micromagnetism and formation of domains

2.1.1 Micromagnetism

Micromagnetism (originally called micromagnetics) is a continuum theory, which started in the 1930s with the pioneer work of Landau and Lifshitz [53] on the interpretation of domain configurations. The other contributions of Brown [54, 55], Bloch [56], Néel [57], Kittel [58, 59] and other authors [60–63] from around 1930s to 1950s established this theory as an efficient tool to describe magnetization processes and the characteristic properties of the hysteresis loops [64]. This theory describes the magnetization on a length scale which is large enough to replace the discrete atomic spins by a continuous function of position, i.e., $\mathbf{M}(\mathbf{r})$, and small enough to resolve the transitions of magnetization between magnetic domains [2, 53, 55]. The magnetization $\mathbf{M}(\mathbf{r})$ is generally nonuniform, but a continuously varying function of position $\mathbf{r}$. $\mathbf{M}(\mathbf{r})$ varies in direction only: its magnitude is the spontaneous (or saturation) magnetization M_s. Thus we can write

$$\mathbf{M}(\mathbf{r}) = M_s\,\mathbf{m}(\mathbf{r}); \quad \mathbf{m}\cdot\mathbf{m} = 1. \tag{2.1}$$

$\mathbf{m}$ is a unit vector in the direction of $\mathbf{M}(\mathbf{r})$. As the adjacent magnetizations $\mathbf{m_i}$ and $\mathbf{m_j}$ at positions $\mathbf{r_i}$ and $\mathbf{r_j}$ are assumed "almost" parallel and there exists no abrupt change, therefore,

$$|\,\mathbf{m_i} - \mathbf{m_j}\,| \approx 0 \quad \text{for} \quad |\,\mathbf{r_i} - \mathbf{r_j}\,| < l_{ex}. \tag{2.2}$$

Here l_{ex} is an exchange length which is described by the exchange interaction (exchange interaction will be discussed below) between the adjacent magnetizations which results in their almost parallel alignment for ferromagnetic materials.

In micromagnetism, the total energy E_{tot} of a magnetic material is composed of several different energy contributions, i.e., the exchange energy E_{ex}, anisotropy energy E_{K}, Zeeman energy E_{Z}, demagnetization energy E_{D}, and magnetoelastic energy E_{me}, which is written as [2]

$$E_{\mathrm{tot}} = E_{\mathrm{ex}} + E_{\mathrm{K}} + E_{\mathrm{Z}} + E_{\mathrm{D}} + E_{\mathrm{me}}. \tag{2.3}$$

In order to achieve a stable magnetic configuration in an existing situation, the total energy is minimized by an interplay of different contributing energies. This process leads to the formation of domains and domain walls inside ferromagnetic materials. The most common approach to find the equilibrium state of the material is to solve the Landau-Lifshitz-Gilbert (LLG) equation of motion (will be discussed below, equation (2.23)), which is a torque equation relating the time evolution of $\mathbf{M}(\mathbf{r},t)$ to the torque exerted by an effective field $\mathbf{H_{eff}}(\mathbf{r},t)$ (equation (2.19)) inside the material.

Exchange energy

The exchange interaction is an interaction which couples two neighboring spins, and it is responsible for parallel or antiparallel alignment of the neighboring spins. It arises from the quantum mechanical principle of exchange symmetry, which states that no observable physical quantity should change after exchanging two indistinguishable particles. The exchange energy can be written as [65]

$$E_{\mathrm{ex}} = -2\sum_{\mathrm{ij}} J_{\mathrm{ij}}\, \mathbf{S_i} \cdot \mathbf{S_j} = -2\sum_{\mathrm{ij}} J_{\mathrm{ij}}\, S^2\, \mathbf{m_i} \cdot \mathbf{m_j}, \tag{2.4}$$

where $\mathbf{S_i}$ and $\mathbf{S_j}$ are two magnetic spins located on neighbouring sites $\mathbf{r_i}$ and $\mathbf{r_j}$, respectively. S is the spin quantum number. $\mathbf{m}$ is a unit vector along the local spin direction and J_{ij} is the Heisenberg exchange integral. Since it is a short-range interaction, one can consider the sum from the nearest neighbors only. The sign of J_{ij}, i.e., $J_{\mathrm{ij}} > 0$ or $J_{\mathrm{ij}} < 0$, determines whether the material is ferromagnetic (parallel alignment of the neighbouring spins) or antiferromagnetic (antiparallel alignment of the neighbouring spins), respectively.

The exchange energy of a unit volume for a cubic lattice system of lattice constant a is given by [65]

$$E_{\mathrm{ex}} = \frac{nJS^2}{a} \int_{\mathrm{V}} \left[(\nabla m_{\mathrm{x}})^2 + (\nabla m_{\mathrm{y}})^2 + (\nabla m_{\mathrm{z}})^2\right] \mathrm{d}V. \tag{2.5}$$

Where m_x, m_y and m_z are the magnetization components along the orthogonal x, y and z axes. The coefficient of the right hand side of the equation (2.5) is an exchange stiffness constant A_{ex}, proportional to the exchange constant J and is measured in Jm^{-1} (erg cm^{-1}, in the CGS). A_{ex} defines the strength of the magnetic coupling, and therefore describes how difficult it is to deviate a spin from the direction of the exchange-coupled field. The number n is equal to 1 for the simple cubic (sc) structure, 2 for the body-centered cubic (bcc) structure, and 4 for the face-centered cubic (fcc) structure [65].

Magnetocrystalline anisotropy energy

In ferromagnetic materials, one crystallographic axis is or more than one axes are easy to magnetize compared to the other crystallographic axes. The crystallographic axes which are easy to magnetize are called easy axes, whereas the other axes are called hard axes. The total free energy of the magnetic materials depends on the direction of the magnetization relative to their crystallographic axes. This form of anisotropy arises from the spin-orbit interactions of the atoms [10]. Frequent magnetocrystalline anisotropy energies considered are for the cubic and the uniaxial systems.

For the cubic case the magnetocrystalline anisotropy energy is [2]

$$E_K^c = \int_V [K_{c1}(m_x^2 m_y^2 + m_x^2 m_z^2 + m_y^2 m_z^2) + K_{c2}(m_x^2 m_y^2 m_z^2)]\, dV. \tag{2.6}$$

Where m_x, m_y and m_z are the magnetization components along the cubic axes, i.e., x, y and z axes and K_{c1} and K_{c2} are the first and second order cubic anisotropy constants. Usually K_{c1} is in the range of $\pm 10^4$ Jm^{-3} for different materials [10]. The higher-order energy terms are usually neglected because of the thermal agitation of magnetic spins [2]. Also sometimes K_{c2} is so small that the term involving can be neglected [10]. When K_{c2} is zero, the direction of easy magnetization is determined by the sign of K_{c1}. If K_{c1} is positive as in the case of iron and cubic ferrites containing cobalt, $\langle 100 \rangle$ is the easy direction [10]. If K_{c1} is negative as in the case of nickel and all cubic ferrites containing no or very little cobalt, $\langle 111 \rangle$ is the easy direction [10].

The uniaxial anisotropy energy is usually written as [2]

$$E_K^u = \int_V [K_{u1}\, sin^2(\theta) + K_{u2}\, sin^4(\theta)]\, dV. \tag{2.7}$$

K_{u1} and K_{u2} are the first- and second-order uniaxial anisotropy constants and θ is the angle between the magnetization direction and the easy axis of the material.

When both K_{u1} and K_{u2} are positive, there exists an easy axis for the magnetization. Cobalt, barium ferrite, and many rare earth transitional metal intermetallic compounds behave in this way [10]. In the case of both K_{u1} and K_{u2} are negative an easy plane perpendicular to the anisotropy axis exists. If K_{u1} and K_{u2} have opposite signs, the easy directions lie on a cone surface [2, 10]. The K_{u1} value can reach upto 10^7 Jm^{-3} for rare earth transition metal permanent magnet materials, whereas the higher order uniaxial anisotropy energies are usually neglected for being very small [2].

Zeeman energy

The Zeeman energy is due to the interaction of the magnetization $\mathbf{M}$ with an externally applied magnetic field $\mathbf{H_{app}}$. The magnetization inside the material is preferentially aligned along the applied magnetic field direction in order to minimize the torque applied by the external field. This energy is given as [2]

$$E_Z = -\mu_0 \int_V \mathbf{M} \cdot \mathbf{H_{app}} \, \mathrm{d}V, \tag{2.8}$$

where μ_0 is the permeability constant.

Demagnetization energy

When a specimen is magnetized, the free magnetic poles which appear on its ends produce a magnetic field both inside and outside the sample. The field inside the sample is directed opposite to the magnetization and called demagnetizing field. The field outside the sample is called stray field. For a uniformly magnetized ellipsoid this field can be expressed as [66]

$$\mathbf{H_D} = -\mathcal{N}\,\mathbf{M}, \tag{2.9}$$

where $\mathcal{N}$ is a demagnetizing tensor.

The demagnetizing or stray field $\mathbf{H_D}$ can be calculated from the magnetic scalar potential $\Phi(\mathbf{r})$ from the relation

$$\mathbf{H_D} = -\nabla\Phi(\mathbf{r}), \tag{2.10}$$

as a result from $\mathbf{H_D}$ being irrotational (i.e., $\nabla \times \mathbf{H_D} = 0$). The scalar potential is given by [67]

$$\Phi(\mathbf{r}) = \frac{1}{4\pi}\left[-\int_V \frac{\nabla \cdot \mathbf{M}(\mathbf{r}')}{|\mathbf{r} - \mathbf{r}'|} \, \mathrm{d}V' + \int_S \frac{\mathbf{M}(\mathbf{r}') \cdot \mathbf{n}}{|\mathbf{r} - \mathbf{r}'|} \, \mathrm{d}S' \right], \tag{2.11}$$

where $\mathbf{n}$ is a unit vector pointing outward from the surface and $\rho_{\mathrm{m}} = -\nabla \cdot \mathbf{M}$ and $\sigma_{\mathrm{m}} = \mathbf{M} \cdot \mathbf{n}$ are the volume and surface charge densities, respectively. It is therefore common to use the notion of magnetic "sources" and "sinks" that act like positive and negative magnetic charges, just like in electrostatics but with the difference that magnetic charges never occur isolated but always exist in balancing pairs. The corresponding field obtained from equations (2.10) and (2.11) is [67]

$$\mathbf{H_D} = \frac{1}{4\pi}\left[-\int_{\mathrm{V}} \frac{(\mathbf{r}-\mathbf{r}')\nabla \cdot \mathbf{M}(\mathbf{r}')}{|\mathbf{r}-\mathbf{r}'|^3}\,\mathrm{d}V' + \int_{\mathrm{S}} \frac{(\mathbf{r}-\mathbf{r}')\mathbf{M}(\mathbf{r}')\cdot\mathbf{n}}{|\mathbf{r}-\mathbf{r}'|^3}\,\mathrm{d}S' \right]. \tag{2.12}$$

The demagnetization energy (also known as stray-field or self energy) for such a magnetic material is expressed as

$$E_{\mathrm{D}} = -\frac{\mu_0}{2}\int_{\mathrm{V}} \mathbf{M} \cdot \mathbf{H_D}\,\mathrm{d}V. \tag{2.13}$$

As the demagnetizing field $\mathbf{H_D}$ is always directed opposite to the magnetization direction $\mathbf{M}$, the demagnetization energy E_{D} is either positive or zero.

Magnetoelastic energy and magnetostriction

The magnetoelastic energy of a magnetic solid arises from an interaction between the magnetization $\mathbf{M}$ and the strains $\varepsilon_{\mathrm{ij}}$. The magnetoelastic energy is the increase in the anisotropy energy of a magnetic solid submitted to an applied stress. Its expression for a cubic crystal is given by [59]

$$E_{\mathrm{me}} = \int_{\mathrm{V}} [B_1(\alpha_1^2\varepsilon_{\mathrm{xx}} + \alpha_2^2\varepsilon_{\mathrm{yy}} + \alpha_3^2\varepsilon_{\mathrm{zz}}) + B_2(\alpha_1\alpha_2\varepsilon_{\mathrm{xy}} + \alpha_2\alpha_3\varepsilon_{\mathrm{yz}} + \alpha_3\alpha_1\varepsilon_{\mathrm{zx}})]\,\mathrm{d}V, \tag{2.14}$$

where B-factors are the magnetoelastic coupling constants and α_{i} are the direction cosines.

Magnetostriction is a property of ferromagnetic materials that causes them to change their dimensions as their magnetic state is changed. It is measured by the relative linear deformation λ as below

$$\lambda = \frac{\delta l}{l}, \tag{2.15}$$

where l is the original length of the material and δl is the change in the length due to the change of magnetization.

For a cubic crystal material with saturation magnetostriction λ_{s}, the magnetoelastic

energy E_{me} related to a stress σ is given by [65]

$$\frac{E_{\mathrm{me}}}{V} = \frac{3}{2}\lambda_{\mathrm{s}}\,\sigma sin^2\theta, \tag{2.16}$$

where θ is the angle between the direction of the magnetization and the direction along which the magnetostriction is measured.

Note that, in order to distinguish the strain ε caused by an applied stress, the magnetically induced strain is denoted by a different symbol λ.

Effective-field and Landau–Lifshitz–Gilbert equation

The free energy function of a magnetic material might have several local minima, where each of them is corresponding to a possible magnetic stable state. According to the variational principle, the magnetization distribution at equilibrium satisfies the following conditions simultaneously,

$$\delta E_{\mathrm{tot}}(\mathbf{m}) = 0 \quad \text{and} \quad \delta^2 E_{\mathrm{tot}}(\mathbf{m}) > 0. \tag{2.17}$$

Where $\delta E_{\mathrm{tot}}(\mathbf{m}) = E_{\mathrm{tot}}(\mathbf{m}+\delta\mathbf{m}) - E_{\mathrm{tot}}(\mathbf{m})$ represents an infinitesimal variation of the energy induced by a small change in the magnetization $\delta\mathbf{m}$. The energy variation of a magnetic body with uniaxial magnetocrystalline anisotropy can be written as [68]

$$\begin{aligned}\delta E_{\mathrm{tot}}(\mathbf{m}) = \mu_0 \int_{\mathrm{V}} M_{\mathrm{s}} \left[\frac{2A_{\mathrm{ex}}}{\mu_0 M_{\mathrm{s}}}\nabla^2\mathbf{m} + \frac{2K_{\mathrm{u}}}{\mu_0 M_{\mathrm{s}}}(\mathbf{u_k}\cdot\mathbf{m})\,\mathbf{u_k} + \mathbf{H_{app}} + \mathbf{H_D}\right]\cdot\delta\mathbf{m}\,\mathrm{d}V \\ + \int_{\mathrm{S}} 2A_{\mathrm{ex}}\left(\mathbf{m}\times\frac{\partial\mathbf{m}}{\partial\mathbf{n}}\right)\mathrm{d}S,\end{aligned} \tag{2.18}$$

where $\mathbf{u_k}$ is the unit vector along the magnetocrystalline easy axis. The quantity between the brackets from the first term represents an effective field,

$$\mathbf{H_{eff}} = \frac{2A_{\mathrm{ex}}}{\mu_0 M_{\mathrm{s}}}\nabla^2\mathbf{m} + \frac{2K_{\mathrm{u}}}{\mu_0 M_{\mathrm{s}}}(\mathbf{u_k}\cdot\mathbf{m})\,\mathbf{u_k} + \mathbf{H_{app}} + \mathbf{H_D}. \tag{2.19}$$

In the general case, $\mathbf{H_{eff}}$ is defined as the variational derivative of the free energy density $\epsilon_{\mathrm{tot}} = \partial E_{\mathrm{tot}}/\partial V$ with respect to the magnetization, i.e.,

$$\mathbf{H_{eff}} = -\frac{1}{\mu_0 M_{\mathrm{s}}}\frac{\delta\epsilon_{\mathrm{tot}}}{\delta\mathbf{m}}. \tag{2.20}$$

To obtain the equilibrium condition, both the surface and volume integrals from

equation (2.18) must vanish. This is possible if simultaneously two conditions are fulfilled [68]

$$\frac{\partial \mathbf{m}}{\partial \mathbf{n}} = 0 \quad \forall \quad \mathbf{r} \in S \quad \text{and} \quad \mathbf{m}(\mathbf{r},t) \times \mathbf{H}_{\mathbf{eff}}(\mathbf{r},t) = 0 \quad \forall \quad \mathbf{r} \in V. \tag{2.21}$$

These conditions were deduced by Brown [54] and therefore are called Brown equations. Their solutions specify the equilibrium state. The first one is a Neumann boundary condition, which forces the magnetization to be stationary near the sample surface S. The second equation states that for a magnetization distribution to be at equilibrium, the torque acting on $\mathbf{M}$ due to the effective field $\mathbf{H}_{\mathbf{eff}}$ must be zero everywhere (the magnetization is aligned with the effective field).

The Brown equations define the equilibrium state of a magnetic system, but they do not specify how the system reaches this state. The magnetization dynamics can be accessed through the LLG equation. The starting point is represented by the Larmor equation [65],

$$\frac{\mathrm{d}\mathbf{M}}{\mathrm{d}t} = -\gamma\,(\mathbf{M} \times \mathbf{H}), \tag{2.22}$$

which describes the magnetization's gyrotropic reaction in the presence of the magnetic field $\mathbf{H}$. Here $\gamma = 2.21 \times 10^5$ m(As)$^{-1}$ is the Gilbert gyromagnetic ratio. The Larmor equation is conservative. Its solution corresponds to a magnetization which precesses endlessly around the field, with constant precession angle and energy. However, in real ferromagnetic materials, dissipation processes cause the system to minimize its energy and to reach, after certain time, a stable state ($d\mathbf{M}/dt = 0$). In order to take account of dissipation, a term was added to equation (2.22), allowing the magnetization to reach static equilibrium. Gilbert [69] introduced magnetic damping as a viscous force proportional to the time-derivative of the magnetization. The Gilbert equation of motion includes precession and relaxation [65]

$$\frac{\mathrm{d}\mathbf{M}}{\mathrm{d}t} = -\gamma\,(\mathbf{M} \times \mathbf{H}_{\mathbf{eff}}) + \frac{\alpha}{M_\mathrm{s}}\left(\mathbf{M} \times \frac{\mathrm{d}\mathbf{M}}{\mathrm{d}t}\right). \tag{2.23}$$

The damping α is a dimensionless phenomenological constant, arising from all dissipation processes (e.g., magnon-magnon scattering, magnon-phonon scattering, Eddy currents). The meaning and the measurement of α is an intricate matter since its value depends not only on the material but also on the experimental conditions [70]. For most common ferromagnetic materials α is a scalar ranging from 5×10^{-4} to 0.1 [71–73]. Equation (2.23) is known as the LLG equation which is commonly used in

micromagnetic simulations to model the temporal behavior of the magnetic samples within a magnetic field.

2.1.2 Formation of domains and domain walls

In Fig. 2.1, schematics of the formation of domains with the consequent minimization of the stray field of a magnetic sample are drawn. Fig. 2.1(a) describes a uniformly magnetized ferromagnetic rectangular sample. The arrow inside the sample shows the direction of the magnetization, whereas the arrows outside the sample describe the stray field at the sample ends, respectively. The stray field can be reduced by a subdivision of the sample's uniform magnetization state into two antiparallelly magnetized regions, as described in Fig. 2.1(b). Such regions with uniform magnetizations are called magnetic domains [10, 59]. These domains are separated by transition regions called domain walls, shown as broken lines in Figs. 2.1(b) and (c). However, from the demagnetization energy equation (2.13) it is clear that the demagnetization energy is reduced by minimization of both the stray field and the total magnetization $\mathbf{M}(\mathbf{r})$ of the sample under consideration. The schematic shown in Fig. 2.1(b) minimizes the vector sum of the magnetization (total magnetization), whereas the stray field is still produced by the surface charges ($\sigma = \mathbf{M} \cdot \mathbf{n}$) formed on the sample ends. The surface charges are avoided with the formation of closure end domains [2, 58, 74] which close the magnetic flux inside the sample as shown in Fig. 2.1(c).

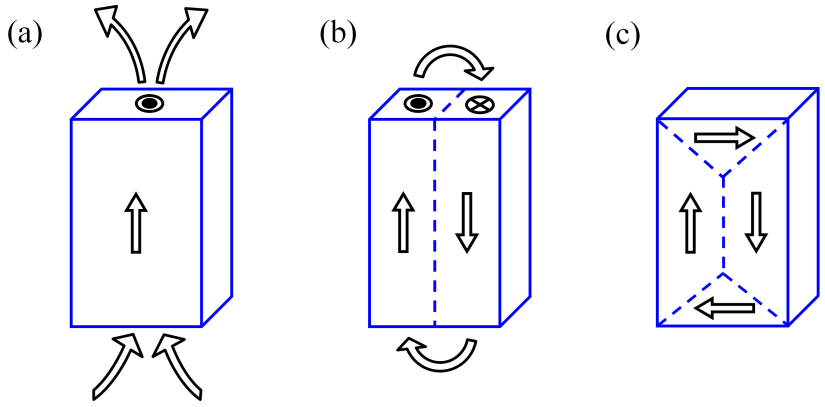

Figure 2.1: Schematics showing the stray-field minimization by formation of domains inside a ferromagnetic sample.

For energy minimization, the magnetization inside the transition regions (domain walls) must rotate gradually. More gradual is the rotation of the magnetization, lower

is the exchange energy of the domain walls because the angle between the neighboring magnetic moments will decrease. This, in turn, increases the magnetic anisotropy energy (if the magnetic sample possess an anisotropy), as the domain wall becomes wide and a large number of the wall's magnetic moments will lie along the magnetic hard axis. Therefore, the domain walls are formed to minimize the demagnetization energy, whereas the number and widths of the domain walls are limited by the increase in anisotropy and exchange energies. Hence, the formation of domains and domain walls inside a magnetic sample is the result of an interplay between the demagnetization, exchange and anisotropy energies of the sample.

However, there exists a critical size of the sample, below which the magnetization does not divide into domains [10]. Below the critical size, it becomes energetically unfavorable to create domain walls as the lowering in the demagnetization energy is not sufficient to compensate the increase in the exchange and anisotropy energies.

2.2 Types of domain walls in soft ferromagnetic materials

There exist a vast variety of the domain walls depending on the intrinsic parameters such as anisotropy and stress as well as the extrinsic parameters such as shape and thickness of the material [2]. However, in general, the domain walls are classified into two basic types known as Bloch and Néel walls [10].

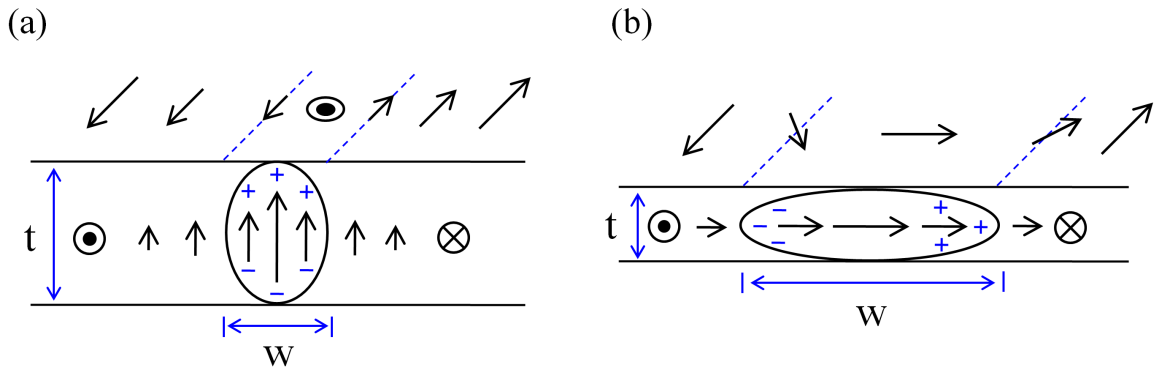

Figure 2.2: Schematics showing the magnetizations inside a Bloch (a) and Néel wall (b), respectively. Figures adapted from Ref. [2].

Figure 2.2 shows sketches of the Bloch and Néel walls inside infinitely extended thin films which have an in-plane magnetic anisotropy, respectively. In the Bloch wall configuration, the magnetization inside the wall rotates perpendicular to the film plane, whereas the magnetization inside the Néel walls rotates in the plane of the film [2]. The

out-of-plane orientations of the magnetization inside the Bloch walls induce opposite magnetic charges on the upper and lower surfaces of the walls, respectively, as shown in Fig. 2.2(a). The in-plane orientations of the magnetization inside the Néel walls induce opposite magnetic charges on the sides of the wall, as shown in Fig. 2.2(b). Néel [75] realized that the standard wall theory of Bloch walls does not hold for films thinner than the width of the domain wall. The interaction between the magnetic charges induced on the surfaces makes the Bloch walls energetically unstable. The argument follows as: if the cross-section of the domain wall is approximated in an elliptical shape of height t and width W as shown in Fig. 2.2, then the demagnetizing factor for the Bloch wall is $N_{\mathrm{B}} = W/(W+t)$. If the thickness of the film (t) becomes smaller than the wall width (W), the demagnetization energy increases which makes the flipping of the domain wall magnetization from the out-of-plane (Bloch type) to in-plane (Néel type) orientation. The demagnetizing factor for the Néel wall configuration is $N_{\mathrm{N}} = t/(W+t)$, which is smaller than N_{B} for $W > t$ [2].

The width (W_{B}) and energy density (σ_{B}) of a 180° Bloch wall can be written as [66]

$$W_{\mathrm{B}} = \pi\sqrt{\frac{A_{\mathrm{ex}}}{K_{\mathrm{u}}}} \quad \text{and} \quad \sigma_{\mathrm{B}} = 4\sqrt{A_{\mathrm{ex}}K_{\mathrm{u}}}. \tag{2.24}$$

The width (W_{N}) and energy density (σ_{N}) of a 180° Néel wall are written as [66]

$$W_{\mathrm{N}} = \pi\sqrt{\frac{A_{\mathrm{ex}}}{K_{\mathrm{u}} + (1/2)\,\mu_0 M_{\mathrm{s}}^2}} \quad \text{and} \quad \sigma_{\mathrm{N}} = 4\sqrt{A_{\mathrm{ex}}(K_{\mathrm{u}} + \frac{1}{2}\mu_0 M_{\mathrm{s}}^2)}. \tag{2.25}$$

The ratio of the anisotropy constant K_{u} to the stray-field constant K_{D}, i.e.,

$$Q = \frac{K_{\mathrm{u}}}{K_{\mathrm{D}}} = \frac{2K_{\mathrm{u}}}{\mu_0 M_{\mathrm{s}}^2}, \tag{2.26}$$

is known as the quality factor of magnetic materials. Materials with a very small quality factor, i.e., $Q \ll 1$, are called soft magnetic materials. In soft magnetic materials, due to the absence of a crystallographic or a field-induced anisotropy, the magnetization can easily orients within the film in order to minimize the demagnetization energy. Therefore, soft magnetic materials show various different types of domain walls due to the intrinsic and/or extrinsic influences as described above. In the following subsections, different types of domain walls with the change of the thickness of Py films (see section 3.1 for details about the magnetic and structural characteristics of Py) will be discussed. In micro-patterned thin films, typically, 90° and 180° domain walls exist in their magnetic ground states (the lowest energy state) and zero-field states with

magnetic flux-closed configurations. So the configurations of 90° and 180° domain walls are discussed in the following subsections.

2.2.1 Symmetric Néel walls

In Py films at thicknesses below approximately 20 nm, all domain walls' magnetization stays in the plane of the film, i.e., one finds Néel type orientation, because of the minimization of the demagnetization energy as discussed above. Figure 2.3 describes the schematics of 90° Néel walls in this thickness regime, respectively. As the magnetization configuration in both halves of the domain walls is mirror symmetric, these domain walls are called symmetric Néel walls (SNWs) [2].

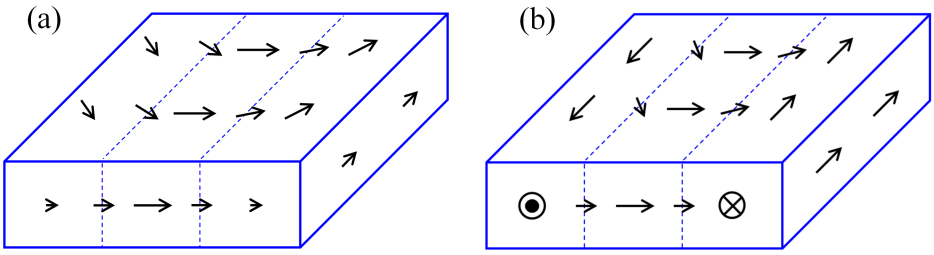

Figure 2.3: Schematics of (a) a 90° and (b) a 180° SNW, respectively. To represent the projections of the magnetization vectors on the sample surfaces, the arrows of varied lengths are drawn.

In Fig. 2.3, if we look from the top surfaces, the magnetization inside both 90° and 180° domain walls rotates with counter-clockwise orientation. However, these domain walls also exist with clockwise rotation of magnetization and they have equal energies for both rotation orientations [2, 66].

2.2.2 Cross-tie walls

A 90° SNW has only 12% of the energy of a 180° SNW [2]. As the in-plane magnetization configurations in the SNWs (Fig. 2.3) produce magnetic charges on both sides of the wall as described in Fig. 2.2(b), therefore the energy of a SNW also increases due to the increase of the film thickness. As a result, above approximately 20 nm thickness a 180° SNW transforms into a cross-tie arrangement of 90° SNWs called Cross-tie wall (CTW) [76, 77]. This domain wall is stable from approximately 20 to 100 nm thickness [78].

In Fig. 2.4, a schematic of a CTW is shown. The magnetizations inside the wall are arranged in circular and cross configurations which generate vortices and antivortices

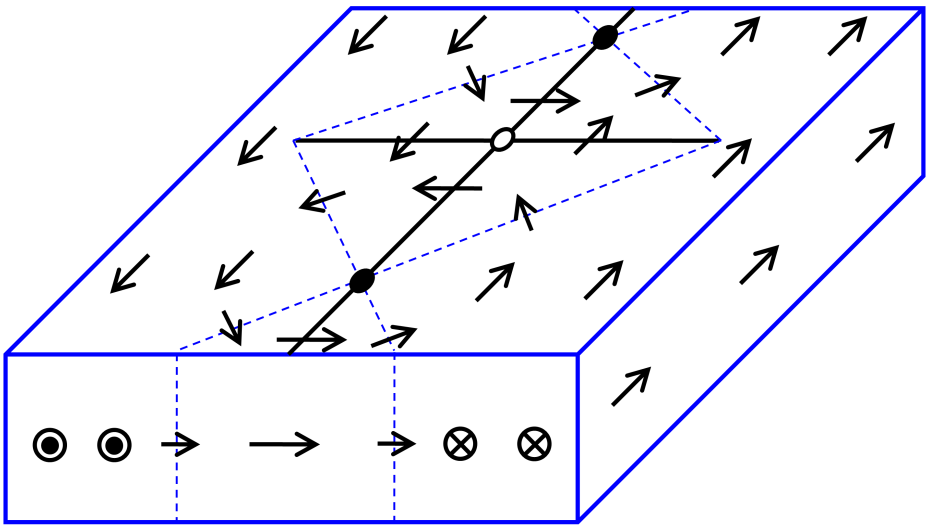

Figure 2.4: A schematic of a CTW. The vortex and antivortex cores are shown with filled and open dots, respectively.

(see subsection 2.4.1) also known as circular and cross Bloch lines inside the walls, respectively [2]. The circular and cross Bloch lines are indicated by filled and open dots in Fig. 2.4. All domain walls in this thickness regime are 90° SNWs. The wall segments of the CTW (i.e., 90° SNWs) switch their magnetization across the circular and cross Bloch lines. The magnetization inside a CTW is in the plane of the film except at the center of circular and cross Bloch lines, where the magnetization points out-of-plane of the film.

It is important to mention that the CTW separates two anti-parallel domains, as visible in Fig. 2.4. Therefore, a CTW is actually a 180° domain wall composed of 90° wall segments. The other 90° domain walls in this thickness regime are the 90° SNWs (Fig. 2.3(a), as described above in the previous subsection 2.2.1).

2.2.3 Asymmetric domain walls

The domain walls to be discussed in this subsection are stable in somewhat thicker films than those in which SNWs and CTWs are stable, i.e, above approximately 100 nm thick Py films. These domain walls are called ADWs or vortex walls because they have one or two vortex structures along the wall axes (in the cross-section of the wall) which are placed asymmetrically to the center of the walls. These domain walls were derived by Hubert [79] and LaBonte [80] independently in 1969 from the SNWs and symmetric Bloch walls (shown in Fig. 2.2) by avoiding the stray field on the wall

surfaces and allowing an asymmetry in the wall structure with respect to the wall plane. Ideally, the ADWs derived by Hubert [79] and LaBonte [80] are divergence-free. However, the domain walls existing in real magnetic films are not completely divergence-free and produce stray field [81, 82], as the complete divergence-free domain walls would have higher energies. ADWs are further classified into asymmetric Néel walls (ANWs) and asymmetric Bloch walls (ABWs), as presented in Figs. 2.5(a) and (b), respectively. Their detailed cross-sectional magnetization is shown in Figs. 2.5(c) and (d), respectively. These domain walls have SNW-type magnetization at the surfaces called Néel caps (NCs), which are joined with symmetric Bloch wall type orientations in the interiors of the walls called Bloch cores, as shown in Fig. 2.6(a).

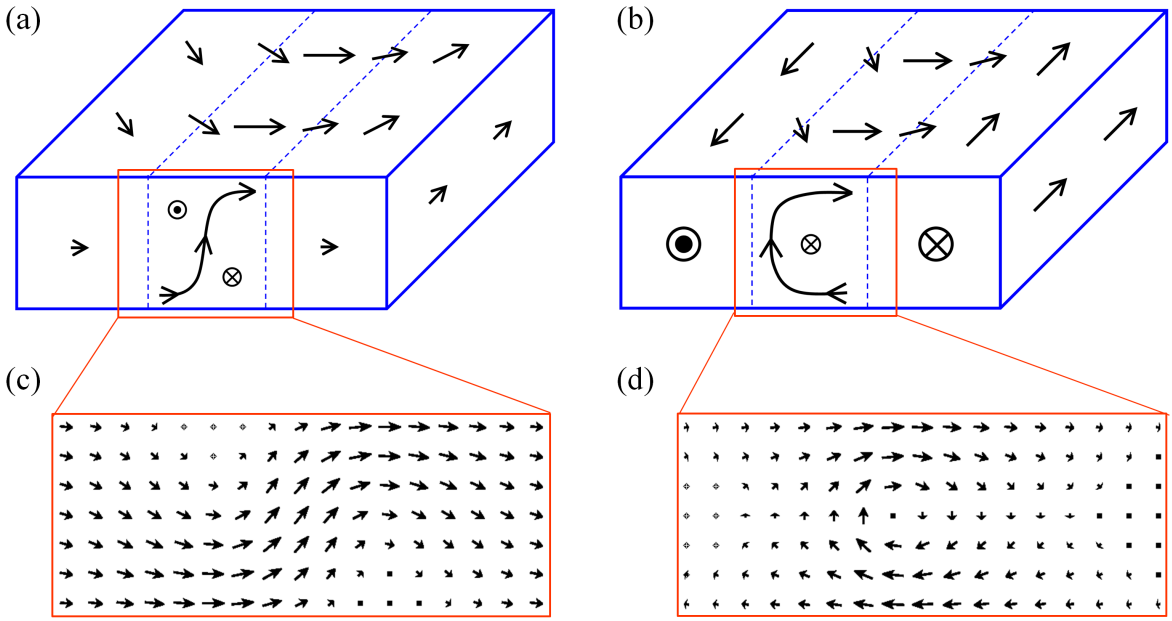

Figure 2.5: Schematics of (a) a 90° ANW and (b) a 180° ABW. Curved lines show the cross-sectional magnetization of the domain walls. (c) and (d) show their detailed cross-sectional views, respectively.

The ANWs have "S" type of cross-sectional magnetization configuration, whereas the ABWs have "C" type of cross-sectional magnetization configuration. ANWs are formed for wall angles approximately from 40° up to 150° (see Fig. 2.10) [83]. The upper and lower NCs in ANWs are formed on the left and right sides of the Bloch cores or vice versa, as shown in Fig. 2.6(b). For higher wall angles up to 180°, ABWs are formed (see Fig. 2.10) [83]. In ABWs both the upper and lower NCs are formed on the same side of the Bloch cores as shown in Fig. 2.6(c).

Figures 2.5(a) and (b) show counter-clockwise oriented asymmetric domain walls

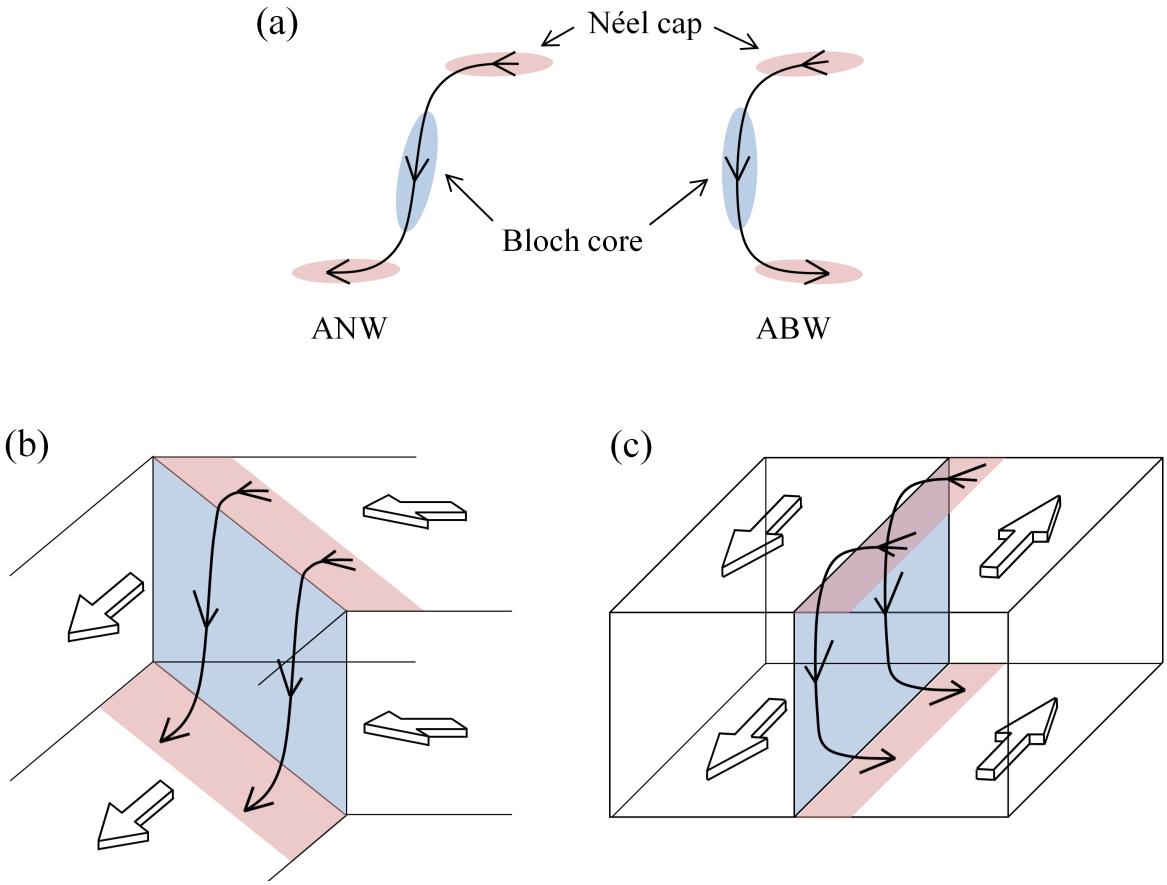

Figure 2.6: (a) NC and Bloch core components inside an ANW and an ABW. More detailed schematics of (b) a 90° ANW and (c) a 180° ABW along with the adjacent domains, respectively. Bold arrows represent the magnetization inside the adjacent domains, whereas the magnetization inside the domain walls is represented by curved lines. Grayish-pink and blue shaded areas represent NCs and Bloch cores inside the domain walls, respectively.

(if one looks from the top surface). However, as the asymmetric domain walls have both in-plane and out-of-plane components of the magnetization, in addition to the switching of the in-plane orientation at the NCs there is another degree of freedom which is the switching of the Bloch core. As a result, four different magnetization configurations of each ANWs and ABWs are possible, as shown in Fig. 2.7. All these respective configurations of ANWs and ABWs have the same energies [2].

In Fig. 2.8, a three-dimensional magnetization configuration in a 400 nm thick 2.3×6.7 µm^2 Py sample is shown. Figures 2.8(a) and (b) show the magnetization at the upper and lower surfaces of the sample, respectively. It is visible that a vortex is formed at the right end of the 180° ABW at the upper surface and at the left end of the 180° ABW at the lower surface of the sample, respectively. In Figs. 2.8(c) and

(d), Bloch cores inside the ANWs and ABWs are shown as magnetization iso-surfaces for out-of-plane magnetization components. In Fig. 2.8(d), it is visible that the Bloch core of the ABW is connected to the vortex cores at both surfaces. The change in the (surface) magnetic configuration with thickness results from the two-dimensional configuration of the ADWs.

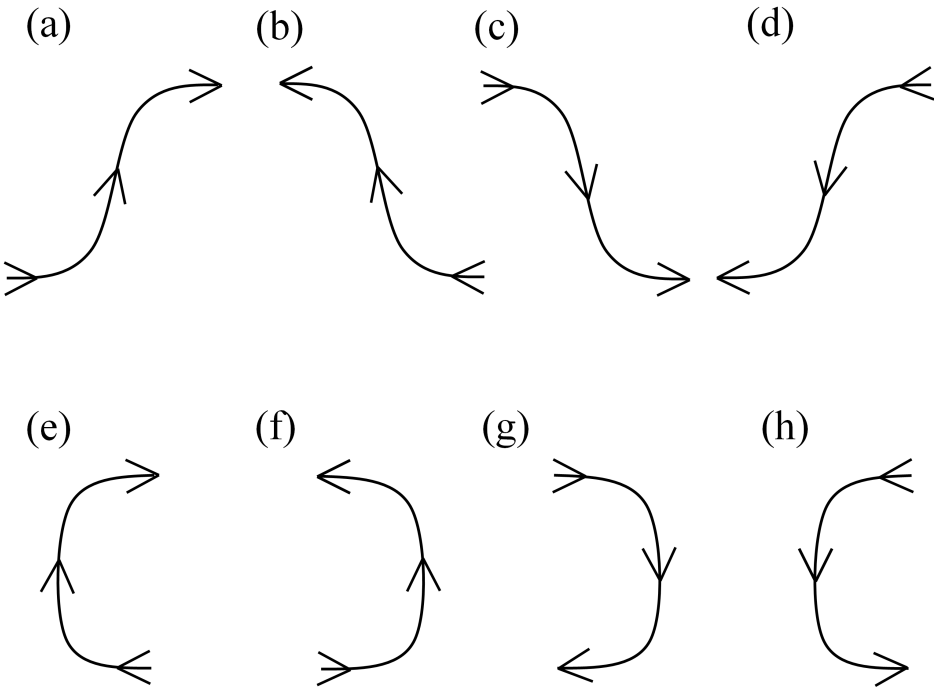

Figure 2.7: Four energetically equivalent configurations of (a) to (d) an ANW and (e) to (h) an ABW.

The size of the vortex structure (i.e., the width of the Bloch core) in the cross-sections of the ADWs is controlled by the thickness of the film. As in the low-anisotropy materials for a stray field free configuration, the exchange energy is a significant energetic contribution. But the vortex cannot lower its exchange energy by increasing its size which is limited by the thickness of the film.

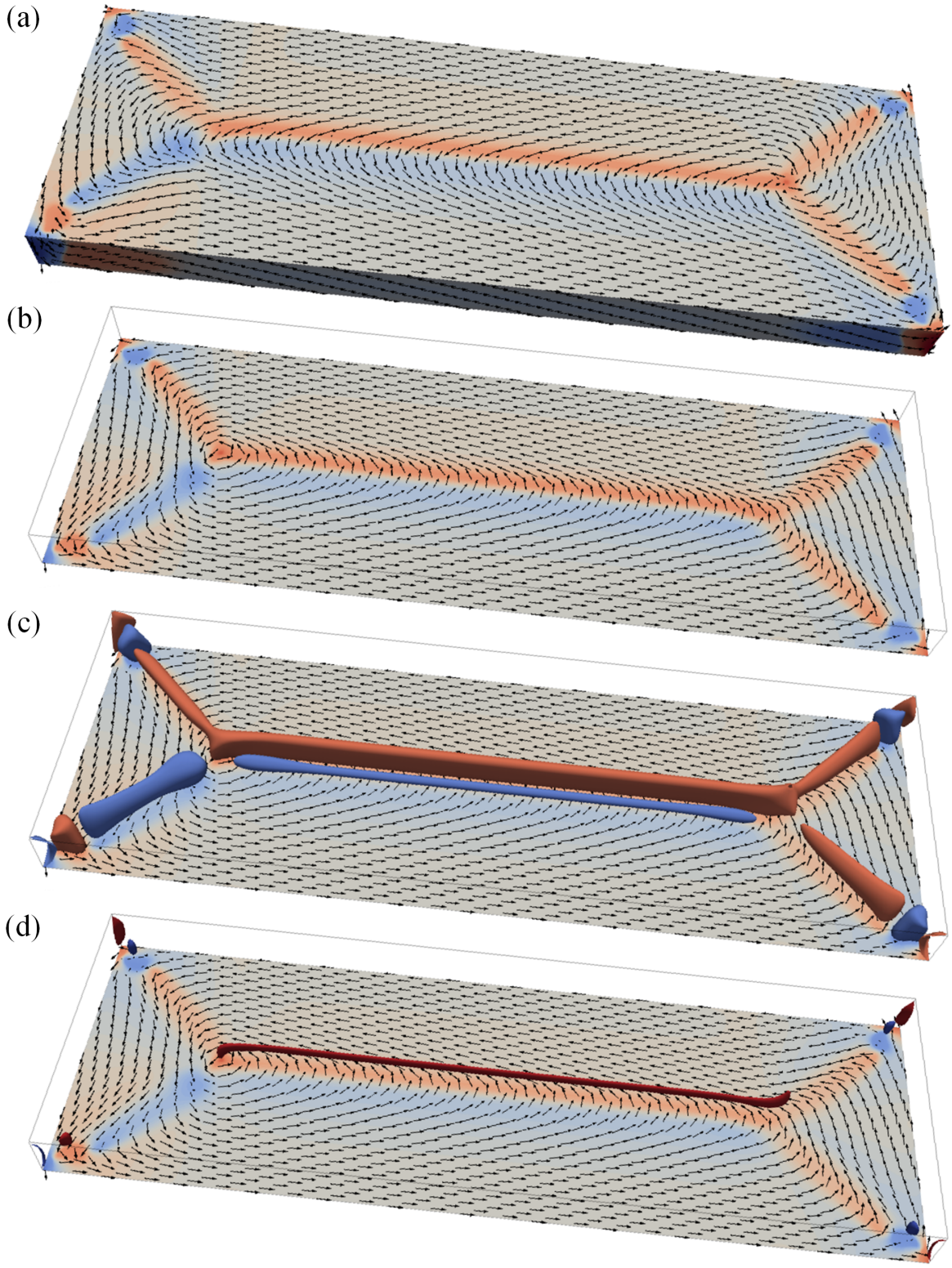

Figure 2.8: A landau domain magnetization configuration in a 400 nm thick Py sample. (a) Magnetization at the top surface and sides of the sample. (b) Magnetization at the bottom surface of the sample. In (c) and (d), in addition to the magnetization at the bottom surface, magnetization iso-surfaces of the out-of-plane magnetization components at $M_z = \pm 0.5 M_s$ and $M_z = \pm 0.9 M_s$ are shown, respectively. Red-brown and blue colors (both on the iso-surfaces and on the sample surfaces) correspond to the upwards and downwards oriented magnetization, respectively.

2.2.4 Domain walls in bulk soft magnetic materials

Above a thickness of the order of $5\sqrt{A_{ex}/K_u}$ (which is about 2 µm for Py films assuming $K_u \approx 100$ Jm^{-3} [2]) the energetical difference between the ABWs and ANWs disappears [2, 84]. Above this thickness, a wall structure develops, which is still related to the ABW. Instead of a single vortex in the middle (interior of the wall), vortices are formed that are confined to the neighborhood of the surfaces. In the interior, this divergence-free wall assumes a one-dimensional character with a rotation parallel to the wall plane like in a classical Bloch wall, and at the surfaces, the vortices close the magnetic flux with a Néel-like rotation right at the surface, shown in Fig. 2.9. Rave and Hubert [85] found by numerical simulation that the surface wall width steadily increases with thickness, whereas the interior wall width approaches the expected classical value of $\pi\sqrt{A_{ex}/K_u}$. Consequently, the domain wall widths in bulk materials are not localized in the case of zero anisotropy, in contrast to the thin films.

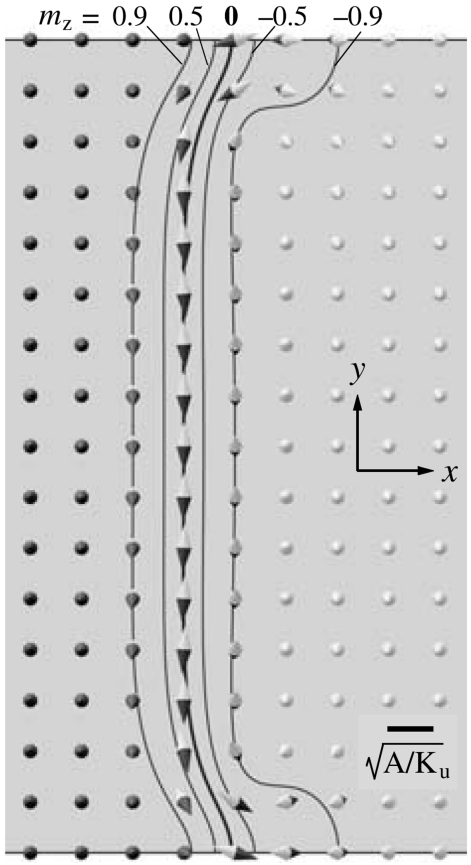

Figure 2.9: Cross-sections of a domain wall in a soft magnetic film with a thickness of $20\sqrt{A_{ex}/K_u}$. The contour lines indicate the wall by lines of constant m_z magnetization [85].

2.3 Domain-wall phase diagram

Figure 2.10 shows a phase diagram of different types of domain walls in Py films with $Q = 2.5 \times 10^{-4}$ (see equation (2.26)), as a function of the film thickness and wall angles [2, 86]. Other parameters are the typical Py material constants such as an exchange stiffness constant A_{ex} (or A) $= 10^{-11}$ Jm^{-1} and $M_s = 1$ T. This phase diagram is also approximately valid for other soft magnetic materials, which have quality factor close to 2.5×10^{-4} and easy axes parallel to the film plane.

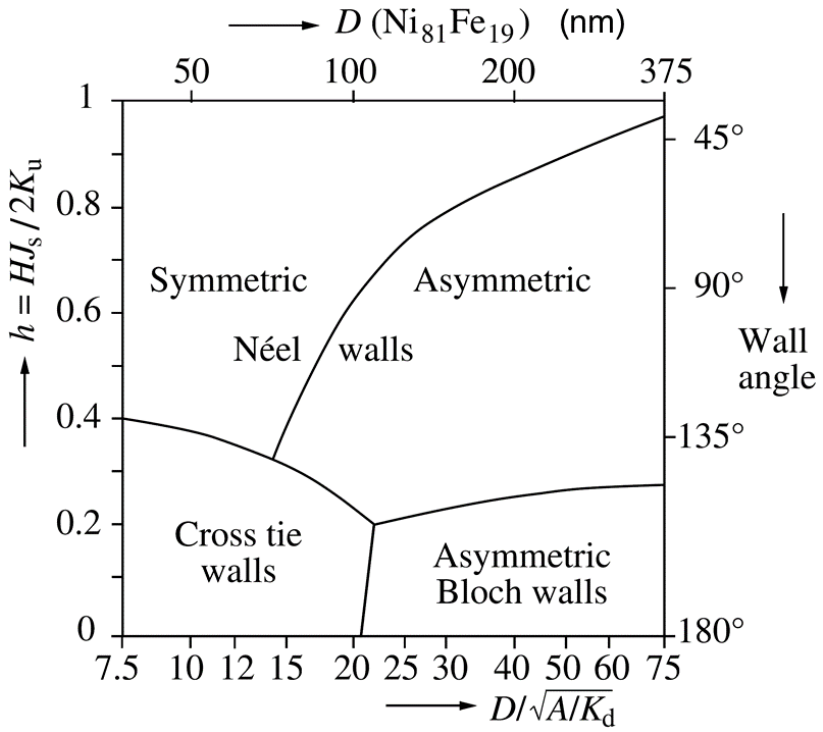

Figure 2.10: Phase diagram of domain walls in Py thin films as a function of film thickness D (denoted by t in this thesis) and wall angle [2].

The angle of a domain wall within an externally applied field perpendicular to the wall-axis changes with the rotation of the magnetization inside the adjacent domains, as shown in Fig. 2.11. The angle of the wall decreases with the increase of the applied field because the magnetization inside the adjacent domains starts aligning along the direction of the applied field. In Fig. 2.10, h is the normalized parameter of the externally applied field, where $J_s = \mu_0 M_s$ and M_s is the saturation magnetization.

From Fig. 2.10, SNWs are the only stable domain walls in a large field at all thicknesses. The applied magnetic field forces the magnetization inside the domain

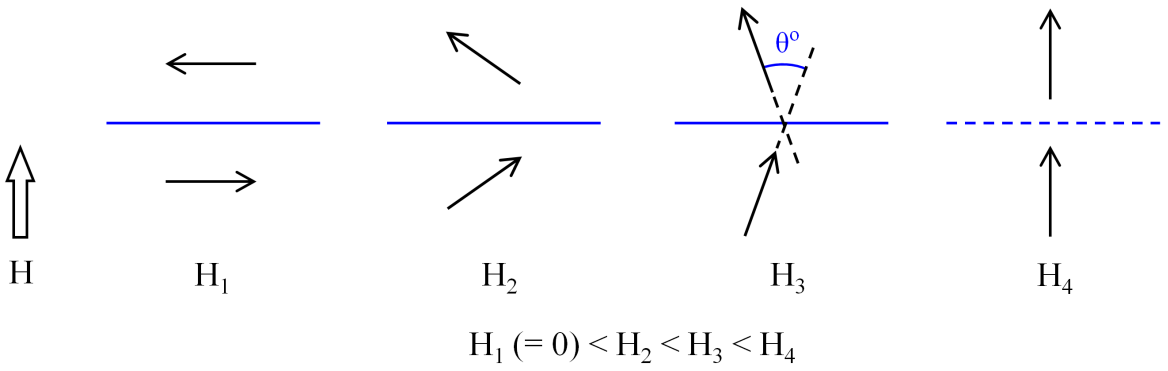

Figure 2.11: Schematics of the change in angle of domain wall (blue line) with the change of an applied field. Black arrows represent magnetization directions inside the adjacent domains.

walls to stay in the plane of the films. For films with thicknesses approximately below 100 nm, as the field is reduced, the increase in the energy of the wall with the increase of the domain-wall angle results in the transformation of the SNW into cross-tie patterns of 90° SNWs (CTW, as discussed in subsection 2.2.2). Whereas the SNWs in thicker films first transform into ANWs and later into ABWs with the reduction of the applied magnetic field in order to avoid the stray field [2, 86].

Here, it is important to mention that the symmetric Bloch walls, shown in Fig. 2.2(a), do not exist in soft magnetic materials. Due to a very small or negligible anisotropy energy, the magnetization at the wall surfaces orients in the plane of the film in order to minimize the demagnetization energy. However, in common conception, the SNWs are called Néel walls and ADWs are called Bloch walls.

2.4 Vortices, antivortices and Bloch points

Magnetic materials, especially soft magnetic materials with anisotropy energies much smaller than the demagnetization energy or $Q \ll 1$ (see equation (2.26)), tend to avoid the stray field as far as possible. The solution is to fulfill the conditions $\nabla \cdot \mathbf{M}(\mathbf{r},t) = 0$ and $\mathbf{M}(\mathbf{r},t) \cdot \mathbf{n} = 0$ with a constant modulus of $\mathbf{M}(\mathbf{r},t)$. Such pole-free magnetization vector fields are possible only for infinitely extended two-dimensional bodies [87]. For real finite three-dimensional bodies, ideal stray-field-free magnetization configurations do not exist. From the topological point of view, a unit vector field cannot be combed everywhere parallel to a closed surface. At least two singular points have to be present at the surface where the vector field is not parallel to the surface of the body [87, 88].

As discussed in subsection 2.1.2, domain walls are formed as a result of the stray field minimization. However, from the topological argument discussed above, minimization of a stray field also leads to other topological defects in the vector field configuration such as vortices, antivortices, Bloch points (BPs), bubble domains and skyrmions etc. [88]. In this section, only vortices, antivortices and BPs are discussed, which are relevant to the scope of this thesis.

2.4.1 Vortices and antivortices

In Fig. 2.12, schematics of the detailed magnetization inside a vortex and an antivortex are shown, respectively. In both vortices and antivortices, the in-plane magnetization rotates by 360° along a closed loop path surrounding them. In order to minimize the exchange energy, magnetization in the centers of both vortices and antivortices turn out-of-plane of the film (i.e., parallel to the z axis in Fig. 2.12). Because from the basis of micromagnetics, $\mathbf{M}(\mathbf{r},t)$ is a function of position and time while its modulus stays constant. A full in-plane magnetization would lead to a singularity of the exchange-energy density, which is avoided by turning magnetization out of the film plane. The regions with the out-of-plane-oriented magnetization are called cores of vortices and antivortices. The core region in soft magnetic materials is typically of the size of 10 nm in width [2, 87]. Around the vortex core, the in-plane magnetization makes a closed flux loop as shown in Fig. 2.12(a). This results in the switching of the in-plane magnetization across the central core. Whereas, around the antivortex core, in addition to the switching of the in-plane magnetization across the central core, there also exist two in-plane directions along which the magnetization is directed towards and away from the central core, respectively, as shown in Fig. 2.12(b). In Figs. 2.12(c) and (d), the out-of-plane magnetization profiles are also shown in the cross-sectional schematics.

The vortices and antivortices are also further characterized by their polarity (p), chirality (c) and winding numbers (x). The polarity of the vortices and antivortices is defined as ± 1 depending on the upwards or downwards out-of-plane oriented magnetization inside the core, respectively. The chirality is only defined for vortices as a clockwise and counter-clockwise sense of magnetization rotation around the core. The winding number (also called vorticity), is $+1$ for a vortex, regardless of the clockwise or counterclockwise chirality, and -1 for an antivortex. The winding number is calculated as the change in the angle of the local magnetization, integrated over a loop around the vortex or antivortex core, divided by 2π. Another topological invariant is the Skyrmion number $q = \pm xp/2$ ($+$ sign for the top surface and $-$ sign for the bottom surface). In

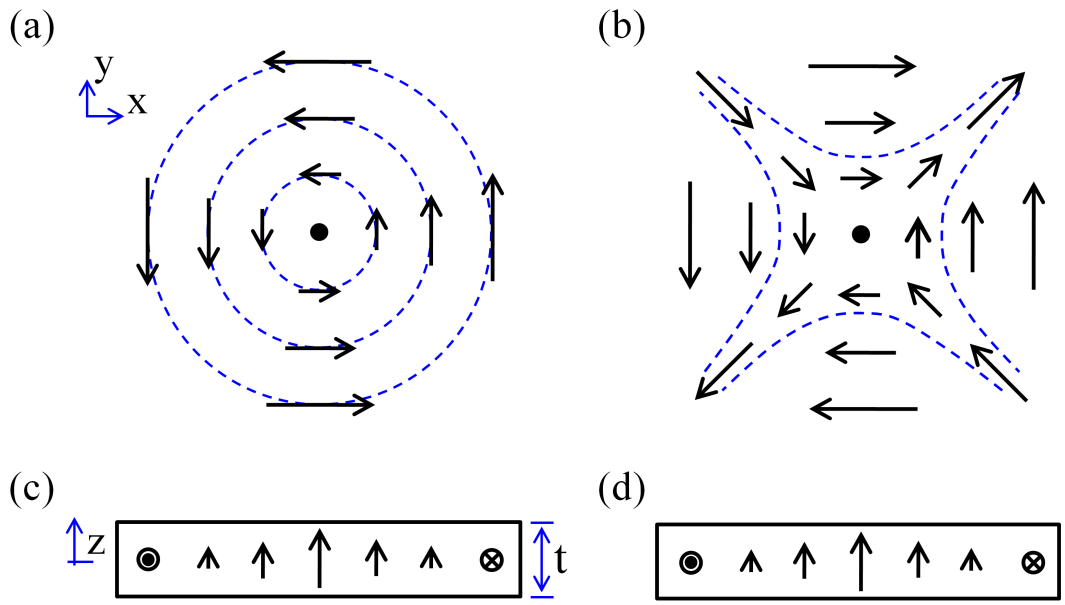

Figure 2.12: Schematics of a vortex in (a) and (c) and an antivortex in (b) and (d), respectively. (a) and (b) describe the the top views of the vortex and antivortex, respectively. (c) and (d) show the cross-sectional views of the vortex and antivortex, respectively. Schematics adapted from Ref. [2].

thin-film elements, the Skyrmion number can be considered as a topological invariant for each surface.

2.4.2 Bloch points

Although micromagnetics assumes a continuous variation of the magnetization vector $\mathbf{M}(\mathbf{r},t)$ with position, Feldtkeller proved that some magnetic configurations demand the topological presence of singularities, called BPs [89]. The BPs are singular magnetic configurations in micromagnetics where a noncontinuous transformation between two opposite magnetizations occurs. These are topological point defects. At the center of the BP structure, it is not possible to assign a magnetization direction. This is in obvious disagreement with the fundamental assumption of the micromagnetic theory that modulus of $\mathbf{M}(\mathbf{r},t)$ stays constant. Therefore, the magnitude of the gradient of $\mathbf{M}(\mathbf{r},t)$ tends to infinity in its neighborhood. BP cannot be investigated within the framework of micromagnetics. But it can be shown that all the magnetization directions occurring on a closed surface surrounding the singular point, can be transferred onto the surface of a unit sphere of magnetization directions [2]. If we try to shrink the surrounding surfaces towards the transition region, a theorem of the topology states

that there exists no continuous path from the surface to the transition region with a well-defined magnetization direction [2]. At least one singularity must exist inside the surface. Furthermore, by considering the topological argument, the BP is the only stable singularity in ferromagnets [88, 90]. Therefore, BPs cannot appear alone, either they are created in pairs or enter from the boundary of the ferromagnet [90, 91]. Essentially, they consist of a small region of a few lattice constants in which the ferromagnetic order is destroyed.

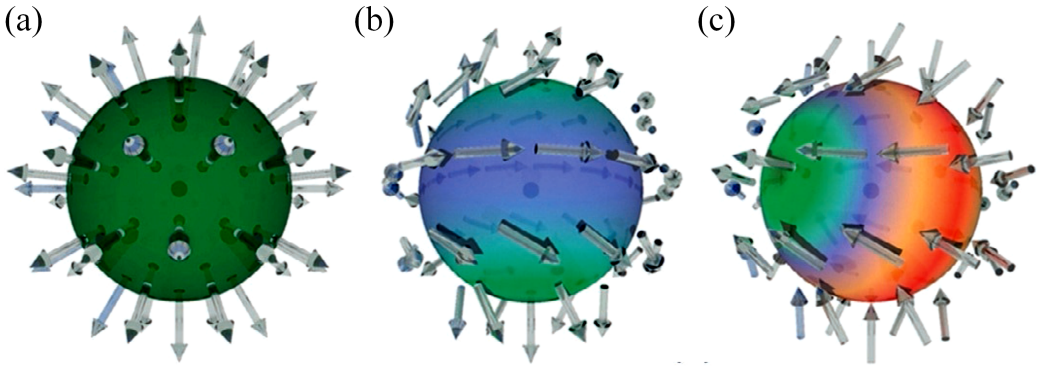

Figure 2.13: Different types of BP structures as discussed in the text [92]. (a) A purely radial "hedgehog"-type BP, (b) a BP with an azimuthal vortex in the central plane, and (c) a variant of case (b) where the vortex is replaced by an antivortex.

Considering a sphere with a radius R surrounding the BP but far enough so that micromagnetic theory can be applied, Feldtkeller [89] showed that the leading energy is the exchange energy, which is given by [91]

$$E_{\mathrm{ex(BP)}} = 8\pi A_{\mathrm{ex}}\, R. \tag{2.27}$$

Where A_{ex} is the exchange constant. Topologically, the simplest configuration of the BP assumes the form $\mathbf{M}(\mathbf{r},t) = \pm M_{\mathrm{s}}$ in which the magnetization directly diverges or converges thereby defining "positive" and "negative" BPs, respectively. These BP configurations are also called hedgehog BPs and are shown in Fig. 2.13(a). This configuration has the highest demagnetization energy, as it builds up a large monopole in the center. This monopole charge is reduced in Fig. 2.13(b) by a 90° rotation of the magnetic moments and forms an anisotropic structure, with a vortex perpendicular to the axis of the rotation. Another variant of this vortex-type, axial BP structure has a magnetic antivortex instead of a vortex in the plane perpendicular to the rotation axis, shown in Fig. 2.13(c). Actually, an infinite number of BP configurations can occur.

A good description of the various BP configurations such as divergent, convergent, circulating and contra-circulating etc. can be found in Ref. [93].

2.5 Micromagnetic transition structures inside domain walls

The macroscopic properties of magnetic materials, which are important from the practical point of view, such as magnetic hysteresis, are substantially determined by the types of the spatial magnetization configurations formed and their modifications under external influences. The spatial distribution of the magnetization has a hierarchical structure, i.e., a ferromagnetic sample is divided into domains by domain walls, while the domain walls themselves may contain segments of different magnetization distributions separated by localized TSs, shown as blue rectangular blocks in the simplified schematics in Fig. 2.14. Although the TSs are small from the macroscopic point of view, they have sizes significantly exceeding the interatomic distances, and therefore the magnetization $\mathbf{M}(\mathbf{r})$ can be considered as a continuously varying function of position $\mathbf{r}$. TSs have significant influence on both static and dynamic properties of domain walls [2, 5, 9, 22, 26, 31, 34, 94–96]. In Figs. 2.14(a) and (b), TSs inside one-dimensional (i.e., SNWs) and two-dimensional (i.e., ANWs and ABWs) domain walls are shown, respectively. The TSs are further composed of vortices, antivortices and BPs. Since in Py films the domain-wall configuration changes from one-dimensional to two-dimensional at a thickness of approximately 100 nm, the internal configuration of the TSs also changes with the film thickness. The TSs inside the one-dimensional and two-dimensional domain walls are discussed in detail in the following subsections.

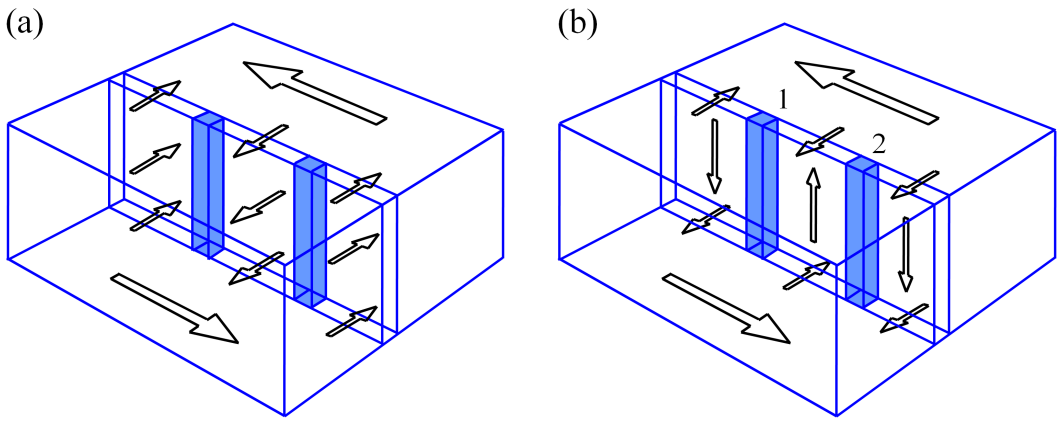

Figure 2.14: Simplified schematics of TSs inside (a) a SNW and (b) ANW/ABW. TS "1" is between two ABWs and TS "2" is between an ANW and an ABW.

2.5.1 Transition structures inside one-dimensional domain walls

Most domain walls in the absence of an applied magnetic field exist along with their equivalent forms (equal energy configurations) inside micro-structured thin films. The CTW shown in Fig. 2.4 belongs to one of such domain wall types, where the alternately reversed magnetization components of SNWs are co-existing inside the main wall. In Py films of a thickness regime approximately from 20 to 100 nm, vortices and antivortices exist as TSs inside the one-dimensional SNWs. Below 20 nm thickness, the domain walls avoid the formation of TSs for energetic reasons [2].

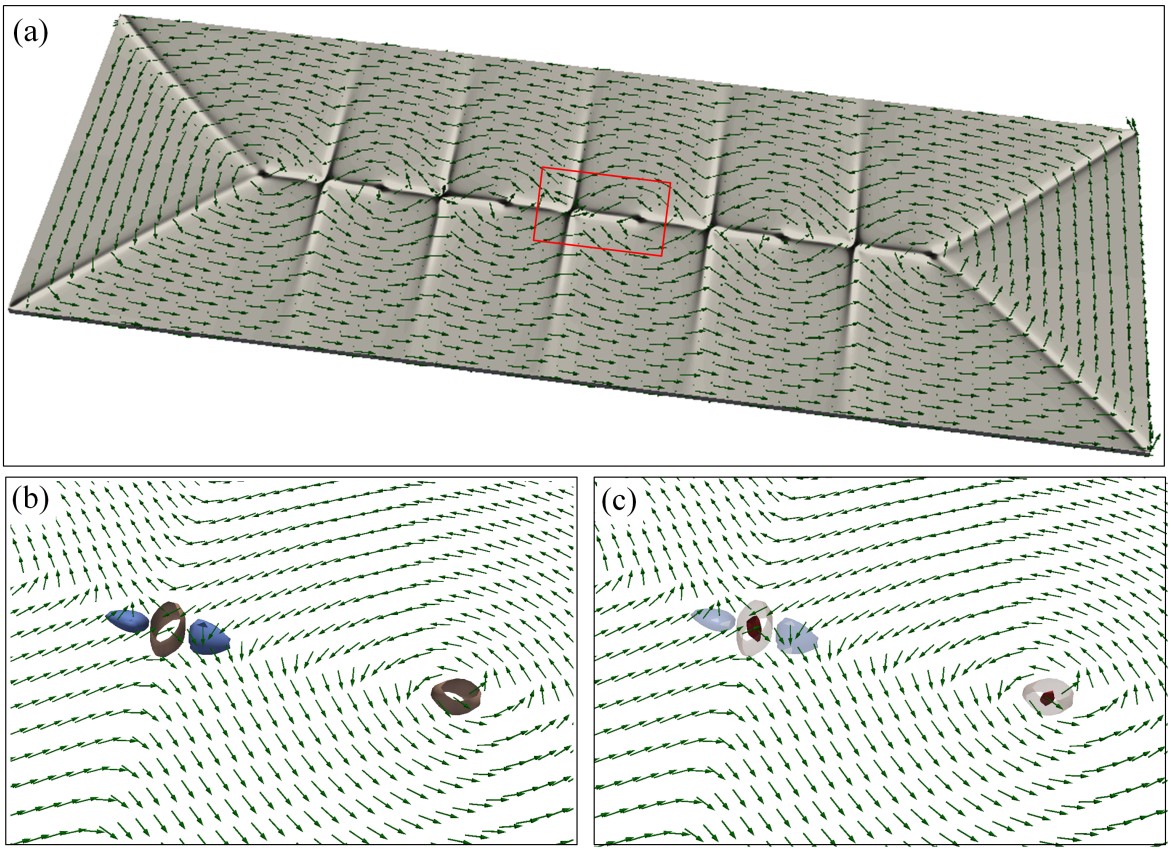

Figure 2.15: (a) A CTW in a 50 nm thick 2.3×6.7 µm^2 Py sample. (b) and (c) show iso-surfaces of the out-of-plane magnetization at $M_z = \pm 0.2 M_s$ and $M_z = \pm 0.7 M_s$ in the area selected from (a), respectively. In (c), the transparent magnetization iso-surfaces correspond to $M_z = \pm 0.2 M_s$.

In Fig. 2.15, a detailed magnetization configuration around a pair of a vortex and an antivortex inside a CTW is shown. Figures 2.15(b) and (c) show the magnetization iso-surfaces of the out-plane magnetization components inside the area selected in Fig. 2.15(a). The magnitude of the out-of-plane component of the magnetization decreases

with the distance from the centers of the cores. From these images, it is clear that except in the cores of vortices and antivortices, the magnetization inside the domain walls is in the plane of the film.

2.5.2 Transition structures inside two-dimensional domain walls

As discussed above in subsection 2.2.3, in the absence of an external magnetic field, the ANWs and ABWs each have four energetically equivalent forms shown in Fig. 2.7. Due to the history of the system or the effect of some external factors, a domain wall can be composed of several segments of these different magnetization configurations. The domain wall segments of different configurations are separated by TSs. However, as the domain walls in this thickness regime are two-dimensional in magnetization, the TSs are more complex in magnetic configuration than for the lower thickness regime i.e., for approximately 20 to 100 nm thickness. A few out of many possible TSs inside two-dimensional domain walls are discussed below.

In Fig. 2.16, a three-dimensional magnetization configuration in a 180° domain wall inside a 130 nm thick 2.3×6.7 µm^2 Py patterned film is shown. Figures 2.16(a), (b) and (c) show the magnetization configurations at the top, middle and bottom surfaces of the right end of the pattern shown in Fig. 2.16(d). A single vortex in the center of the wall at the upper surface is visible in Fig. 2.16(a). In the interior of the wall, no clear vortex or antivortex is visible in Fig. 2.16(b). At the bottom surface, two vortices at the end of the domain wall and a single antivortex in the center of the wall are visible in Fig. 2.16(c). This confirms the three-dimensional configuration of the magnetization at this thickness. Moreover, it can be seen that the orientations of the NCs' magnetization switch at the upper and lower surfaces. Also the NCs' magnetization orientation across the vortex at the upper surface and across the antivortex at the lower surface switches. In Figs. 2.16(e) and (f), iso-surfaces of the out-of-plane magnetization components of $\pm 0.25 M_\mathrm{s}$ and $\pm 0.75 M_\mathrm{s}$ are shown, respectively. In Fig. 2.16(f), it is visible that the out-of-plane magnetization switches its orientation along the domain-wall-axis. This 180° domain wall is composed of two segments of upwards and downwards oriented ABWs. The TS which is composed of a vortex at the upper surface and an antivortex at the bottom surface separates the ABWs shown in Figs. 2.7 (e) and (h), respectively.

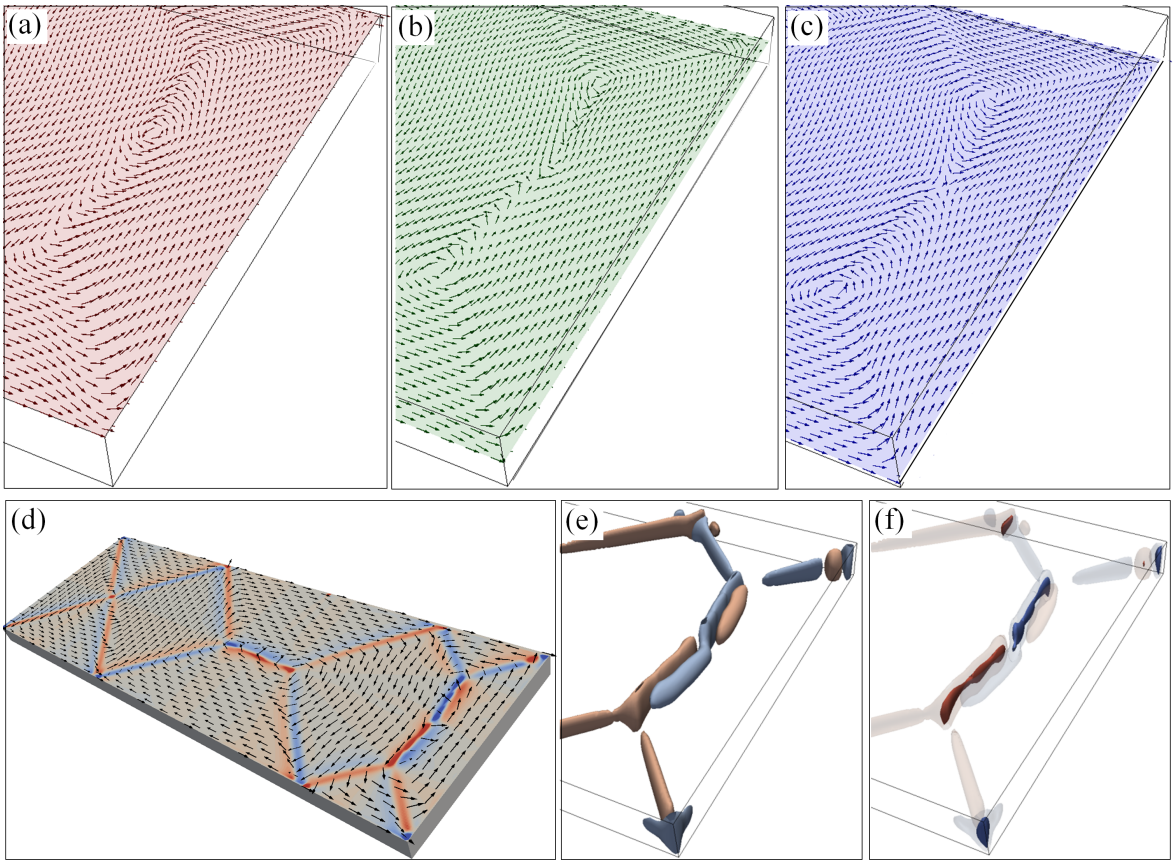

Figure 2.16: Detailed magnetization configurations at the top (a), middle (b) and bottom (c) surfaces of the right end of the 130 nm thick 2.3×6.7 µm^2 Py sample shown in (d). Magnetization iso-surfaces with $M_z = \pm 0.25 M_s$ (e) and $M_z = \pm 0.75 M_s$ (f) describe the out-of-plane magnetization inside the domain walls, respectively. In (f), the transparent magnetization iso-surface corresponds to $M_z = \pm 0.25 M_s$. Red-brown and blue iso-surfaces in (e) and (f) represent upwards and downwards oriented magnetizations, respectively.

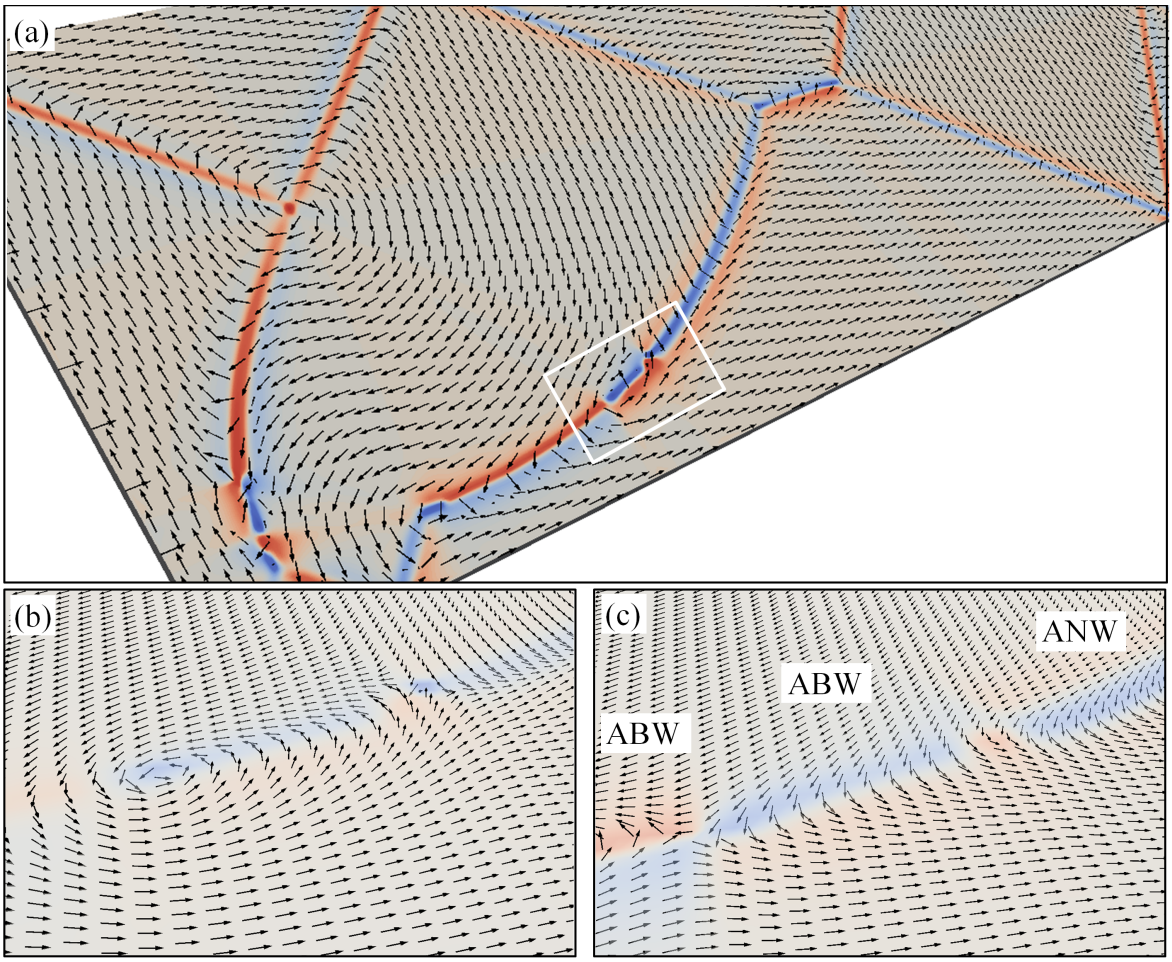

Figure 2.17: A part of the magnetization in a 130 nm thick 5×18 µm^2 Py sample shown in (a). The detailed magnetizations from the top surface (b) and the bottom surface (c) of the marked area from (a) are shown.

In Fig. 2.17, two TSs in a 130 nm thick 5×18 µm^2 Py pattern are shown. One TS is between two ABWs and another one is between an ABW and an ANW. In this image the TS between the ABWs is the same TS as already described in Fig. 2.16. The other TS with the switching of the NC magnetization, containing an antivortex at the upper surface (Fig. 2.17(b)) and showing an absence of a vortex or an antivortex at the lower surface (Fig. 2.17(c)), is a TS between an ABW and an ANW. This TS is between the domain walls shown in Figs. 2.7(c) and (h).

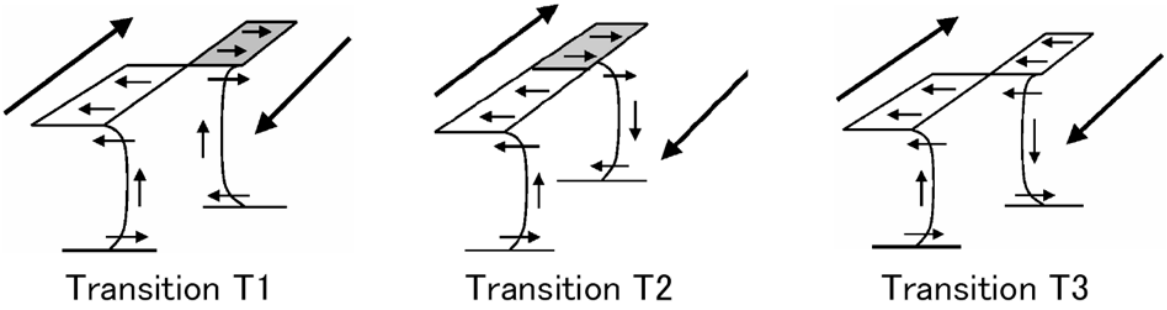

Figure 2.18: Schematics of different types of TSs between ABWs [6].

Several authors have described the detailed magnetization configurations of various types of TSs between different types of ABWs [6, 9, 96–100] as well as between different types of ANWs [9, 97, 101]. There exist three types of TSs between ABWs; named T1, T2 and T3 shown in Fig. 2.18. M. Redjdal et al. [99] explained the detailed magnetization configurations of these TSs as shown in Fig. 2.19. Iso-surfaces A and C represent the NC magnetization with $M_x = \pm 0.9 M_s$ and the iso-surface B represents the Bloch core of the domain walls with a magnetization of $M_z = \pm 0.9 M_s$. Iso-surface D represents the vortex-antivortex core with a $M_x = \pm 0.9 M_s$. Figures 2.19(a), (b) and (c) describe the T1, T2 and T3 TSs, respectively. For T1 and T2 TSs, a vortex and an antivortex were formed at opposite surfaces of the film, whereas a pair of a vortex and an antivortex was observed at one surface and no vortex or antivortex at the other surface in the T3 TS. Each arrow corresponds to the magnetization vector in the respectively indicated planes. However, V. V. Zverev et al. [9] and H. Asada et al. [6] found no vortex and antivortex at both surfaces of the film in the T3 TS. This discrepancy can be attributed to the fact that the calculation procedures used were different in their studies. V. V. Zverev et al. [9] observed a BP in the center of the T3 TS.

Just as in ABWs, fourfold degeneracy in ANWs also suggests the presence of at least three types of TSs. Micromagnetic simulations of two TS types were performed in Ref. [101] for 60 nm thick iron films with the boundary surface parallel to the crystallographic plane (001). The third type of the TS with two BPs in Py films was examined in Ref. [9].

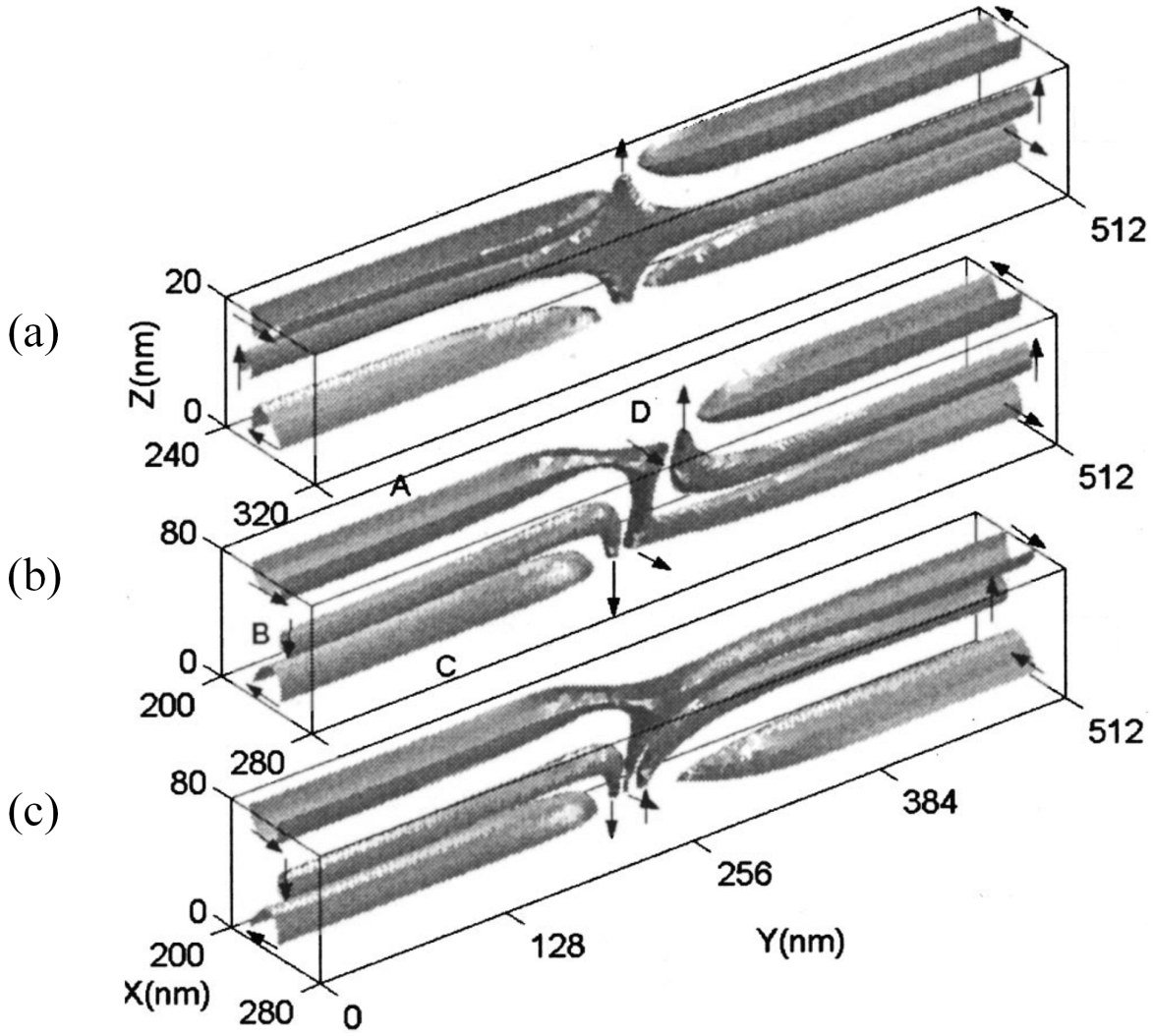

Figure 2.19: (a) "T1", (b) "T2" and (c) "T3" TSs between ABWs [99].

2.6 Stripe domains

2.6.1 Stripe domains and their origin

Some magnetic materials show periodic stripe patterns rather than the usual single- or multi-domain configurations as magnetization at the surface. Garnets [102], FeSi sheets [103], shape memory alloys [104, 105], various amorphous alloys [106] and a variety of thin films [107–109] show such patterns. These stripe patterns are formed from both in-plane [103–105] and out-of-plane orientations of the magnetization [102, 104, 106–109]. An out-of-plane magnetization generates magnetically charged stripes. A component of the magnetization is alternately tilted upwards and downwards to the plane of the film

which in turn produces opposite magnetic charges arranged in a periodic fashion in the form of stripes at the surface of the film. These magnetic patterns of periodic stripes are called stripe domains.

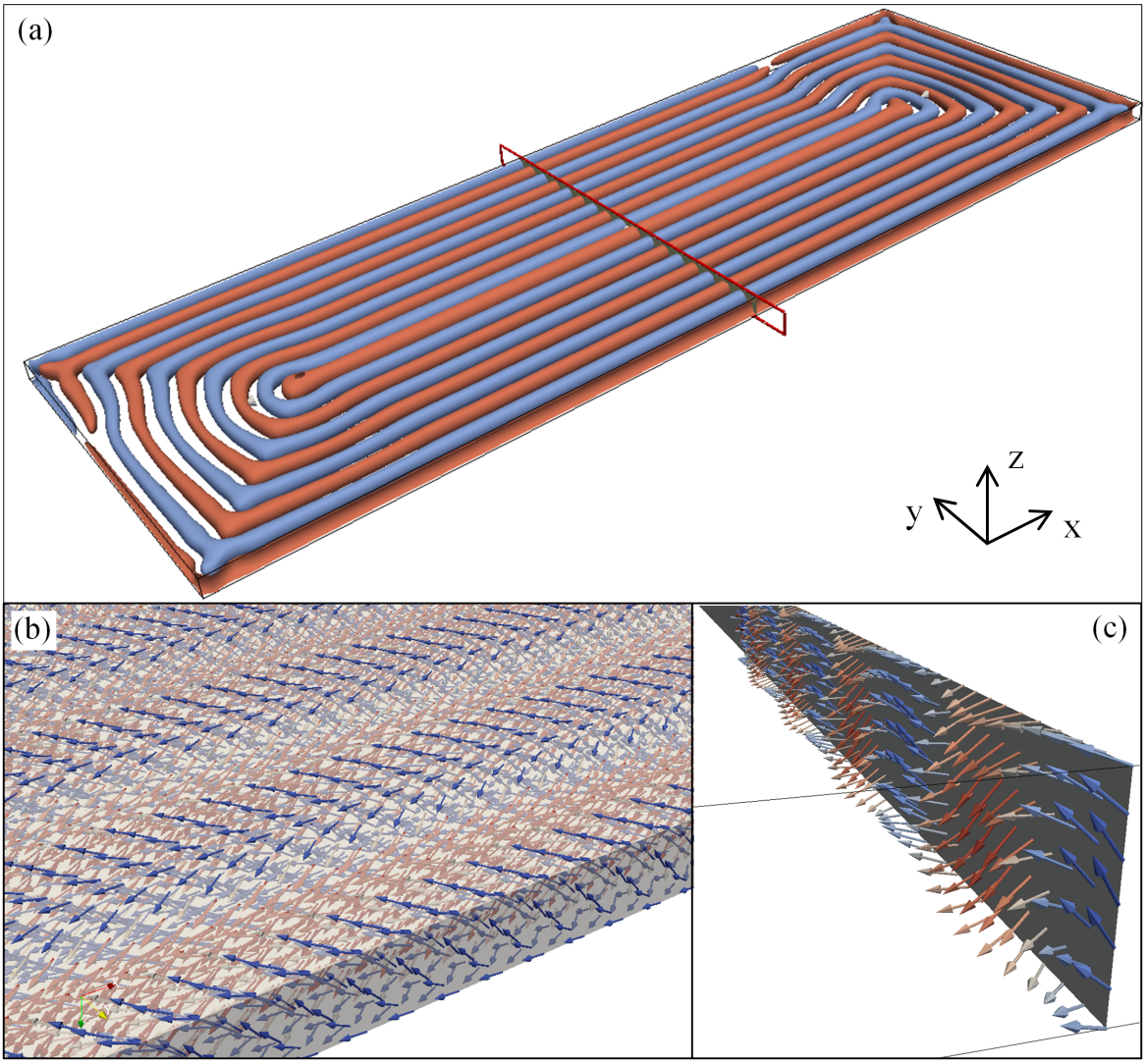

Figure 2.20: In (a) magnetization iso-surfaces with $M_z = \pm 0.5 M_s$ for stripe domains in a 140 nm thick 2.3×6.7 µm^2 Py sample are shown. Red and blue iso-surfaces represent upwards and downwards oriented magnetization, respectively. In (b), a part of the magnetization close to the front edge of the sample, which is parallel to the x axis is shown in detail. In (c), The magnetization configuration of a cross-section indicated in (a) is shown.

Figure 2.20 describes the stripe domains inside a 140 nm thick 2.3×6.7 µm^2 Py sample. In Fig. 2.20(a), the alternately upwards and downwards tilted components of the magnetization inside the film are shown with red and blue iso-surfaces for

$M_z = \pm 0.5 M_s$, respectively. A closer look at the edge of the pattern is shown in Fig. 2.20(b). A cross-section taken from Fig. 2.20(a) shown in Fig. 2.20(c) describes the orientations of the magnetizations inside the stripe domains.

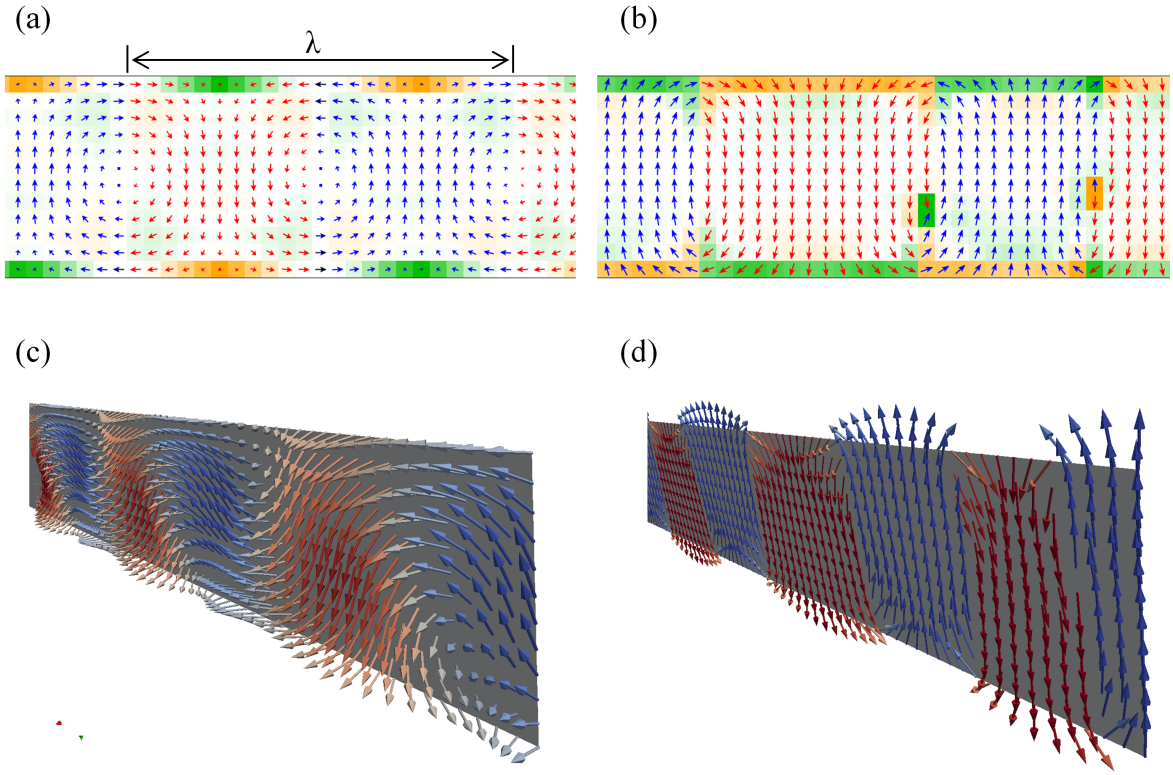

Figure 2.21: (a) and (c) describe weak stripe domains, while (b) and (d) describe strong stripe domains. λ is the periodicity of the stripe domains.

Stripe domains originate from an interplay of a perpendicular (or out-of-plane of the film) induced (from stress, field applied during deposition and columnar grains) and/or magnetocrystalline anisotropy with an in-plane shape anisotropy of the films. The perpendicular anisotropy forces the magnetization to align out-of-plane of the film, whereas the shape anisotropy tries to keep the magnetization along the in-plane orientation in order to minimize the demagnetization energy of the film. The total energy of the film with perpendicular anisotropy is minimized by the formation of alternately arranged upwards and downwards oriented uniform domains as first speculated by C. Kittel in 1946 [58]. However, in stripe domains, there is a strong variation of the magnetization directions across the film thickness, as seen in Fig. 2.20(c). Therefore, the stripe domains are not domains in the common sense but involve only a small component of the total saturation magnetization. In materials with weak perpendicular

anisotropy, the magnetic flux inside the out-of-plane oriented domains is mostly closed at the surfaces by an in-plane rotation of the magnetization at the surfaces as shown in Figs. 2.21(a) and (c). Such stripe domains are called weak stripe domains. With the increase of the perpendicular anisotropy in the materials, the magnetic flux of the out-of-plane oriented domains is opened more and more at the surfaces due to the increase of the out-of-plane tilt of the magnetization inside the domains as shown in Figs. 2.21(b) and (d). Such stripe domains with opened magnetic flux at the surfaces are called strong stripe domains [2, 109].

2.6.2 Critical thickness and phase diagram of stripe domains

Due to the interplay of the perpendicular and the in-plane shape anisotropy, there exists a critical thickness of the film beyond which the formation of the stripe domains takes place [2, 11, 12, 109, 110]. As the thickness of the film increases, the in-plane shape anisotropy becomes less dominant (see section A.1 in the appendix) and the magnetization starts tilting towards out-of-plane orientation due to the perpendicular anisotropy. Just above the critical thickness, the magnetization still lies predominantly in the plane of the film, where the deviation from the homogeneous in-plane orientation is very small. The critical thickness varies with the film deposition conditions because they have an influence on the induced and crystalline anisotropies (with the change of the film composition and/or stress etc.) of the films [15, 111–113].

Holz and Kronmüller in 1969 [12] calculated the critical thickness and the phase diagram of weak stripe domains, shown in Fig. 2.22. Critical thickness D_{cr} (denoted by t_{cr} in this thesis) and periodicity λ_{cr} (indicated in Fig. 2.21(a)) of the stripe domains at the critical thickness as a function of perpendicular anisotropy K (denoted by K_{u} as uniaxial anisotropy in this thesis) are plotted in reduced units. The phase diagram is divided into three regions. In region I, i.e., below the critical thickness $D_{\mathrm{cr}}/(\pi\sqrt{A/K})$ curve and for anisotropy $K/I_{\mathrm{s}}^2 < 2\pi$ (where $I_{\mathrm{s}}^2 = \mu_0 M_{\mathrm{s}}^2/(4\pi)$), the magnetization lies in the film plane and the domains are separated either by the SNWs or CTWs (discussed in sections 2.2.1 and 2.2.2, respectively). In region II, i.e., above the critical thickness $D_{\mathrm{cr}}/(\pi\sqrt{A/K})$ curve and for anisotropy $K/I_{\mathrm{s}}^2 < 2\pi$, stripe domains are formed. Just above the critical thickness curve, weak stripe domains are formed. Inside this region for thickness much larger than D_{cr}, strong stripe domains are formed. The stripe-domain structure goes over to the usual macroscopic domain structure where the domains are separated by 180° symmetric Bloch walls. The weak stripe domains gradually evolve towards the strong stripe domains. Inside region III, i.e., for $K/I_{\mathrm{s}}^2 > 2\pi$, a homogeneous

distribution of the magnetization parallel or antiparallel to the easy axis is formed irrespective of the thickness of the film. In this region, the critical thickness becomes zero, while the stripe-domain width diverges. For finite lateral extensions, one has Bloch walls with strong stripe domains in this region as in region II for a thickness much larger than the critical thickness.

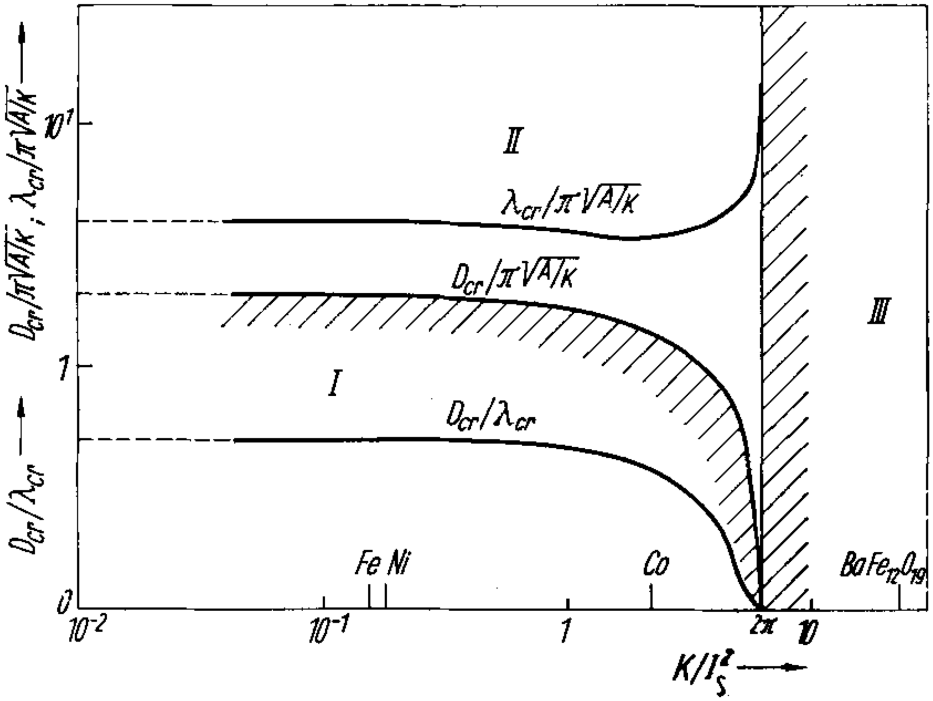

Figure 2.22: The critical thickness D_{cr} (or t_{cr}) and critical periodicity λ_{cr} of the stripe domains defined in reduced units as a function of K/I_{s}^2 (or $K_{\mathrm{u}}/I_{\mathrm{s}}^2$, where $I_{\mathrm{s}}^2 = \mu_0 M_{\mathrm{s}}^2/(4\pi)$) of a magnetic thin film [12].

From Fig. 2.22, for soft magnetic materials (i.e., with $Q \ll 1$ or $K_{\mathrm{u}} \approx 0$), the critical thickness and the critical period of the weak stripe domains approaches [12],

$$t_{\mathrm{cr}} \equiv D_{\mathrm{cr}} = 2\pi\sqrt{\frac{A_{\mathrm{ex}}}{K_{\mathrm{u}}}} \quad \text{and} \quad \lambda_{\mathrm{cr}} = 4\pi\sqrt{\frac{A_{\mathrm{ex}}}{K_{\mathrm{u}}}}. \tag{2.28}$$

The phase diagram shown in Fig. 2.22 is valid in the absence of any external field. Within an externally applied in-plane magnetic field, the value of the critical thickness changes. With the increase of the external field, the critical thickness as well as the perpendicular anisotropy required for the formation of stripe domains increases [11, 12]. In other words, for each thickness there exists a critical value of the in-plane external field, only below this field value stripe domains are formed. For soft magnetic materials,

the expressions for the critical thickness and critical period of weak stripe domains in the presence of an applied field is calculated according to Ref. [2]:

$$t_{\mathrm{cr}} \equiv D_{\mathrm{cr}} = 2\pi \frac{\sqrt{A_{\mathrm{ex}}/K_{\mathrm{u}}}}{1-h}, \tag{2.29}$$

$$\lambda_{\mathrm{cr}} = 2\, t_{\mathrm{cr}} \sqrt{\frac{1-h}{1+h}}, \quad \text{where} \quad h = \frac{1}{2} H_{\mathrm{app}}\, \mu_0 M_{\mathrm{s}}/K_{\mathrm{u}}. \tag{2.30}$$

Another critical thickness for strong stripe domains is calculated by F. Virot et. al. [109], shown in Fig. 2.23. In this plot, the solid line corresponds to the critical thickness for the formation of weak stripe domains as plotted in Fig. 2.22 in reduced units. The dashed line is the reduced critical thickness of strong stripe domains which is a cross-over line between the weak and the strong stripe phases.

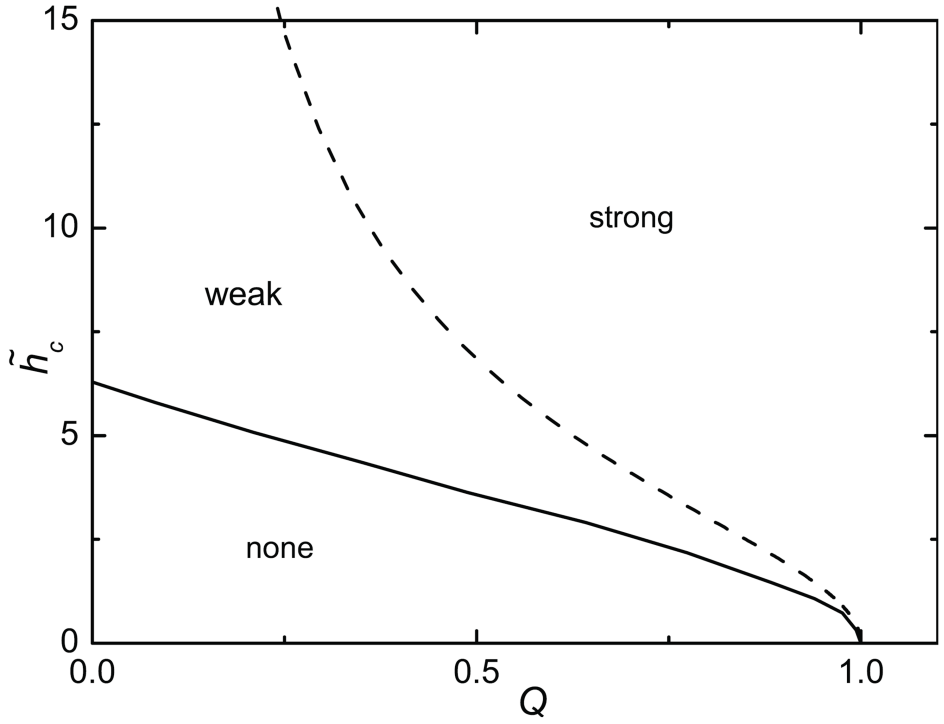

Figure 2.23: Phase diagram of magnetic domains in thin films which describes the stability range of weak and strong stripe domains. A reduced critical thickness $\tilde{h_{\mathrm{c}}} = t_{\mathrm{cr}}/\sqrt{A_{\mathrm{ex}}/K_{\mathrm{u}}}$ is calculated as a function of the quality factor $Q = 2K_{\mathrm{u}}/(\mu_0 M_{\mathrm{s}}^2)$ [109].

3 Materials and methods

3.1 Permalloy

3.1.1 Technical history of permalloy

Py is a ferromagnetic alloy of Nickel (Ni) and Iron (Fe), usually referred to an alloy of nominal 80 wt% Ni and 20 wt% Fe contents [114–116]. It was invented by the physicist Gustav Elmen in 1914 at Bell Telephone Laboratories, where he observed remarkable magnetic properties in alloys of Ni-Fe with more than 30 wt% Ni content [115]. In 1923, he found that with heat treatments the permeability of Py can be enhanced up to 90,000 for 78.2 wt% Ni and 21.3 wt% Fe along with other additives [115]. In 1924, soon after the discovery of the high permeability of Py, four million US dollars were invested by the Western Union Telegraph company on Py to enhance the communication-message speed in transatlantic cables (shown in Fig. 3.1(a)) [117]. Py was wrapped on the inner copper cable in the submarine transatlantic cables to compensate the inductance of the long cables as shown in Fig. 3.1(b). It increased the message speed five times more than that of any cable laid before [117]. This method of cable compensation declined in the 1930s, but during the World War 2 many other applications of Py were found in transportation-automotive, railway, aviation, marine, telephone and radio industry, owing to its magnetic properties and as well as its lightweight and increased corrosion resistance compared to other materials such as steel and cast iron [51, 118]. Later, with the invention of the thin film fabrication techniques, new applications of Py thin films in magnetosensors such as giant magnetoresistance, bio-sensors, magneto-electronics, data storage, magnetic heads of computers hard disks and microwave electronic devices were found [119, 120].

(a)

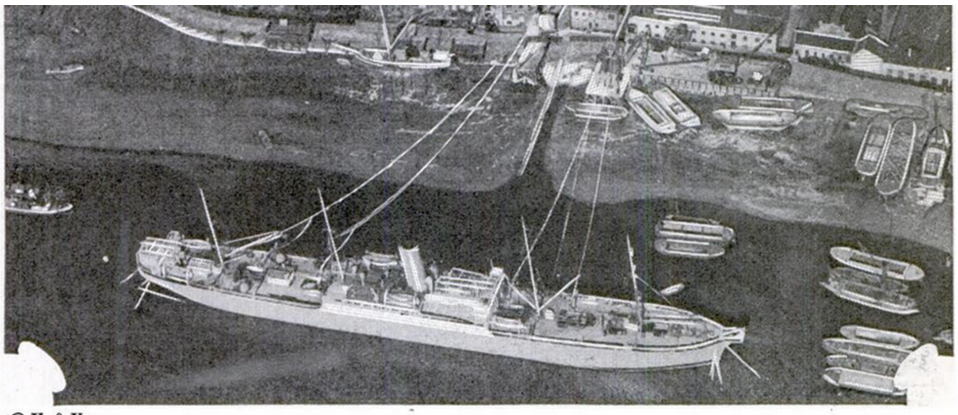

© U. & U.
Cable Ship Loading 2,360 Miles of Permalloy Submarine Cable at Greenwich, England, for New America-Azores Link of the Direct Line to Italy

"Four Millions on 'Permalloy'—to Win!"

Once More of a Gamble than a Horse Race, New Transatlantic Cable Speeds Messages Five Times Faster than Before

By EARL CHAPIN MAY

THIS is not a race-track yarn. It is the story of messages flashed along thousands of miles of track laid on the bottom of the seven seas. "Permalloy" is not a horse, but an alloy of about eighty per cent nickel and twenty per cent iron, which promises to revolutionize submarine-cable transmission.

America exchanged information only by mail or by word of mouth. About ten days elapsed between sending and receiving a message. The first official transatlantic cable message of twenty-one words was thirty-five minutes in transmission. The average speed of the 732 messages carried by that first cable was two words

(b)

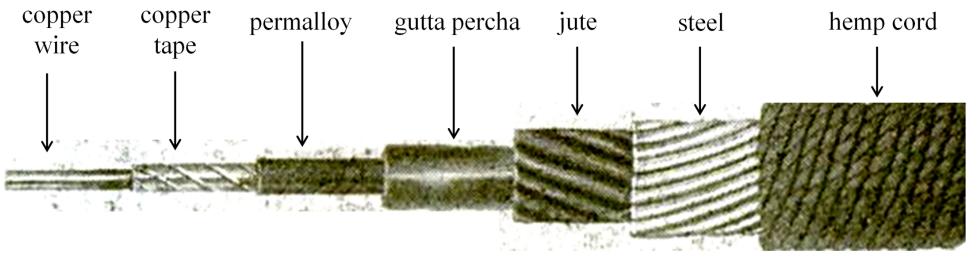

Figure 3.1: A clipping from the famous science and technology magazine "Popular Mechanics" published in December 1925 [117]. (a) An article about the successful application of Py in transatlantic cables in order to increase the telegraphic message speed was published. (b) A transatlantic telecommunication submarine cable used in the 1920s. The central copper wire carried the current. In case the central wire was broken, the wrapped flexible copper tapes carried the current. Py was used for inductive compensation of the cable. A thick layer of gutta percha was used as insulation to avoid leakage of the current in sea water. Jute wrapping cushioned the pressure of the deep sea water. Steel armor wires were wrapped to avoid cable from injury along with final wrappings of the tarred hemp cords [117].

3.1.2 Magnetic and structural properties of permalloy

Under ambient conditions Ni_xFe_{1-x} alloys form either a bcc crystal structure at the Fe-rich side or an fcc crystal structure at the Ni-rich side with a borderline at the stoichiometry of $x \approx 0.35$ [121, 122]. Py with $0.35 \leqslant x \leqslant 0.90$ composition is very ductile which allows making very thin ribbons of down to 2.5 µm thicknesses or wires of 10 µm diameters and can be annealed at high temperatures [114]. Also, Py with these compositions is one of the most versatile soft magnetic alloys. With suitable alloy additives (such as C, Si, P, Cu, Cr, Mu etc.) and proper processing, the magnetic properties can be controlled within a wide range and a strong uniaxial anisotropy can be easily obtained. A value of $\sim$ 100,000 of the initial permeability has been achieved in a number of alloys (of Py) at room or at cryogenic temperatures [114]. Values of a coercive field from 0.0002 to 1 mT can be adjusted [114]. One may also choose either a square hysteresis loop with the remanence practically equal to saturation, or a skewed hysteresis loop with no remanence. Hence, Ni_xFe_{1-x} alloys are ideal for transformers, magnetic shielding, magnetic amplifiers, and memory applications [114].

In 1950, Bozorth [116] reported the magnetic properties of Py in a full range of composition. Permeability is influenced remarkably by heat treatment and increased to maximum with rapid cooling for $x \approx 0.79$, as shown in Fig. 3.2(a). Another permeability peak was observed at $x \approx 0.45$. The crystalline anisotropy approached zero in the composition range of $0.63 \leqslant x \leqslant 0.74$ depending on the cooling rate, as shown in Fig. 3.2(b). The magnetostriction of Py films varies with both the film composition and their crystal textures. Thin films are often deposited with well-defined crystal texture. However, the crystal texture quality can vary depending on the deposition conditions [112, 113, 122, 123]. The magnetostriction coefficient λ in polycrystalline films is averaged over all single crystal λ values [113, 123, 124]. Py films with fcc lattice structure grow with a preponderance of [111] crystal orientation along the film normal [125, 126]. The magnetostriction coefficient for polycrystalline Py films can be written as $\lambda = \alpha\lambda_{100} + \beta\lambda_{111}$, where α and β are averaging constants. For Py with $0.79 \leqslant x \leqslant 0.80$, $\lambda_{111} \approx 0$ and $\lambda_{100} \neq 0$, whereas for x ≈ 0.45, $\lambda_{100} \approx 0$ and $\lambda_{111} \neq 0$. As the crystal structure also plays a role in determining magnetostriction, the alloy composition at which $\lambda = 0$ (i.e., when either λ_{111} and α are zero or λ_{100} and β are zero) is not unique. In Fig. 3.2(c), $\lambda = 0$ in the range of $0.79 \leqslant x \leqslant 0.82$. The scattered solid circles and the triangular points in Fig. 3.2(c) are the measurements performed by Klokholm and Aboaf [124] on evaporated and sputtered Py films, respectively. The line drawn through the square points is the result of Masiyama [127]. The general conclusion based on the

result shown in Fig. 3.2(c) is that the magnetostriction goes to 0 at about $x \approx 0.815$. In practice $\lambda = 0$ is difficult to attain. However, λ can be small, positive or negative, by a judicious choice of starting compositions (of alloy source) and deposition parameters.

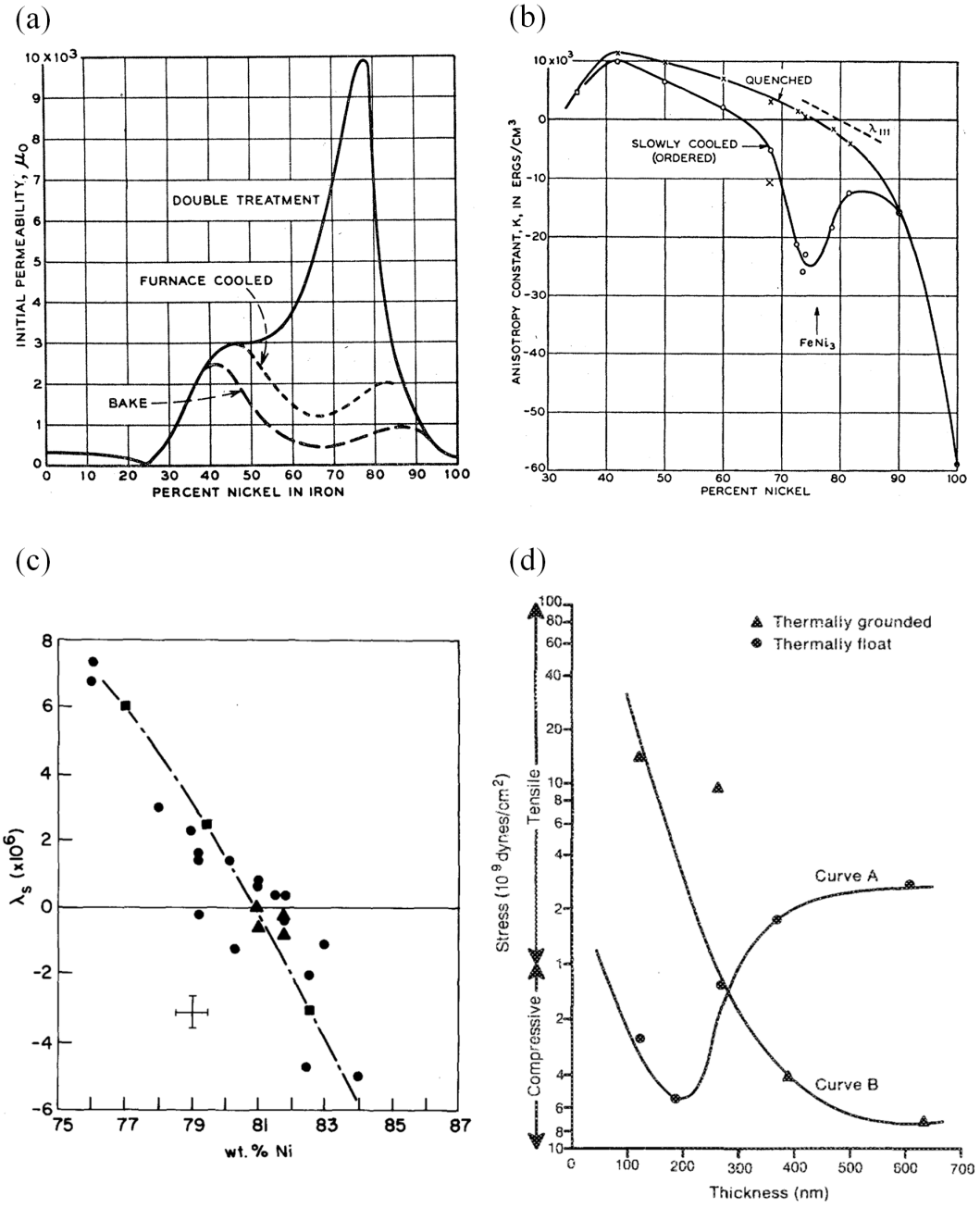

Figure 3.2: Magnetic and structural properties of Py. (a) and (b) describe permeability and crystalline anisotropy as a function of film composition and heat treatments reported in Ref. [50], respectively. (c) Saturation magnetostriction of Py films near the Ni composition for which saturation magnetostriction is zero [124]. (d) Variation of stress inside Py films as a function of thickness and deposition conditions [128].

There exists a vast literature in which stress of Py films has been extensively studied as a function of the types of the substrate, buffer layers, film composition, deposition methods and their parameters [11, 13, 15, 122–124, 128]. The magnitude and type of the stress (compressive or tensile) inside Py films change with deposition conditions as well as the thickness of the films. The variation of the stress with film thickness has been observed in many metallic films [129], and can be attributed to the grain morphology difference at different film thickness. Several different mechanisms for the origin of the thin film's intrinsic stress have been reported. These mechanisms include lattice expansion, surface tension, grain coalescence, the effect of the annealing on the grain boundary, defects, and impurity incorporation [130, 131]. During the film growth, one or several of these mechanisms can become dominant at a given thickness [12, 15, 112, 113, 123]. Typical behavior of the stress in $Ni_{81}Fe_{19}$ films as a function of the film thickness and the substrate temperature is shown in Fig. 3.2(d). The variation trend of the stress in Py films shown in Fig. 3.2(d) is not unique, because all the above listed mechanisms for the origin of the film stress are functions of deposition techniques and their parameters.

3.2 Sample fabrication and techniques

Two types of samples were prepared in this doctoral work: continuous Py thin films of varying thicknesses deposited on Si substrates and patterned microstructures of Py films of different shapes and thicknesses on Si substrates. For sample fabrications, EBL and sputter-deposition techniques were used. For continuous thin film samples, Py films were directly deposited by sputtering on cleaned Si substrates. Whereas, for micro-patterned films, first the desired patterns in polymer layers coated on Si substrates were formed with EBL and later Py films were deposited. The detailed description of the sample-fabrication steps with EBL and basics of sputter deposition are discussed below.

3.2.1 Electron-beam lithography

To write patterns on polymer coated Si-substrates, a Hitachi S4500 Field-Emission Scanning Electron Microscope (SEM) equipped with a Raith-ELPHY quantum attachment was used, shown in Fig. 3.3. ELPHY quantum is a lithography tool developed by Raith to produce micro- and nanostructures using electron-beam writing in connection with a SEM or Focused Ion Beam (FIB) systems equipped with beam blankers (to

divert the e-beam from the "electron-optic axis" of the SEM column) [132]. It consists of a sophisticated scan-generator electronics (hardware), a powerful PC-based operating software as well as a range of interfaces and supporting means for the "writing tool", i.e., the SEM.

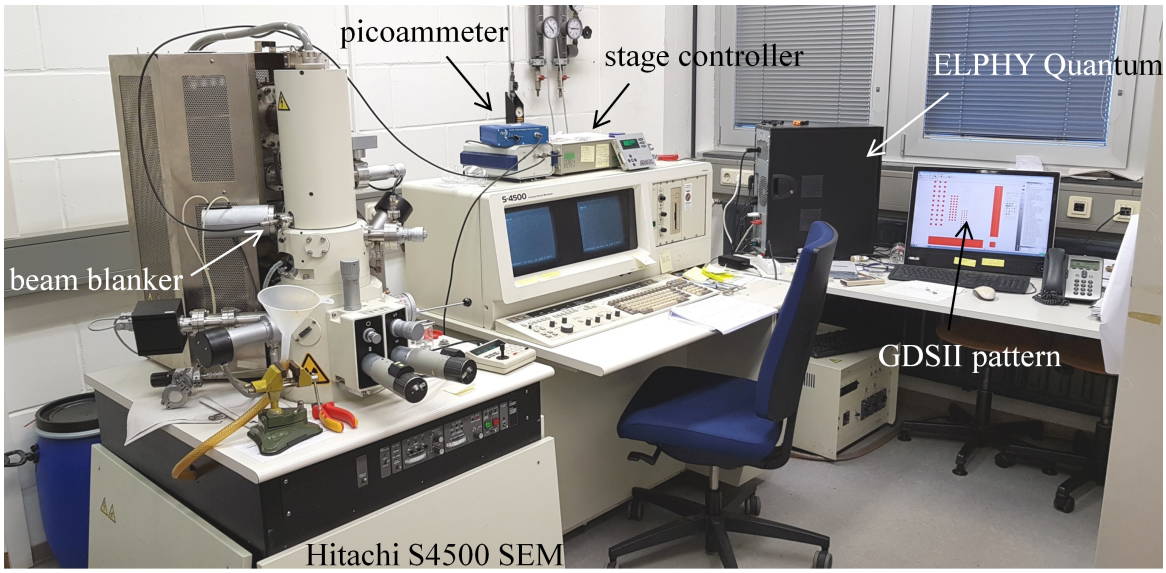

Figure 3.3: Hitachi S4500 SEM along with Raith-ELPHY quantum attachment used for EBL.

Si(100) p-type/Boron-doped wafers were cut into small pieces of edge lengths around 0.5 cm. The wafer pieces were cleaned in an ultrasonic bath for 5 minutes each in acetone, isopropanol and deionized water, consecutively. Afterwards, these Si substrates were dried with N_2 gas flow. Two different types of positive Poly Methyl Methacrylate (PMMA) solutions 3% 950k PMMA (950 000 amu) and 4% 600k PMMA (600 000 amu) dissolved in anisol were used to prepare samples. To fabricate Py microstructures of thicknesses below 150 nm, a single layer of 950k PMMA was spin-coated onto the Si substrates with 4000 rpm for 30 seconds, as drawn in Fig. 3.4(a). Whereas, for thicker Py microstructures, first a double layer of 600k PMMA was spin-coated onto Si substrates with 2000 rpm for 30 seconds and later a single layer of 950k PMMA was spin-coated with 4000 rpm for 30 seconds. The PMMA coated Si substrates were baked after each spin-coating on a hot plate for 10 minutes at 140 ^{o}C to evaporate the solvent. All the above procedures were performed inside a class-100 clean-room.

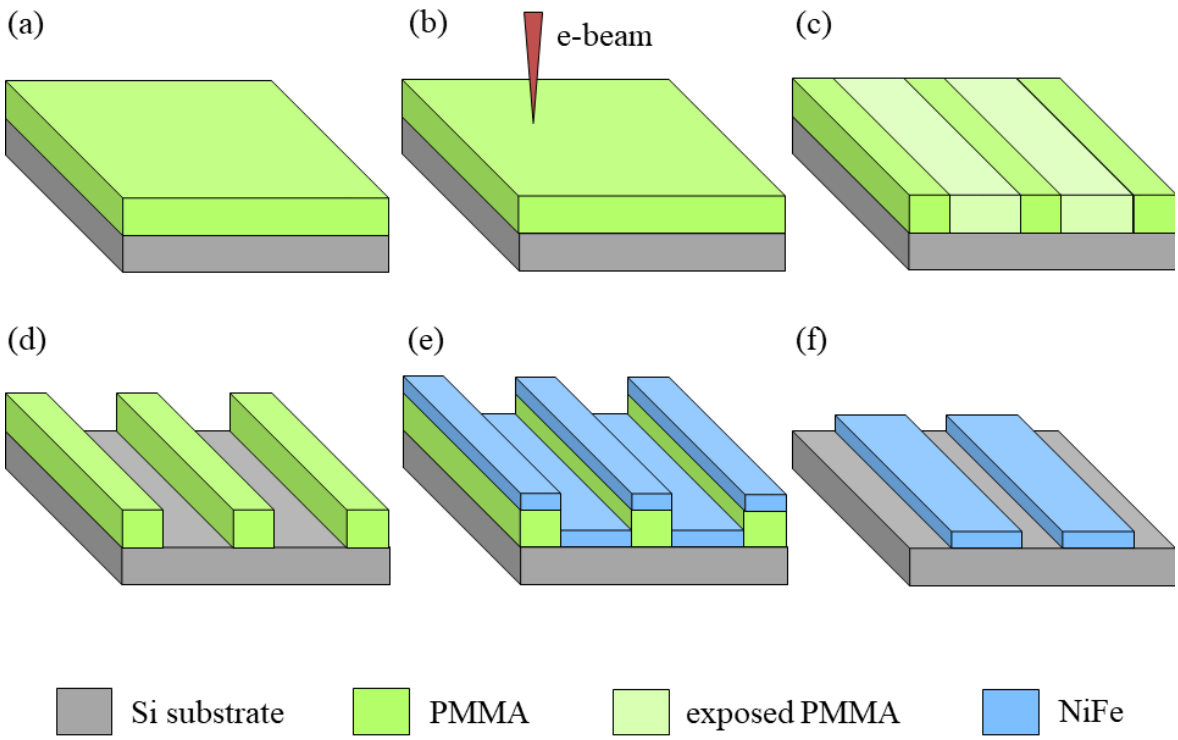

Figure 3.4: Sample fabrication steps using EBL and sputter deposition. (a) PMMA coated on top of Si substrate using spin-coating. (b) Writing pattern with e-beam. (c) The pattern of the exposed PMMA. (d) Dissolution of the exposed PMMA in the developer solution. (e) Deposition of NiFe film by sputtering. (f) Dissolution of the remaining PMMA in acetone in the final lift-off process.

Figure 3.4 describes the following EBL patterning and Py deposition steps. For patterning of polymer-coated substrates, samples were inserted inside the SEM and the e-beam calibration was performed. The patterns of squares, rectangles, circles and ellipses of various aspect ratios drawn in the Graphic Database System (GDSII) Editor were written with a calibrated e-beam (Figs. 3.4(b) and (c)). GDSII is an industry standard database file format for data exchange of integrated circuit layout artwork [133]. It is a binary file format representing planar geometric shapes, text labels, and other information about the layout in hierarchical form. E-beam doses of 430 and 650 $\mu C(cm)^{-2}$ for single layer and triple layers PMMA-coated substrates were applied, respectively. The polymer chains inside the e-beam exposed areas of the positive PMMA break down which results in the dissolution of the exposed PMMA areas in developer solutions. For all samples, the PMMA-coated Si substrates after e-beam writing were dipped in an isopropanol bath for 1 minute for pattern development (Fig. 3.4(d)). The development process was stopped by submerging the samples in deionized water. The

samples were later dried with N_2 gas flow and fixed inside a sputtering chamber for Py deposition (the basic sputter deposition is described in subsection 3.2.2 below). After sputtering Py films of desired thicknesses, the samples were submerged inside a hot acetone bath (60 ^{o}C) for 10 minutes for the lift-off process (Figs. 3.4(e) and (f)). In the lift-off step, the unexposed PMMA (the remaining PMMA after the development) was dissolved which left the desired micropatterned structures of Py film, as shown in Fig. 3.4(f).

3.2.2 Sputter deposition

Sputter deposition is a vacuum-based physical vapor deposition technique in which the material to be deposited is ejected from a target, called source, onto a substrate such as a Si wafer. The target is connected to the negative terminal of a DC or RF power supply, as shown in Fig. 3.5 for a DC-magnetron sputtering. Therefore, the target is also known as a cathode. Typically, several kilovolts are applied to it. The substrate which faces the cathode can be grounded, electrically floated, biased positively or negatively, heated, cooled, or even some combinations of them [130]. After the evacuation of the sputter chamber, an inert gas, typically Ar, is introduced which serves as a medium in which the plasma of the source material, gas ions and electrons, is initiated and sustained. The gas pressure usually ranges from a few to around 100 µbar. Ionization of the Ar gas initiates with the motion of the stray-free electrons under the influence of the high potential applied between the electrodes. On its way, the electron encounters a neutral Ar gas atom and collides with it to produce a positively charged ion and two more free electrons. The newly generated free electrons go on to ionize more Ar atoms resulting in a cascade effect which continues until the gas breaks down into ions. The plasma generation is optimized by determining the gas pressure required for maximum efficiency. If the pressure is too low, there would be not sufficient collisions between the electrons and gas atoms to sustain a plasma. If the pressure is too high, there would be too many collisions that electrons would not have enough time to gain energy in order to ionize the Ar atoms. Positively charged Ar ions strike the target and eject target atoms through momentum transfer, as shown in Fig. 3.5. The sputtered target atoms enter and pass through the plasma region to eventually deposit on the substrate. In addition to the sputtered target atoms, other particles, such as secondary electrons, desorbed gases, and negative ions as well as X-ray and photon radiations are emitted from the target [130]. In the electric field, the negatively charges ions are also accelerated toward the substrate to bombard the growing film.

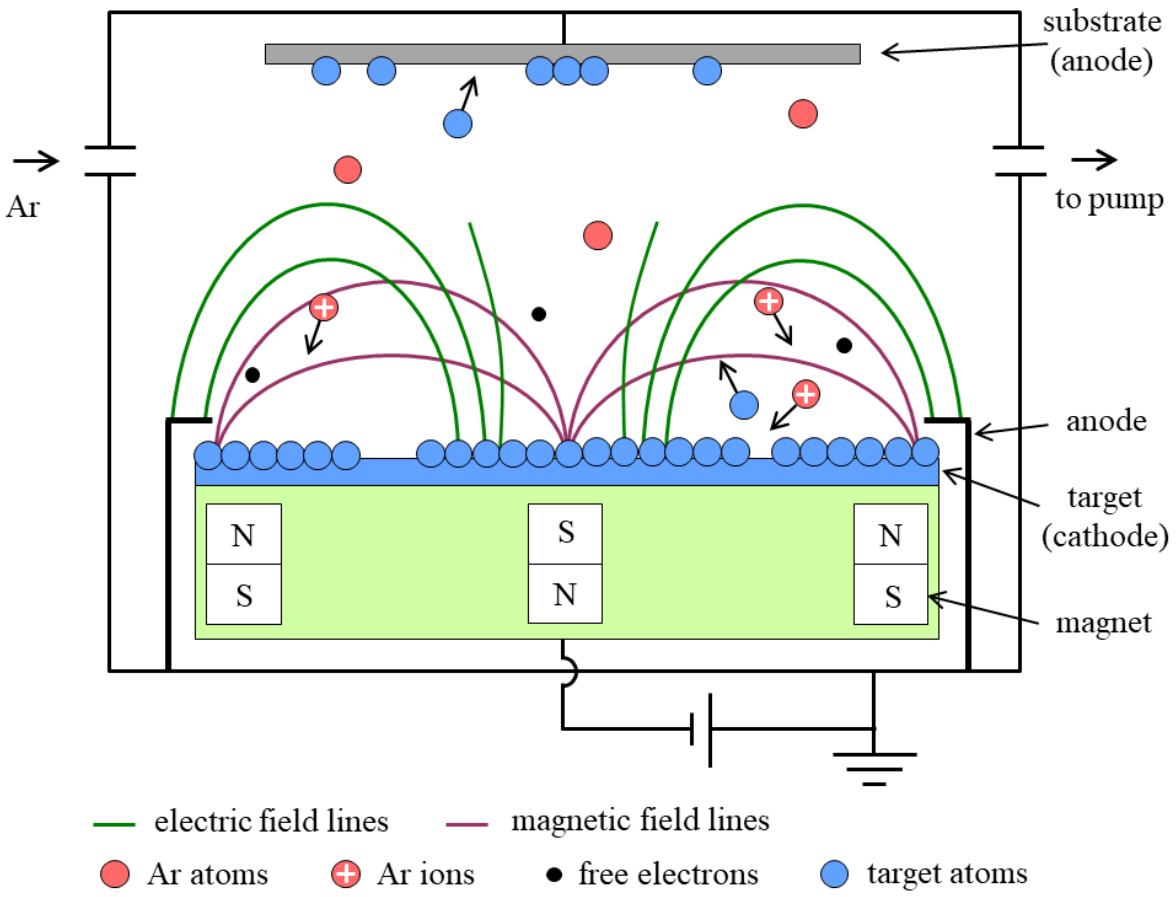

Figure 3.5: A schematic representation of the DC-magnetron sputtering technique.

DC- and RF-sputterings are two common variations of the sputter deposition techniques. In DC-sputtering a direct current is applied to the electrode. However, the major limitation of the DC-sputtering is that it is not possible to sputter insulator materials like quartz. Due to the high resistivity, an impossibly large voltage ($\sim 10^{12}$ V) is required [130]. Practically it limits the DC sputtering to materials of a resistivity less than 10^6 Ω-cm (no insulators). This problem is avoided by applying an alternating current at typical frequencies from 5 to 30 MHz. For a small portion of the frequency cycle, the direction of the ion and electron flow is reversed. This prevents the charge build-up on the insulating surfaces. Moreover, strong permanent magnets are used under the target material in order to produce a closed magnetic field loop in the vicinity of the target as shown in Fig. 3.5. They are used to trap the electrons and enhance both the efficiency of the initial ionization process by prolonging the electron residence time in the plasma and thus increase the possibility of ion collisions. This allows the plasma to be generated at a lower pressure which reduces both the background gas

incorporation in the growing film and energy loses of the sputtered atoms during gas collisions.

3.3 Sample characterization techniques

3.3.1 Magnetic Force Microscopy

MFM is a type of Scanning Probe Microscopy where a sharp magnetized tip attached to a cantilever is used to scan the magnetic sample in order to map the magnetic features of the sample surface. In this technique, the magnetic stray field from the sample surface is detected through the tip-sample interaction. A schematic diagram of the basic working of a MFM is shown in Fig. 3.6. Typical dimensions of the cantilever are a length of 200 µm, a width of 40 µm, a thickness of 20 µm, a tip length of 15 µm and a tip-apex diameter of 15 nm [134, 135]. The force on the tip from the sample stray field is detected based on the reflection of a laser signal from the deflecting cantilever to a photodiode as described in Fig. 3.6. Other important components of MFM include piezo-scanner and controller. The piezo-scanner moves the sample in x, y and z directions during the measurements. The piezo-scanner movements are controlled by the voltage signals sent by the controller to two pairs of electrodes inside and outside the piezo-tube of the scanner. A typical signal value is 1 V which results in a 1 to 10 nm displacement [135]. The sample is scanned in a raster mode with a typical scan range from a few tens of nanometers to 200 µm. The typical imaging time ranges from a few minutes to approximately 30 minutes. For magnetic force measurements, the Si or SiN cantilevers are coated with a ferromagnetic layer of few tens of nanometers thickness [136–139]. Using special FIB milled and carbon-needle cantilevers coated with a ferromagnetic layer, a lateral resolution of MFM down to 10 nm has been achieved [140, 141].

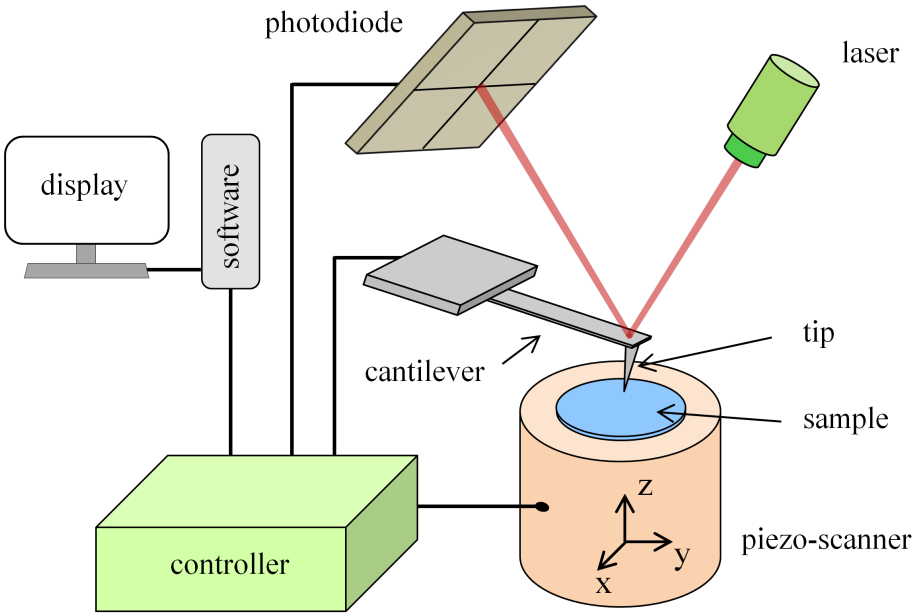

Figure 3.6: A schematic representation of the basic principle of an atomic/magnetic force microscope.

In the static-mode, if a force **F** is exerted on the tip by the sample stray field, the cantilever gets deflected towards or away from the sample surface by a distance $\Delta\mathbf{Z} = \mathbf{F}/k$, where k is the spring constant of the cantilever in the z direction, usually in the range of 0.01 to 100 Nm^{-1}. Forces in the range of tens of a pN and above are measured [135].

In the dynamic-mode, for small deflections, the cantilever can be modeled as a damped harmonic oscillator with a mass m, an ideal spring constant k, and a damper d. If an external piezo-driven oscillating force $\mathbf{F_z}$ with frequency ω is applied to the cantilever, then the tip will be displaced by an amount **Z** in the z direction. Moreover, the displacement will also harmonically oscillate, but with a phase shift θ between the applied force and cantilever displacement:

$$\mathbf{F_z} = F_0\, cos(\omega t) \quad \text{and} \quad \mathbf{Z} = Z_0\, cos(\omega t + \theta). \tag{3.1}$$

The amplitude and phase shift are given by [142, 143]

$$Z_0 = \frac{F_0/m}{\sqrt{(\omega_\mathrm{n}^2 - \omega^2)^2 + (\omega_\mathrm{n}\,\omega/q)^2}}, \quad \text{and} \quad \theta = arctan\left[\frac{\omega_\mathrm{n}\,\omega}{q(\omega_n^2 - \omega^2)}\right]. \tag{3.2}$$

Here the quality factor of resonance q (proportional to the ratio of the energy stored in cantilever to the energy lost per cycle), resonance angular frequency ω_n and damping factor δ are given by

$$q = 2\pi \frac{(1/2)\, k Z_0^2}{\pi d\, Z_0^2\, \omega_\mathrm{n}} = \frac{1}{2\,\delta}, \quad \omega_\mathrm{n} = \sqrt{\frac{k}{m}} \quad \text{and} \quad \delta = \frac{d}{2\sqrt{mk}}. \tag{3.3}$$

In MFM, the force on the tip increases when the tip approaches the sample. Using a first-order Taylor approximation for very small deflections of the cantilever compared to the tip-sample distance, the increase of the force results in the modification of the spring constant to $k_{eff} = k \pm \partial \mathbf{F_z}/\partial \mathbf{Z}$, depending on whether the force is repulsive or attractive, respectively [142, 144]. In case of a very small cantilever deflection (which is the usual case in MFM), $\partial \mathbf{F_z}/\partial \mathbf{Z}$ can be considered as a constant, this results in a change $\Delta\,\omega_\mathrm{n}$ in natural resonance frequency ω_n of the cantilever as

$$\omega_\mathrm{n}^{'} = \omega_\mathrm{n} \sqrt{1 \pm \frac{1}{k} \frac{\partial \mathbf{F_z}}{\partial \mathbf{Z}}}, \quad \Delta\,\omega_\mathrm{n} = \omega_\mathrm{n}^{'} - \omega_\mathrm{n} \approx \pm \frac{\omega_\mathrm{n}}{2k} \frac{\partial \mathbf{F_z}}{\partial \mathbf{Z}}. \tag{3.4}$$

The approximation is valid for $\Delta\,\omega_\mathrm{n} \ll \omega_\mathrm{n}$. The frequency shift is typically in the range of 1 to 50 Hz for cantilevers with a resonant frequency of $\omega_\mathrm{n} \approx 100$ kHz [135]. Note the sign of $\Delta\,\omega$. For instance, the coordinate system is such that positive z direction is pointing away perpendicular to the sample surface so that an attractive force would be in the negative direction ($F_0 < 0$), and thus the gradient of $\mathbf{F_z}$ is positive. Consequently, for attractive forces, the resonant frequency of the cantilever decreases, while for repulsive forces the resonant frequency increases (as described by the equation (3.4)). The final image displayed on the computer monitor is encoded in such a way that attractive forces are generally depicted in dark color while repelling forces are coded bright [136].

Imaging modes

AFM can be operated in three different imaging modes: contact, non-contact and tapping (or intermittent) mode [135, 145]. The contact mode is performed in static-mode operation while the other two imaging modes are performed in dynamic-mode operation.

In contact mode, the tip is "dragged" on the sample-surface. The topography of the surface is measured either using the deflection of the cantilever directly or using a feedback signal required to keep a constant bend in the cantilever during the scan

[135]. As the measurement of a static signal is prone to noise and drift, low stiffness cantilevers (i.e. cantilevers with a low spring constant) are used to achieve a large enough deflection signal while keeping the interaction force low [142, 145]. The contact mode AFM is always performed at a tip-sample distance where the overall force is repulsive, because the attractive force at larger tip-sample distance could cause a "snap-in" of the cantilever. However, there are certain drawbacks associated with this mode of operation such as the combination of normal force and lateral force created by dragging motion of the probe tip across the sample result in high contact stresses which can damage the sample and/or the tip [146].

In non-contact mode, the cantilever is vibrated near its resonant frequency, but the oscillation amplitude is of the order of approximately 1 to 10 nm [146]. The tip oscillates in the attractive force regime just above the surface contamination layer and never contact the surface [145]. Either the amplitude or the resonance frequency is maintained constant through the feedback loop. The spring constant of the cantilever used in this mode is greater than that of the cantilever used in contact mode in order to avoid the tip getting pulled to the surface by attractive forces. However, non-contact mode has certain drawbacks. Combination of weak interactive van der Waals forces and large spring constants causes the signal to be small, which causes unstable feedback and slower scan speeds [146]. Also, the lateral resolution is lower than the contact or tapping mode because of the larger tip-sample separation [143, 146].

In tapping mode, also the cantilever is vibrated near its resonance frequency but with an oscillation amplitude from around 20 to 200 nm [146]. The tip in this imaging mode taps the surface with its each vibration swing. The amplitude of the cantilever is such that the probe oscillates from repulsive to attractive force regime and maintains enough energy for the tip to tap through and back out of the surface contamination layer [145]. The tip-sample interaction alters the amplitude, resonance frequency and phase angle of the oscillating cantilever. This mode is suitable for imaging of soft samples. Although the resolution is similar to contact mode, the applied forces are lower [146].

Lift mode

For MFM, a two-pass technique known as lift mode is used in order to separate the effects of mechanical forces from magnetic forces [136], shown in Fig. 3.7. In this technique, first, a height profile is recorded in the first pass in tapping mode, shown in Fig. 3.7(a). At the end of the first pass, the probe is lifted typically from 30 to 100 nm

above the surface. Then it is moved along the previously mapped height contour at a constant lift height, as shown in Fig. 3.7(b). During this second pass, the changes of the probe resonant frequency or the phase are monitored, which are caused by the long-range magnetic forces, see Fig. 3.7(c). This approach allows to separate the topographic and magnetic effects. However, the two-pass technique requires twice more time for imaging. There are also other disadvantages, such as, a remote position of the probe during the second pass, which reduces the resolution and sensitivity of the magnetic imaging [136].

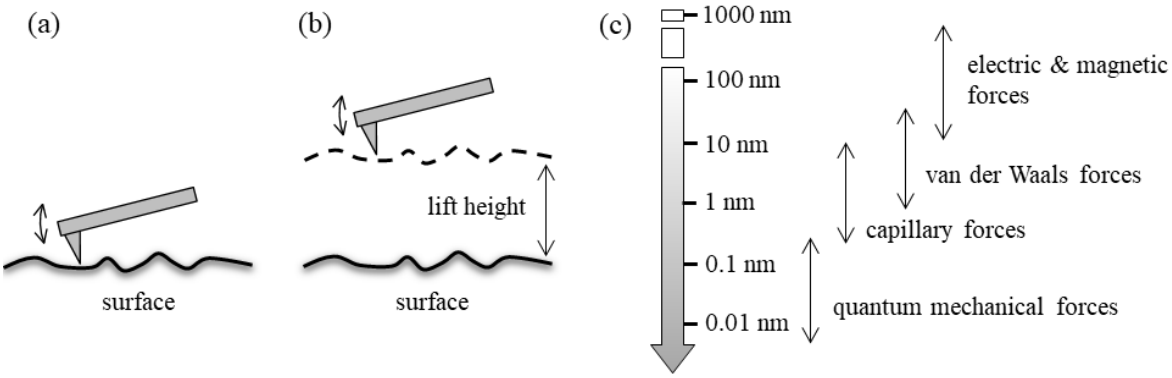

Figure 3.7: (a) Cantilever scans the sample surface topography. (b) Cantilever ascends to a lift height and scans with the topography profile while responding to magnetic forces. (c) Approximate range of the different dominant-force interactions between the sample surface and tip of the cantilever. Figure (c) adapted from Ref. [139].

Image formation

The force derivative $\partial\mathbf{F}/\partial\mathbf{Z}$ can originate from a wide range of sources, including electrostatic probe-sample interactions, van der Waals forces, damping, or capillary forces (shown in Fig. 3.7(c)) [139]. However, MFM relies on those forces that arise from a long-range magnetostatic coupling between the probe and sample. This coupling depends on the internal magnetic structure of the probe, which greatly complicates the mechanism of contrast formation.

In general, a magnetized MFM tip brought into the stray field of a sample or vice versa (a magnetic sample brought into the stray field of an MFM tip), has the magnetostatic energy E

$$E = -\mu_0 \int_{\mathrm{V}} \mathbf{M_{tip}} \cdot \mathbf{H_{sample}} \, \mathrm{d}V_{\mathrm{tip}} = -\mu_0 \int_{\mathrm{V}} \mathbf{M_{sample}} \cdot \mathbf{H_{tip}} \, \mathrm{d}V_{\mathrm{sample}}, \qquad (3.5)$$

where μ_0 is the vacuum permeability and $\mathbf{M}$ and $\mathbf{H}$ are the magnetization and stray field, respectively. The force acting on a MFM tip can thus be calculated by

$$\mathbf{F} = -\nabla E = \mu_0 \int_{\mathrm{V}} \nabla(\mathbf{M_{tip}} \cdot \mathbf{H_{sample}})\,\mathrm{d}V_{\mathrm{tip}} = \mu_0 \int_{\mathrm{V}} \nabla(\mathbf{M_{sample}} \cdot \mathbf{H_{tip}})\,\mathrm{d}V_{\mathrm{sample}}. \quad (3.6)$$

The sample stray field can be calculated from a magnetostatic potential as below

$$\mathbf{H_{sample}}(\mathbf{r}) = -\nabla \Phi_{\mathrm{sample}}(\mathbf{r}), \quad (3.7)$$

where $\Phi_{\mathrm{sample}}(\mathbf{r})$ is created by any ferromagnetic sample from its magnetization vector field $\mathbf{M_{sample}}(\mathbf{r})$ [147]:

$$\Phi_{\mathrm{sample}}(\mathbf{r}) = \frac{1}{4\pi}\left(\int_{\mathrm{S}} \frac{\mathbf{M_{sample}}(\mathbf{r}') \cdot \mathbf{n}}{\mid \mathbf{r} - \mathbf{r}' \mid} \,\mathrm{d}S' - \int_{\mathrm{V}} \frac{\nabla \cdot \mathbf{M_{sample}}(\mathbf{r}')}{\mid \mathbf{r} - \mathbf{r}' \mid} \,\mathrm{d}V' \right). \quad (3.8)$$

Here, $\mathbf{n}$ is an outward normal vector from the sample surface. The first (two-dimensional) integral covers all surface charges created by magnetization components perpendicular to the surface, while the second (three-dimensional) integral contains the volume magnetic charges resulting from interior divergences of the magnetization vector field.

A limitation of the use of MFM is that the magnetic configuration of the sensing probe is rarely known in detail [148–151]. As a consequence, MFM generally cannot be performed in a quantitative way. Furthermore, because MFM is sensitive to the strength and polarity of near-surface stray fields produced by ferromagnetic samples, rather than to the magnetization itself, it is usually not straightforward to deduce the overall domain topology from a MFM image [152, 153]. The problem of reconstructing a concrete arrangement of the inner and the surface magnetic charges from their stray fields is not solvable. MFM can, however, be used to compare the experimentally detected stray-field variation of a micromagnetic object to that obtained from certain model calculations (such as micromagnetic simulations) [152, 154, 155]. This often enables to classify the magnetic object under investigation. Thus, even without detailed quantitative analysis, the qualitative information collected by the microscope can be very useful [154–156].

MFM setup utilized

In this doctoral work, a Bruker MultiMode 8 atomic force microscope (AFM) placed on an anti-vibration optical table was utilized for the topographic and magnetic domain imaging of the samples, as shown in Fig. 3.8. For magnetic imaging, Olympus

OMCL-AC240TS cantilevers [134] were sputter-coated with a CoCr layer. The tip-apex diameter of these cantilevers is about 14 nm. By coating a 30 nm thick $Co_{85}Cr_{15}$ layer on these cantilevers, a lateral resolution down to $\sim$ 30 nm was achieved. A CoCr coating provides an optimum compromise between a high magnetic sensitivity, a good stability of the tip-magnetization and a low tip stray-field for high resolution magnetic imaging [157]. The AFM head was placed inside a pair of em coils for investigations within an externally applied magnetic field. With these coils, a magnetic field of up to $\pm$80 mT in the plane of the sample could be applied. The inset image in Fig. 3.8 shows the details of sample, cantilever and cantilever holder inside the AFM head. An optical microscope was used for the placement of the cantilever on the sample and for the adjustment of the laser with respect to the photodiode (see Fig. 3.6).

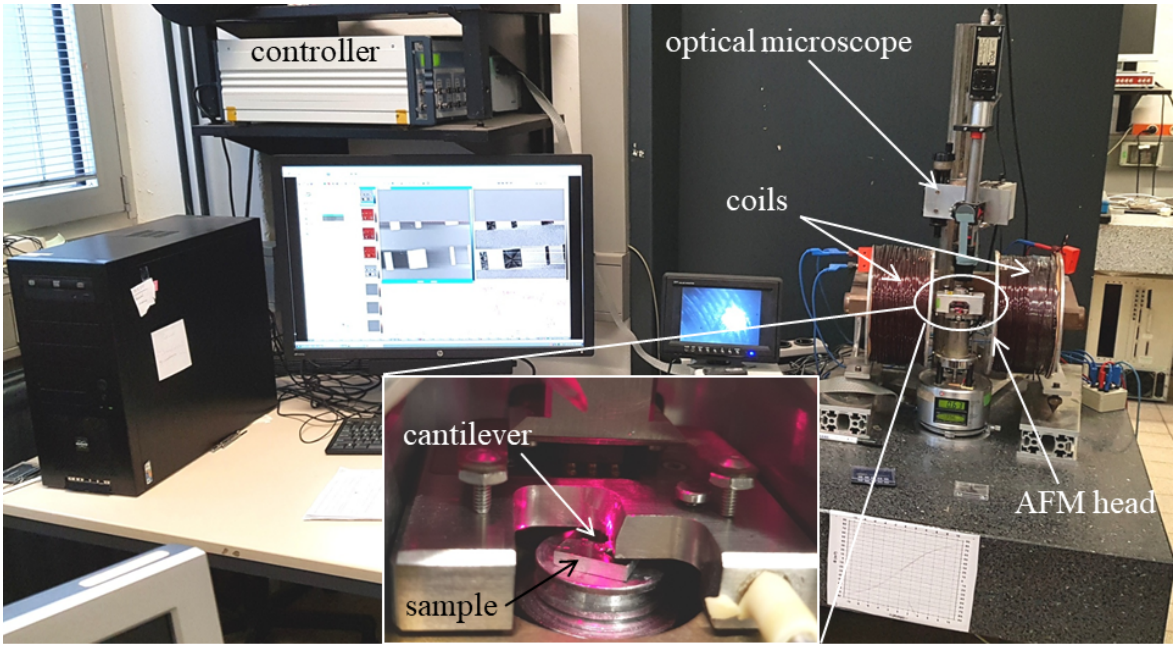

Figure 3.8: Bruker MultiMode 8 atomic/magnetic force microscope used for the topographic and magnetic imaging of patterned Py thin films. The inset image shows details inside the AFM head. The cantilever is not clearly visible in the image.

3.3.2 Vibrating Sample Magnetometer

A Vibrating Sample Magnetometer (VSM) is used to measure magnetic properties of materials. It was invented by Simon Foner in 1955 at the MIT Lincoln Laboratory [158]. In this instrument, a magnetic sample is placed inside a uniform magnetic field, which induces a magnetization $\mathbf{M}$ inside the sample. A set of coils called pickup or sensing

coils is placed in the proximity to the sample. The sample which is fixed to a sample rod is vibrated sinusoidally using a piezoelectric material with a typical frequency from 60 to 80 Hz and at an amplitude of approximately 1 mm, respectively. When the sample vibrates, it introduces perturbations in the external magnetic field, which is sensed by the pickup coils in terms of induced electromotive force (emf) defined by Lenz's law of magnetic induction. The induced emf voltage in the pickup coil is proportional to the sample's magnetic moment but does not explicitly depend on the strength of the applied magnetic field. In a typical setup, the emf voltage is measured by a lock-in amplifier using the piezoelectric signal as a frequency reference. It is also possible to record the hysteresis loop of any material by sweeping the magnetic field. Further details about the VSM technique can be found in Ref. [158, 159].

In this doctoral work, VSM was used to measure the hysteresis loops with a magnetic field applied in- and out-of-plane of the Py continuous thin films. Magnetic parameters such as coercivity and saturation magnetization of the films were determined.

3.3.3 X-Ray Diffraction

X-Ray Diffraction (XRD) is a nondestructive technique for characterizing crystalline materials. With this technique, information about the crystal structure, crystalline phase, preferred crystal orientation (texture), and other structural parameters, such as average grain size, strain and crystal defects can be obtained [160, 161]. In this technique, XRD peaks are produced from constructive interference of a monochromatic beam of X-ray diffracted at specific angles from various sets of lattice planes in a sample. Peak intensities, positions and widths are determined by the distribution of atoms within the lattice (crystal structure) of the sample. Further details about the XRD can be found in Ref. [160, 161].

In this doctoral work, XRD was used to determine the crystal texture, average grain size and structural morphology of the Py continuous thin films.

3.3.4 Transmission Electron Microscope

Transmission Electron Microscopy (TEM) is a microscopic technique in which a beam of electrons is transmitted through a thin sample (typically thinner than 100 nm) to form an image. The specimen is usually placed on a copper-grid suspension. An image is formed from the interaction of the electrons with the sample when the beam is transmitted through the sample. The image is then magnified and focused onto an imaging device, such as a fluorescent screen, a layer of photographic film, or a sensor

such as a charge-coupled device [162]. The image contrast depends on the density of the sample under observation. In the normal operation mode (i.e., the bright-field mode), low-density regions of the sample produce bright contrast as more electrons pass through the sample and high-density regions of the sample produce dark contrast. The main application of a TEM is to provide high magnification images with resolution down to around 0.2 nm of the internal structure of a sample [163]. TEM is a major analytical method in the physical, chemical and bio sciences. Further details about the TEM can be found in Ref. [162, 164].

In this doctoral work, TEM was utilized to observe the cross-sectional morphology of Py continuous and patterned thin films.

3.4 Micromagnetic simulations

Micromagnetic simulations are performed to understand and visualize the behavior of the magnetization and domain walls in micro- and submicro-scale systems [70, 165, 166]. The most prevalent micromagnetic simulation technique is to find an equilibrium magnetization configuration of a ferromagnetic body by successive iteration of minimizing its total energy under certain conditions [165, 167, 168]. For a given initial condition, the final magnetization configuration is reached when the successive iteration does not further lower its total energy (see equation (2.3)).

The simulation as a whole is run in large increments called stages. Individual stages are run in several smaller increments called iterations or steps. The iterations are run by evolvers, which update the magnetic state of the sample from one iteration to the next iteration. The evolvers, in turn, are controlled by drivers. Stages are run by drivers, which coordinate how the simulation evolves as a whole. New conditions are introduced at the beginning of each stage. The drivers hand a magnetization configuration to the evolvers with a request to advance the configuration. The evolvers then update the magnetization of the sample. It is the role of the drivers, not the evolvers, to determine when a simulation stage or run is complete [52]. The length of a stage (i.e., the number of iterations or steps in that particular stage) is controlled by the user, who defines the stopping criterion in the driver. Depending on the stopping criterion, a stage can have as few as one iteration to as many as thousands of iterations. Therefore, a prudent choice for the stopping criterion is required. Once the stopping criterion is reached, a new stage begins.

There are two types of evolver-driver pairs, i.e., time and minimization evolvers-driver pairs [52]. Time evolvers track LLG dynamics (equation (2.23)), whereas, minimization

evolvers locate the local minima in the energy surface through direct minimization techniques. For a certain driver to be used its corresponding evolver must be used in conjunction, i.e., time evolvers must be paired with time drivers, and minimization evolvers must be paired with minimization drivers.

A number of micromagnetic solvers (to solve LLG equations numerically) are available based on two common approaches: finite-difference method (FDM) [70, 169] and finite-element method (FEM) [70, 170]. OOMMF [52], MuMax [171, 172] and MicroMagus [173] are FDM based, whereas Nmag [174], MicroMagnum [175], magpar [176], TetraMAG [177] and FeeLLGood [178] are FEM based few micromagnetic solvers out of many others [166]. In both approaches, the sample is divided into a large number of cells. Each cell is assigned with a single spin which is the average magnetization of the cell. The size of each cell is generally kept smaller than the exchange length ($\sqrt{2A_{\mathrm{ex}}/\mu_{\mathrm{o}}M_{\mathrm{s}}^2}$) of the material under consideration in order to take into account of the exchange interactions among the spins in addition to the magnetostatic interactions among them. In FDM the space is discretized by a regular cubic lattice [169]. As a result for a complicated geometry like curved boundary or irregular microstructures, FDM creates some artificial edge roughness. The FEM can solve the above mentioned problem. For FEM the solution domain is discretized into finite elements [170]. Depending upon the dimension of the problem, these can be triangles, squares, or rectangles in two dimensions or tetrahedrons, cubes, or hexahedra for three-dimensional problems [170]. As a result it is easier to construct complex geometries using this method. However, the FEM is much slower in the evaluation of magnetostatic field and consume more computer memory as compared to the FDM [179]. Therefore, for larger problems it is easier and reasonable to use FDM rather than FEM technique.

3.4.1 Object-Oriented MicroMagnetic Framework simulations

For micromagnetic simulations, OOMMF, an open source micromagnetic software developed at National Institute of Standards and Technology, Gaithersburg, by Mike Donahue and Don Porter is used [52]. OOMMF is written in C++ and Tcl languages. In OOMMF, a sample or space is discretized into small cuboidal cells of the same dimensions as mentioned above. All the required parameters such as bulk-saturation magnetization, exchange-stiffness constant, magnetocrystalline anisotropy, Zeeman field, sample geometry and dimensions and cell parameters are provided at the initialization of the simulation, as described in the flow chart shown in Fig. 3.9, through a file called “MIF file”. The “MIF file” is written in the Tcl/Tk script. In addition to these

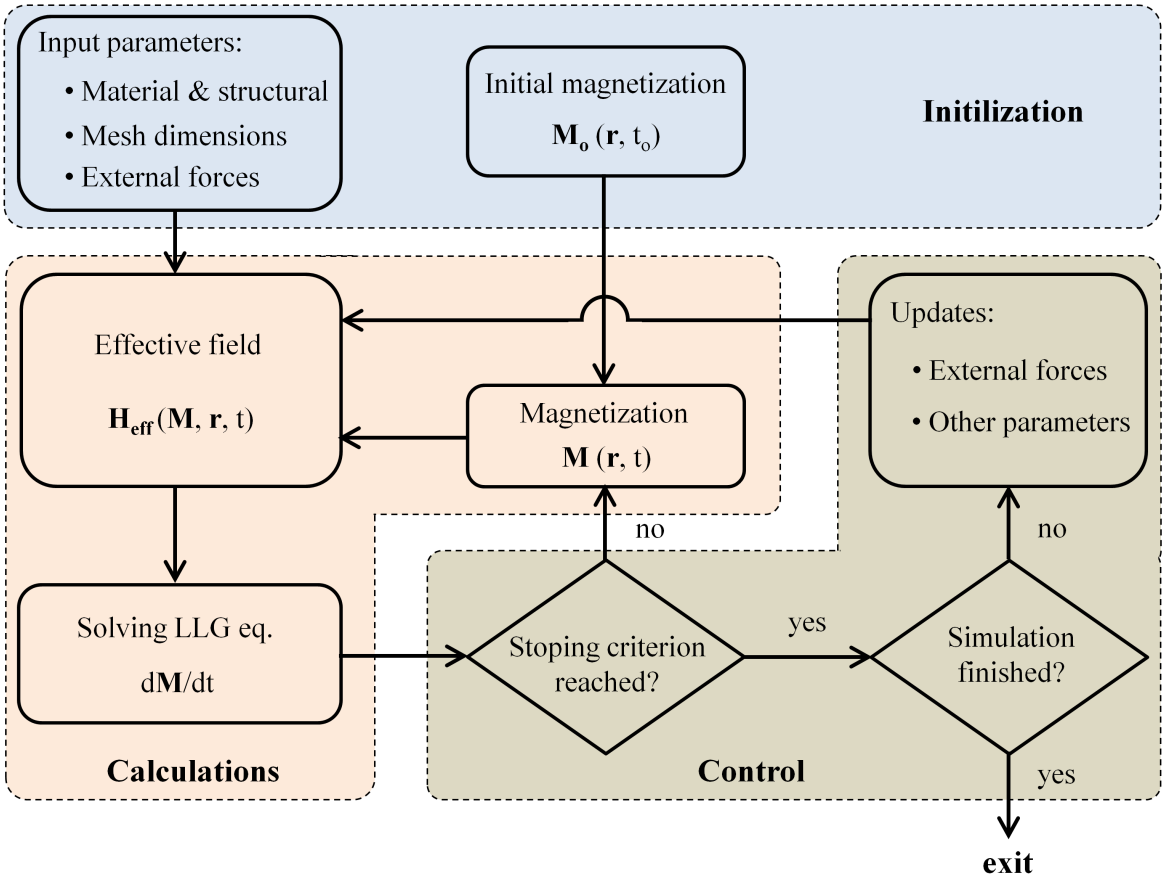

Figure 3.9: A typical flow-chart for static micromagnetic simulations.

parameters, an initial magnetic state of the sample magnetization is also provided at the starting point of the simulation, as shown in Fig. 3.9.

Once the initialization is complete, the simulation can be started and the actual calculations are performed by the evolvers. The evolver first calculates the effective field (equation (2.19)) at each point (or cell) of the system based on all energy contributions for the given initial magnetization configuration. Later, it updates a small change in the magnetization at each point by solving the LLG equation (equation (2.23)). The whole system is updated simultaneously and the calculation of a new effective field for the updated magnetization configuration and the subsequent change in the magnetization is carried out in a loop in several iterations until an equilibrium state is reached. The step size Δt for the first iteration in the problem run is selected according to the maximum change in $\mathbf{m}$ specified by a user-defined "start_d$\mathbf{m}$" value [52]. The next iteration proceeds with this step size. If an error "Error$_i$" for the change of magnetization at each cell location i after this step size is smaller than a certain value, this step size is selected

for the next iteration otherwise a smaller step size is chosen [52]. The equilibrium state is determined by the predefined convergence criterion by defining the stopping value for d$\mathbf{M}$/dt in the "MIF file". The typical stopping value for d$\mathbf{M}$/dt is set in such a way that the maximum torque experienced by the magnetization under the effective field, $\mid \mathbf{M} \times \mathbf{H_{eff}} \mid / {M_S}^2$ goes below 1×10^{-5} [167]. At the stopping time, the maximum value of d$\mathbf{M}$/dt across all spins (or inside all cells) drops below the set value and a stage of the simulation is completed. After finishing off a stage (or as an equilibrium state is found), the drivers further check whether the simulation is completed or other updates such as a change in the applied filed for hysteresis loop are required. If any parameter is updated, then again new calculations of the effective field and change in the magnetization start as a next stage based on the previously calculated equilibrium state, as shown in Fig. 3.9. When all the predefined stages in the "MIF file" are completed, the simulation stops. The textual output data of the simulation which is not of the vector-field format is obtained in an "ODT file" [52]. Whereas, the vector-field format data is obtained in "OVF" and "OMF files" [52].

In this doctoral work, the OOMMF software was utilized to perform micromagnetic simulations of Py patterned thin films of various shapes and thicknesses. Micromagnetic behavior of TSs inside domain walls within and without applied external magnetic field was investigated by three-dimensional static simulations. The OOMMF software used in this doctoral work was a Central Processing Unit (CPU) based software. However, recently the Graphics Processing Unit (GPU) based OOMMF has been released which offers up to 32 times speed-up of the micromagnetic simulations [180].

4 Influence of sputtering conditions on domain configurations in patterned thin films

4.1 Introduction

Well-defined, stable and repeatable magnetic domain configurations are required for various devices based on magnetic thin films [22, 181–183]. However, even for a fixed geometry, patterned films often show more than one domain configuration in their zero-field (or remanent) states [35, 36, 184–186]. Some of these zero-field states have complex domain configurations which are undesirable from the application point of view [187–190]. The Landau-domain state in squares (Fig. 4.1(a)) [191, 192] and single-vortex state in disks (Fig. 4.1(e)) [24, 193] are simple and technically important [24, 181, 182] zero-field states. In Landau configuration, four triangular closure domains keep the magnetic flux almost completely within the structure. The four-fold magnetic symmetry results in the formation of a single vortex in the center of the square structure [24]. However, apart from the Landau-domain configuration, square-patterned films also show tulip [2, 194], diamond [184, 195] or many other irregular domains configurations [187–190] in the absence of external fields, as shown in Figs. 4.1(a) to (d), respectively. Similarly, disk-patterned films show various other domain configurations in addition to the single-vortex state such as triangular and diamond-domain states, as shown in Figs. 4.1(e) to (g), respectively. Zero-field domain configurations are determined by various structural properties such as geometry [2, 184, 191], intrinsic stress [13, 187], grain morphology [14, 16, 17, 195, 196], magnetocrystalline anisotropy [2, 59] as well as direction and strength of the magnetic field possibly applied during the fabrication processes [2, 125, 187]. Moreover, due to the influences of the magnetic history [197] such as trapped vortices from previous reversals [39, 40] and the changes of energy landscapes with the variation of the magnetization sweep rate [35, 36, 185], often

some of the higher energy states stabilizes instead of the true ground state, i.e., the lowest-energy state.

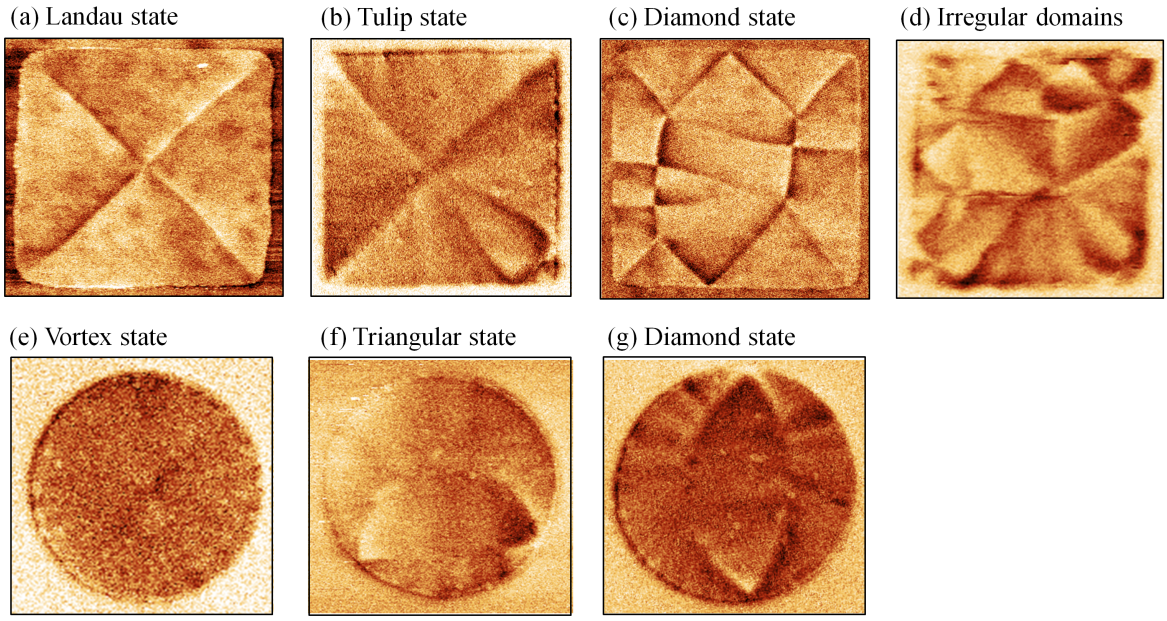

Figure 4.1: A few different zero-field states out of a large number of possible domain configuration states in square- and disk-shaped Py patterns of 5 µm edge length or diameter, respectively. The thicknesses are in the range of 50 to 70 nm.

Py with a $Ni_{80}Fe_{20}$ (wt%) composition is a frequently used magnetic material for both basic research and technical applications [51] because of its negligibly small magnetocrystalline anisotropy and almost vanishing magnetostriction coefficient [50, 124] (discussed in section 3.1). Due to the soft magnetic properties of the Py films, their domain configurations are mainly defined by the shape and dimensions of a given geometry [2, 84]. However, with the deviation of the structural characteristics from their ideal bulk characteristics [50], soft magnetic properties of Py films can easily deteriorate due to the development of an anisotropy resulting from the grain morphology [110, 198] and/or from the stress in conjunction with a nonzero magnetostriction of the films [199, 200]. This results in an increase of the degrees of freedom which determine the magnetic properties of the films. This, in turn, leads to an increase of the complexity of the observed ground-state domain configurations [187].

The structural characteristics of the films vary with the deposition parameters. Among various thin-film deposition techniques, sputter deposition (see subsection 3.2.2) allows the adjustability of a number of parameters in order to achieve the desired qualities of a film from wide ranges of materials [201]. The composition, uniformity, adhesion

strength, stress and grain morphology of the film can be controlled by optimizing the substrate bias voltage [128, 202–204], buffer layers at the film-substrate interface [205, 206], substrate heating [203, 207], sputtering power [128, 202] and working gas (Ar) pressure [15, 208, 209] during the sputter deposition. Especially, by varying Ar pressure, crucial deposition parameters such as flux rate, composition, incidence angles and energies of the adsorbing atoms on the substrate can be controlled [15, 209, 210]. Py films become magnetically softer [15, 204, 208] and their surface roughnesses decrease [208] upon decreasing the Ar pressure during the sputter deposition.

In this chapter, the structural and magnetic properties of square-patterned Py films are investigated. The films were deposited by DC-magnetron sputtering upon varying Ar pressure between 1.5 and 30.0 µbar. Ground-state domain configurations were imaged by MFM and their magnetic energies were calculated. It is demonstrated that the Landau-domain configuration in Py films can reliably be achieved with low-pressure sputtering. By increasing Ar pressure, the complexity of the ground-state configurations increases.

4.2 Experimental and micromagnetic simulation details

Continuous and patterned Py films were prepared by DC magnetron sputtering. Si substrates without oxide layers were first cleaned in an ultrasonic bath in acetone and isopropanol solutions, consecutively, and later washed with deionized water and dried in a N_2 gas flow, respectively. To prepare patterned samples, cleaned Si substrates were spin-coated by PMMA layers. PMMA-coated substrates were patterned using EBL (see section 3.2 for details). The pattern consists of arrays of 5×5 µm^2 squares and 5 µm diameter disks, each with 10 µm edge-to-edge interspacing. A 5 cm diameter $Ni_{80}Fe_{20}$ (wt%) Py target was used for all depositions. However, the elemental composition of the deposited film can vary from the target composition depending on the sputtering parameters [15, 209]. Substrates of 0.5 cm edge lengths were fixed at a distance of 11 cm from the target without cooling. The base pressure in the sputtering chamber was approximately 6.0 nbar. Different depositions were performed setting the Ar pressure to 1.5 µbar, 5.0 µbar, 7.0 µbar and 30.0 µbar, respectively. The vertical and horizontal components of the magnetron's residual magnetic field at the substrate location were around 0.4 mT and 0.2 mT, respectively. Such a small residual magnetic field has a negligible influence on the structural and magnetic properties of the sputtered films [66, 125]. Also, no additional magnetic field was applied to the substrates during sputtering. The DC power was kept approximately at 104 Watt. This optimal value

was selected out of a range of achievable DC powers for the sputtering pressure from 1.5 µbar to 30.0 µbar. The films were deposited with thicknesses between 50 nm and 70 nm. No capping layer was deposited on Py films. After the deposition, a lift-off process was performed in acetone, and the samples were finally cleaned in de-ionized water. The continuous film samples were prepared by sputtering Py films directly onto cleaned Si substrates.

Structural and magnetic properties investigations were carried on both continuous and patterned Py film samples. The crystallographic structures of the films were analyzed by a PANalytical X'Pert MRD diffractometer with CuKα radiation (λ = 0.15406 nm). The cross-sectional morphology of the continuous Py films was examined with a JEOL JEM2011 TEM and a JEOL ARM200F Scanning Transmission Electron Microscope (STEM). The topography was analyzed with a Bruker MultiMode 8 AFM (see subsection 3.3.1). Olympus OMCL-AC240TS cantilevers [134] with a 14 nm tip-apex diameter and 0.05 nm vertical sensitivity [211, 212] were used. The elemental composition of the Py films was investigated with a Genesis 2000 energy-dispersive X-ray spectroscopy (EDX). For the magnetic measurements, the in-plane and out-of-plane magnetic hysteresis loops of the continuous films were measured with a DMS model 10 vector VSM. The magnetic domain configurations of the patterned Py films were analyzed with the MFM mentioned in subsection 3.3.1.

Energies of the different types of the domain configurations in a Py square were micromagnetically calculated. The OOMMF software [52] with a cubic cell of 10 nm edge length was used to carry the three-dimensional simulations. The saturation magnetization of $M_s = 860$ kAm^{-1}, an exchange constant of $A_{ex} = 13 \times 10^{-12}$ Jm^{-1}, and a gyromagnetic ratio of $\gamma = 2.21 \times 10^5$ m(As)$^{-1}$ were assumed in the simulations. To perform the static simulations, a damping parameter of $\alpha = 0.5$ was applied. The convergence criterion $| \mathbf{M} \times \mathbf{H_{eff}} | / M_s^2 \leq 1 \times 10^{-5}$ as a torque-minimization condition was employed in the calculations.

4.3 The crystal structure and morphology as a function of the argon pressure

Figure 4.2 shows the XRD patterns of a bare Si substrate and of Py films sputtered on top of the substrates at different Ar pressures. From Fig. 4.2 it is clear that with the increase of the Ar pressure, the basic crystal structure of the Py films remains unchanged, whereas the intensities of all XRD peaks decrease. All Py films show a

fcc phase with a preponderance of (111) crystallographic planes oriented parallel to the film surface. The crystallite size calculated by the Williamson-Hall method [213] remains in the 9-12 nm range. With increasing Ar pressure, a peak with increasing intensity at 53.6° was observed. Comparing the Py films XRD patterns with that of the bare Si substrate, it became obvious that this peak is due to the substrate. The appearance of this substrate peak indicates the reduction of the number of crystallites in Py films with increasing Ar pressure, because the thickness of the Py film prepared at 30.0 µbar is almost same as that of Py film prepared at 1.5 µbar. The thicknesses of the Py films prepared at different Ar pressures are listed below in tabel 4.1. The thicknesses of the Py films were measured from the cross-sectional images taken by TEM.

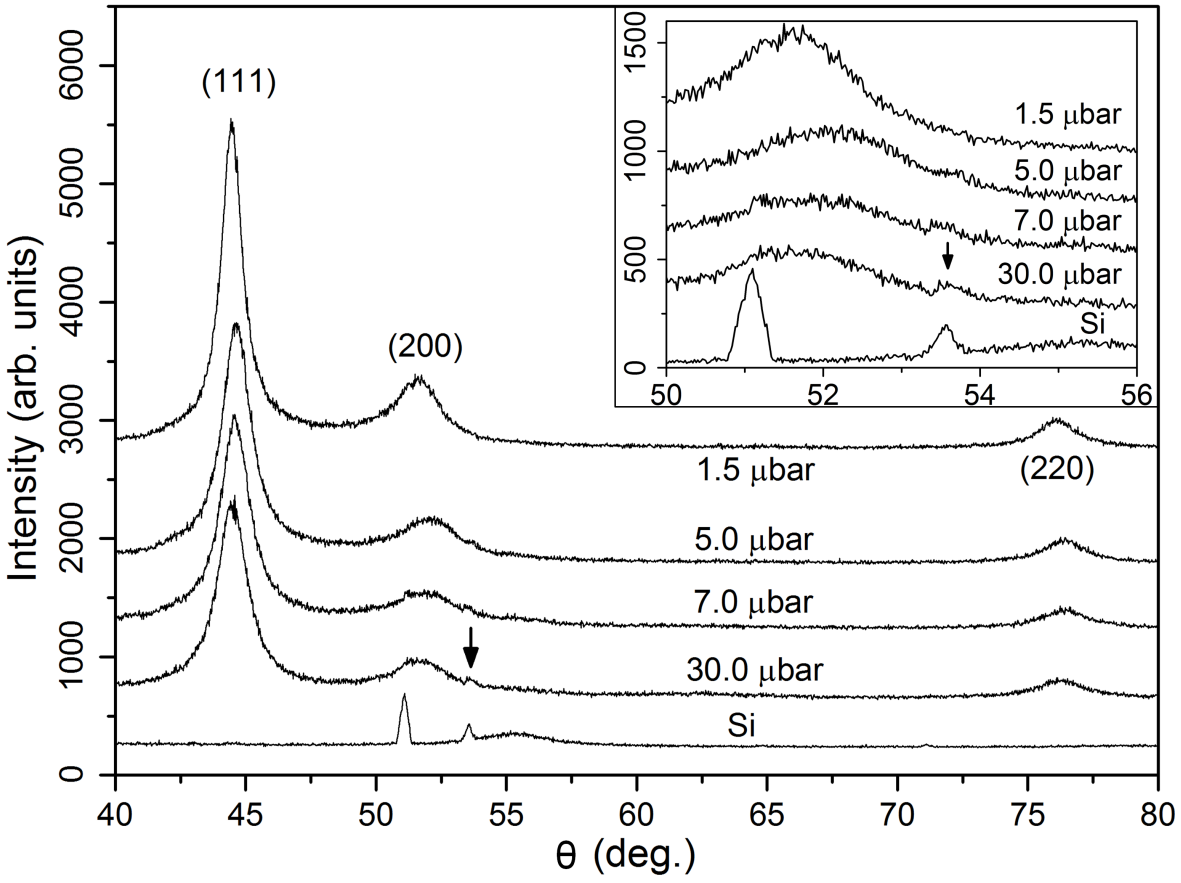

Figure 4.2: XRD patterns of a bare Si substrate and of Py films deposited at different Ar pressures. The inset image shows a detailed view of the influence of the Si substrate on the Py XRD patterns. The substrate peak from the Py XRD pattern is indicated by a black arrow. A slight shift of the peak position for films prepared at 5.0 and 7.0 µbar Ar pressure could be due to the change of stress inside the films [160].

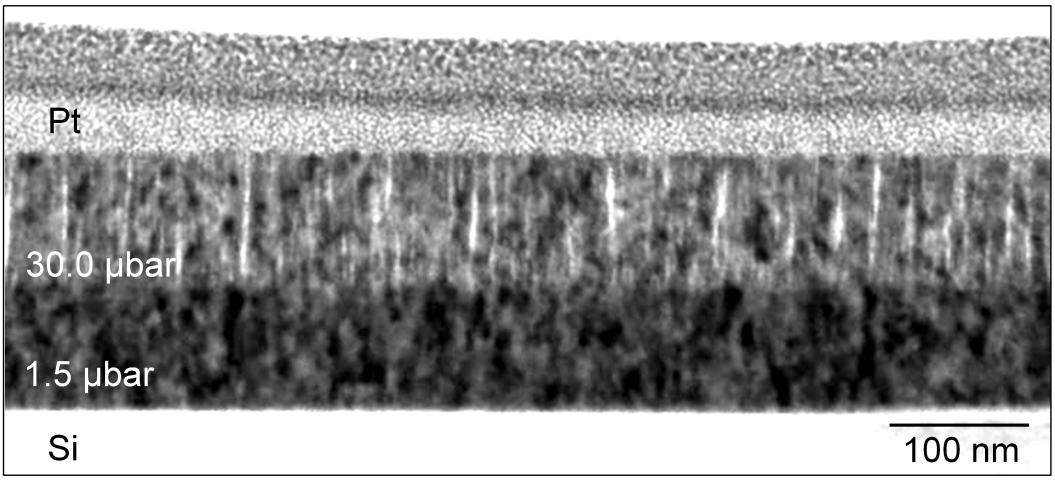

Figure 4.3: A bright-field TEM image of the cross-sectional grain morphologies of Py films grown consecutively on a Si substrate at 1.5 µbar and 30.0 µbar Ar pressures, respectively. A capping layer of Pt was deposited on top to protect the Py films during the necessary FIB treatment.

Structures of the Py films prepared at 1.5 µbar and 30.0 µbar Ar pressures were investigated in more detail by TEM and AFM. To observe the cross-sectional grain morphology, a slice of both films deposited on top of each other was prepared by Ga^+ FIB milling. From the TEM analysis shown in Fig. 4.3, it is clearly visible that the film deposited at 1.5 µbar Ar pressure grew with a denser morphology, whereas the film deposited at 30.0 µbar shows columnar grains separated by non-magnetic inter-grain boundaries. Further the TEM observations of the cross-sectional grain morphologies of separated Py films are shown in the appendix (see Fig. A.4 in section A.2). The comparison of Fig. 4.3 with Fig. A.2 proves that the growth of the second layer on top of the first did not alter the grain morphologies of the both films. The elemental composition measured from the film prepared at 30.0 µbar Ar pressure with Electron-Energy-Loss-Spectroscopy (EELS) is shown in Fig. 4.4. The line profile of the elemental composition shows an increase of the oxygen content at the inter-grain boundaries as seen in Fig. 4.4. Since this measurement was performed at high vacuum ($\sim$ nbar) inside the STEM chamber, so there was no atmospheric-oxygen present at the inter-grain boundaries. Therefore, the increase of the oxygen content at the inter-grain boundaries is due to the oxidation of the Py grains [214, 215]. AFM images in Fig. 4.5 show an increase in the surface roughness of the film with increasing Ar pressure. The rms roughness increased from 0.2 nm at 1.5 µbar to 1.1 nm at 30.0 µbar, respectively.

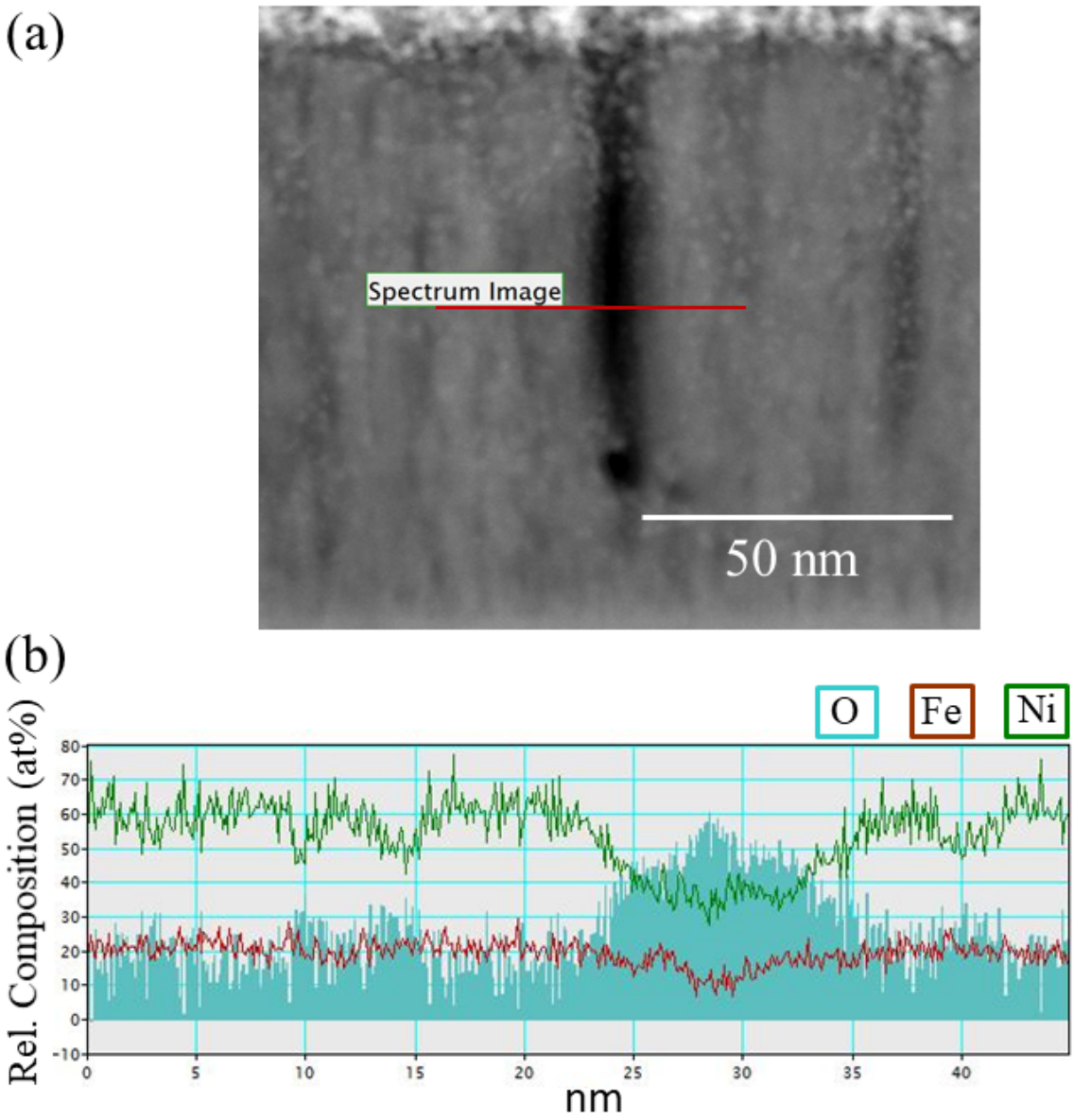

Figure 4.4: (a) A cross-section of the Py film deposited at 30.0 µbar Ar pressure taken with a STEM in the dark-field mode. (b) Electron Energy-Loss Spectroscopy line profile of a gap between columnar grains formed inside the film. The red line in (a) indicates the path along which the elemental composition was measured.

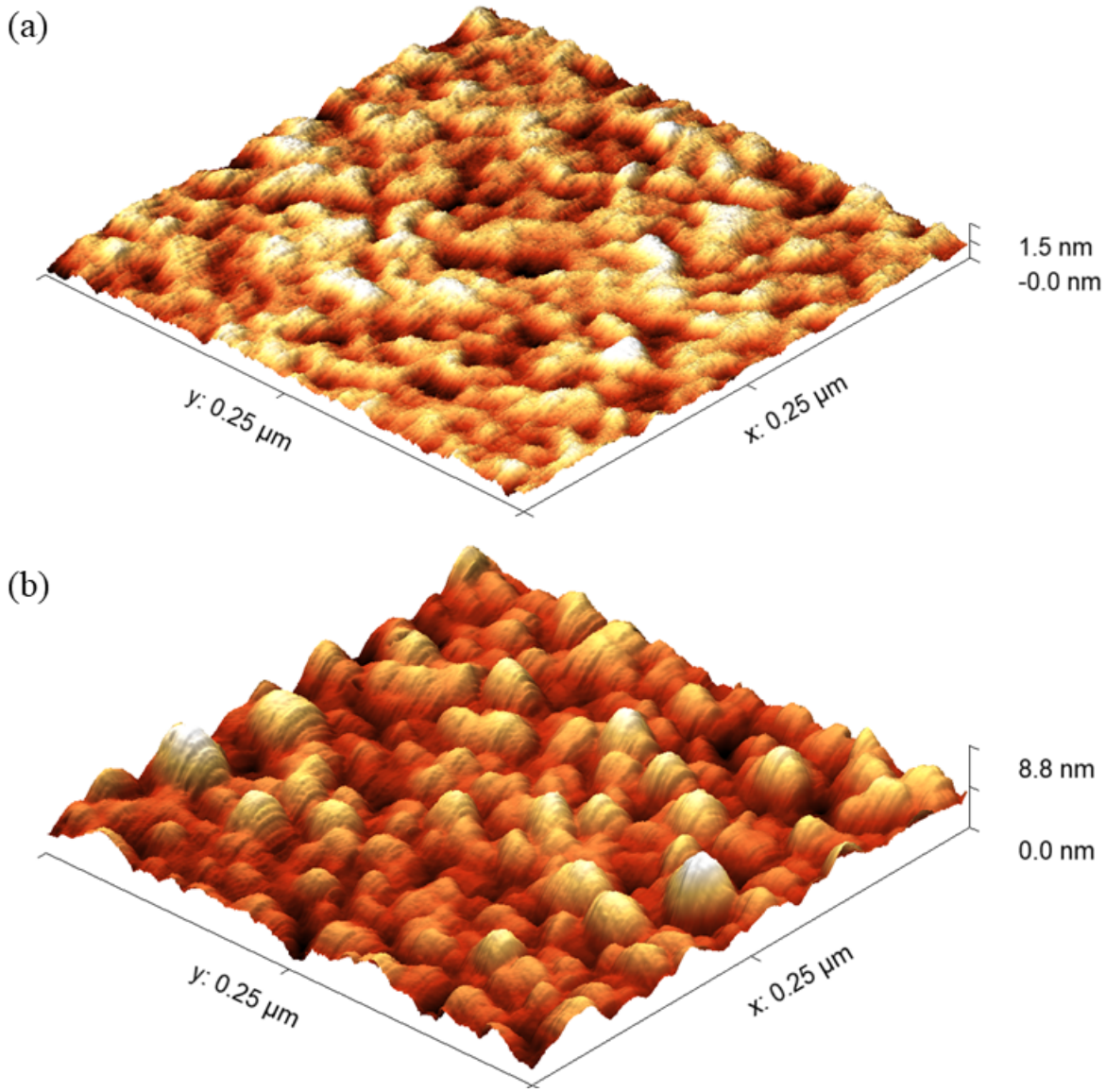

Figure 4.5: AFM images of the surface morphology of Py films prepared at (a) 1.5 µbar and (b) 30.0 µbar Ar pressures.

4.4 Magnetic hystereses as a function of the argon pressure

In Figs. 4.6(a) and (b), the in-plane and out-of-plane magnetic hysteresis loops of the continuous Py films prepared at varying Ar pressures are shown, respectively. From these VSM results, it is obvious that the saturation magnetization of the Py films decreased with the increase of the Ar pressure. The ratios of the saturation magnetization of the films (M_s^f) to bulk value ($M_s^b = 860$ kAm^{-1}) are shown in table 4.1. The in-plane saturation field measured from Fig. 4.6(a) increased from 15 mT to

more than 1200 mT with the increase of Ar pressure. The film prepared at 30.0 µbar Ar pressure did not saturate up to 1200 mT as shown in the inset image in Fig. 4.6(a). The out-of-plane saturation field decreased according to Fig. 4.6(b) from 1300 mT to 600 mT with the increase of Ar pressure. Also, the in-plane coercivities ($\mu_0 H_c^{\text{in-plane}}$) of the Py films increased from 0.12 mT to 4.30 mT, as specified in table 4.1.

The film deposition rate shown in table 4.1 was calibrated using a quartz crystal microbalance. The deposition rate decreased with the increase of Ar pressure. At high Ar pressure the number of collisions of the sputtered target atoms with the Ar atoms and ions increases. As a result the sputtered atoms scatter by large angles and less number of sputtered atoms reach at the substrate [130].

The elemental composition measured with EELS, shown in Fig. 4.4, of the film prepared at 30.0 µbar Ar pressure is quite different than measured with EDX, shown in table 4.1. These two measurements were performed on two different samples prepared at same sputtering conditions. The reasons of too low Ni at% in EELS measurement are not known yet, till the time of describing the results in this thesis. However, the EELS measurement was performed only to prove the oxidation of the films at the pores rather than measuring the composition of the film.

Ar Press. (µbar)	Dep. rate (nm/min)	thickness (nm)	Ni (Ni:Fe) (wt%)	O (Ni:Fe:O) (wt%)	$\mu_0 H_c^{\text{in-plane}}$ (mT)	M_s^f/M_s^b
1.5	18.6	65	81.0	3.0	0.12	0.92
5.0	13.2	50	82.9	5.0	0.40	0.77
7.0	10.7	51	84.4	8.5	5.73	0.63
30.0	4.0	67	84.3	14.6	4.30	0.53

Table 4.1: Sputtering parameters, structural and magnetic properties of deposited Py films. Ni wt% values are calculated considering Ni and Fe as components. Whereas, O wt% values are calculated considering Ni, Fe and O as components.

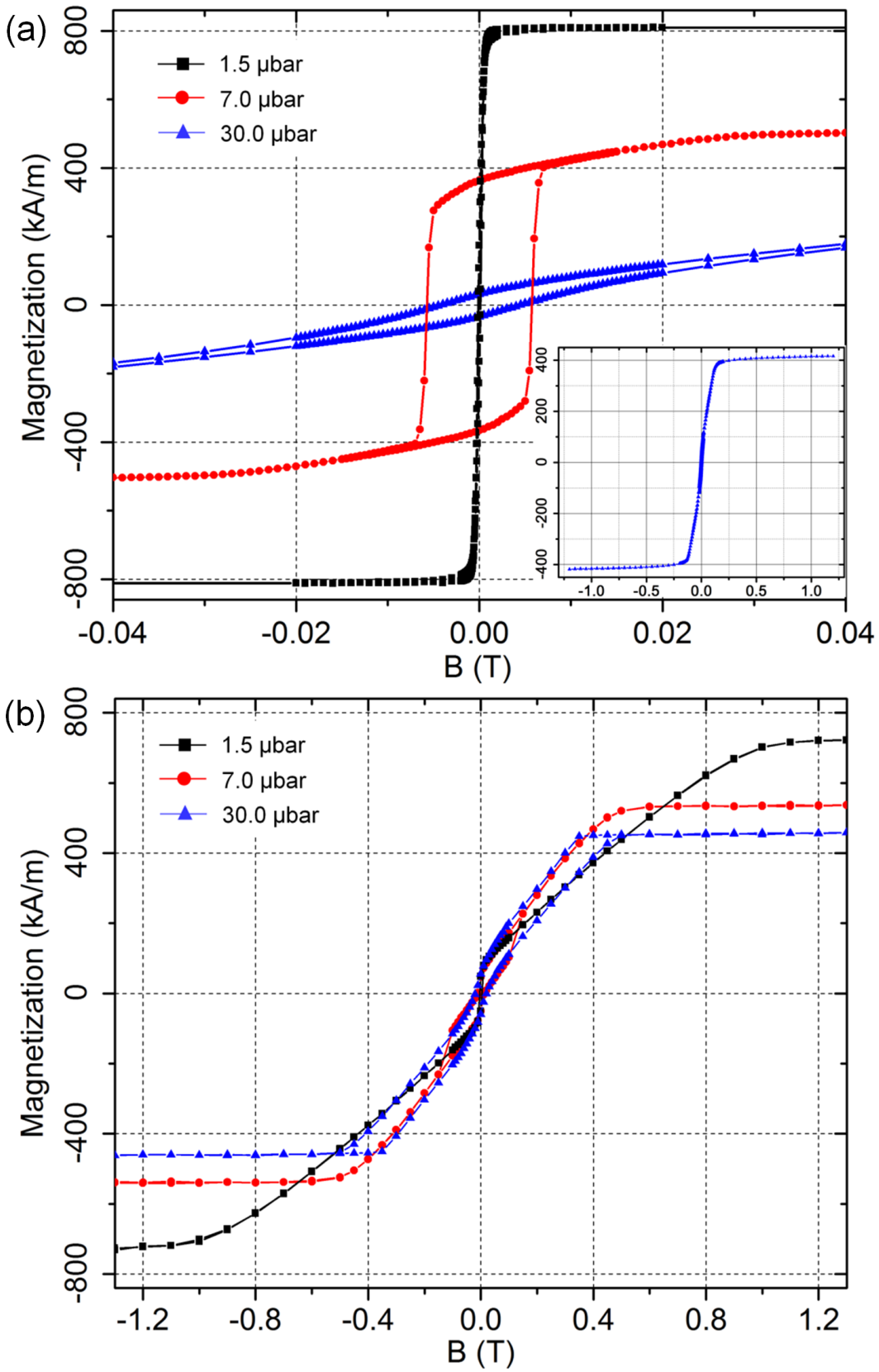

Figure 4.6: In-plane (a) and out-of-plane (b) magnetic hysteresis loops of Py films prepared at different Ar pressures. The inset image in (a) shows an in-plane hysteresis loop of the film prepared at 30.0 µbar Ar pressure with an applied field of up to 1.20 T.

4.5 Experimentally observed domain configurations at varying argon pressure

Figure 4.7 shows MFM images of remanent domain configurations, i.e., the zero-field states of the patterned Py films prepared at different Ar pressures. Nine out of two hundred squares patterned in each array are shown. Domain configurations in disks prepared at 1.5 and 5.0 µbar Ar pressures are shown in appendix (see Fig. A.5 in section A.3). In Fig. 4.7, Landau domains in Fig. 4.7(a), tulip domains in Fig. 4.7(b), irregular domains in Fig. 4.7(c) and no domain configurations in Fig. 4.7(d) are visible. The number of squares showing the Landau, tulip, diamond and irregular domain states as remanent states were counted after each hysteresis loop. For the squares prepared at 1.5 µbar Ar pressure, approximately 90% of the squares showed the Landau domain state. The remaining squares showed either tulip or diamond domain states. For the squares prepared at 5.0 µbar Ar pressure, no square showed the Landau domain state as the remanent state. However, approximately 60% of the squares showed multiple tulip domain configurations as remanent states. For repeated hysteresis loops, positions of the tulip configurations with respect to the corners of the squares changed. Remaining squares showed irregular domains with complex arrangements of vortices and antivortices (see Fig. 2.12) in their remanent states. For the squares prepared at 7.0 µbar Ar pressure, again no Landau domain configuration was observed, but more than approximately 80% of the squares showed irregular domains and the remaining squares showed multiple tulip configurations at the corners. For the squares prepared at 30.0 µbar Ar pressure, no clear domain configuration was observed at any applied field value from zero to 80 mT.

In order to understand the formation of the remanent domain configurations in squares prepared at different Ar pressures, their evolution was studied in more detail. For this purpose, MFM images were taken in external fields between the saturation and remanent states as shown in Figs. 4.8, 4.9, and 4.10, respectively. Two squares from each array were respectively selected for the observations.

For the squares prepared at 1.5 µbar Ar pressure upon reduction of the applied field from the saturated stage Fig. 4.8(a), the well-defined S-state end domains [184, 195, 216] formed at the edges as seen in Fig. 4.8(b). With further decreasing the field, the S-state end domains expanded inside the squares as shown in Figs. 4.8(c) and (d). At 2.4 mT in Fig. 4.8(e), S-state end domains in the right square evolved into a four-domain configuration with a vortex formed close to the upper edge of the square. In the left square, the S-state end domains evolved to form a domain wall close to the left edge of

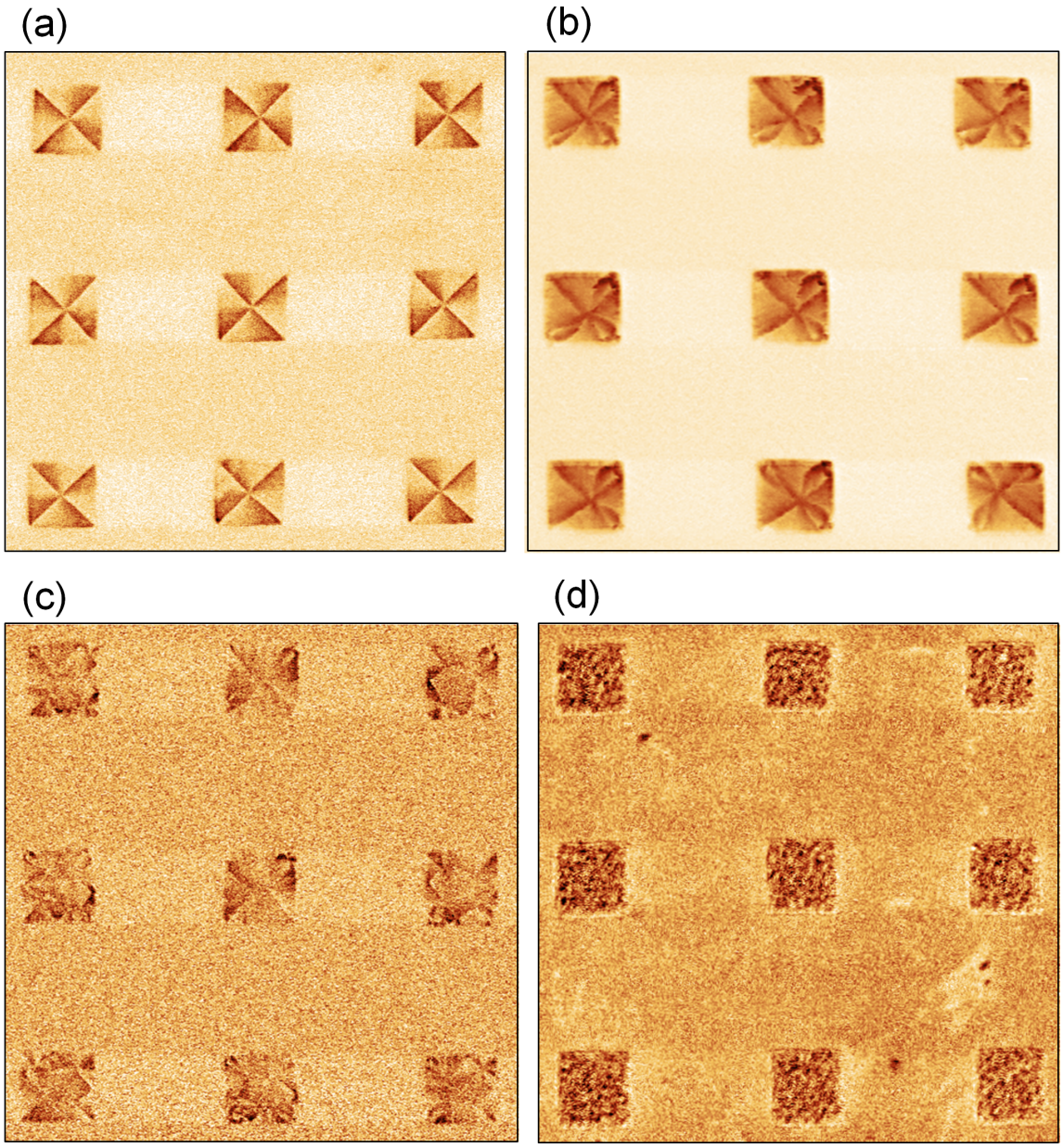

Figure 4.7: MFM images in the remanent states of Py squares of 5 µm edge lengths prepared at (a) 1.5 µbar, (b) 5.0 µbar, (c) 7.0 µbar and (d) 30.0 µbar Ar pressure, respectively.

the square and a vortex close to the upper edge of the square. Below 2.4 mT external field, the domain wall formed close to the left edge of the left square was pushed out of the square, and the vortices formed close to the upper edges of both squares moved towards the centers to form four domains inside the squares, as shown in Fig. 4.8(f). At zero field, the Landau domain state was established in both squares.

For the squares deposited at 5.0 µbar Ar pressure and shown in Fig. 4.9, the

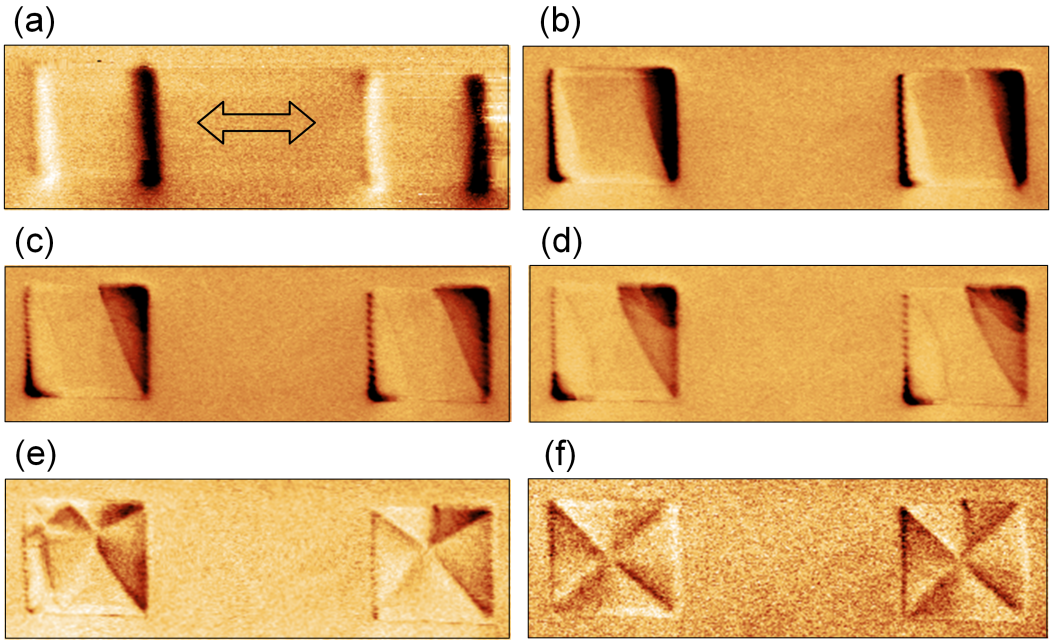

Figure 4.8: MFM images of two 5×5 µm^2 Py squares prepared at 1.5 µbar Ar pressure and scanned at (a) 16.0 mT, (b) 9.0 mT, (c) 6.0 mT, (d) 3.6 mT, (e) 2.4 mT and (f) zero field. The left-right arrow in (a) represents the axis of the applied magnetic field.

well-defined S- or C-state end domains [184, 195, 216] were not formed. Upon reduction of the applied field from the saturation state seen in Fig. 4.9(a), multiple domain walls were nucleated from the edges as seen in Figs. 4.9(b) and (c). Upon further reduction of the field, multiple vortices and antivortices were nucleated which led to the formation of multiple tulip configurations at the corners of the squares, as shown in Figs. 4.9(d) to (f). The remanent configurations close to the corners of the squares differed from one square to another square.

For the squares deposited at 7.0 µbar of Ar pressure, the reduction of the applied field from saturation again did not result in the well-defined S- or C-state end domains, as seen in Figs. 4.10(a) to (c). Domain walls being primarily perpendicular to the applied field were nucleated as shown in Figs. 4.10(d) to (f). This explains the increase of the remanent magnetization with increasing sputtering pressure observed in Fig. 4.6(a). Detailed magnetization configurations in the remanent states of the squares differed from each other.

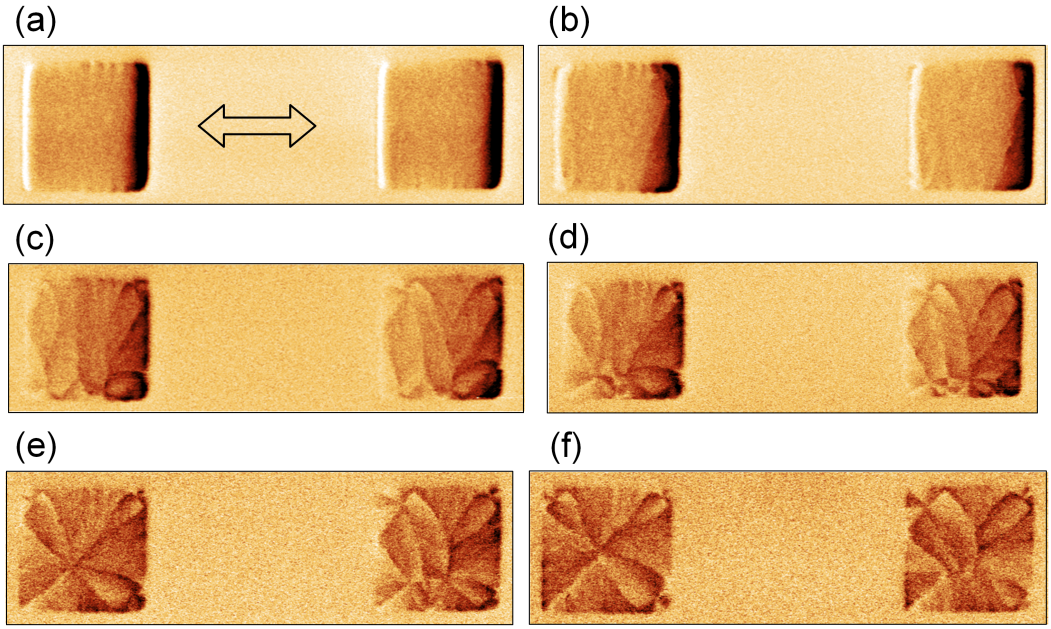

Figure 4.9: MFM images of two 5×5 µm^2 Py squares prepared at 5.0 µbar Ar pressure and scanned at (a) 16.0 mT, (b) 8.4 mT, (c) 2.5 mT, (d) 2.2 mT, (e) 0.9 mT and (f) zero field. The left-right arrow in (a) represents the axis of the applied magnetic field.

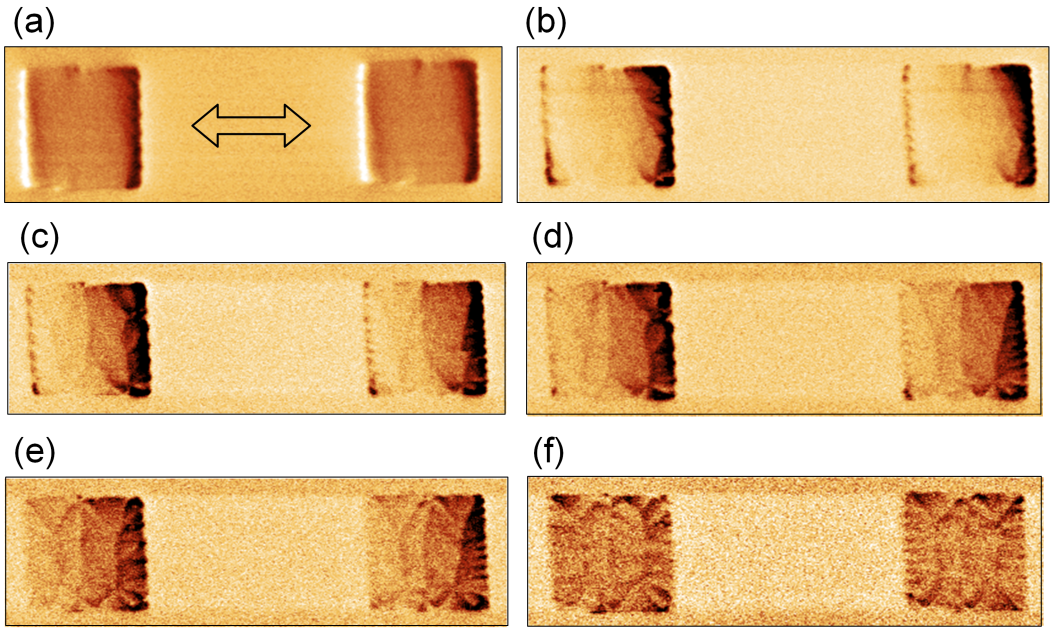

Figure 4.10: MFM images of two 5×5 µm^2 Py squares prepared at 7.0 µbar Ar pressure and scanned at (a) 16.0 mT, (b) 6.0 mT, (c) 3.9 mT, (d) 3.1 mT, (e) 1.9 mT and (f) zero field. The left-right arrow in (a) represents the axis of the applied magnetic field.

4.6 Energies of the zero-field domain configurations

In Fig. 4.11, out of a large number of possible zero-field domain configurations, four experimentally relevant domain configurations calculated for a 60 nm thick 5×5 µm^2 Py film are shown. No grain morphology was assumed in the simulations. Landau, tulip and irregular domain configurations were obtained by selecting a random magnetization configuration as an initial stage. The diamond configuration was obtained from a seven-domain configuration initial stage. For Landau and diamond configurations, the magnetization was allowed to relax according to the convergence criterion mentioned in section 4.2, whereas for tulip and irregular domain configurations, simulations were stopped before convergence. Corresponding magnetic energies are listed in table 4.2. The Landau state configuration has the lowest energy. The energy of the tulip state is higher because of the formation of an extra vortex and domain walls at the corner of the patterned film. The diamond domain configuration with multiple vortices and antivortices has even higher energy. An irregular domain configuration shown in Fig. 4.11(d) has the highest energy.

Domain configuration	Energy (eV)
Landau	2727.7
Tulip	3302.0
Diamond	7016.0
Irregular	9606.4

Table 4.2: Different domain configurations and their magnetic energies.

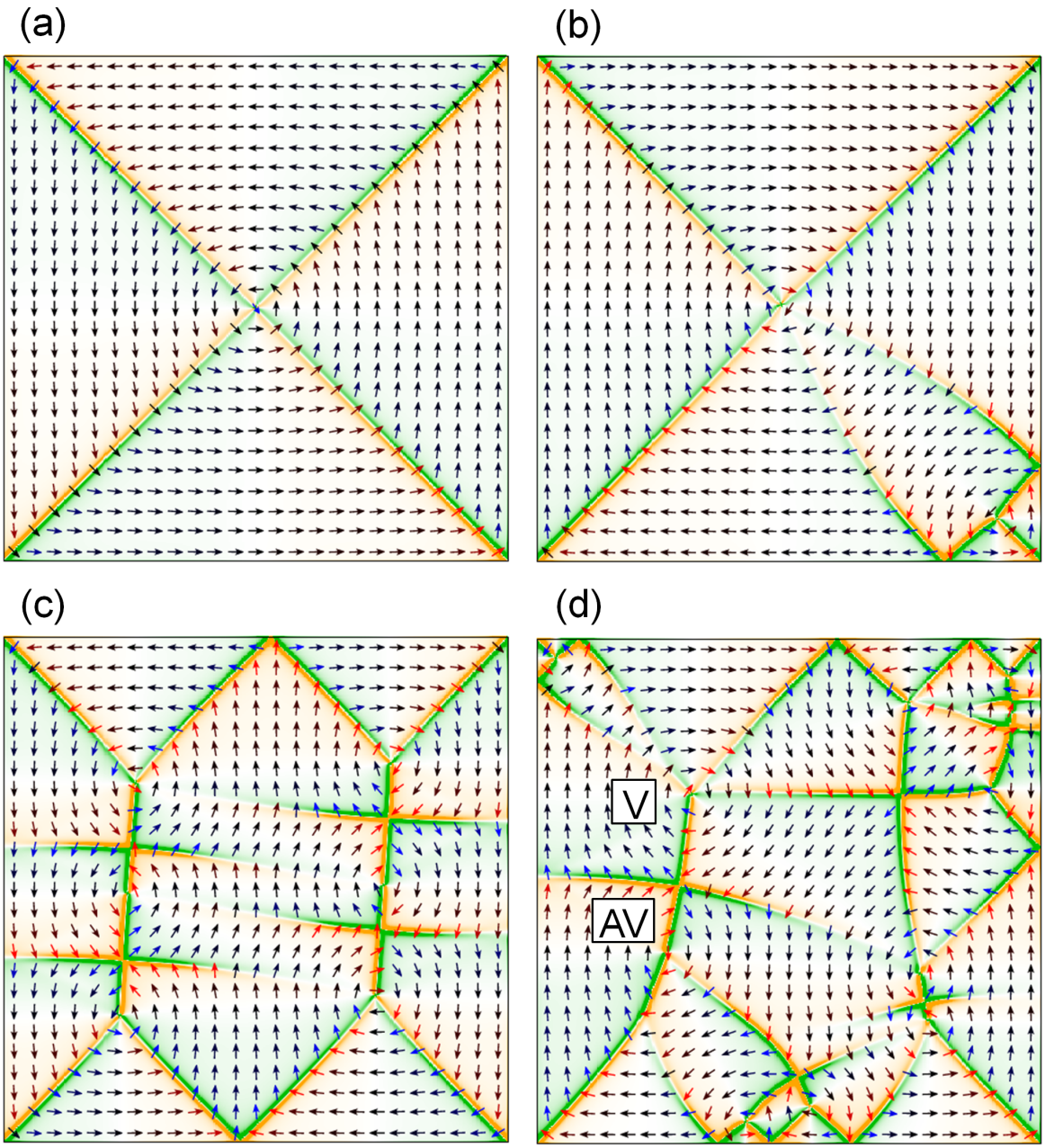

Figure 4.11: OOMMF-simulated domain configurations of a 60 nm thick 5×5 µm^2 Py square. (a) Landau state, (b) tulip state, (c) diamond state and (d) an irregular domain configuration shown with a vortex (V) and an antivortex (AV) indicated. Each arrow represents an averaged magnetization vector inside 20×20 adjacent cells on the sample surface. Black arrows represent the in-plane magnetization, whereas blue and red arrows are the in-plane projections of the magnetization vectors tilted upwards and downwards, respectively. Orange and green areas represent positive and negative charge-density locations, respectively. Images are shown in the order of increasing energy of the domain states.

4.7 Discussion

From the XRD and TEM measurements shown in Figs. 4.2 and 4.3, respectively, and as well from the reduction of the saturation magnetization in table 4.1, it is clear that the grain morphology of the films changed from denser to more porous with the increase of the Ar pressure during sputtering. At high Ar pressure, the sputtered atoms reach at the substrate with less energy and have low surface mobility as they lost a big part of their energy on collisions with Ar atoms and Ar ions [130]. Also, due to the increased number of collisions at higher Ar pressure, the sputtered atoms reach at the substrate surface at oblique angles [130]. The oblique incidence of the sputtered atoms creates an atomic-shadow effect [217, 218]. Because of a low surface mobility of the deposited atoms, they can not overcome the effect of atomic-shadow and therefore the films at higher Ar pressure grow with large voids and columnar grains [217, 219, 220]. With decreasing film density, the exchange interactions between the grains of the polycrystalline films are expected to become weaker [17]. This, in turn, explains why the average size of the magnetic domains inside the squares decreased with the increase of Ar pressure, as observed in Figs. 4.7, 4.8, 4.9 and 4.10. Moreover, EDX data presented in table 4.1 proves that the stoichiometry of the films prepared at 1.5 µbar Ar pressure is closest to the target composition ($Ni_{80}Fe_{20}$). Thus, the magnetostriction coefficient of those films is the lowest [124, 200]. Because of the relatively high density and low magnetostriction coefficient, the lowest in-plane coercivity and saturation field were observed, as shown in Fig. 4.6(a). In this case, magnetic domains inside the squares were solely defined by the shape of the squares rather than by the film morphology. This led to the formation of the well-defined end domains and the magnetization always evolved to the Landau-domain configuration in the zero-field state, which is the lowest energy state for an ideal dense film without granular texture and stress, as seen in section 4.6. With the increase of Ar pressure, the film growth involved more and more columnar grains separated by oxides. This inevitably resulted in an increase of pinning sites for the vortices, antivortices and domain walls. Consequently, the in-plane coercivity and in-plane saturation field increased, as seen in Fig. 4.6(a). Moreover, the Ni content was found to increase when Ar pressure was increased. This is due to the reduced relative mean free path of the sputtered Fe atoms with respect to the Ni atoms [15, 221]. The increase of the Ni content, and hence the magnetostriction coefficient of the film, made the magnetization sensitive to the stress inside the film. As a result, irregular and smaller domains, especially at the sample edges, were formed because of the local variation of the stress at the edges [187]. Therefore an increase in the complexity of

the end domains was observed in Figs. 4.9 and 4.10. The increased number of pinning sites and the increased magnetostriction coefficient of the film led to stabilization of the multiple tulip configurations and irregular domains in remanent states, which are energetically less favorable states for an ideally dense and stress-free film as seen in section 4.6. Stress and the reduced inter-granular exchange interactions inside the films prepared at higher Ar pressures induced energy barriers in the magnetic energy landscape and in consequence stabilized these local minimum energy states. Moreover, local variations in the tulip and irregular domains configurations from one square to another one indicate that the remanent states in these cases are not well-defined. Films prepared at 30.0 µbar Ar pressure do not show any visible domain contrast in the MFM data, as presented in Fig. 4.7(d). This could be due to the complete oxidation of the porous films exposed to the atmospheric oxygen [214, 215]. EDX analysis in table 4.1 confirms the increase of the oxygen content with increasing Ar pressure.

With increasing Ar pressure, a decrease of the saturation field in the out-of-plane hysteresis loops (Fig. 4.6(b)) indicates an increase in the perpendicular anisotropy inside the films. The granular shape anisotropy induces perpendicular anisotropy inside those films prepared at relatively high Ar pressures [110, 198]. The shape anisotropy calculated by assuming perfect non-interacting columnar grains of 10 nm diameter (the average grain size calculated from the XRD measurements) for the film prepared at 30.0 µbar Ar pressure is 52 $\mathrm{kJm^{-3}}$ [222]. Whereas, the perpendicular anisotropy ($K_\mathrm{p} = (\mu_0 M_\mathrm{s}^2/2)(1 - H_\mathrm{p}^\mathrm{sat}/M_\mathrm{s})$) calculated from the out-of-plane hysteresis loop (Fig. 4.6(b)) for this film is 6.4 $\mathrm{kJm^{-3}}$. The large difference between the two anisotropy constants indicates a non-zero interaction between the grains. In addition, the stress-induced anisotropy also contributes to the perpendicular anisotropy of the films. However, the calculation of the strength and orientation of the stress-induced anisotropy is beyond the scope of the investigations shown in this chapter. Therefore, a conclusion of the interaction between the columnar grains and contribution of stress-induced anisotropy in the total perpendicular anisotropy of the film is ambiguous.

4.8 Conclusion

To conclude, it is shown that the well-defined Landau-domain configuration can be obtained in Py thin film squares by sputtering at a low Ar pressure, i.e, at 1.5 µbar. With the increase of the pressure, the soft magnetic properties of the films deteriorated rapidly. This was due to an increased Ni content, a decrease of the film density and growth of the columnar grains in the films. The decrease in the film density resulted in

a reduction of the inter-grain exchange interactions and to an increase in the number of pinning sites for vortices, antivortices and domain walls. In this case, domain configurations were more determined by the morphology of the films rather than by the shape of the patterned thin film. Moreover, an increase of the in-plane coercivity and in-plane saturation field was observed due to the increase of the Ni content and the reduction of the inter-grain exchange interaction. The formation of the columnar grains on increasing the Ar pressure resulted in the increase of the perpendicular anisotropy inside the films.

5 The role of vortex-antivortex pairs in the magnetization reversal of patterned thin films

5.1 Introduction

A detailed understanding of the magnetization-reversal process is important both in fundamental research on magnetic materials and in applications, e.g., data storage devices [223, 224]. In general, magnetization reversal in magnetic films proceeds with the nucleation and expansion of reversed domains [225]. In micro-patterned films, domain walls nucleate and form multiple junctions which lead to the formation of clusters of the walls at the edges and within the sample [226–228]. Moreover, micromagnetic entities such as vortices, antivortices [37, 229, 230] as well as singularities (BPs) [231] nucleate inside the domain walls as their TSs during the magnetization-reversal processes. In soft magnetic films of a thickness of approximately below 20 nm, domain walls avoid to have any TS due to energetic reasons [2]. However, as discussed in chapter 2 in subsection 2.5.1, for the intermediate film thicknesses, i.e., for approximately 20 to 100 nm, vortices and antivortices exist as TSs inside domain walls [2, 230], whereas complex arrangements of vortices, antivortices and BPs form three-dimensional TSs in thicker films (above approximately 100 nm) (see subsection 2.5.2 for details) [2, 97, 99, 232].

Different types of domain configurations within and without applied fields have been explored in the films of intermediate thicknesses due to their applications in magnetic data storage [233], sensors [233, 234] and other devices [235]. Such studies involve investigations of the influence of the magnetic history [39, 40, 197], field-sweep rates [35, 36, 186] and shape and size of the films [236, 237] on magnetization reversals. The micromagnetic behavior of vortices and antivortices such as their nucleation, displacement and annihilation was studied in this context [35–38, 94]. Vortices show a mobility above a certain threshold field [38], whereas antivortices stay more or less

fixed and tend to pin the motion of the domain walls [38, 94]. Also, it was found that the trapping of the vortices at the sample edges lowers their reversal fields [39, 40]. The micromagnetic behavior of vortices and antivortices varies with the change of the field-sweep rate, which alters the evolution of the domain configuration formed in the course of the reversal process [35, 36]. Since the domain configurations define typical magnetic characteristics of thin films such as the coercivity [39, 40, 47], the shape of the hysteresis loop [39, 40] and the magnetoresistance [42, 43], it is crucial to understand the role of vortices and antivortices in the evolution of domains. However, except for a few regular domain configurations such as Landau [36, 237], diamond [36, 237] and concertina domains [226, 228, 238], the formation of complex domains with coupled vortices and antivortices [187, 188, 239–241] is not completely understood.

In this chapter, the role of vortices and antivortices in the magnetization reversal of patterned Py films of intermediate thicknesses is reported. By applying in-plane magnetic fields during MFM measurements, magnetization reversals along the sample's long and short axes are compared, respectively. Contributions of different magnetic energies in the evolution of the domain configurations are evaluated by using micromagnetic simulations.

5.2 Experimental and micromagnetic simulation details

Py patterns of 9×18 µm^2 dimensions were fabricated using EBL and DC magnetron-sputtering techniques (see section 3.2 for details). The Py film were deposited at 3.0 µbar Ar pressure at a constant sputter rate of 18 nm/min. The thicknesses of the films were chosen to be 50 nm. At this thickness, CTWs containing vortex-antivortex pairs (VAVPs) are formed (see subsection 2.2.2) [2, 230, 242]. For micromagnetic simulations, a cubic cell of $20 \times 20 \times 50$ nm^3 dimensions was used. The rest of the experimental deposition and micromagnetic simulation parameters were chosen as described in section 4.2 of chapter 4.

5.3 Magnetization switching of patterned permalloy films along their easy and hard axes

5.3.1 Easy axis switching

For the easy axis switching (EAS) process, MFM measurements and micromagnetic simulation results are shown in Figs. 5.1 and 5.2, respectively. Before the measurement, the sample was saturated by an external in-plane magnetic field applied along the −y direction. When the field was reduced, the magnetization at the sample ends formed S-shaped closure domains [201, 243], as seen in Figs. 5.1(a) and 5.2(a). In these images, an edge cluster of three domain walls [228, 244] was also observed at both ends of the sample. A more detailed view of this wall-cluster is shown in Fig. 5.3 and schematically drawn in Fig. 5.4. This wall-cluster evolved with the change of applied field. From Fig. 5.4, it can be seen that with the reduction of the applied field as the magnetization inside the upper-end domain relaxed more along the upper edge of the sample, the angle of the middle wall (which is connected between the edge and the corner of the sample) of the wall-cluster increased. The schematics in Figs. 5.4(a) to (d) are drawn according to the decrease of the applied field. More detailed information about the domain wall clusters can be found in Refs. [2, 226–228, 244].

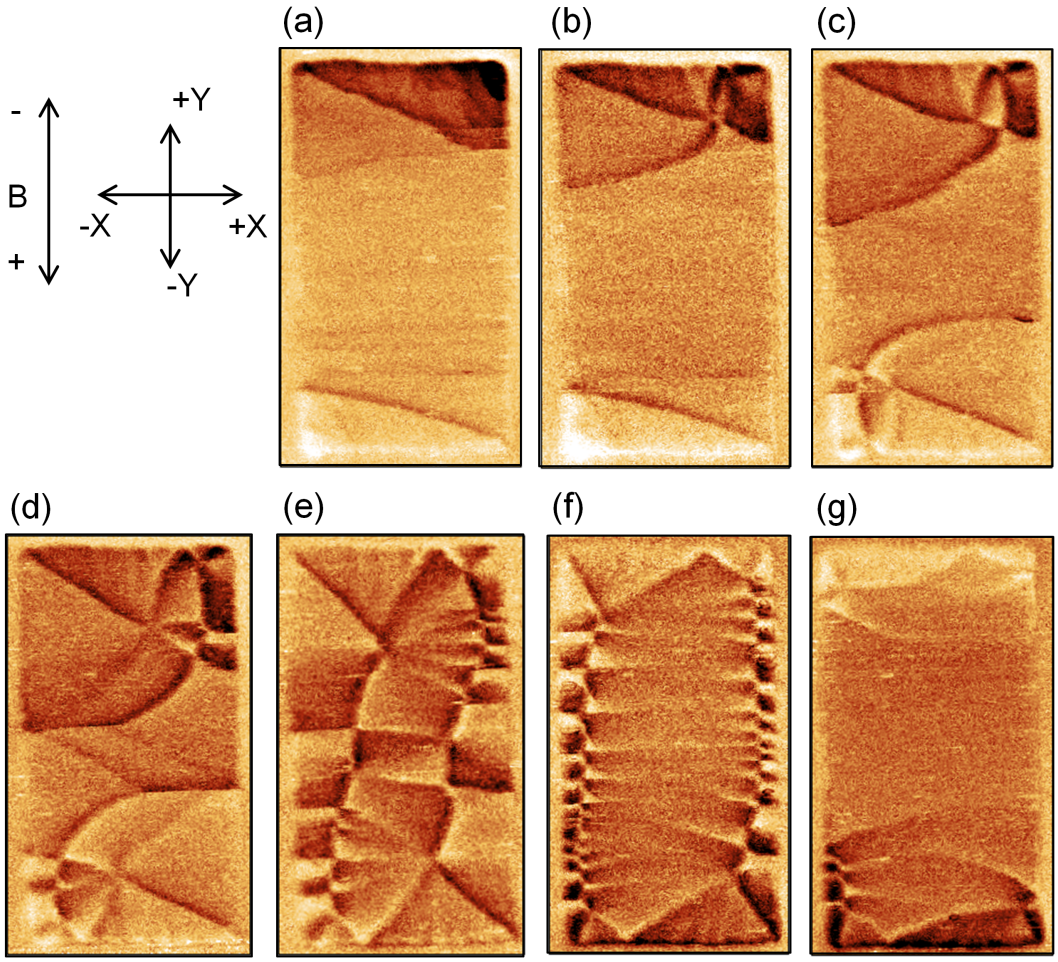

Figure 5.1: Magnetization reversal of a Py bar sample parallel to its long axis. The magnetic field was swept from +80 mT to −80 mT. The MFM images were taken at (a) +2.0 mT, (b) +1.7 mT, (c) +0.7 mT, (d) zero, (e) −0.1 mT, (f) −1.5 mT, and (g) −2.3 mT, respectively.

All domain walls at this thickness (i.e., 50 nm) are SNWs (see subsection 2.2.2). But there is a considerable difference between the energies of the 90^o and 180^o SNWs. The energy of a 90^o SNW is only 12% of the energy of a 180^o SNW [2]. According to the model developed by Middlehoek [245], in a Py ($Ni_{80}Fe_{20}$) film with a thickness below 90 nm, a SNW with an angle larger than 100^o splits into a periodic cross pattern of 90^o SNWs, i.e., a CTW (see subsection 2.2.2). The phase boundary (and hence the wall-angle), which separates the stability range of the SNWs and CTWs for a particular material, varies with both the film thickness as well as the applied field (see Fig. 2.10) [2, 86, 245].

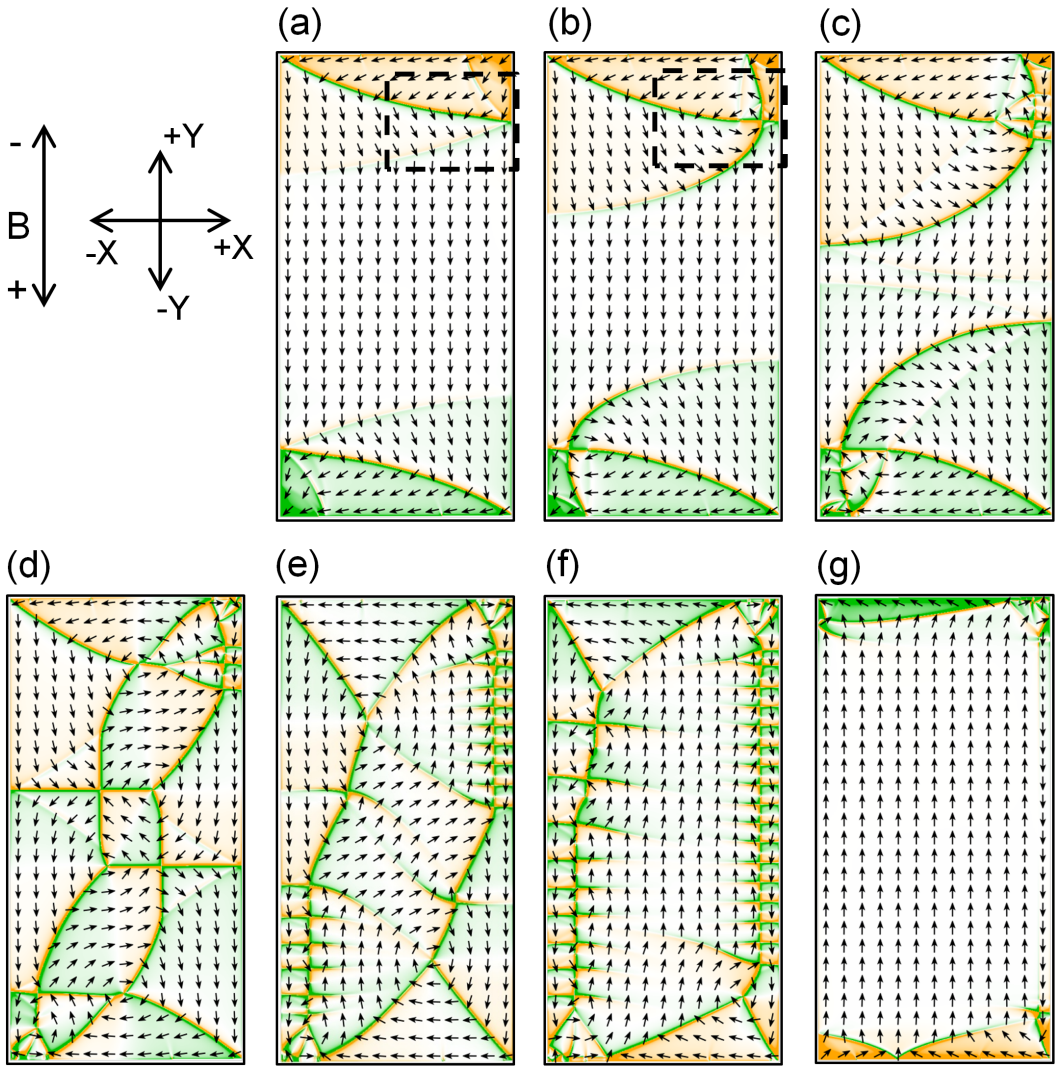

Figure 5.2: Micromagnetic simulation results of the magnetization reversal parallel to the long axis of a Py sample. The magnetic field was swept from +500 mT to −500 mT. For the presented images, the field steps are: (a) +1.8 mT, (b) +1.2 mT, (c) +0.6 mT, (d) zero, (e) −0.6 mT, (f) −3.1 mT, and (g) −8.9 mT, respectively. Each arrow in (a) to (g) represents an averaged magnetization inside 35 × 35 adjacent cells. Orange and green areas represent positive and negative charge densities, respectively. The marked areas in (a) and (b) are shown in details in Fig. 5.3.

In the 50 nm thick Py film under investigations, the splitting of the SNW close to the knot of the edge cluster (which is the middle wall of the edge cluster) into a CTW was observed for angles more than 115^o, as seen in Fig. 5.3. This splitting of the edge-cluster SNW occurred due to the nucleation of a single pair of vortex and antivortex, as seen in Figs. 5.1(b) and 5.2(b). In Fig. 5.3, detailed magnetic configurations of the edge cluster before the nucleation of a VAVP and the consequent reversal of a segment of the domain wall magnetic moments after the nucleation of a VAVP are presented in

the MFM and simulation results. The VAVP formed during the magnetization reversal process created a segment in the wall with the magnetic moment aligned parallel to the applied magnetic field. This reversed magnetization segment of the domain wall further stretched when the vortex moved towards the other edge of the Py sample, on further increasing the magnetic field along the +y direction. Because of the low mobility of antivortices [94, 246], the antivortex stayed fixed near its nucleation site close to the sample edge. Such reversed segments of the domain walls were formed near both ends of the sample. They act as channels to let the magnetic flux flow from one end to the opposite end of the sample. Hence the magnetization of the Py sample reverses. Observations near the remanent state, i.e., as shown in Figs. 5.1(d) and (e), imply that the domain wall grown from the first nucleated antivortex, i.e., the wall connected with the antivortex in Fig. 5.3(b), joined with the vortex from the opposite end of the sample. Consequently, the Py sample reversed its magnetization by forming two CTWs along its long axis as observed in the MFM measurements presented from Figs. 5.1(d) to (f) and confirmed by the simulation results presented from Figs. 5.2(d) to (f). Upon further increasing the magnetic field along the +y direction, these CTWs were expelled out of the long edges of the sample. Finally, the Py sample was saturated along the +y direction.

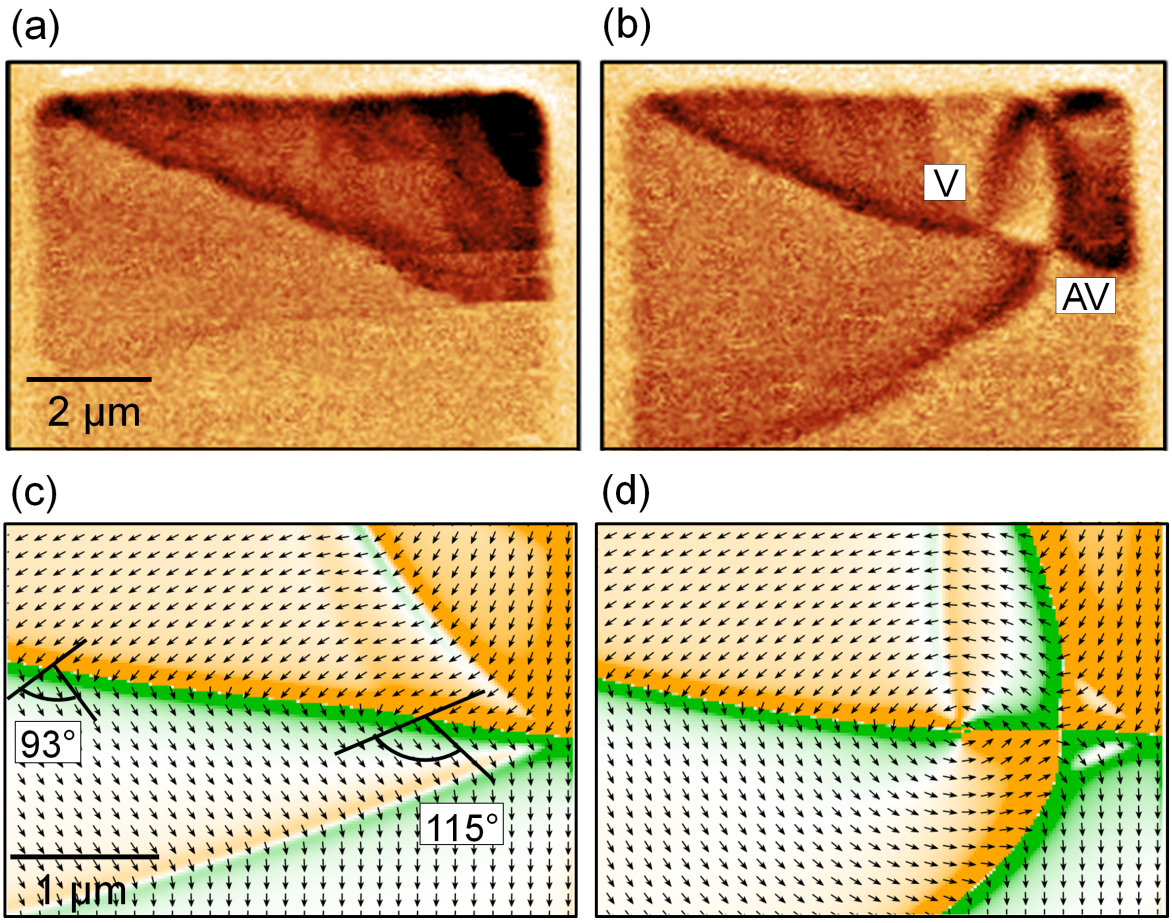

Figure 5.3: MFM images (a) and (b) show the nucleation of a vortex (V) and an antivortex (AV) close to the edge cluster knot. Corresponding calculated results taken from the areas marked in Figs. 5.2(a) and (b) are shown in (c) and (d) in this figure, respectively. A splitting of the domain wall was observed at a 115^o angle of the magnetization in simulated results. Each arrow in (c) and (d) represents an averaged magnetization inside 7×7 adjacent cells. Orange and green areas represent positive and negative charge densities, respectively.

The increase in the number of VAVPs from Figs. 5.1(d) to (f) was due to the build-up of magnetic charges when the domain walls moved close to the sample edge [242, 247]. This extra charge was reduced by the nucleation of new VAVPs, so the domain walls shared more magnetic flux with adjacent domains at VAVP locations [248].

In the MFM measurement results presented in Fig. 5.1, the splitting of the domain wall edge cluster into a VAVP was not observed simultaneously at the upper and the lower edge clusters of the sample, as seen in Fig. 5.1(b). This could be due to the nonideal rectangular shape of the sample and/or existence of pinning sites for the motion of domain walls [38, 189].

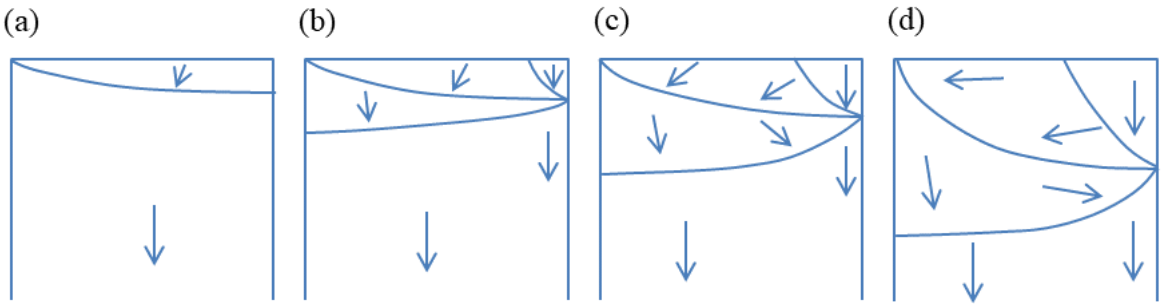

Figure 5.4: Schematics showing the evolution of an edge cluster of domain walls formed in Figs. 5.1 and 5.2. In (a) an end domain is formed with magnetization slightly tilted away from the initial direction of saturation (along −y direction). (b) An edge cluster of three domain walls [2, 228, 244] is formed as the magnetization inside the end domain relaxes further along the upper edge with the reduction of the applied field. In (c) and (d) the angle of the middle wall of the edge cluster increases more as the field is further reduced.

5.3.2 Hard axis switching

For the hard-axis switching (HAS) process, MFM measurement and micromagnetic simulation results are shown in Figs. 5.5 and 5.6, respectively. For the interpretation of the magnetic configurations formed during the HAS process, schematics of the magnetization reversal steps are presented in Fig. 5.7. The sample was initially saturated by an in-plane magnetic field applied along the −x direction before the measurement. Initial closure domains with edge clusters were formed when the applied field was reduced, as shown in Fig. 5.5(a) and in a detailed magnetization view shown in Fig. 5.6(a). The corresponding magnetic configuration is drawn in Fig. 5.7(a). Further reducing the field, domain walls from the edge clusters formed at the lower end of the sample merged to form a CTW along the x axis of the sample, which is visible in Figs. 5.5(b) and 5.6(c).

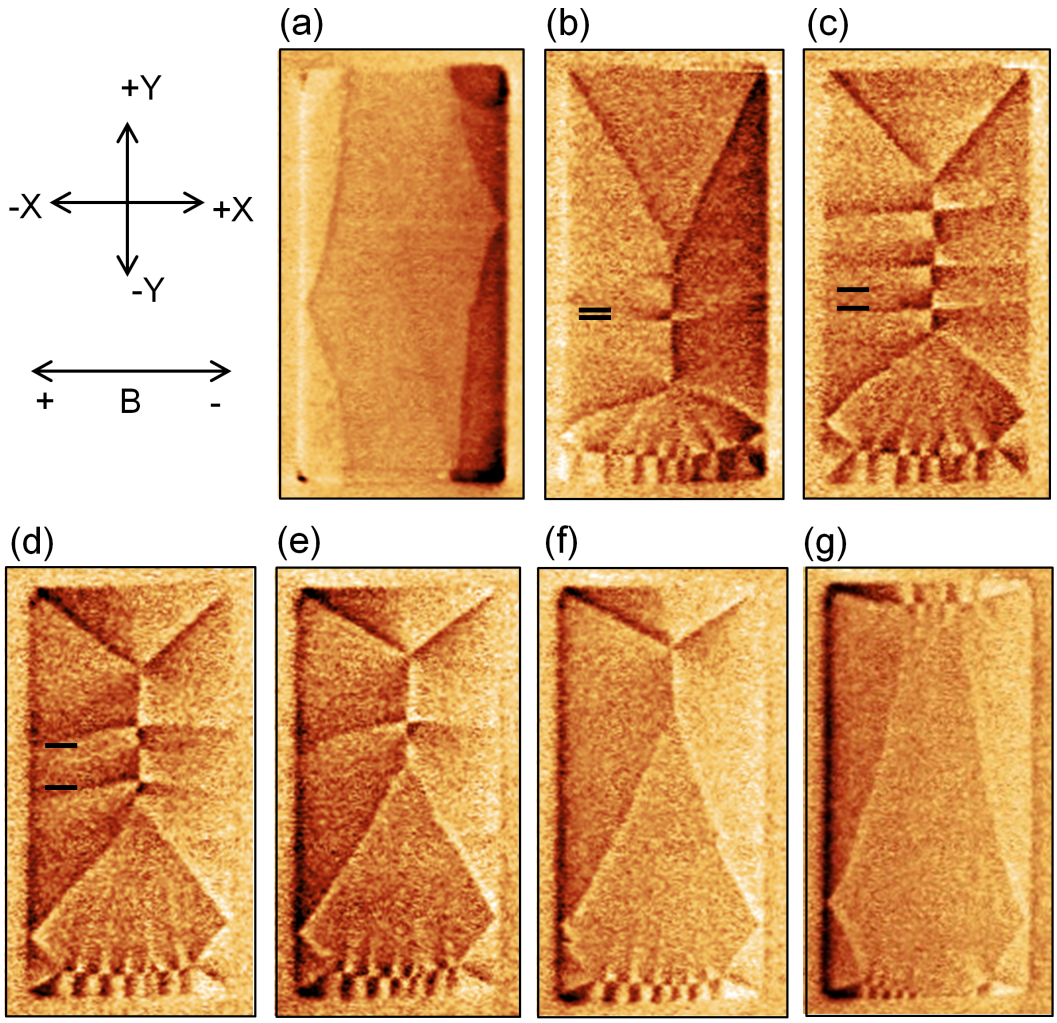

Figure 5.5: Magnetization-reversal of a Py bar sample parallel to its short axis. The magnetic field was swept from +80 mT to −80 mT. MFM images were taken at (a) +3.0 mT, (b) +1.9 mT, (c) zero, (d) −1.1 mT, (e) −1.7 mT, (f) −2.2 mT, and (g) −3.8 mT, respectively. Black markers indicate the enlargement of the domain-wall segments with magnetic moments parallel to the direction of the applied field.

Another domain wall parallel to the y axis of the sample, which is an SNW, was formed as the closure domains enlarged and their domain walls merged when the magnetic field was reduced. Magnetic moments inside this SNW were oriented parallel to the direction of the magnetic moments in the upper triangular domain, i.e., along the −x direction, as shown in Fig. 5.6(c) and drawn in Fig. 5.7(b). This SNW was observed to be connected between two domain-wall cluster knots [228]. The lower cluster knot is equipped with a vortex while the upper one is a vortex-free knot as seen in Fig. 5.6(c). This configuration is also shown in Fig. 5.7(b) with a detailed description of the orientations of the magnetic moments.

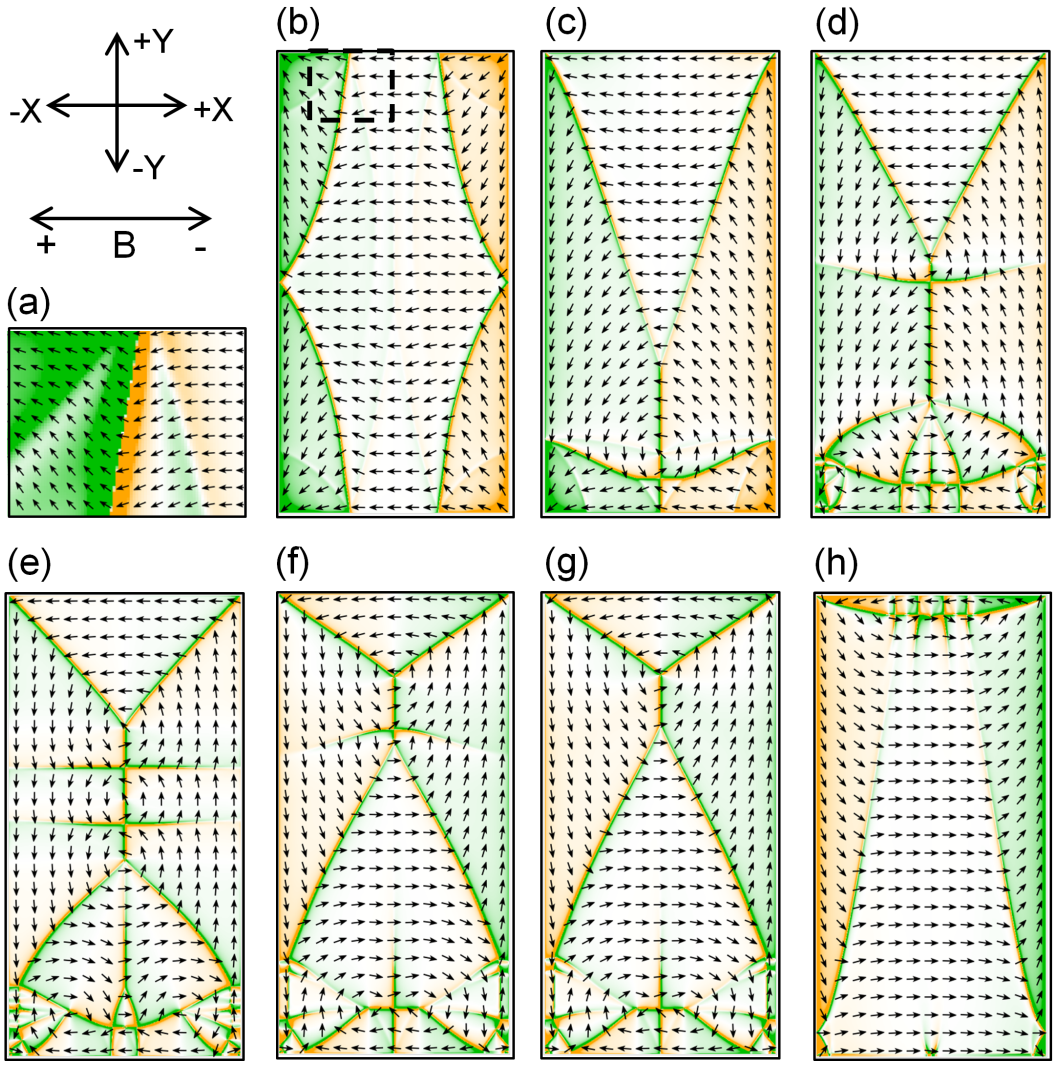

Figure 5.6: Micromagnetic simulation results of the magnetization reversal parallel to the short axis of a Py sample. The magnetic field was swept from +500 mT to −500 mT. (a) describes a detailed magnetization in one of the edge clusters of the domain walls taken from (b). Each arrow in (a) represents an averaged magnetization inside 7×7 adjacent cells. For the presented images, the field steps are: (b) +3.7 mT, (c) +2.5 mT, (d) +2.0 mT, (e) zero, (f) −1.8 mT, (g) −2.0 mT, and (h) −6.8 mT, respectively. Each arrow in (b) to (h) represents an averaged magnetization inside 35×35 adjacent cells. Orange and green areas represent positive and negative charge densities, respectively.

Simplified schematic configurations of a domain-wall cluster knot without and with a vortex are shown in Figs. 5.8(a) and (b), respectively. In these images, it is shown that a vortex may or may not forms at the wall-cluster knot depending on the orientations of the magnetizations around the knot [228].

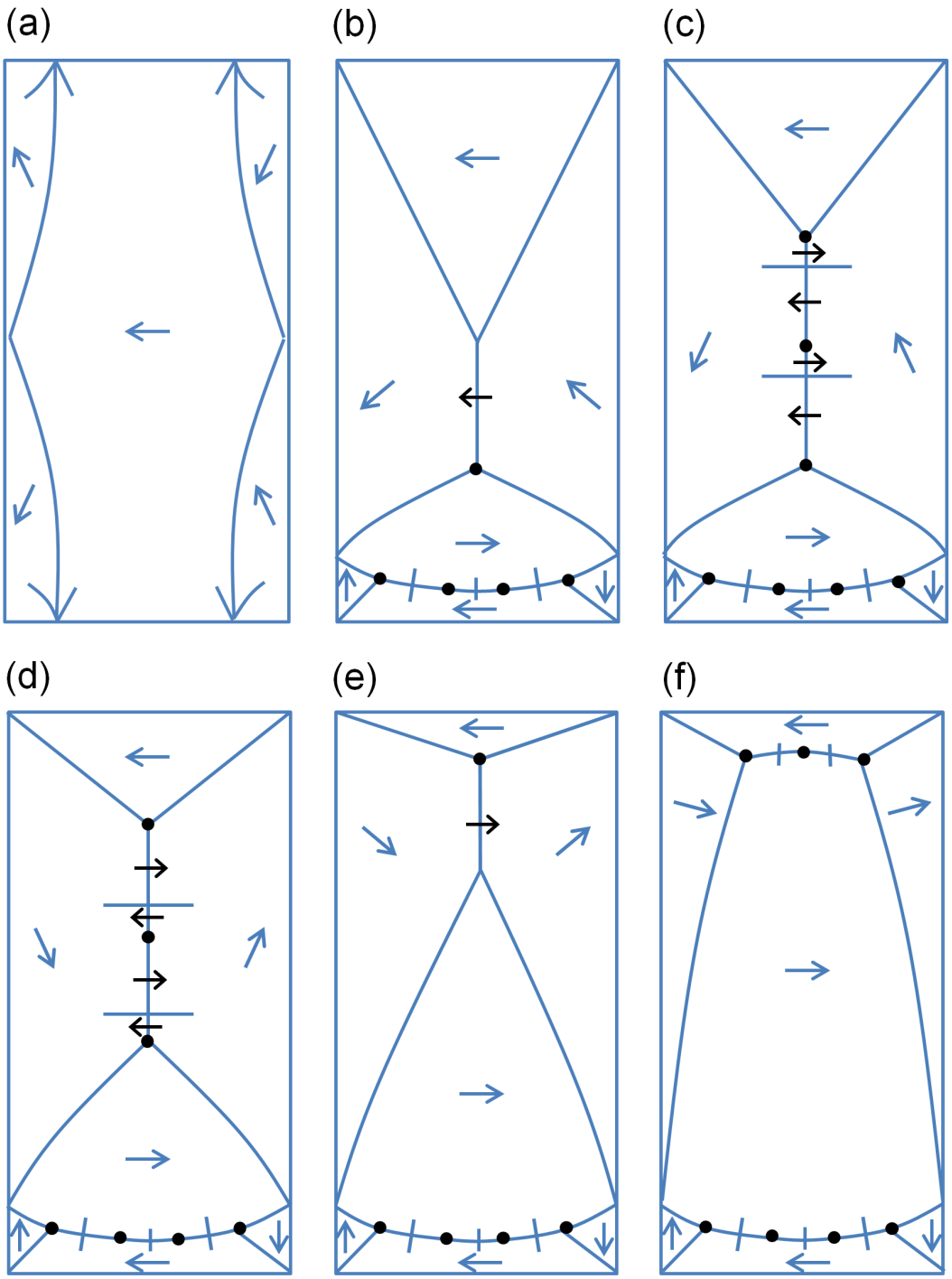

Figure 5.7: Schematic diagrams of the short-axis magnetization-reversal steps revealing the vortex-(shown as a black dot) transport mechanism between the domain wall cluster knots. Magnetization directions inside the domain walls are indicated by black arrows, while the magnetization directions inside the domains are indicated by blue arrows. Detailed magnetization configurations inside the CTWs formed along the short axis are ignored for the sake of simplicity.

As the SNW formed parallel to the y axis of the sample (in Figs. 5.6(c) and 5.7(b)) has magnetic moments parallel to the magnetic moments in the upper triangular domain, the magnetic flux is closed by forming a vortex at the lower cluster knot. When the applied field approached zero as presented in Fig. 5.5(c) and 5.6(e), the upper cluster knot (of the domain wall formed along the y-axis) moved along the +y direction. The angle of the SNW (formed along the long axis) increased as the applied field was reduced, which was due to the rotation of the magnetic moments inside the adjacent domains (see Fig. 2.11 in section 2.3). This SNW transformed into a CTW due to energetic reasons as described above when its wall angle increases above 115^o, as shown in Figs. 5.5(b) and 5.6(d) [86, 245]. The upper cluster knot was not vortex-free anymore at that moment, as shown in Figs. 5.6(d) and 5.7(c). Vortex and antivortex always nucleate and annihilate in pairs [2, 249]. Such nucleation of a VAVP and motion of a vortex between the two neighboring antivortices is indicated by black markers in Figs. 5.5(b) to (d). The nucleation of VAVPs generated segments inside the SNW with a reversed magnetization, i.e., along the direction of the increasing applied field. The wall segments within the black markers showing contrast from dark to bright along the +x direction in Fig. 5.5 are the reversed magnetization segments nucleated inside the SNW. Such favorable wall segments are visible in terms of arrows pointing along the +x direction inside the SNW in the simulated results from Figs. 5.6(d) to (f) and along the right direction in the schematics of Figs. 5.7(c) and (d), respectively. The lengths of these segments increased when the reverse magnetic field strength was increased. The annihilation of the vortices with the next neighboring antivortices instead of its co-nucleated antivortices led to the transfer of a resulting single vortex from the lower cluster knot to the upper one. Such transfer is described from Figs. 5.7(b) to (e) in detailed steps, where the domain wall segments with arrows pointing to the right direction nucleate and enlarge at the expense of the segments with arrows pointing to the left direction. At -2.2 mT, as shown in Fig. 5.5(f), the VAVPs annihilated each other and again an SNW was formed with a reversed magnetization. The magnetic flux transferred across the domain wall with the assistance of a resulting single vortex transported along the axis of the domain wall as the magnetization inside the adjacent domains rotated from −x direction towards +x direction. At this moment, as shown in Fig. 5.6(g) and 5.7(e), again the domain wall along the y axis of the sample has only one vortex which is attached to the upper cluster knot. The magnetic flux formed a closed loop around this knot.

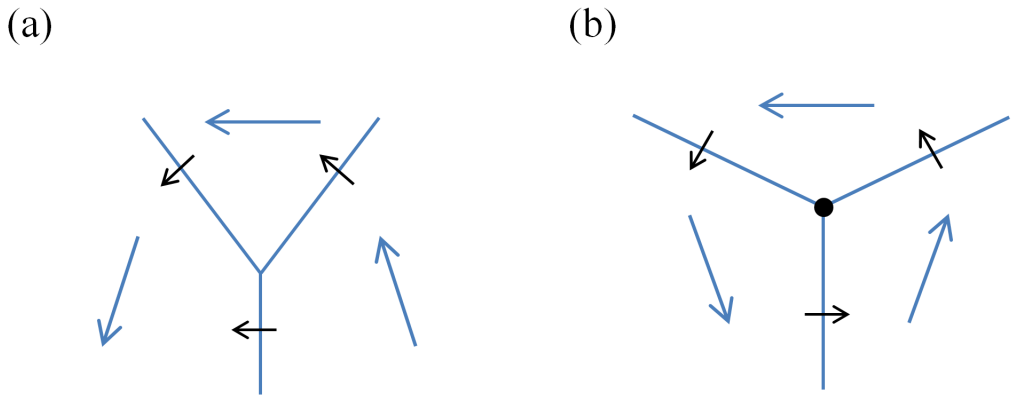

Figure 5.8: Simplified schematics showing a cluster of domain walls (a) without and (b) with a vortex (shown as a black dot) at the cluster knot, respectively. Blue lines represent the domain walls. Magnetizations inside the domains and domain walls are represented by blue and black arrows, respectively.

Further increase of the magnetic field pushed the lower cluster knot along the +y direction and the upper cluster knot bifurcated into a CTW, which is presented in Figs. 5.5(g) and 5.6(h) and drawn in Figs. 5.7(e) and (f). This bifurcation of the vortex into a CTW reduced the density of the charge which was collected around the cluster knot as it moved close to the edge of the sample [247]. The magnetic configuration within a larger field, i.e., at −3.8 mT in Fig. 5.5(g) near the saturation field, was similar to the EAS configuration with two parallel CTWs.

5.3.3 Contribution of the magnetic energies

In Fig. 5.9, calculated (simulated) magnetic energies within varied applied fields are shown. Changes in the magnetic energy landscape during the EAS and HAS processes were interpreted qualitatively. In simulations, the maximum field up to ±500 mT was applied, whereas the results in Figs. 5.2 and 5.6 within the field-range of around ±10 mT are shown. Only in this field-range significant changes in the domain configurations were observed. However, the exchange and demagnetization energies beyond ±10 mT field-range approached very slowly to zero and maximum, respectively. This is due to the existence of the persistent end domains which have magnetization slightly tilted away from the saturation orientation. A very high magnetic field is required to completely orient the magnetization in the end domains along the applied field direction [250].

Based on the demagnetization energy presented in Fig. 5.9(a), it is concluded that different demagnetizing fields due to the different sample aspect ratios created different

configurations of the closure domains and of the wall clusters during the EAS and HAS processes. A smaller aspect ratio in the HAS generated a larger demagnetizing field compared to that in the EAS at the saturated state [251]. This larger demagnetization energy decreased more steeply in the case of the HAS compared to that of the EAS due to the rotation of the magnetic moments inside the larger closure domains formed during the HAS. The smaller value of the demagnetization energy for the HAS in the remanent state as shown in Fig. 5.9(a) revealed the formation of a more perfect flux-closed solenoidal configuration in the HAS than in the case of the EAS. The larger exchange energy in remanent state for the EAS, as shown in Fig. 5.9(b), is because of an increased number of VAVPs created near the remanent state compared to the HAS. Closer positioning of the VAVPs leads to an enlargement of the angles between the neighboring magnetic moments and hence increases the exchange energy. This means that the VAVP transformations inside the domain wall which transform the SNW into a CTW took place in an applied field range which is below the exchange-energy peaks presented in Fig. 5.9(b). The Zeeman energy calculated in Fig. 5.9(c) is of the order of 10^2 and 10^3 times larger than the demagnetization and exchange energies, respectively. So the Zeeman energy dominated the magnetization reversal process. Therefore the total energy, as shown in Fig. 5.9(d), has a response and magnitude similar to the Zeeman energy under different applied fields. However, the Zeeman energy, being the product (mathematically) of the field strength and the magnetization of the sample (see equation (2.8)), is comparatively smaller than the demagnetization and exchange energies near the zero-field state, i.e., the remanent state. Domain wall TSs, i.e., vortices and antivortices, are formed because of the competition between the demagnetizing field and exchange interaction [2]. The demagnetization field favors curling of the magnetization in order to reduce the magnetic charges, while the exchange interaction tries to avoid the curl and divergence of the magnetic moments. Thus most of the transformations inside the domain wall only occurred near the remanent state where the Zeeman energy had a very weak influence on the magnetic moments inside the domain walls.

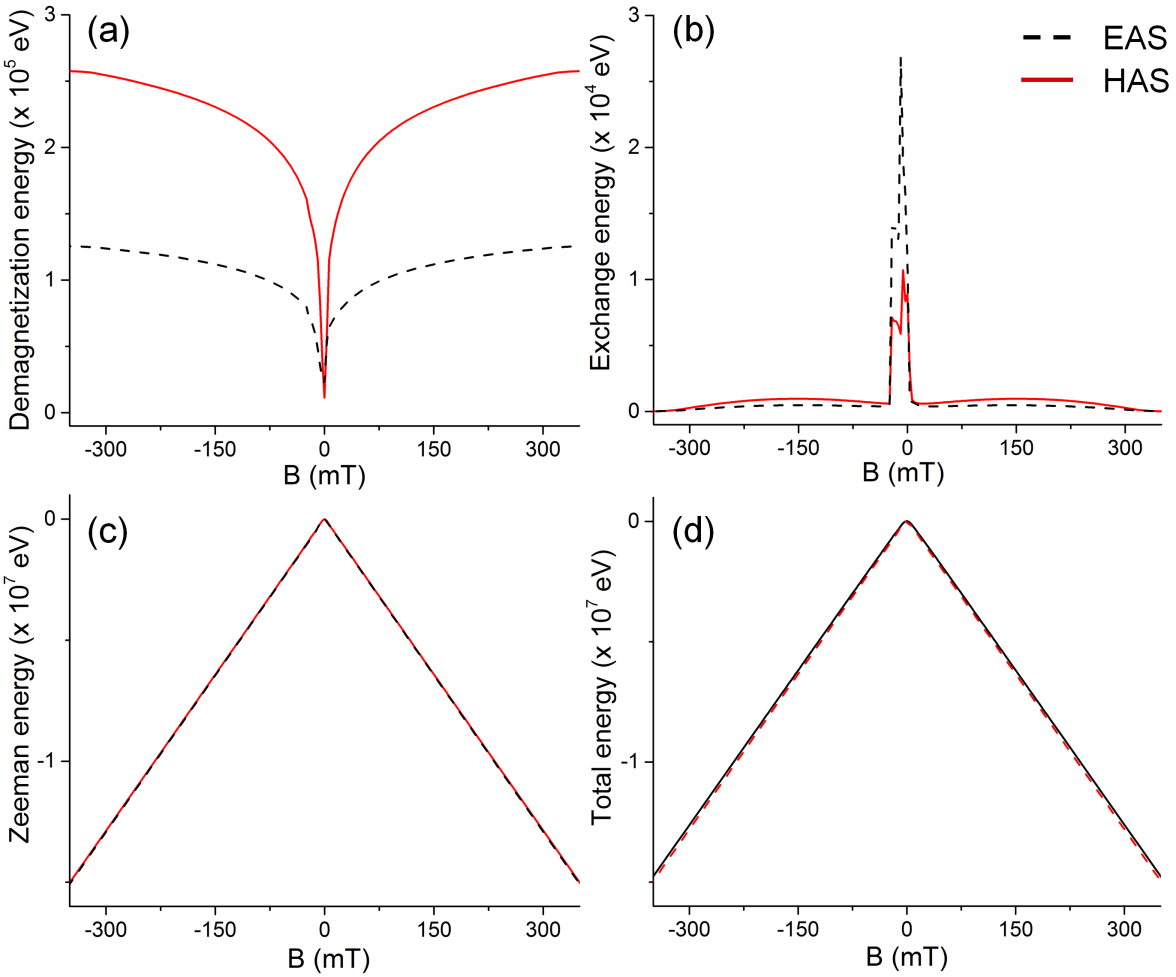

Figure 5.9: Simulation results of the (a) demagnetization (b) exchange, (c) Zeeman and (d) total energies under varying field strengths during the magnetization reversals along the long and short axis of the Py sample. The magnetic field was swept from +500 mT to −500 mT.

5.4 Modes of edge cluster evolution and formation of different domain configurations

Figure 5.10 shows two different modes of the evolution of a domain-wall edge cluster (shown in Fig. 5.4(d)). Figures 5.10(a) to (b) describe the nucleation of a VAVP at the domain-wall edge cluster. This mode has already been discussed in subsection 5.3.1 and described in Fig. 5.3. In the MFM scanned results shown in Figs. 5.10(d) to (e), two domain walls parallel to the long axis of the sample in the remanent state are formed, when a VAVP is formed at both ends of the sample, which is already discussed in subsection 5.3.1.

Figures 5.10(b) to (c) describe another mode of the evolution of the domain-wall edge cluster. In this mode, a domain of a reversed-magnetization is formed with the subsequent expulsion of the antivortex (due to the applied field) from the sample edge. For this mode, the MFM images in Figs. 5.10(f) to (g) show the formation of a triangular closure domain in the lower half of the sample in the remanent state, when the domain of the reversed-magnetization is formed only at one end of the sample. However, when such domains of the reversed-magnetizations are formed at both ends of the sample, a diamond domain in the remanent state is formed, as described in the MFM results shown in Figs. 5.10(f) to (h).

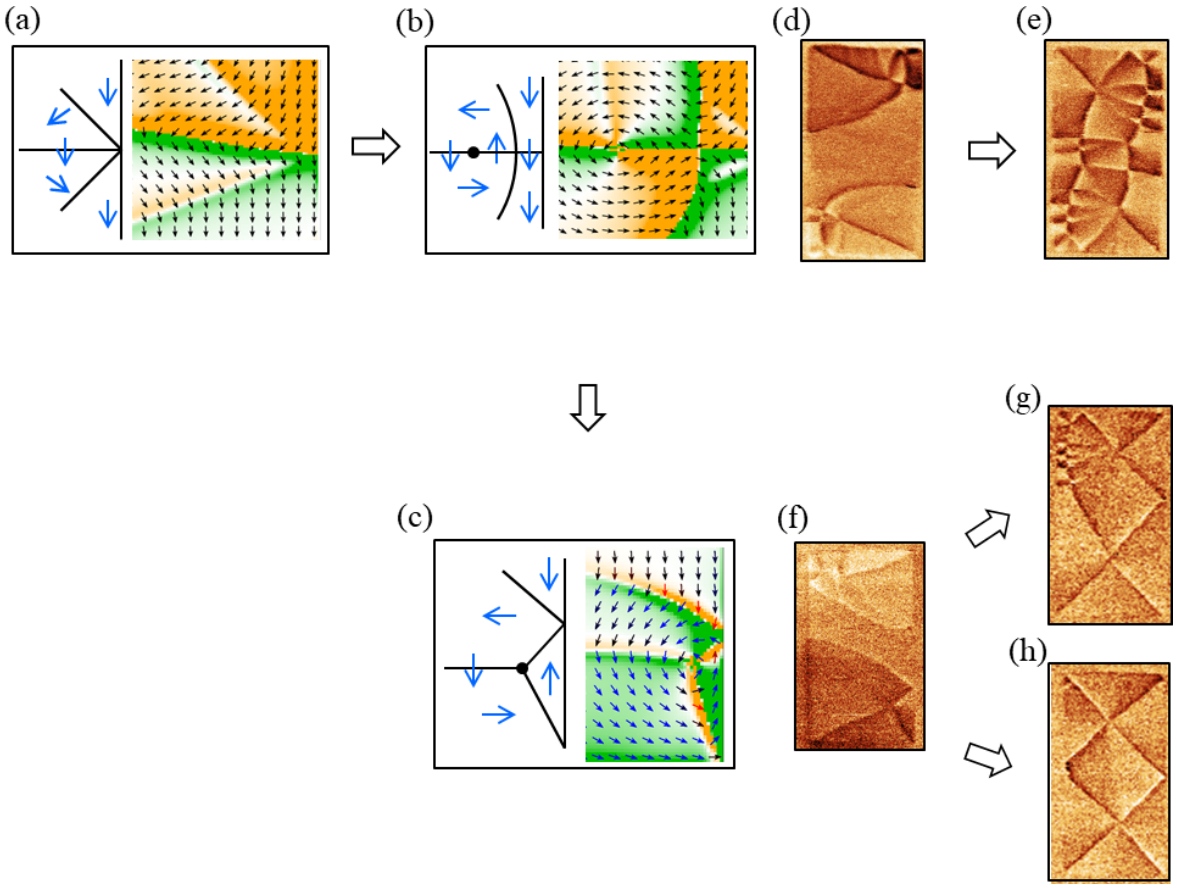

Figure 5.10: In (a), (b) and (c) an evolution of a domain-wall edge cluster is described through schematics and simulated results. MFM images (d) and (f) are the magnetic states scanned at high magnetic fields, whereas (e), (g) and (h) are the remanent states.

5.5 Stochasticity in the modes of magnetization reversals

The experimentally observed magnetization reversals presented in this chapter are not deterministic processes. It was observed that the magnetization reversal could proceed

through a different zero-field state on repeating the hysteresis loop, as already discussed in above section 5.4. However, the simulated magnetization reversals are deterministic processes, unless any parameter is varied. No temperature dependence was considered in the simulations [252]. In Fig. 5.11 the HAS of a 50 nm thick 9×18 µm^2 Py sample was subsequently repeated by slightly varying the direction of the applied magnetic field. The field was applied at an angle of 0.1° to the short axis of the sample. On comparing the magnetization reversal processes shown in Figs. 5.6 and 5.11, it was found that a slight change in the direction of the applied field can change the mode of the magnetization reversal in simulations. A slight asymmetry in the initial end-domains formed in Fig. 5.11(b) lead to the formation of a S-state configuration [184, 195, 216] in Fig. 5.11(c), whereas no clear S- or C-state configuration [184, 195, 216] was observed in Fig. 5.6 (where the field was applied exactly parallel to the short axis of the sample). In Figs. 5.6 and 5.11, different initial end-domains lead to a variation in the mode of the magnetization reversal.

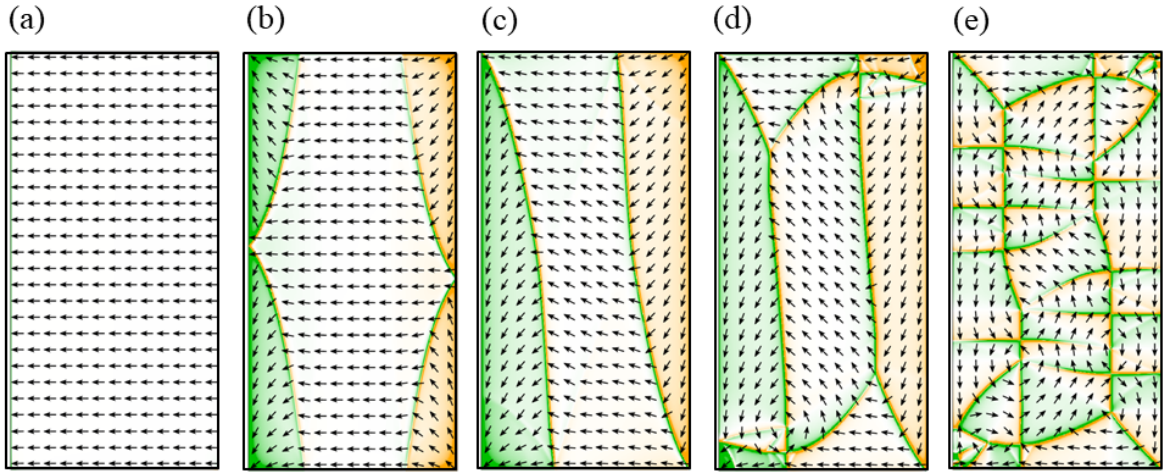

Figure 5.11: Micromagnetic simulation results of the magnetization reversal of a Py sample with a magnetic field applied at an angle of 0.1° to the short axis of the sample. The applied field was changed to (a) +376.2 mT, (b) +5.0 mT, (c) +3.4 mT, (d) +1.9 mT, and (e) zero, respectively. The magnetic field was decreased from +500 mT. Each arrow represents an averaged magnetization inside 35×35 adjacent cells. Orange and green areas represent positive and negative charge densities, respectively.

In Figs. 5.12(a) and (b) the domain configurations at +5.6 mT field applied parallel and at an angle of 0.1° to the short axis are shown, respectively. The energy difference between these domain configurations is around 33 $k_\mathrm{B}T$ (where k_B is the Boltzmann constant and T is the temperature). This energy difference reduces further down to the order of $k_\mathrm{B}T$ (thermal energy) if the angle between the applied field and the short

axis of the sample is further decreased. Such magnetic states of very small energy differences could be considered as the energy states existing at the branching locations (one of such location is marked with a dashed circle) in an energy (of the magnetic states) versus the applied field plot as shown in Fig. 5.12(c). If the energy differences between the states at the branching locations are smaller than the thermal energy, the thermal fluctuations could make the mode of magnetization reversal nondeterministic in the experimental investigations.

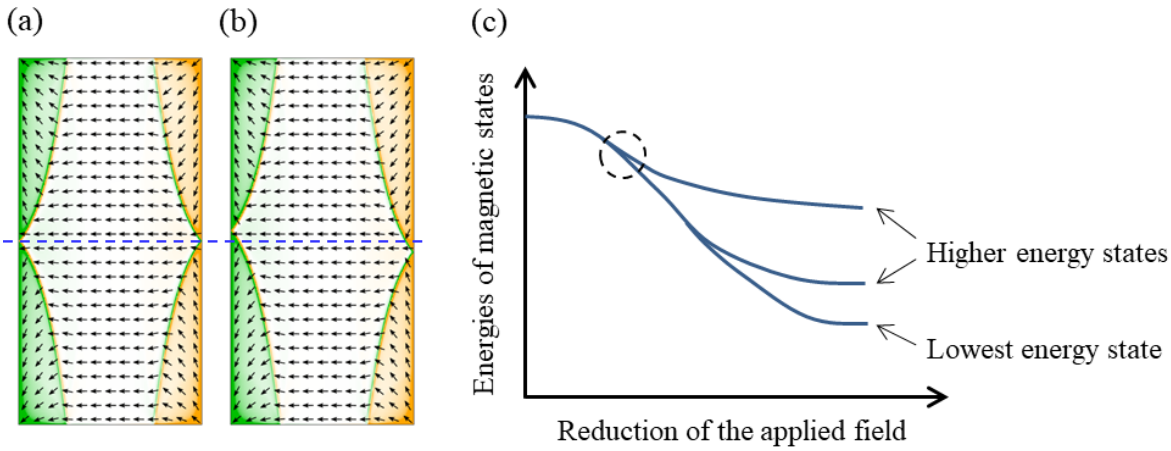

Figure 5.12: Domain configurations inside a 50 nm thick 9×18 µm^2 Py sample at +5.6 mT field applied (a) parallel and (b) at an angle of 0.1° with respect to the short axis. The magnetic field was decreased from +500 mT. Blue brocken line indicates the asymmetric end-domains in (b). Each arrow represents an averaged magnetization inside 35×35 adjacent cells. Orange and green areas represent positive and negative charge densities, respectively. (c) A speculative variation of the energies of different magnetic states with the reduction of an applied field. Energy barriers are not drawn for the simplicity.

Such branching of the magnetization reversal modes could occur at various stages of the magnetization reversal, which leads to the modification of the magnetic energy landscape [35, 36, 185]. As an example, an expulsion of an antivortex was observed in Fig. 5.10, which changed the remanent (zero-field) state. Also, from the simulated magnetization-reversal mode with an asymmetric initial end-domains (shown in Fig. 5.11(b)), a remanent state containing two domain walls along the long axis of the sample was formed as seen in Fig. 5.11(e). However, in the experimental investigations in Fig. 5.5(a), though the initial end-domains were asymmetric, the magnetization reversal proceeded through the formation of a single domain wall along the long axis of the sample at the remanent state as seen Fig. 5.5(c). So, there exists a branching of the reversal mode between the magnetic states shown in Figs. 5.5(a) and (b).

In simulations, in the larger aspect-ratio rectangular samples than those discussed above in this chapter, the initial asymmetric end-domains can also form for the case of a magnetic field applied exactly parallel to the edges of the sample. Therefore, the mode of the magnetization reversal in simulations can not be changed by just varying the orientation of the applied field for all samples of different shapes and thicknesses. In addition to a slight variation in the angle of the applied field and shape of the sample, there exist several other parameters such as the initial magnetization (chosen before starting the hysteresis loop), dimensions of the cells and step-size of the applied field which can alter the modes of the magnetization reversals in simulations.

5.6 Conclusion

In this chapter, it is shown that the basic role of vortices and antivortices in the magnetization reversals is to create segments of reversed magnetizations inside the walls. These segments act as the channels to transfer magnetic flux across the walls. Expansion of these segments with the increase of reversed applied field formed domains of reversed magnetization inside the films. However, the overall domain configurations changed with the change of the applied field direction due to the different evolution of the wall clusters. During the reversal, magnetic flux transferred across the walls by transporting a resulting single vortex along the wall-axes. Also, based on the analysis of the interplay of the different magnetic energies, a range of the magnetic field was defined within which the nucleation and subsequent annihilation of the TSs inside the walls took place. This narrow and near-remanent state field range suggests that the demagnetization and exchange energies should be kept larger than the Zeeman energy for the analysis of the behavior of the TSs of domain walls.

Moreover, it is described that the experimental magnetization-reversals are nondeterministic processes. A variation in the evolution of domain-wall cluster due to a change in the behavior of vortices and antivortices alters the mode of magnetization-reversal and consequently different remanent states are formed. Also, in micromagnetic calculations, it is found that a slight variation of the simulation parameters could change the mode of the magnetization-reversal.

Since the simulations were used only to support and better understand the experimental observations, no new conclusions solely based on the simulations are drawn. Therefore, the presented interpretations of the magnetization processes such as the behavior of VAVPs and evolution of domain-wall clusters are still reliable from the physics point of view, despite being the experimental results nondeterministic and the

calculated results sensitive to the simulation parameters.

6 Reversal of the internal magnetizations of the one- and two-dimensional domain walls

6.1 Introduction

The control and manipulation of the internal magnetization configuration of domain walls is a subject of intense research in magnetism [22, 26, 253–255]. The switching of the bi-stable orientation of the internal magnetization of walls is purposed for data storage [22, 253, 256] and sensor [255] applications. Also, controlled magnetization configurations of the domain walls are required for reliable operation of racetrack memories [23, 26, 254] and spin-wave-based logic operation circuits [257–259]. The internal configurations of domain walls depend on the magnetic anisotropy and thickness of the constituting material [2]. As discussed in section 2.2, in a soft magnetic material such as Py, the configurations of the domain walls change from one-dimensional to two-dimensional at around 100 nm with the increase of the film thickness [2, 86]. In Py film of a thickness of approximately $\leq$ 20 nm, one-dimensional SNWs exist (see subsection 2.2.1 for details). The magnetization inside the SNW is oriented in the plane of the film. For an intermediate film thickness from approximately 20 to 100 nm, CTWs exist, which are composed of oppositely oriented one-dimensional SNW segments separated by vortices and antivortices (see subsection 2.2.2 for details) [3, 4]. In thicker films, two-dimensional ADWs exist. ADWs possess both in-plane and out-of-plane orientations of the magnetization inside their configurations (see Fig. 2.5). They minimize their stray field by the formation of NCs at both surfaces and vortex-like structures in the cross-sections of the walls [79, 85]. ADWs are further classified into ABWs and ANWs depending on their "C" and "S" type cross-sectional magnetization configurations, respectively (see subsection 2.2.3 for details).

Domain walls also transform their internal magnetizations within an applied magnetic field (see Fig. 2.10). These transformations proceed with the nucleation of various types of TSs inside the walls. These TSs separate wall-segments of different configurations. Different types of TSs in one-dimensional and two-dimensional domain walls have

already been discussed in subsections 2.5.1 and 2.5.2, respectively. However, despite the existence of a vast knowledge of TSs and various types of domain walls, the role of TSs in transformations of the internal magnetizations of two-dimensional domain walls has never been investigated in detail.

In this chapter, a report on the role of the vortices and antivortices as the TSs in the reversal of internal magnetic configurations of one-dimensional and two-dimensional domain walls in Py films is given. Patterned structures of Py films of 40 nm and 130 nm thicknesses were fabricated in order to investigate the magnetization configuration transformations inside one-dimensional and two-dimensional domain walls in an in-plane magnetic field, respectively. For the investigations inside a single domain wall, the short axis magnetization switching of the elongated rectangular structures of 2.3×6.7 μm^2 was selected. This configuration favors the formation of a single domain wall perpendicular to the direction of the applied magnetic field. The evolution of the domain-wall magnetization configurations under varying field strengths was investigated by MFM. Also, micromagnetic simulations were performed to understand three-dimensional magnetization transformations inside the domain walls.

6.2 Experimental and micromagnetic simulation details

Py patterns of 2.3×6.7 μm^2 dimensions were fabricated using EBL and DC magnetron sputtering techniques. The Py films of 40 and 130 nm thicknesses were deposited at 2.0 µbar Ar pressure with a constant sputter rate of 18 nm/min. For micromagnetic simulations, a cubic cell of $20 \times 20 \times 10$ nm^3 dimensions was used. The rest of the experimental deposition and micromagnetic simulation parameters were chosen as described in section 4.2 of chapter 4.

6.3 Reversal of the internal magnetic configuration of one-dimensional domain walls

The domain configurations investigated by MFM at various applied fields and the schematic diagrams of a segment of the domain wall for varying magnetization configurations are shown in Fig. 6.1. Corresponding simulated images are shown in Fig. 6.2. The sample was initially saturated along the +y direction. When the field was reduced, the domain walls formed along the long edges of the sample (not shown in the results) joined to form a single domain wall (parallel to the x axis), as shown in Figs. 6.1(a)

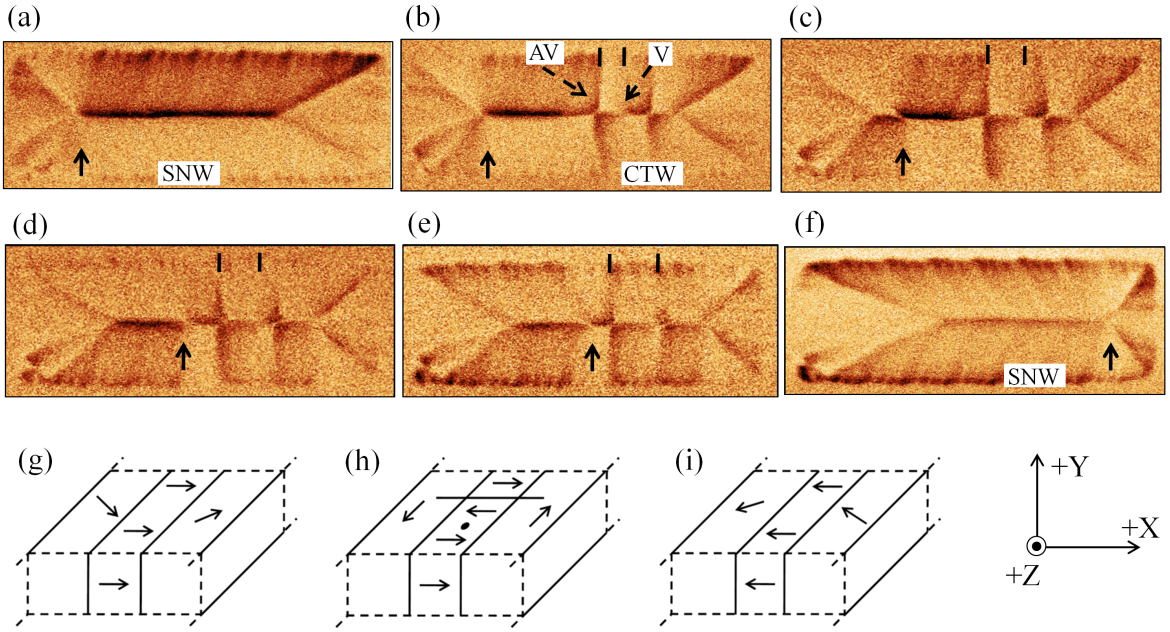

Figure 6.1: MFM images of a 40 nm thick 2.3×6.7 µm^2 Py sample at (a) +3.4 mT, (b) +1.7 mT, (c) zero, (d) −2.0 mT, (e) −3.1 mT and (f) −6.4 mT. The magnetic field was swept from +80 mT to −80 mT. The magnetic field was applied along the short axis of the sample, i.e., along the y axis as described. Figures (a) to (f) show transformation steps of a SNW into a CTW and back to a SNW. The position of a vortex (V) and an antivortex (AV) nucleated inside the CTW is shown in (b). The nucleation and expansion of a reversed magnetization domain-wall segment are marked from (b) to (e). Black arrows mark the displacement of the vortex inside the domain wall. The schematic illustrations of SNWs and CTW are shown in Figs. (g) to (i).

and 6.2(a). This domain wall was connected to two domain-wall junctions at its ends. In the MFM image in Fig. 6.1(a), this domain wall formed a bipolar contrast changing its appearance from bright to dark, while in the simulated image in Fig. 6.2(a) the domain-wall contrast changes from orange to green along the +y direction, respectively. Opposite magnetic charges inside the two halves of the wall, which were produced by an in-plane rotation of the magnetization inside the domain wall, produced a bipolar contrast in the MFM scan. A continuous contrast of this wall along its length indicates the absence of any TS inside the wall. In Fig. 6.1(a), the domain wall forming the upper trapezoidal-shaped domain (the domain formed with the upper long edge of the sample) changes its contrast at the left domain wall junction, while, the contrast of this domain wall remains unswitched at the right domain-wall junction. The switching of the domain-wall contrast at the left wall junction indicates the presence of a vortex on the left domain-wall junction. This vortex is indicated by a black arrow in Fig. 6.1(a). The domain-wall junctions without and with a vortex were already described in Fig.

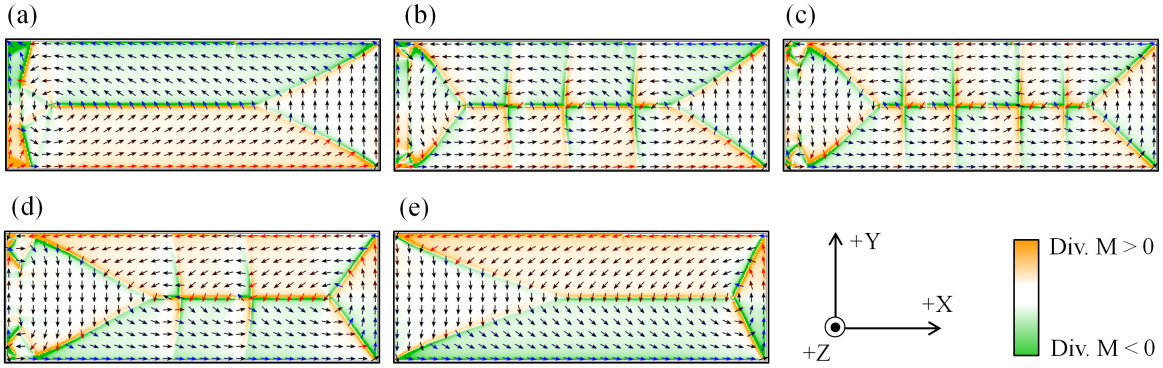

Figure 6.2: OOMMF-simulated images of a 40 nm thick 2.3×6.7 µm^2 Py sample at (a) +8.0 mT, (b) +5.3 mT, (c) zero, (d) −5.3 mT and (e) −13.3 mT. The magnetic field was swept from +500 mT to −500 mT. The magnetic field was applied along the short axis of the sample, i.e., along the y axis as described in the figure. Each arrow represents an averaged magnetization vector inside 11×11 adjacent cells at the sample surface. Black arrows are in-plane magnetization vectors, whereas blue and red ones are the in-plane projection of magnetization vectors tilted upwards and downwards, respectively. Orange and green areas represent positive and negative charge densities, respectively.

5.8 in chapter 5. The domain wall formed parallel to the x axis is a SNW with a vortex formed on its left end. This is also confirmed in Fig. 6.2(a) with the magnetization inside the SNW oriented along the +y direction. A schematic illustration of a segment of such a SNW is shown in Fig. 6.1(g). The angle of this SNW increased with the reduction of the applied external field because the magnetization inside the adjacent domains relaxed more along the edges of the sample (as shown in Fig. 2.11). This, in turn, increased the magnetic charges inside the domain wall and hence decreased the stability of the domain wall. When the external field was reduced further, i.e., at +1.7 mT (Fig. 6.1(b)), the SNW was stabilized with the nucleation of VAVPs as TSs. Locations of a vortex and an antivortex in one of the VAVPs are indicated in Fig. 6.1(b). The nucleation of VAVPs transformed the SNW into a CTW [3, 4]. In a 40 nm thick Py film, the SNW with the wall angle larger than approximately 100° transforms into a cross-tie pattern of 90° SNWs, [77, 86] because a 90° SNW has only 12% energy of the 180° SNW [2]. Such a transformation of the SNW into a CTW was observed in the simulated results in Fig. 6.2(b), as the angle of the SNW in Fig. 6.2(a) approached approximately 115°. A schematic configuration of such a CTW segment is shown in Fig. 6.1(h). In Fig. 6.1(b), the nucleation of two VAVPs creates segments of the oppositely oriented magnetization inside the domain wall, i.e., dark-brown to bright-brown color along the +y direction. One of the reversed magnetization domain wall segment in between a vortex and an antivortex is marked by black markers in

Fig. 6.1(b). The broken arrows indicate the locations of a vortex and an antivortex in Fig. 6.1(b). The nucleation of the segments with a reversed domain-wall contrast, i.e., the green to orange along the +y direction, in the simulated results is shown in Fig. 6.2(b). Such reversed segments inside the domain wall enlarged with the further increase of the applied field strength along the −y direction, as indicated by the markers in Figs. 6.1(b) to (e) in the MFM images, and shown in Figs. 6.2(b) to (d) in the simulated results. When the field was further increased along the −y direction, the antivortices located at the cross-ties of the 90° SNWs stayed more or less fixed at their nucleation sites, while the vortices were displaced towards the +x direction and annihilated with the next-neighboring antivortices rather than with the co-nucleated antivortices. The displacement of the vortex, which appeared at the left end of the SNW (location indicated by an arrow), towards the +x direction is shown in Figs. 6.1(b) to (e). The consequent switching of the domain wall contrast as a result of the displacement of the vortex is visible in these images. Displacements of all vortices towards the +x direction and their consequent annihilation with the corresponding next-neighboring antivortices lead to switching of the whole domain-wall magnetization orientation from the +y direction to the −y direction. Finally, again an SNW was formed showing a continuous bipolar contrast with a single vortex attached at the right end of this domain wall, as shown in Figs. 6.1(f) and 6.2(e). A segment of such a switched SNW is illustrated in Fig. 6.1(i). In this process, a resulting single vortex was displaced from the one end to the other end of the SNW, by the assistance of VAVPs nucleation and annihilation, to switch the domain-wall magnetization.

6.4 Reversal of the internal magnetic configuration of two-dimensional domain walls

In order to interpret the surface magnetization of the sample observed by MFM measurements as shown in Fig. 6.3, the domain configurations are visualized in different planes along the thickness of the sample as shown in Fig. 6.4, as well as along the cross-sections of the domain wall, by three-dimensional micromagnetic simulations as shown in Figs. 6.5 and 6.6. To specify the different planes of views, the coordinate axes of the sample are chosen as described in Fig. 6.4, where the scales along the x, y and z axes vary from 0 to 6700 nm, 0 to 2300 nm and 0 to 130 nm, respectively. For a general specification of the different planes of views, the dimensions along all axes are converted into a dimensionless 0 to 1.0 scale. Figure 6.3 shows MFM results of the

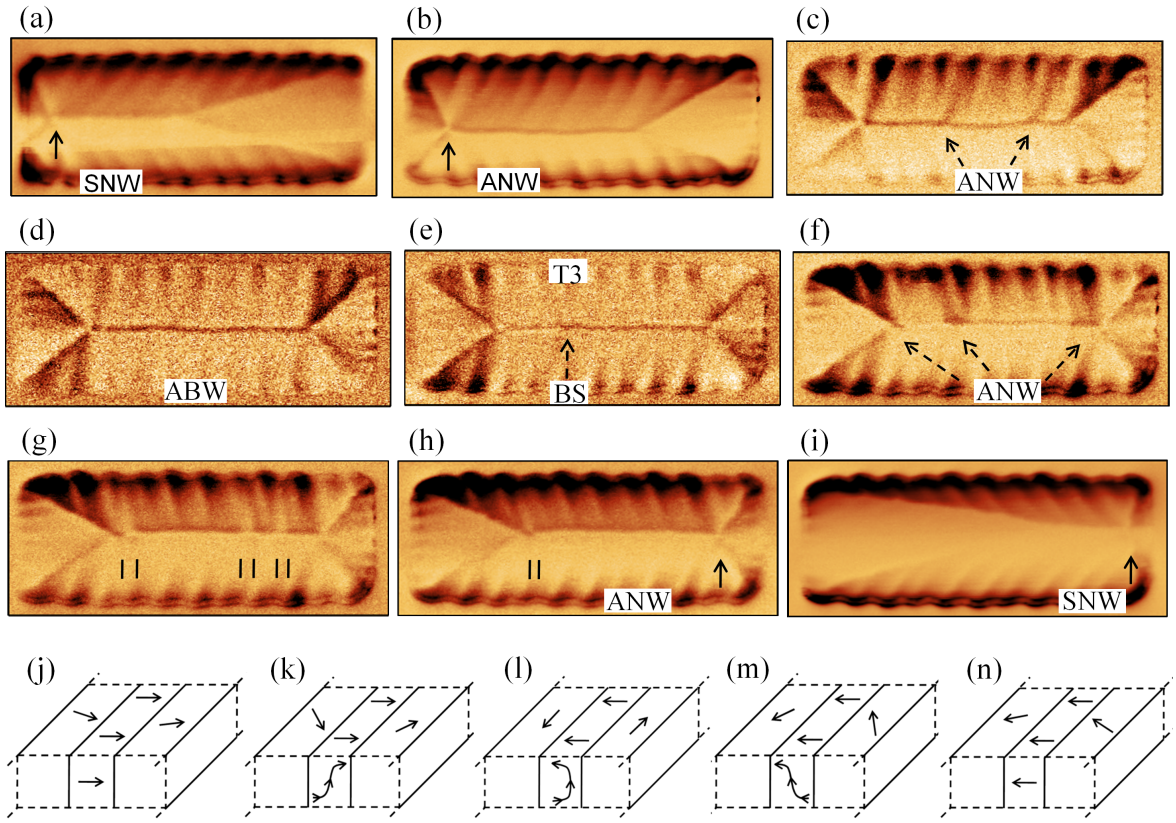

Figure 6.3: MFM images of a 130 nm thick 2.3 × 6.7 μm^2 Py sample at (a) +19.3 mT, (b) +16.7 mT, (c) +4.8 mT, (d) zero, (e) −3.8 mT, (f) −7.2 mT, (g) −8.5 mT, (h) −11.4 mT and (i) −27.7 mT. The magnetic field was swept from +80 mT to −80 mT. The magnetic field was applied parallel to the short axis of the sample. In (e) a location of the switching of the Bloch core, i.e., a Bloch Switch (BS), is indicated. Figs. (a) to (i) show transformation steps of a SNW into an ADW and back to a SNW. Schematic illustrations of SNWs and ADWs are shown in Figs. (j) to (n).

sample at different fields during the switching of the sample's magnetization parallel to the y axis (i.e., parallel to the short axis of the sample). OOMMF-simulated images of the domain configurations in three different xy planes of the sample along the thickness, i.e., the lower plane (Z = 0), middle plane (Z = 0.5) and upper plane (Z = 1.0) for different fields, are shown in Fig. 6.4. The locations of the vortices and antivortices are indicated in the upper and lower planes. The corresponding cross-sectional images of the domain wall in the yz-planes at different field steps are presented in Fig. 6.5.

The sample was first saturated along the +y direction. When the field was reduced to +19.3 mT, the domain walls formed along the long edges (not shown in the results) joined to form a single domain wall (parallel to the x axis), as shown in Fig. 6.3(a). This domain wall is connected to two domain-wall junctions at its ends. This domain wall forms a bipolar contrast both in the MFM image Fig. 6.3(a) and in the simulated

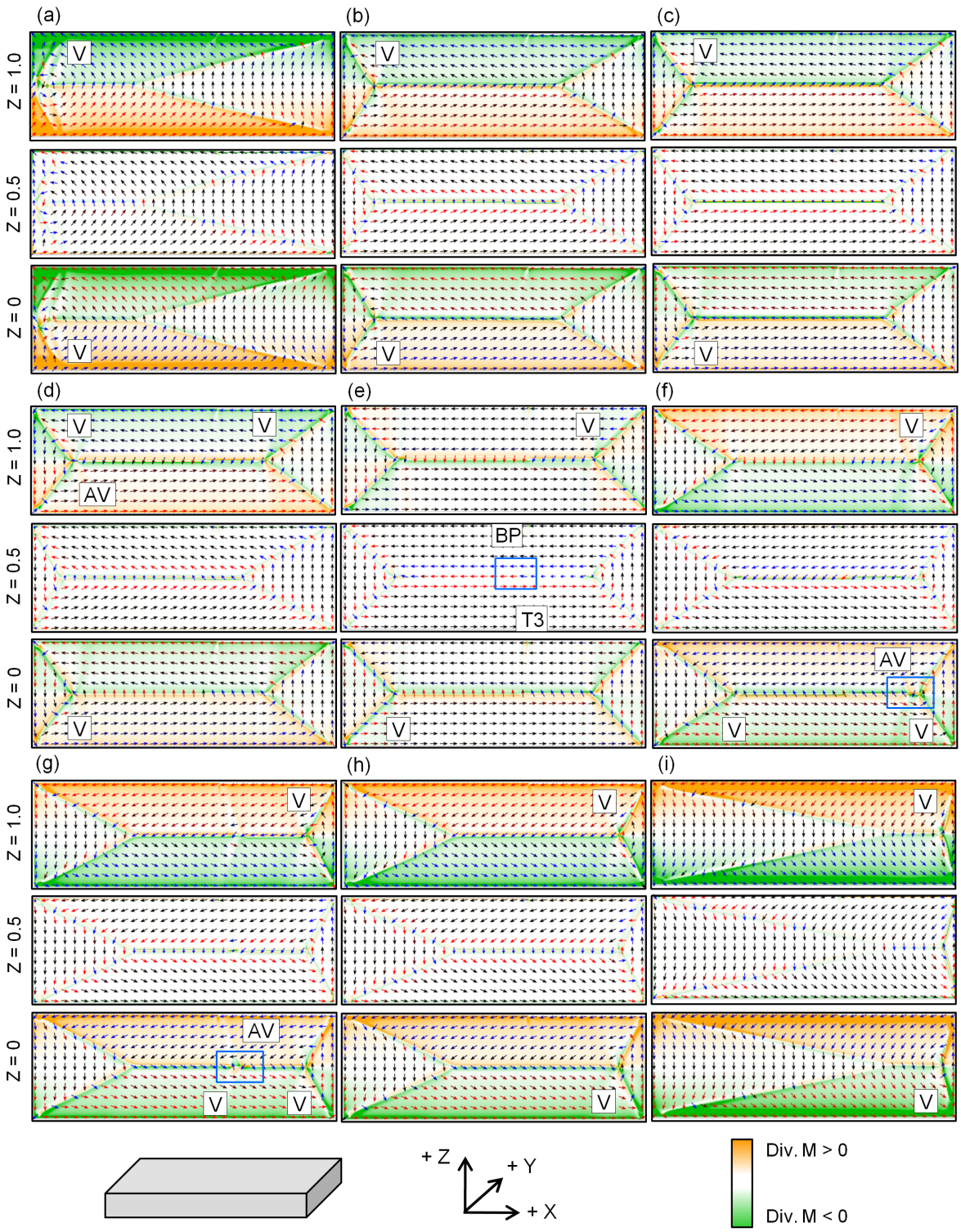

Figure 6.4: OOMMF-simulated results of a 130 nm thick 2.3×6.7 µm^2 Py sample at (a) +42.3 mT, (b) +19.3 mT, (c) +11.7 mT, (d) +11.3 mT, (e) zero, (f) −15.5 mT, (g) −23.9 mT, (h) −27.2 mT and (i) −45.4 mT. The magnetic field was swept from +500 mT to −500 mT. The magnetic field was applied parallel to the short axis of the sample. Three images corresponding to three xy-planes, i.e., Z = 0, Z = 0.5 and Z = 1.0, along the thickness of the sample are shown for each magnetic field step. Positions of the vortex (V), antivortex (AV) and Bloch point (BP) are marked inside the images. Each arrow represents an averaged magnetization vector inside 11×11 adjacent cells. Black arrows are in-plane magnetization vectors, whereas blue and red ones are the in-plane projection of magnetization vectors tilted upwards and downwards, respectively. Orange and green areas represent positive and negative charge densities, respectively.

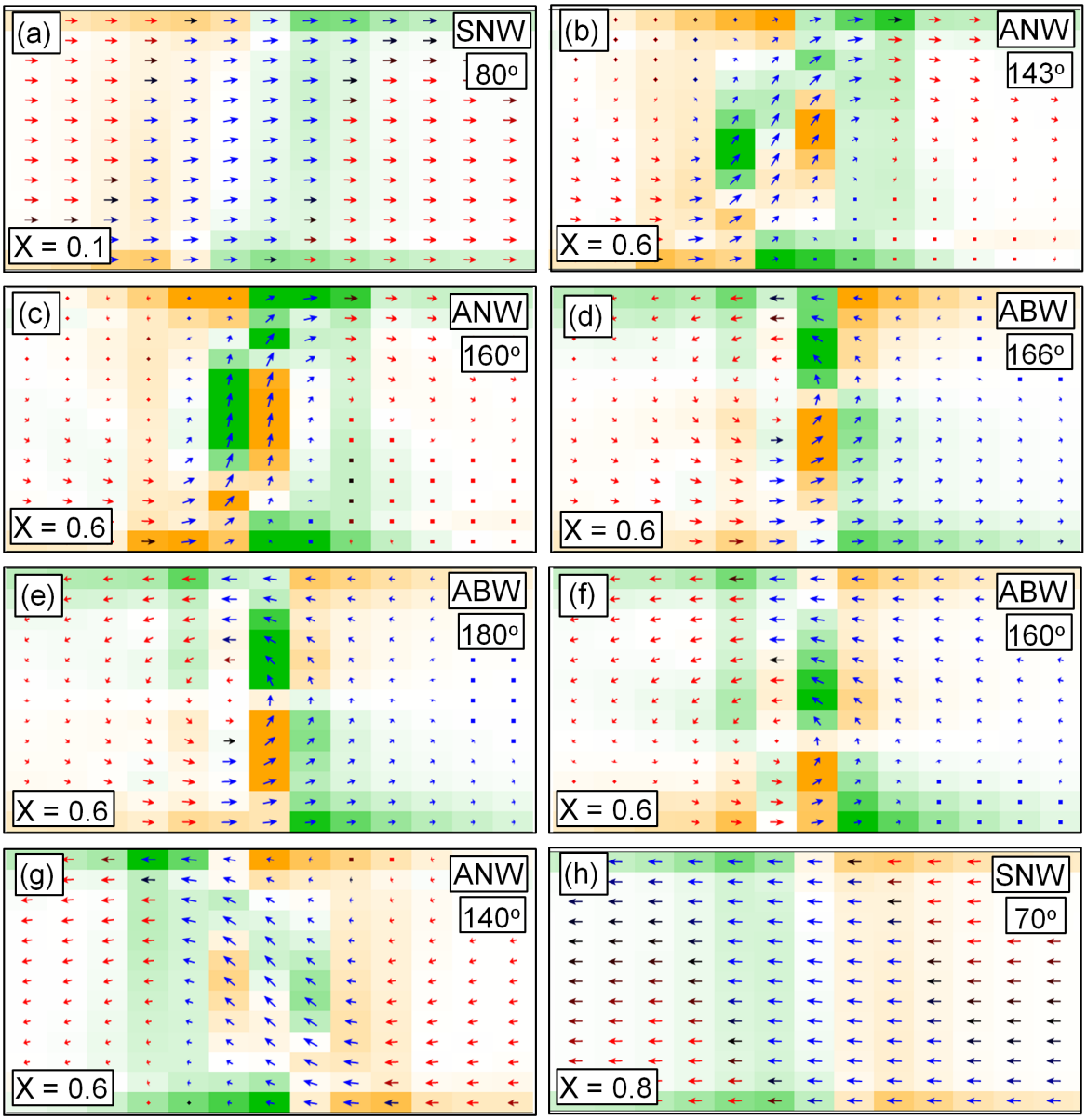

Figure 6.5: Cross-sectional images of the domain wall along the yz-planes taken from Fig. 6.4 at (a) +42.3 mT, (b) +19.3 mT, (c) +11.7 mT, (d) +11.3 mT, (e) zero field, (f) −15.5 mT, (g) −27.2 mT and (h) −45.4 mT. The X value in each image indicates the location along the x axis at which the cross-sections are taken. The angle of the domain wall is measured from the middle planes presented in Fig. 6.4. The images show a complete thickness of the sample i.e., 130 nm parallel to the z axis, while a 260 nm long segment of the sample parallel to the y axis is selected to describe the cross-sectional magnetization configuration of the domain wall. Each arrow represents an averaged magnetization vector inside a single cell. Black arrows represent the in-plane magnetization, whereas the red and blue ones represent the out-of-plane projection of the magnetization inside a single cell. Orange and green areas represent positive and negative charge densities, respectively.

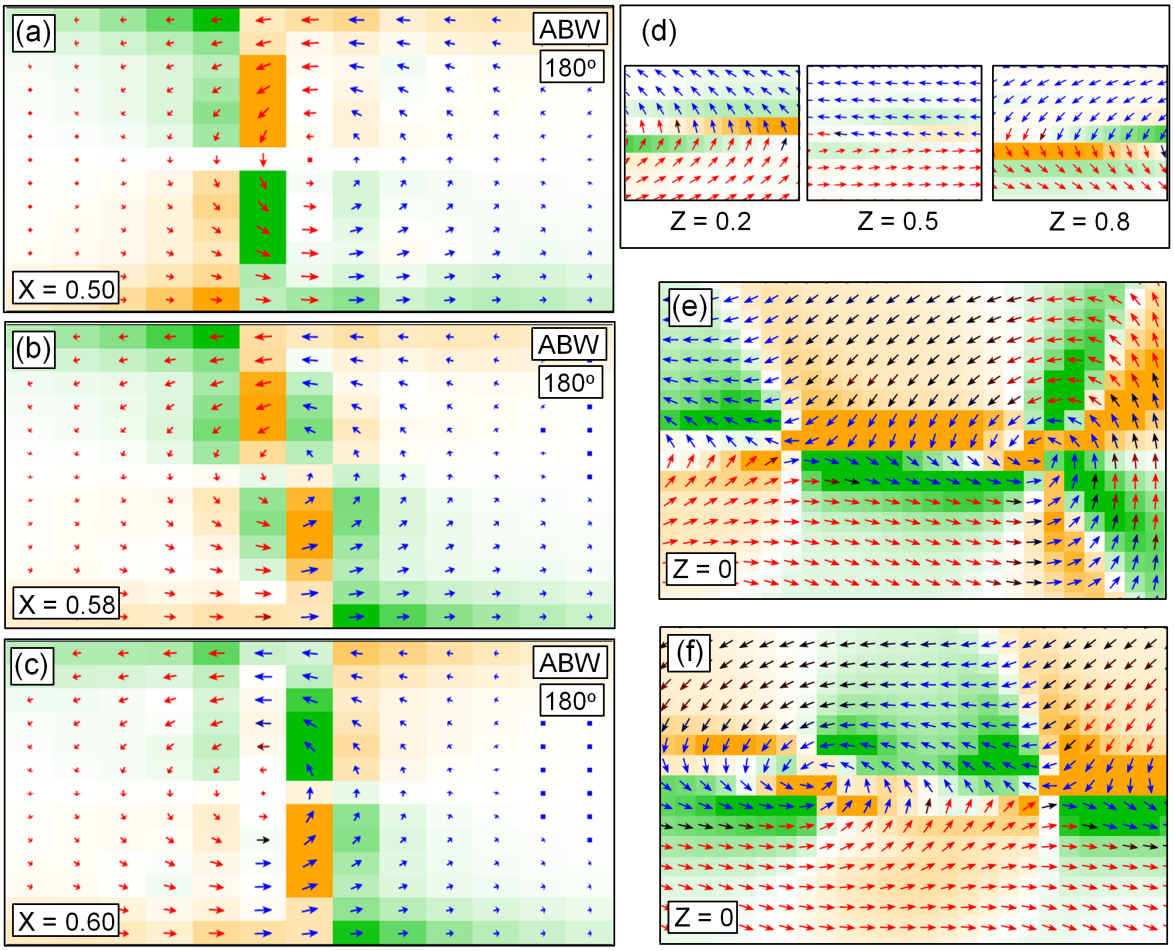

Figure 6.6: (a) to (c) represent cross-sectional images of the "T3" TS inside the ABW in Fig. 6.4(e) taken at from X = 0.5 to X = 0.6. The angle of the domain wall was measured from the middle plane presented in Fig. 6.4(e). (a) to (c) show a complete thickness of the sample i.e., 130 nm parallel to the z axis, while a 260 nm long segment of the sample parallel to the y axis is selected to describe the cross-sectional magnetization configuration of the domain wall. The magnetization configuration in the xy-plane for this TS is shown in (d). (e) shows the magnetic configuration after the nucleation of a VAVP at the lower NC in Fig. 6.4(f). (f) shows the magnetic configuration before the annihilation of the VAVP at the lower NC in Fig. 6.4(g). Black arrows represent the in-plane magnetization, whereas red and blue ones represent the out-of-plane projection of the magnetization inside a single cell. Orange and green areas represent positive and negative charge densities, respectively.

result in Fig. 6.4(a). A continuous contrast of this wall along its length indicates the absence of any TS inside the wall. In Fig. 6.3(a), the domain wall forming the upper trapezoidal-shaped domain (the domain formed with the upper long edge of the sample) changes its contrast at the left domain-wall junction, while, the contrast of this domain wall remains unswitched at the right domain wall junction. The switching of the domain wall contrast at the left wall junction indicates the presence of a vortex at the left domain wall junction (see Fig. 5.8 in chapter 5), which is also confirmed by comparing the MFM result in Fig. 6.3(a) with the simulated result in Fig. 6.4(a). The position of the vortex is marked by a black arrow in Fig. 6.3(a). A cross-sectional image of the wall taken from Fig. 6.4(a) is shown in Fig. 6.5(a). An in-plane orientation of the domain-wall magnetization in the cross-sectional image in Fig. 6.5(a) and a bipolar contrast of this wall in Fig. 6.3(a) indicate that this wall is a SNW. The angle of this SNW is 80° which was measured in the middle plane of Fig. 6.4(a). A schematic illustration of a segment of such an SNW is shown in Fig. 6.3(j). As the applied field strength was further reduced, a reduced magnitude of the MFM bipolar contrast of the domain wall was observed, as shown in Fig. 6.3(b). A cross-sectional view of the domain wall taken from the corresponding simulated image in Fig. 6.4(b) is shown in Fig. 6.5(b). From Fig. 6.4(b) it was observed that the angle of this domain wall increased to 143° and the magnetization configuration inside the domain wall transformed into a curved shape with the overall magnetization still pointing towards the +y direction, as observed in Fig. 6.5(b). With the reduction of the applied field strength, the magnetization inside the adjacent domains relaxed more along the edges of the sample (i.e., parallel to the x axis), the angle of the domain wall increased. The increase of the domain-wall angle led to an increase in the magnetic charges around the wall. But the amount of the magnetic charges (formed as a result of increasing angle) around an SNW configuration at this thickness, i.e., 130 nm, would be much larger compared to the amount of the charges around the same angle SNW in a 40 nm thick sample. Therefore, with the reduction of the applied field strength, the one-dimensional SNW transformed its configuration into a curved shape two-dimensional domain wall, rather than transforming into a cross-tie pattern of one-dimensional 90° SNWs (i.e., into a CTW as observed in the 40 nm thick sample). This domain wall is an ANW, where a partial out-of-plane magnetization orientation in the interior of the wall produces less magnetic charges around the wall, compared to the same angle SNW. An ANW and the magnetization inside adjacent domains are illustrated in a schematic diagram in Fig. 6.3(k). The bipolar nature of the MFM contrast of the ANW observed in Fig. 6.3(b) is because of the orientation of the overall magnetization inside the domain wall along

the +y direction [260, 261]. On further reducing the field strength, in order to avoid magnetic charges due to the increase of the wall angle, the magnitude of the out-of-plane tilting of the magnetization in the interior of the domain wall increased. Therefore, the bipolar character of the MFM contrast of the domain wall further reduced, as seen in Fig. 6.3(c). The cross-sectional view of the domain wall from Fig. 6.4(c) is shown in Fig. 6.5(c). When the applied field was reduced further, the increase in the magnetic charges around the wall was avoided by transformation of the orientation of the overall magnetization along the +z direction (shown in Fig. 6.5(d)). In this process, the magnetization in the interior of the domain wall rotated completely out-of-plane, and the wall transformed into an ABW with the switching of one of the NCs at the surface of the sample. Such transitions of the ANW into an ABW were observed in the MFM measurement, as shown in Fig. 6.3(c), where the remaining ANW segments displaying slight bipolar contrasts are indicated by dotted arrows. In the upper plane (z = 1.0) presented in Fig. 6.4(d), a VAVP nucleated close to the right end of the domain wall. The antivortex nucleated at the right end of the upper NC moved towards the left end in order to switch the upper NC and annihilated with the vortex present at the left end of the upper NC. As antivortices at this thickness have no long "cross-legs" (i.e., CTWs), they move easily. The cross-sectional image in Fig. 6.5(d) taken from Fig. 6.4(d) describes the switching of the upper NC. The ANW to ABW transition stage in Fig. 6.3(c) displays the transformation of the bipolar contrast to a unipolar contrast of the domain wall. Tiny segments of the bipolar contrast at locations close to the dotted arrows indicate the presence of TSs between the ANW and ABW segments of the domain wall. These TSs form vortices and antivortices inside the NCs at the locations of the transformations between different types of ADWs (i.e., between ANWs and ABWs). At zero field, an ABW with a unipolar MFM contrast was formed as shown in Fig. 6.3(d), and in the simulated images in Figs. 6.4(e) and 6.5(e). The schematic orientation of an ABW segment is illustrated in Fig. 6.3(l). A transition between a clockwise and a counter-clockwise ABW was observed by MFM as well as in the simulated results, which is shown in Figs. 6.3(e) and 6.4(e), respectively. The magnetization configuration of the domain wall around this TS is shown in different cross-sectional yz planes in Figs. 6.6(a) to (c), and the configuration in different xy planes in Fig. 6.6(d). This is a "T3" TS between the clockwise and counter-clockwise chiralities of the ABW, where the Bloch core (see Fig. 2.6) of the ABW switched its magnetization orientation, while the orientations of the NCs at both surfaces remained unswitched across this TS [6, 95, 262]. The Bloch switch (BS) in the MFM result Fig. 6.3(e) is observed with a switching of the unipolar contrast of the ABW due to the

switching of the out-of-plane orientation between the +z and −z directions. This TS contains a BP in its center [9, 91, 231, 263]. The equal magnitude of the opposite out-of-plane orientations of the magnetization in Fig. 6.6(b) indicates the location of a BP in the "T3" TS in this simulated result. A further increase in the field strength along the −y direction started saturating the domain wall in the reversed orientation. Therefore, the ABW which is favored only for small or zero fields [2] became unstable and transformed into an ANW with the switching of the remaining NC, i.e., the lower NC. In Fig. 6.4(f), a VAVP nucleated in the lower NC at the right end of the domain wall reversed a segment of the lower NC along the direction of the applied field. A detailed magnetization configuration of this VAVP is shown in Fig. 6.6(e). Such reversals of the NC segments and a consequent transformation of the ABW into an ANW are observed in Fig. 6.3(f). Three such segments of bipolar contrast domain walls nucleated inside the ABW are presented in Fig. 6.3(f). At this field strength, ABWs and ANWs co-exist inside the domain wall. In Fig. 6.3(g), three VAVPs at the transitions between the ANW and ABW segments are indicated by black markers. In Figs. 6.4(g) and 6.6(f), one of such VAVP is shown inside the lower NC, while Fig. 6.5(f) describes the onset of the lower NC switching by pushing the cross-sectional vortex-like structure of the ABW towards the lower NC. VAVPs in Fig. 6.3(g) annihilated with the increase of the strength of the applied field and the domain wall transformed into an ANW as shown in Figs. 6.3(h) and 6.4(h). The cross-sectional image in Fig. 6.5(g) taken from Fig. 6.4(h) indicates an ANW with overall magnetization pointing along the −y direction. The schematic illustration Fig. 6.3(m) describes a segment of such a reversed ANW. Further increase of the magnetic field transformed the ANW into an SNW as shown in Fig. 6.3(i) and 6.4(i), which is confirmed in the cross-sectional image in Fig. 6.5(h). A single vortex present at the right end of this SNW is marked by a black arrow in Fig. 6.3(i), which is confirmed in Fig. 6.4(i). In this process, the magnetization throughout the domain wall rotated again in the in-plane orientation. A reduced angle of the domain wall, i.e., 70° in Fig. 6.5(h), at high magnetic field strength kept the magnetic charges low around the domain wall. A reversed SNW segment is illustrated in Fig. 6.3(n).

6.5 Conclusion

The role of the vortices and antivortices as TSs in the reversal of the internal magnetization of one-dimensional and two-dimensional domain walls in Py thin films is explained. TSs nucleated and annihilated in order to stabilize the domain walls against

the magnetic charges induced inside a varying magnetic field. Segments of the domain walls with reversed magnetization orientations nucleated and enlarged with the nucleation and annihilation of the TSs, respectively. In this process, domain walls completed the switching of their magnetization configurations by transferring a resulting single vortex along their axes. However, with the change of the thickness, the different modes of transformations inside the domain walls led to a change in the behavior of the TSs.

In 40 nm thick films, domain walls switched their magnetization configurations through an in-plane rotation of their magnetization. Nucleation of vortices and antivortices as TSs inside one-dimensional domain walls reduced the magnetic charges by transforming the domain walls into the segments of smaller-angle domain walls. This resulted in the transformation of the SNWs into CTWs. CTWs transformed back into the SNWs with reversed magnetization orientations in order to complete the domain walls' magnetization switching.

Domain walls in 130 nm thick films switched their magnetization configurations through both in-plane and out-of-plane rotations of their magnetizations. First, an out-of-plane rotation of the magnetization in the interior of the domain walls transformed the one-dimensional SNWs into the two-dimensional ANWs. Later, two-dimensional ANWs reversed their magnetization by the in-plane switching of both of their NCs' magnetization configurations with the nucleation of vortices and antivortices inside the NCs. This reversal of the two-dimensional ANWs' magnetization configurations proceeded through their transformations into two-dimensional ABWs. Finally, reversed two-dimensional ANWs transformed into the reversed one-dimensional SNWs by another out-of-plane rotation of the magnetization. Switching of the internal magnetizations of the walls at this thickness proceeded through successive switching of upper and lower NCs, or vice versa, which generated three-dimensional TSs. Three-dimensional TSs at this thickness stabilized the domain walls by changing the shapes of the walls (i.e., by changing ANWs into ABWs), rather than transforming the domain walls into the lower angle segments.

7 Nucleation of stripe domains in ferromagnetic thin films

7.1 Introduction

In the 1960s, thin films of soft magnetic materials, namely of Py were found to display stripe domains (see section 2.6 for details on stripe domains) [11, 264–266], despite having a negligible bulk magnetocrystalline anisotropy [122]. These films develop a perpendicular anisotropy from the internal stress in conjunction with a nonzero magnetostriction coefficient [13, 112, 113] and/or from the columnar grains separated by nonmagnetic intergrain boundaries [198, 267]. In general, both these sources constitute the intrinsic perpendicular anisotropy constant K_{int} of the film. Due to the interplay of the perpendicular and the in-plane shape anisotropy, there exists a critical thickness of the film beyond which the formation of the stripe domains takes place (see subsection 2.6.2) [2, 11, 12, 109, 110]. The critical thickness varies with the film deposition conditions because these have an influence on the K_{int} value [15, 111–113]. Almost fifty years ago, Holz and Kronmüller calculated the domain-phase diagram and the critical thickness as a function of K_{int} in their classical and even today frequently cited work [12]. However, domain walls were completely ignored in the original work because an adequate micromagnetic treatment was beyond the possibilities of a numerical approach at that time. As a result, the domains with an in-plane homogeneous magnetization, separated either by SNWs or CTWs [2], are abruptly superimposed by stripe domains all over the film, when increasing the thickness beyond the critical value [2, 12, 109].

In the past few decades, magnetic thin films showing stripe domains were proposed for Bloch-line memories [18], magneto-optical displays [19] and tunable microwave applications due to the presence of a rotatable anisotropy [20]. Recently, stripe domains have generated new interests for spin-wave propagation in magnonic devices [21] and a nanoscale control of superconductivity in hybrid ferromagnet-superconductor memories [268, 269]. Today, much research is focused on the analysis and manipulation of micromagnetic entities, such as domain walls [22, 25–27], vortices [24, 27, 28]

and skyrmions [270, 271] to enable various new applications of magnetic thin films [22, 24, 26, 271, 272]. Consequently, an increasing interest in the internal structures of domain walls separating stripe domains [273, 274], in the static and dynamic analysis of stripe domains in submicron geometries [275–279] and as well in the local tailoring of perpendicular anisotropies [280, 281] in various thin films has developed. In this context, the influence of reduced lateral dimensions on the orientation of an effective anisotropy in stripe domains was explored [275, 276, 282]. Also, recently it was shown that skyrmions can be created by passing stripe domains through geometrical constrictions [283] as well as by a local tuning of perpendicular anisotropy of thin films [281]. In submicron disks, a range of domain configurations akin to skyrmions besides vortices was observed depending upon the perpendicular anisotropy [277, 284]. The internal structure of vortices and skyrmions, which determines their magnetic properties, can be controlled through the perpendicular anisotropy of the film [277, 278, 281, 285]. Recent research further shows that the perpendicular anisotropy of a thin film modifies the domain-wall internal structures in a subtle way [44].

In this chapter, the role of domain walls and their internal structures in the evolution of stripe domains is focused in order to refine the Holz and Kronmüller domain-phase diagram [12]. For this purpose, MFM investigations on patterned Py thin films of varying thickness were performed and compared the experimental results to those of micromagnetic calculations.

7.2 Experimental and micromagnetic simulation details

The samples consist of 2.3×6.7 µm^2 elongated Py rectangles of a thickness of 120 nm, 140 nm, 180 nm and 240 nm, respectively. As the magnetic properties of the films vary with the deposition conditions [15, 111–113], a constant Ar pressure of 2.0 µbar and a sputter rate of 18 nm/min were maintained during the deposition of all samples.

The micromagnetic simulations were performed with a cubic cell of 20 nm edge length. In order to mimic the Landau domain configuration obtained in the experimental results, the simulations were started from this configuration as the initial state. This initial state was then allowed to relax for different thicknesses at different values of K_{int} in order to match the experimental results most precisely. K_{int} was increased from zero with a step size of 0.5 kJm^{-3} for each thickness. The shape anisotropy of the film was not included in the perpendicular anisotropy constant K_{int}.

The rest of the experimental fabrication and simulation parameters used are as described in section 4.2 of chapter 4.

7.3 Magnetic configuration at different thicknesses

Figure 7.1 shows modifications of the Landau domain configuration at varying sample thickness. In Fig. 7.1(a), for a 120 nm thick sample, the 90° domain walls of the Landau configuration show a continuous bipolar contrast and the 180° domain wall a unipolar one with a reversal along the wall axis. All these domain walls are two-dimensional ADWs with out-of-plane components (Bloch core) of the magnetization in the interior and in-plane components (NCs) of the magnetization at the surfaces to reduce stray-field energy (see Fig. 2.6 in chapter 2) [2, 9, 286].

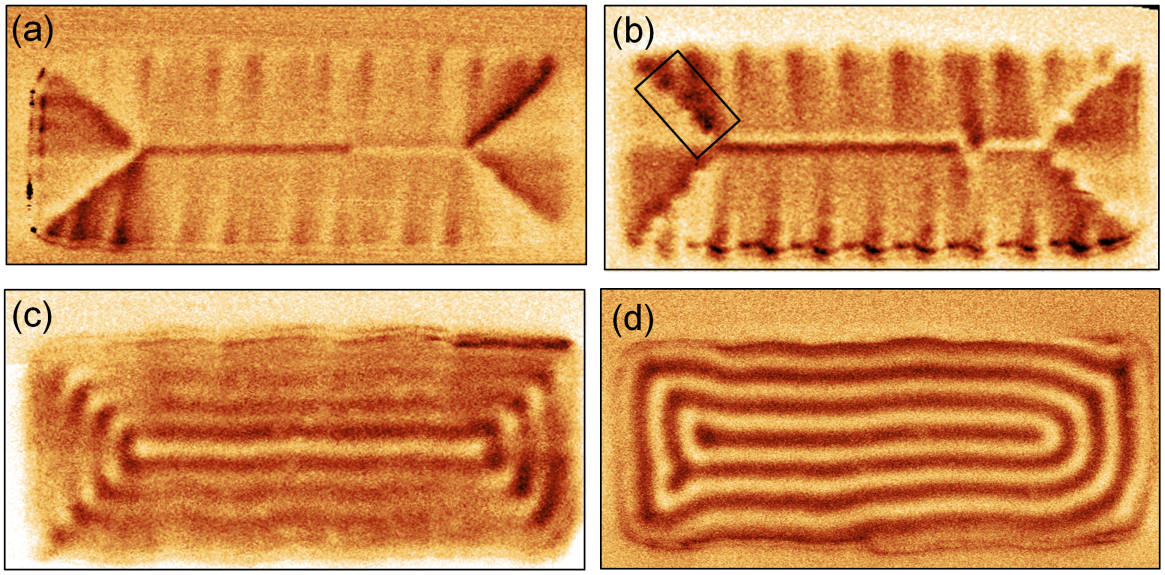

Figure 7.1: MFM images of the Landau domain configurations of 2.3×6.7 µm^2 Py patterns of thickness (a) 120 nm, (b) 140 nm, (c) 180 nm and (d) 240 nm, respectively. The marked area is shown in more detail in Fig. 7.4.

In Fig. 7.1, the 90° domain walls are ANWs and the 180° domain walls are ABWs. The reversal in the MFM contrast of the 180° domain wall in Fig. 7.1(a) is due to a transition between clockwise and counter-clockwise orientations of the Bloch cores (see subsection 2.2.3) [6, 9]. Furthermore, the domains in Figs. 7.1(a) and (b) show a faint spike-shaped contrast at the edges. This contrast was due to magnetic charges evolved at the imperfect edges of the sample. For the 140 nm thick sample, an alternately changing contrast along the 90° ANWs and a bipolar contrast along the 180° ABW were observed, as shown in Fig. 7.1(b). These domain-wall modifications for this sample were clearly not related to the perturbed magnetization close to the nonuniform edges of the sample. Upon increasing the sample thickness to 180 nm, the periodic pattern of the 90° ANWs and the bipolar contrast of the 180° ABW were further extended inside

the domains. At this thickness, a faint stripe contrast was observed inside the domains as shown in Fig. 7.1(c). For 240 nm thickness, clear stripe domains were observed all over the sample, as shown in Fig. 7.1(d).

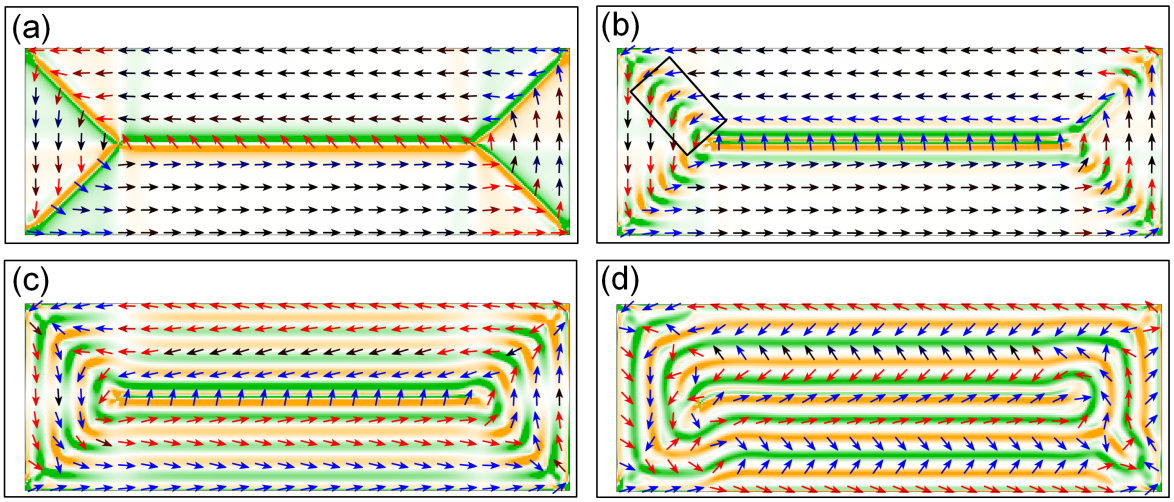

Figure 7.2: OOMMF-simulated images of Landau domain configurations in 2.3×6.7 μm^2 Py patterns of thickness (a) 120 nm with $K_{int} = 0$, (b) 140 nm with $K_{int} = 32.0$ kJm^{-3}, (c) 180 nm with $K_{int} = 22.5$ kJm^{-3} and (d) 240 nm with $K_{int} = 17.0$ kJm^{-3}, respectively. Each arrow represents an averaged magnetization vector inside 14×14 adjacent cells at the sample surface. Black arrows are in-plane magnetization vectors, whereas blue and red ones are the in-plane projections of magnetization vectors tilted upwards and downwards, respectively. Orange and green areas represent positive and negative charge densities, respectively. The marked area is shown in more detail in Fig. 7.4.

Figure 7.2 shows the respective theoretical results. Almost perfect matching was achieved in all cases by choosing appropriate values for K_{int}. Figure 7.3 shows the corresponding cross-sectional images taken from the middle of the samples. In Figs. 7.2(a) and 7.3(a) no perpendicular anisotropy had to be assumed to match the experimental results. The spikes observed in Figs. 7.1(a) and (b) are absent in the calculated images because ideally smooth edges of the sample were assumed. The absence of the transition in the 180° wall from Figs. 7.1(a) and (b) is simply due to the initial assumption of a non-subdivided wall in simulations. For the 140 nm thick sample, no periodic contrast along the 90° domain walls and no bipolar contrast along the 180° domain wall was observed in the simulated images upon assuming a vanishing perpendicular anisotropy. However, a nearly perfect match with the experimental results was obtained upon assuming a perpendicular anisotropy of $K_{int} = 32.0$ kJm^{-3}. This is shown in Fig. 7.2(b). Furthermore, though the finite K_{int} value modified the magnetization inside the

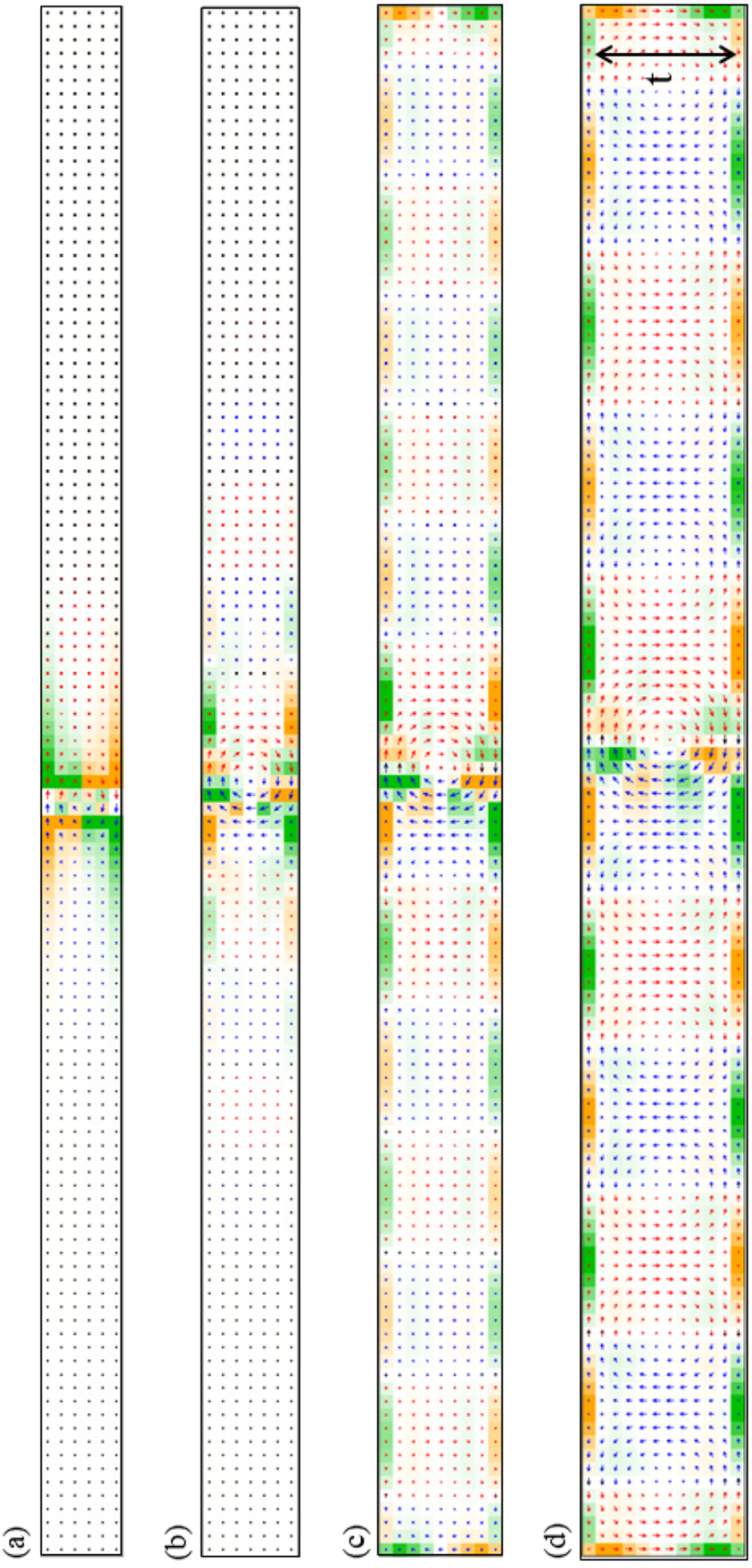

Figure 7.3: OOMMF-simulated cross-sectional images of Py films of a thickness t of (a) 120 nm with $K_{\mathrm{int}} = 0$, (b) 140 nm with $K_{\mathrm{int}} = 32.0\ \mathrm{kJm^{-3}}$, (c) 180 nm with $K_{\mathrm{int}} = 22.5\ \mathrm{kJm^{-3}}$ and (d) 240 nm with $K_{\mathrm{int}} = 17.0\ \mathrm{kJm^{-3}}$, respectively. Red and blue arrows represent the out-of-plane projection of the magnetization inside a single cell. Orange and green areas represent positive and negative charge densities, respectively.

domain walls, the magnetization inside the domains was still completely in-plane. This is in particular evident from Fig. 7.3(b). A satisfying match of the MFM image from Fig. 7.1(c) was obtained by assuming $K_{\text{int}} = 22.5\ \text{kJm}^{-3}$. This is shown in Fig. 7.2(c). The corresponding cross-sectional image in Fig. 7.3(c) clearly indicates the slightly upwards and downwards periodic tilting of the magnetization inside the domains. The tilted magnetization, in turn, produced charges on the sample surfaces. In Fig. 7.2(d), the stripe domains inside the 240 nm thick Py sample were reproduced by assuming $K_{\text{int}} = 17.0\ \text{kJm}^{-3}$. The corresponding cross-sectional image is shown in Fig. 7.3(d). An increased tilting of the magnetization inside the domains is clearly visible.

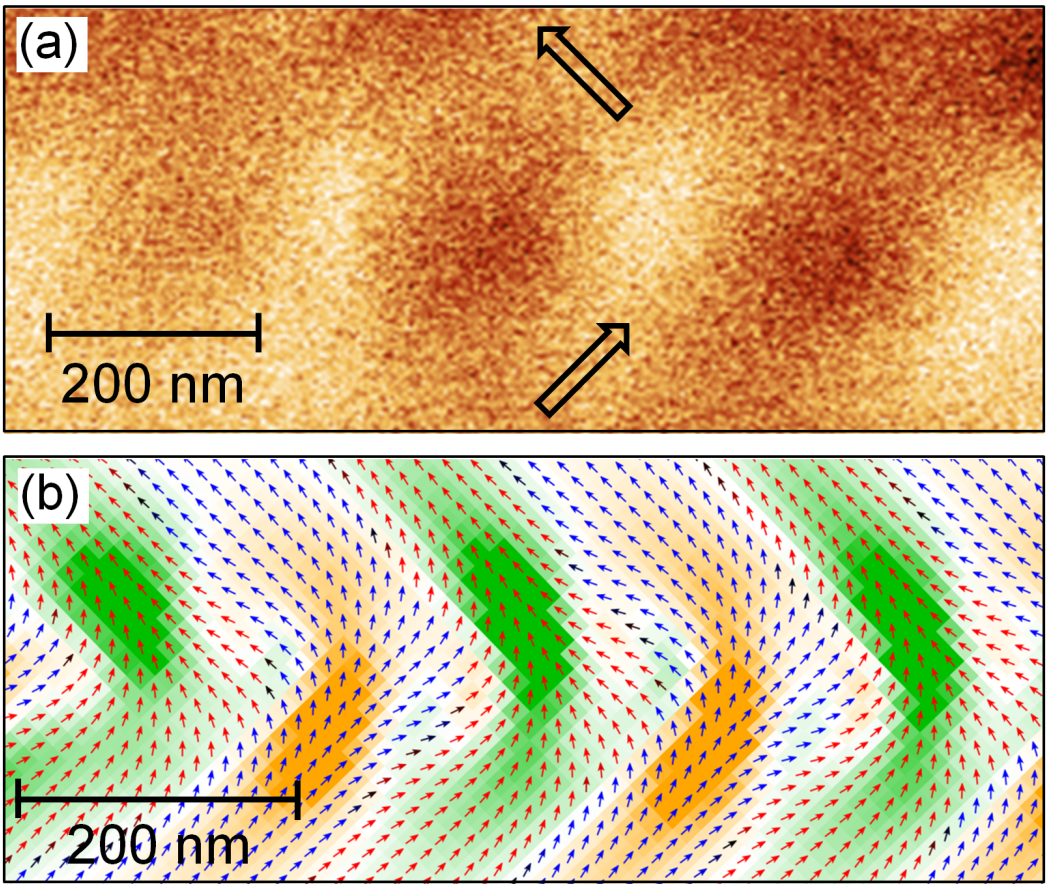

Figure 7.4: Modified 90° ANW of the 140 nm thick sample. (a) Enlarged MFM image of the area marked in Fig. 7.1(b). Arrows represent the direction of magnetization. (b) Simulated data corresponding to Fig. 7.2(b). Each arrow represents an in-plane magnetization vector inside a single cell. Blue and red arrows represent the in-plane projection of magnetization vectors tilted upwards and downwards, respectively. Orange and green areas represent positive and negative charge densities, respectively.

7.4 Perpendicular-anisotropy-modified domain wall

In Fig. 7.4, details in terms of charged segments from a modified 90° ANW are visible. By comparing both images in detail, it becomes clear that the alternately varying magnetic charges along the walls are formed because of alternately upwards and downwards pointing domain wall segments. Since no changes are yet induced within the domains, the domain walls obviously turn out to be magnetically softest.

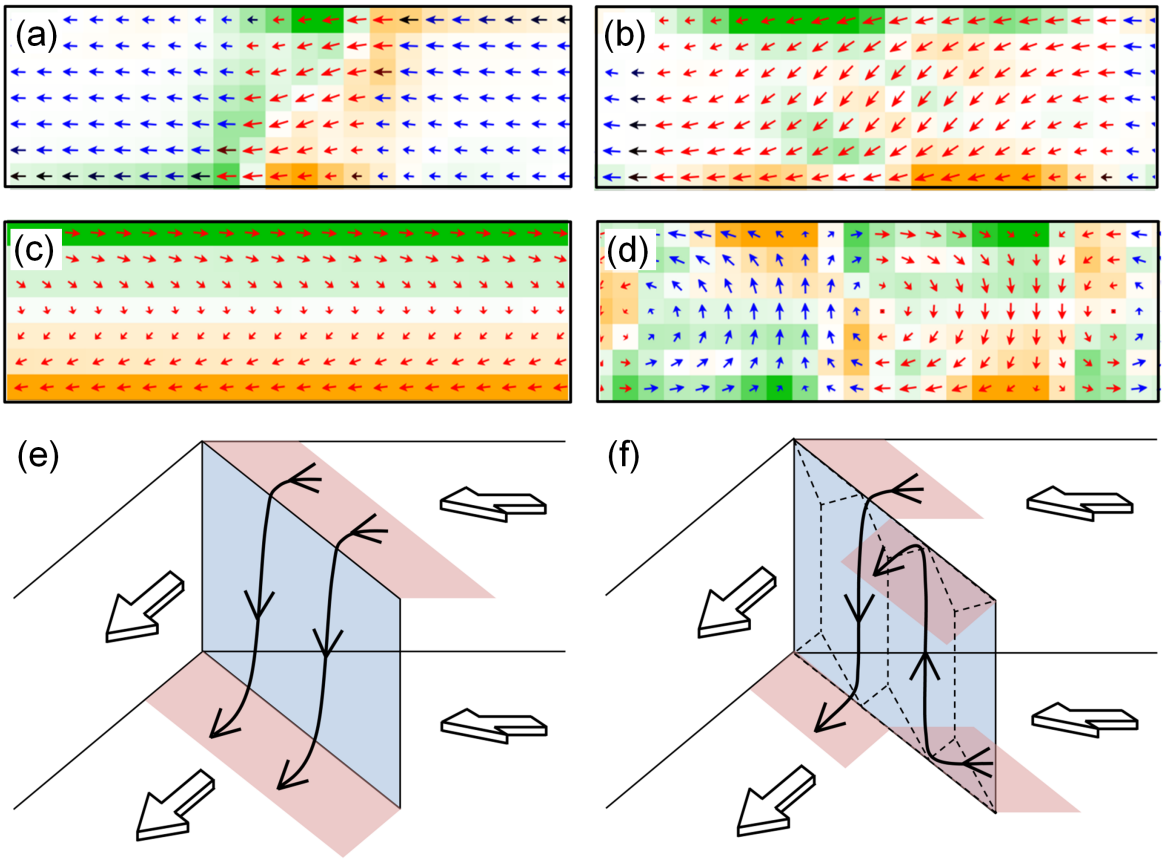

Figure 7.5: A 90° ANW with $K_{\mathrm{int}} = 0$ in (a), (c) and (e) is compared with a 90° ANW with $K_{\mathrm{int}} = 32.0\ \mathrm{kJm^{-3}}$ in (b), (d) and (f) for a 140 nm thick sample, respectively. (a) to (d) show simulated images of the 90° ANW and each arrow in the simulated images represents an out-of-plane projection of the magnetization vector inside a single cell. (a) and (b) show cross-sectional images of the domain wall. (c) and (d) show views along the wall axis. (e) and (f) schematically show the 90° ANW. The bold arrows represent the magnetization inside the domains, whereas the magnetization inside the domain wall is represented by curved lines. The blue shaded areas represent those parts of the ANW which have out-of-plane magnetization components (i.e., Bloch cores) and the grayish-pink shaded areas represent NCs with in-plane components at the surfaces.

In order to explore the three-dimensional modifications of the wall internal structures

induced by the perpendicular anisotropy in more details, magnetization-vector fields were modeled for a 140 nm thick sample for both $K_{\text{int}} = 0$ and $K_{\text{int}} = 32.0$ kJm^{-3}. The resulting configurations of the domain walls are compared in Fig. 7.5. From Figs. 7.5(a) and (b), which are the cross-sectional images of the walls, it is observed that the perpendicular anisotropy increased the magnitude of the out-of-plane tilting in the pre-existing Bloch core of the domain walls. This, in turn, enhanced the divergences of the magnetization at the intersection of the ANW with the sample surfaces and hence increased the charge densities right at the surfaces. Furthermore, from Figs. 7.5(c) and (d), which are the images along the axis of the walls, it is clear that in order to reduce the stray-field energy, the ANW splits into alternately upwards and downwards magnetized segments in its interior. The relative orientation of the upper and lower NCs still remains at 90°. Figures 7.5(e) and (f) schematically illustrate the respective ANW configurations.

Perpendicular anisotropy generates TSs inside the 90° ANW. The TSs inside the wall shown in Figs. 7.4 and 7.5 are formed either between the ANWs shown in Figs. 2.7(a) and (c) or between the ANWs shown in Figs. 2.7(b) and (d), respectively.

7.5 Perpendicular-anisotropy-modified domain wall at different wall angles

The 180° ABWs in all images of Figs. 7.1 and 7.2 do not show alternately varying charges at the sample surfaces. However, the MFM contrast changes from unipolar to bipolar as seen in Figs. 7.1(a) and (b). Subsequently, a faint stripe contrast appeared along the ABW with a further increase of the sample thickness. According to Fig. 7.3, the 180° ABW involves a vortex structure in its cross section (also see Fig. 2.5 in chapter 2). This vortex picks up a big part of the increase in the magnetization divergence and hence prevents the splitting of the out-of-plane components in the interior of the ABWs.

In Fig. 7.6, an in-plane magnetic field was applied along the short axis of a 140 nm thick 2.3×6.7 µm^2 Py sample. The corresponding simulated results for 32.0 kJm^{-3} perpendicular anisotropy are shown in Fig. 7.7. As it is shown in Fig. 2.11, the angle of a domain wall decreased with the increase of an in-plane field applied perpendicular to the wall. The angle of the domain wall formed along the long axis of the sample decreased from Fig. 7.6(a) to (d). This was confirmed in the simulated images from Fig. 7.7(a) to (h). The angle of the domain wall (formed parallel to the long axis)

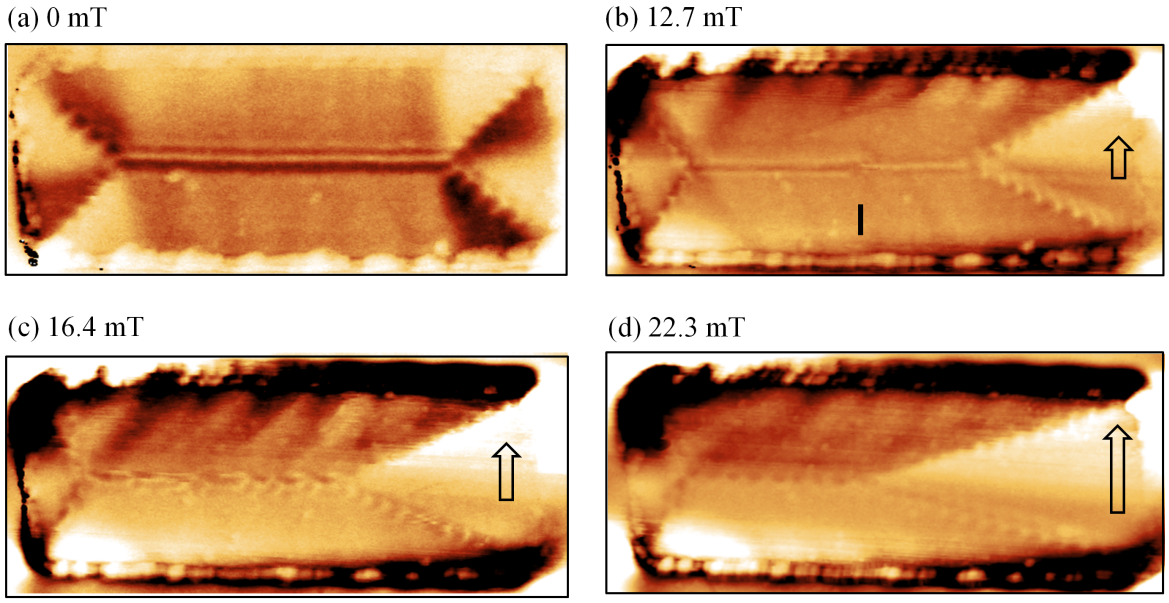

Figure 7.6: MFM images of the domain configurations in a 140 nm thick 2.3×6.7 µm^2 Py sample at different in-plane fields: (a) zero, (b) 12.7 mT, (c) 16.4 mT and (d) 22.3 mT applied parallel to the short axis as indicated by bold arrows.

was measured at the locations marked with black lines in Figs. 7.7(a), (c), (e) and (g), respectively. A TS, marked by a black marker, inside the wall was observed at 12.7 mT in Fig. 7.6(b). On further increasing the applied field a periodic pattern inside the domain wall was observed at 16.4 mT, shown in Fig. 7.6(c). At 22.3 mT the periodicity of the pattern in the domain wall parallel to the long axis became same as the periodicity of the pattern inside other domain walls (i.e., the 90° domain walls). In the simulated results, the formation of the periodic pattern inside the domain wall parallel to the long axis was observed at a wall angle of 90°, shown in Fig. 7.7(g). From the cross-sectional images in Fig. 7.7(b) and (d), it is found that the ABW with one cross-sectional vortex structure transforms into an ANW with two cross-sectional vortices (also discussed in chapter 6, section 6.4 and Fig. 6.5). From Figs. 7.7(g) and (h) it is clear that as the cross-sectional vortices disappeared the domain wall split into alternately arranged upwards and downwards magnetization components.

However, with the increase of sample thickness, the alternate upwards and downwards magnetized segments spread parallel to the 180° ABW on both sides, as seen in Fig. 7.3(b). The expanding segments cross the 90° ANWs and are ultimately extended all over the sample with further increasing thickness. This finally constitutes a complete stripe-domain pattern as predicted by the Holz and Kronmüller nucleation model [12].

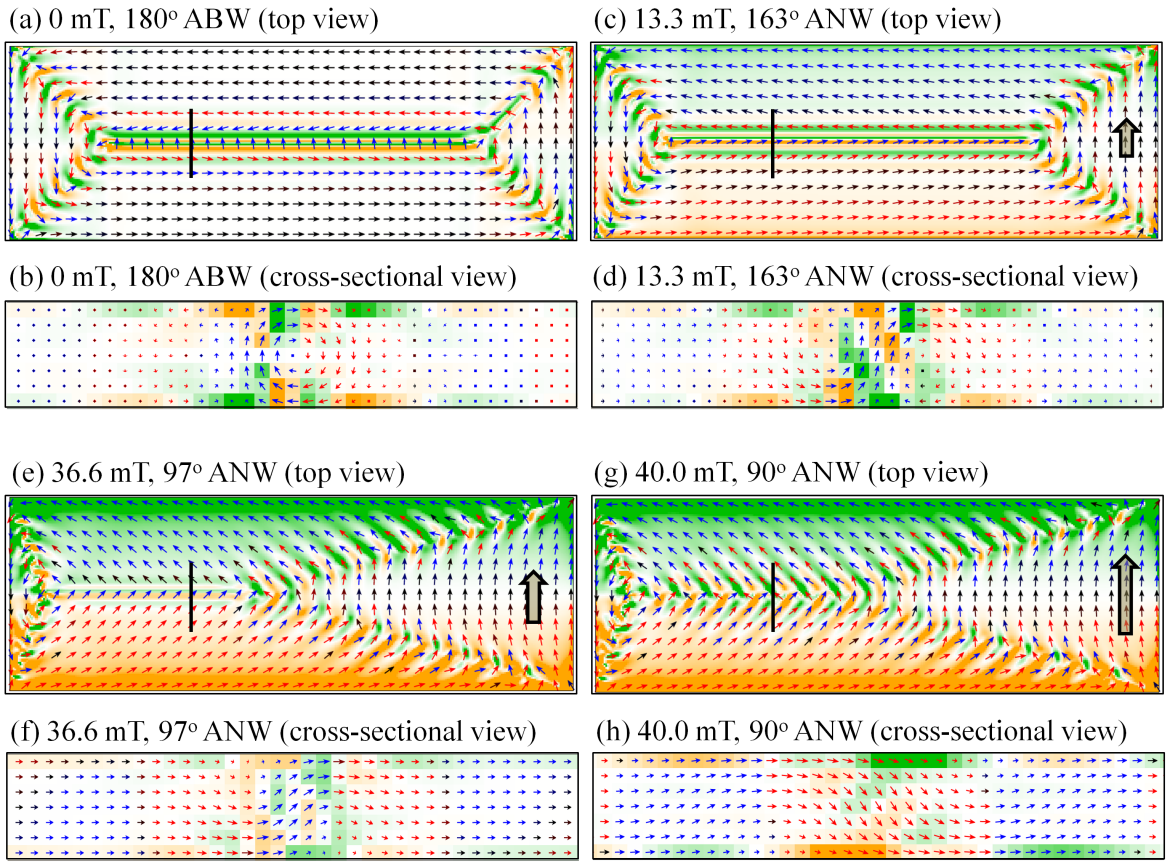

Figure 7.7: OOMMF-simulated images of the top and cross-sectional views of the domain configurations in a 140 nm thick 2.3×6.7 µm^2 Py sample with $K_{\text{int}} = 32.0$ kJm^{-3}. The cross-sectional images are taken at positions indicated by black markers in the top-views. Each arrow in the top-views represents the projection of an averaged magnetization vector inside 9×9 adjacent cells at the sample surface. Each arrow in the cross-sectional images represents an out-of-plane magnetization vector inside a single cell. Blue and red arrows represent the in-plane projection of magnetization vectors tilted upwards and downwards in the respective planes, respectively. Orange and green areas represent positive and negative charge densities, respectively. Bold arrows indicate the direction of the applied in-plane magnetic field parallel to the short axis.

7.6 Threshold value of the intrinsic perpendicular anisotropy

Simulated magnetization iso-surfaces for $M_z = \pm 0.25 M_s$ are shown in Fig. 7.8. In Fig. 7.8(a), no magnetization reversal inside the walls except at the corners was observed. The reversed segments at the corners were formed to reduce the stray field energy. On increasing K_{int} up to 15 kJm^{-3}, no further magnetization reversal inside the domain walls was observed, as seen in Fig. 7.8(b). Selecting any other out-of-plane magnetization component for the iso-surfaces, e.g., $M_z = \pm 0.1 M_s$, did not change the number of reversed segments inside the domain walls. At $K_{\text{int}} = 16.0$ kJm^{-3}, the first

reversed wall segment was observed close to one wall junction, as seen in Fig. 7.8(c). The corresponding value of K_{int} was classified as the threshold anisotropy $K_{\mathrm{int}}^{\mathrm{th}}$. An increase of K_{int} beyond $K_{\mathrm{int}}^{\mathrm{th}}$ induced more and more reversed wall segments, as seen in Figs. 7.8(d) and (e), respectively. At further increasing K_{int}, the alternately arranged wall segments grew more and more and ultimately formed stripe domains, as seen in Fig. 7.8(f).

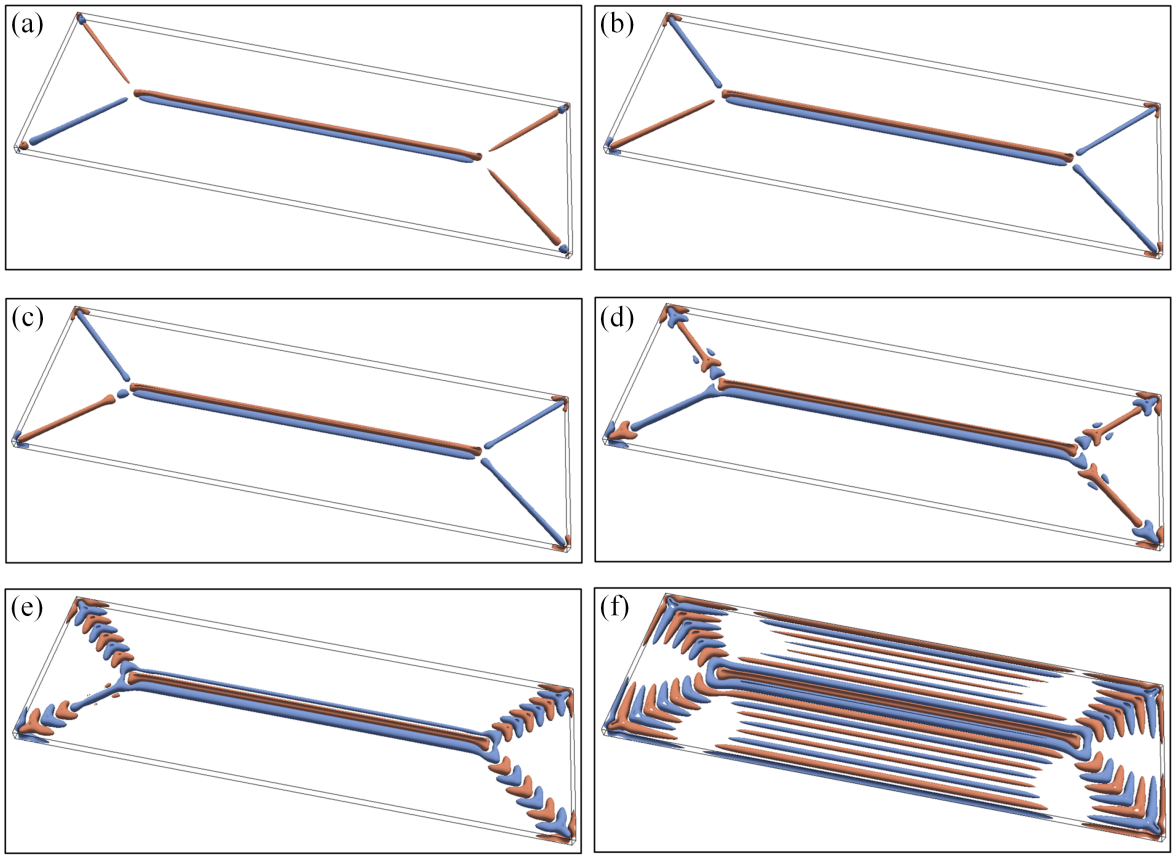

Figure 7.8: OOMMF-simulated domain configurations in terms of magnetization isosurfaces in a 140 nm thick 2.3×6.7 µm^2 Py sample for $M_{\mathrm{z}} = \pm 0.25 M_{\mathrm{s}}$ and (a) $K_{\mathrm{int}} = 0$, (b) $K_{\mathrm{int}} = 15.0$ kJm^{-3}, (c) $K_{\mathrm{int}} = 16.0$ kJm^{-3}, (d) $K_{\mathrm{int}} = 30.0$ kJm^{-3}, (e) $K_{\mathrm{int}} = 32.0$ kJm^{-3} and (f) $K_{\mathrm{int}} = 35.0$ kJm^{-3}, respectively. The blue and red-brown colors represent upwards and downwards oriented magnetization components, respectively.

7.7 Modified domain-phase diagram of stripe domains

In Fig. 7.9, the thickness dependence of K_{int} as obtained from a comparison of experimental and theoretical data is shown. Furthermore, the thickness dependence of a computationally obtained threshold anisotropy $K_{\mathrm{int}}^{\mathrm{th}}$ is shown as well. Figure 7.9 also

shows the classical data calculated by Holz and Kronmüller [12]. Comparing the Holz and Kronmüller data to the results obtained in this chapter, it can be concluded that the domain walls magnetically soften the sample and permit the evolution of premature stripe domains at an anisotropy well below that one needed for sudden nucleation of complete stripe domains. The experimentally observed K_{int} values are well above the threshold values. The K_{int} values for 140 nm and 180 nm thick samples, where no fully developed stripe domains were observed, are above the Holz and Kronmüller values. In Holz and Kronmüller calculations an infinitely extended thin film with an initial uniform in-plane magnetization was assumed, whereas in the micromagnetic simulations presented in this chapter patterned samples of finite dimensions with a Landau domain configuration as an initial magnetization were taken for the calculations. However, the reasons for the K_{int} values of 140 nm and 180 nm thick samples larger than Holz and Kronmüller values are not clear yet. It seems that the domain walls also delay the expansion of stripe domains inside the adjacent domains.

In order to check the robustness of the results with respect to variations of the basic properties of a Py film, changes of $K_{\mathrm{int}}^{\mathrm{th}}$ resulting from the change of up to $\pm 10\%$ in the saturation magnetization ($M_{\mathrm{s}} = 860$ kAm^{-1}) were calculated. Results are shown in Fig. 7.9. An increase of $K_{\mathrm{int}}^{\mathrm{th}}$ is observed for increasing M_{s}. An error bar was added to $\mathrm{K}_{\mathrm{int}}^{\mathrm{th}}$ in accordance to this M_{s} dependence. However, for up to $\pm 10\%$ change in the gyromagnetic ratio (γ) and exchange stiffness constant (A_{ex}), no appreciable change of $K_{\mathrm{int}}^{\mathrm{th}}$ was observed. Also, a particular data point (140 nm, 22.5 kJm^{-3}) on the Holz and Kronmüller nucleation curve is marked in Fig. 7.9. The corresponding calculated magnetization configuration is shown in the inset. Clearly, no stripe domains are observed as predicted by the Holz and Kronmüller nucleation model. This explains why the experimental data points are above the Holz and Kronmüller curve.

A decrease of K_{int} with increasing film thickness as observed here was also reported in Ref. [123]. A plausible explanation for this behavior is that stresses due to the lattice mismatch at the Py-substrate interface decrease with increasing distance to the interface [123, 129]. Therefore, the effective value of K_{int} decreases with increasing film thickness. However, with increasing thickness the in-plane shape anisotropy decreases as well (see section A.1 in the appendix for details). Therefore, above a certain critical thickness stripe domains develop in spite of a decreasing intrinsic perpendicular anisotropy K_{int}.

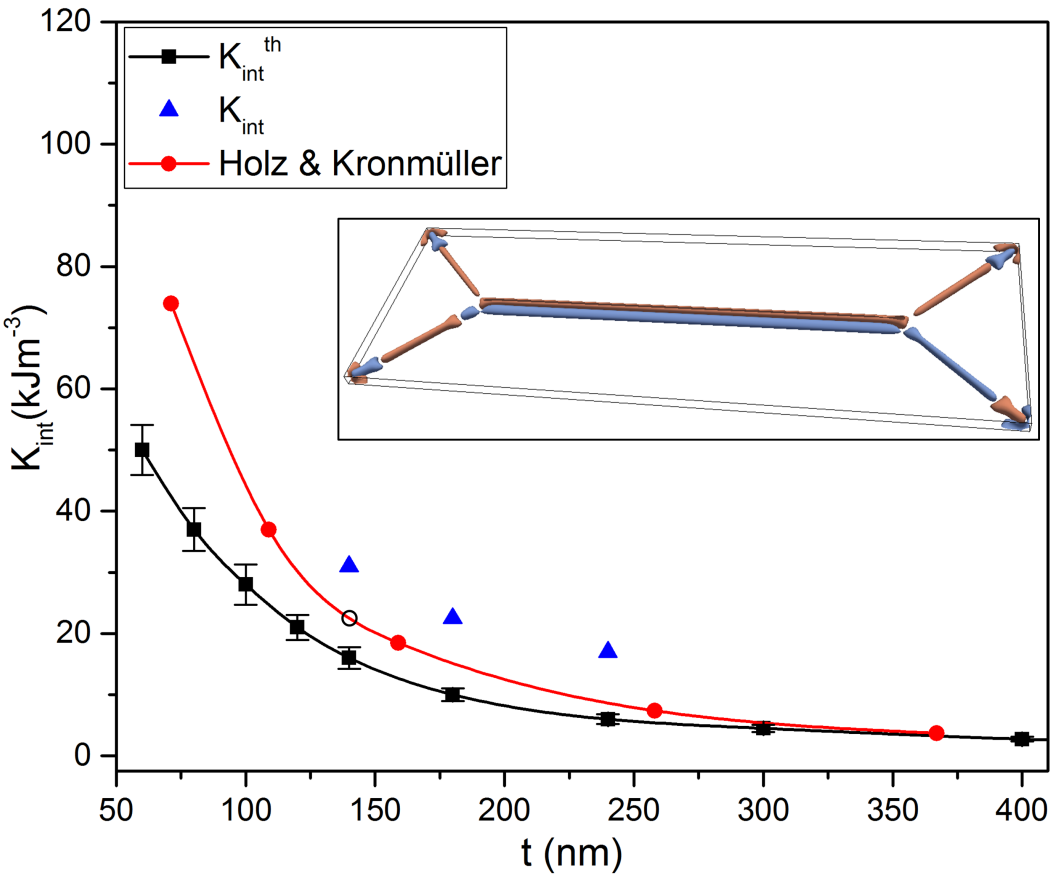

Figure 7.9: Thickness dependence of K_{int} (blue triangles) and $K_{\mathrm{int}}^{\mathrm{th}}$ (black squares) for Py thin films. Data from Holz and Kronmüller [12] is shown as red dots. The area below the $K_{\mathrm{int}}^{\mathrm{th}}$ data points represents the thickness regime in which the perpendicular anisotropy does not induce any magnetization reversal. Uncertainties of $\mathrm{K}_{\mathrm{int}}^{\mathrm{th}}$ for $\pm 10\%$ changes in the saturation magnetization $\mathrm{M_s}$ ($= 860$ kAm^{-1}) of Py films as shown by error bars. The inset shows the domain configuration corresponding to one particular data point (open circle) on the Holz and Kronmüller curve. Blue and red-brown represent upwards and downwards oriented magnetizations, respectively.

7.8 Conclusion

To conclude, the almost fifty years old domain-phase diagram by Holz and Kronmüller [12] has been refined by showing that the formation of stripe domains is an evolutionary and continuous process, which starts well below the critical thickness expected for the formation of the stripe phase from the classical theory [287]. The stripe domains evolve from the domain walls and in particular wall junctions which locally soften the film magnetically. Particularly interesting is that these softening sites shift the development of full stripe domains to film thicknesses which are for a given perpendicular anisotropy even above those values predicted by Holz and Kronmüller [12].

It is shown that the initial changes of the magnetization due to a perpendicular anisotropy start at magnetic inhomogeneities, i.e., domain walls and wall junctions. Structural imperfections and crystalline defects of magnetic films also result in magnetic inhomogeneities [288]. Thus, the presented results are of some general relevance and conclusions are not limited to configurations involving domain walls only. In general, tailoring of internal structures of micromagnetic entities in the context of spintronics is of great importance today [289, 290]. This definitely implies manifold implications of the presented results for applications of magnetic thin films in present and future technologies.

8 Conclusion and outlook

8.1 Conclusion

In this work, detailed magnetizations of domains and domain walls with the change of film deposition-conditions, an externally applied field and a perpendicular anisotropy were analyzed.

It was found that with the increase of the Ar sputtering pressure, pinnings of the TSs and domain walls resulted in complex and irregular domain configurations (see Fig. 4.7). The grain-morphologies of the films changed from dense to porous and their elemental compositions varied more and more away from the target composition, i.e., from $Ni_{80}Fe_{20}$ (wt%) at which the magnetocrystalline anisotropy and magnetostriction coefficient are vanishingly small (see subsection 3.1.2 in chapter 3). This resulted in an increase in the number of pinning sites and the magnetostriction coefficient of the films. Vortices, antivortices and domain walls during their nucleation and displacements got pinned at the pinning sites. The increase of the magnetostriction coefficient of the films made the magnetization sensitive to the stress inside the films. Therefore, the soft magnetic property of the Py films was deteriorated and an increase of the coercivity was observed. Also, the increase of the porosity in the films led to a reduction in the inter-grain exchange interactions. As a result, smaller domains were formed in the patterned films with the increase of the Ar pressure. However, the films prepared at 1.5 µbar Ar pressure showed dense morphology and the film composition was closest to the Py target composition. Due to the less pinning sites and well exchange-coupled grains, larger domains were formed and magnetization was less sensitive to the stress. Therefore, after the removal of the applied field, the domains evolved to the configurations actually defined by the shape and dimensions of the patterned films, i.e., a four domain configuration, which is the lowest energy state in Py square patterned films (see Fig. 4.8).

From the magnetization reversals in patterned films, it was observed that the basic role of the TSs is to let the magnetic flux pass through the domain walls by forming segments of reversed magnetizations inside the walls (see Fig. 5.3). These

segments expanded with the increase of the applied field to form the domains of reversed magnetizations. The magnetization reversal proceeded with the formation of domain walls as clusters and their rearrangements with the nucleation and displacement of vortices and antivortices as the TSs inside the walls. The nucleation of the TSs occurred near the remanent state, where the influence of the applied field on the magnetization inside the domain walls was weak compared to that of the demagnetizing field of the sample. Moreover, it was observed that the behaviors of the vortices and antivortices on repeating the magnetization reversal could change and consequently alter the evolution of the domain configurations.

Magnetic-field-induced transformations in the internal structures of the walls were analyzed in 40 nm and 130 nm thick Py films for one-dimensional and two-dimensional domain walls, respectively. It was observed that these both types of domain walls switched their internal magnetizations with the displacement of a resulting single vortex along their wall-axes. This displacement of a resulting single vortex proceeded with the nucleation of the vortices and antivortices as pairs inside the walls and movements of the vortices toward the next-neighbouring antivortices rather than toward the co-nucleated antivortices for annihilation (see Figs. 6.1 to 6.4). In 40 nm thick films, only one-dimensional domain walls existed within all applied fields. In these films, domain walls switched their internal magnetizations with the in-plane rotations of their magnetizations. The in-plane rotations of the magnetizations of the walls proceeded with the displacements of vortices only, as the antivortices stayed more or less fixed at their locations of nucleations. Nucleation of the vortices and antivortices inside the walls at this thickness reduced the magnetic charges of the walls by transforming the domain walls into cross-tie arranged lower angle wall-segments. In 130 nm thick films, only at high in-plane fields, sufficient enough to orient the domain wall magnetization parallel to the direction of the applied field, one-dimensional domain walls were formed. With the reduction of the applied field, first an out-of-plane rotation of the magnetization in the interiors of the walls transformed the one-dimensional domain walls into two-dimensional domain walls. Afterwards, the two-dimensional domain walls reversed their internal magnetizations at the surfaces by successive in-plane rotations of the magnetizations at the upper and lower surfaces of the walls or vice-versa. Finally, another out-of-plane rotation of the magnetization in the interiors of the walls transformed the two-dimensional domain walls back to one-dimensional domain walls with reversed internal magnetizations compared to the initially formed one-dimensional domain walls. In 130 nm thick films, the in-plane rotations of the magnetizations at the surfaces proceeded with the displacements of both vortices and antivortices. However, for the

domain walls being two-dimensional, certain singularities in the interiors of the walls were also formed. The TSs at this thickness stabilized the domain walls by transforming the shapes of the walls, rather than splitting the domain walls into the lower angle wall-segments as observed in 40 nm thick films (compare Figs. 6.1 and 6.2 with Figs. 6.3 to 6.5).

In addition to the analysis of the domain walls within an applied field, the change of their internal structures due to a perpendicular anisotropy was also investigated. Above a certain thickness of a Py film containing a perpendicular anisotropy, the 90° domain walls were found to split into alternately upwards and downwards tilted wall-segments. This splitting generated TSs inside the 90° walls. However, no TS inside 180° walls was observed due to the presence of a cross-sectional vortex in their internal structures (see Figs. 7.6 and 7.7). The split wall-segments expanded further inside the adjacent domains with the increase of the thickness and consequently formed stripe domains all over the film. In these results, the fifty years old domain-phase diagram from Holz and Kronmüller [12] was refined by showing that the formation of stripe domains is an evolutionary and continuous process, which starts well below the critical thickness at which the stripe-domain phase appeared in their classical theory [287]. The stripe domains evolved from the domain walls and in particular from the wall junctions. The domain walls and their junctions locally soften the film magnetically. It is particularly interesting that these softening sites shifted the development of the full stripe domains to the film thicknesses which are for a given perpendicular anisotropy even above than the thickness-values predicted by Holz and Kronmüller [12] (see Fig. 7.9).

8.2 Outlook of the work

As shown in the results, the TSs inside two-dimensional domain walls are quite complex in terms of their configurations and can involve magnetic singularities. Detailed magnetization configurations of various types of the TSs inside two-dimensional domain walls and their evolution during different magnetization processes are not completely understood. MFM is limited to imaging of the surface magnetization only. Three-dimensional magnetic imaging techniques like X-ray Magnetic Circular Dichroism Photo-Emission Electron Microscopy [291, 292] and Lorentz Transmission Electron Microscopy [263, 293] can be used to experimentally visualize the complex magnetization of the TSs in thin films. Such investigations are in fact important from the prospects of the flourishing three-dimensional nanomagnetism, where unconventional magnetization configurations could offer novel physical effects for future applications [294].

Also, the understanding of the behaviors of the domain walls and their TSs inside multilayered films is crucial. Especially, in trilayer systems in which two ferromagnetic films are separated by a non-magnetic spacer layer, which exhibits a wealth of interesting physical phenomena such as giant magnetoresistance effect [120]. The local stray field from the domain walls and their TSs leads to strongly localized magnetostatic interactions between the two ferromagnetic films, which influences the nucleation barrier for magnetization reversal [295] or the demagnetization of one of the layers [296].

Another interesting aspect of the behavior of the domain walls and their TSs could be explored inside functionally graded materials [297]. Owing to the graded variation in the composition and grain morphology, the properties of functionally graded materials changes significantly and continuously from one surface to another, thus eliminating interface problems like stress concentrations and poor adhesion [297]. The applications of functionally graded materials are increasing in aerospace, defense, nuclear industry, biomedical and energy sectors for their thermal and mechanical properties [298]. However, the magnetic properties of the functionally graded magnetic materials other than steel [299, 300] are barely investigated.

9 Publications and conference contributions

9.1 Publications

- Sukhvinder Singh, Haibin Gao and Uwe Hartmann, Nucleation of stripe domains in thin ferromagnetic films, Phys. Rev. B 98, 060414(R) 2018.
- Sukhvinder Singh, Leon Abelmann, Haibin Gao and Uwe Hartmann, Influence of sputtering conditions on domain configuration in patterned thin films (in preparation), 2019.
- Sukhvinder Singh, Haibin Gao and Uwe Hartmann, The role of vortex-antivortex pairs in the magnetization reversal of patterned thin films (in preparation), 2019.
- Sukhvinder Singh, Haibin Gao and Uwe Hartmann, Magnetization reversal of the internal configurations of one-dimensional and two-dimensional domain walls in thin films (in preparation), 2019.

9.2 Conference contributions

9.2.1 Conference talks

- Sukhvinder Singh, Haibin Gao and Uwe Hartmann, The role of vortex-antivortex pairs in the magnetization reversal of patterned thin films, Joint European Magnetic Symposia (JEMS), Uppsala, 2019.
- Sukhvinder Singh, Haibin Gao and Uwe Hartmann, Nucleation of stripe domains in ferromagnetic thin films, DPG Spring Meeting, Berlin, 2018.
- Sukhvinder Singh, Haibin Gao and Uwe Hartmann, Evolution of stripe domains in ferromagnetic thin films, 2nd IEEE Conference on Advances in Magnetics (IEEE AIM), La Thuile, 2018.

- Sukhvinder Singh, Haibin Gao and Uwe Hartmann, New insights into the permalloy problem: Evolution of stripe domains, One Day workshop - Magnetic Nanoobject, Nancy, 2017.
- Sukhvinder Singh, Haibin Gao and Uwe Hartmann, Flux transfer across domain walls in the patterned permalloy thin films, DPG Spring Meeting, Regensburg, 2016.
- Sukhvinder Singh, Haibin Gao and Uwe Hartmann, The role of vortex-antivortex pairs and cluster knots of domain walls in magnetization reversal, DPG Spring Meeting, Berlin, 2015.
- Sukhvinder Singh, Haibin Gao and Uwe Hartmann, Contributions of domain wall sub-structures to the magnetization configurations, DPG Spring Meeting, Regensburg, 2013.

9.2.2 Conference posters

- Sukhvinder Singh, Leon Abelmann, Haibin Gao and Uwe Hartmann, Influence of sputter conditions on domain configurations in patterned thin films, DPG Spring Meeting, Regensburg, 2019.
- Sukhvinder Singh, Haibin Gao and Uwe Hartmann, Role of vortex-antivortex pairs in the magnetization reversal of permalloy patterned thin films, Joint European Magnetic Symposia (JEMS), Mainz, 2018.
- Sukhvinder Singh, Haibin Gao and Uwe Hartmann, Influence of domain wall substructures on the domain structures of permalloy elements, DPG Spring Meeting, Berlin, 2015.

A Appendix

A.1 The interplay of shape anisotropy and intrinsic perpendicular anisotropy

The volume-averaged [301, 302] demagnetizing factor N_z parallel to the z axis for a ferromagnetic rectangular sample, as shown in Fig. A.1(a), is given by [303],

$$\begin{aligned} N_z = \frac{1}{\pi}\Bigg[& \frac{b^2-c^2}{2bc}\ln\left(\frac{\sqrt{a^2+b^2+c^2}-a}{\sqrt{a^2+b^2+c^2}+a}\right) + \frac{a^2-c^2}{2ac}\ln\left(\frac{\sqrt{a^2+b^2+c^2}-b}{\sqrt{a^2+b^2+c^2}+b}\right) \\ & + \frac{b}{2c}\ln\left(\frac{\sqrt{a^2+b^2}+a}{\sqrt{a^2+b^2}-a}\right) + \frac{a}{2c}\ln\left(\frac{\sqrt{a^2+b^2}+b}{\sqrt{a^2+b^2}-b}\right) + \frac{c}{2a}\ln\left(\frac{\sqrt{b^2+c^2}-b}{\sqrt{b^2+c^2}+b}\right) \\ & + \frac{c}{2b}\ln\left(\frac{\sqrt{a^2+c^2}-a}{\sqrt{a^2+c^2}+a}\right) + 2\arctan\left(\frac{ab}{c\sqrt{a^2+b^2+c^2}}\right) + \frac{a^3+b^3-2c^3}{3abc} \\ & + \frac{a^2+b^2-2c^2}{3abc}\sqrt{a^2+b^2+c^2} + \frac{c}{ab}(\sqrt{a^2+c^2}+\sqrt{b^2+c^2}) \\ & - \frac{(a^2+b^2)^{3/2}+(b^2+c^2)^{3/2}+(c^2+a^2)^{3/2}}{3abc}\Bigg]. \end{aligned} \tag{A.1}$$

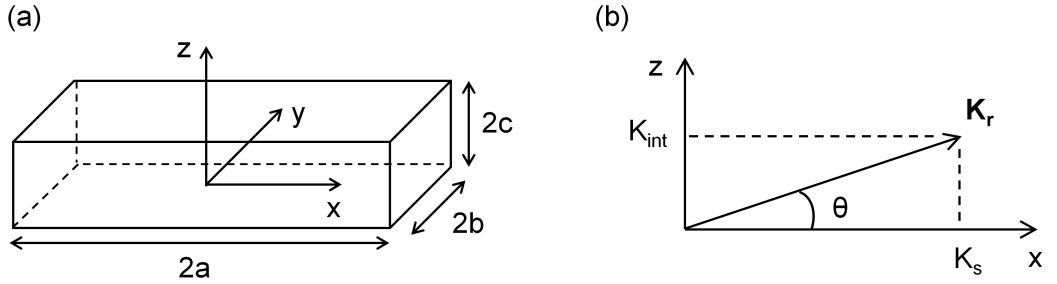

Figure A.1: (a) A ferromagnetic rectangular sample shown with a coordinate system. (b) Resulting anisotropy K_r. K_s is the shape anisotropy and K_{int} is the intrinsic anisotropy.

The other two demagnetizing factors N_x and N_y can be derived from equation (A.1) by applying twice the cyclic permutation $c \to a \to b \to c$ [303]. Therefore, the

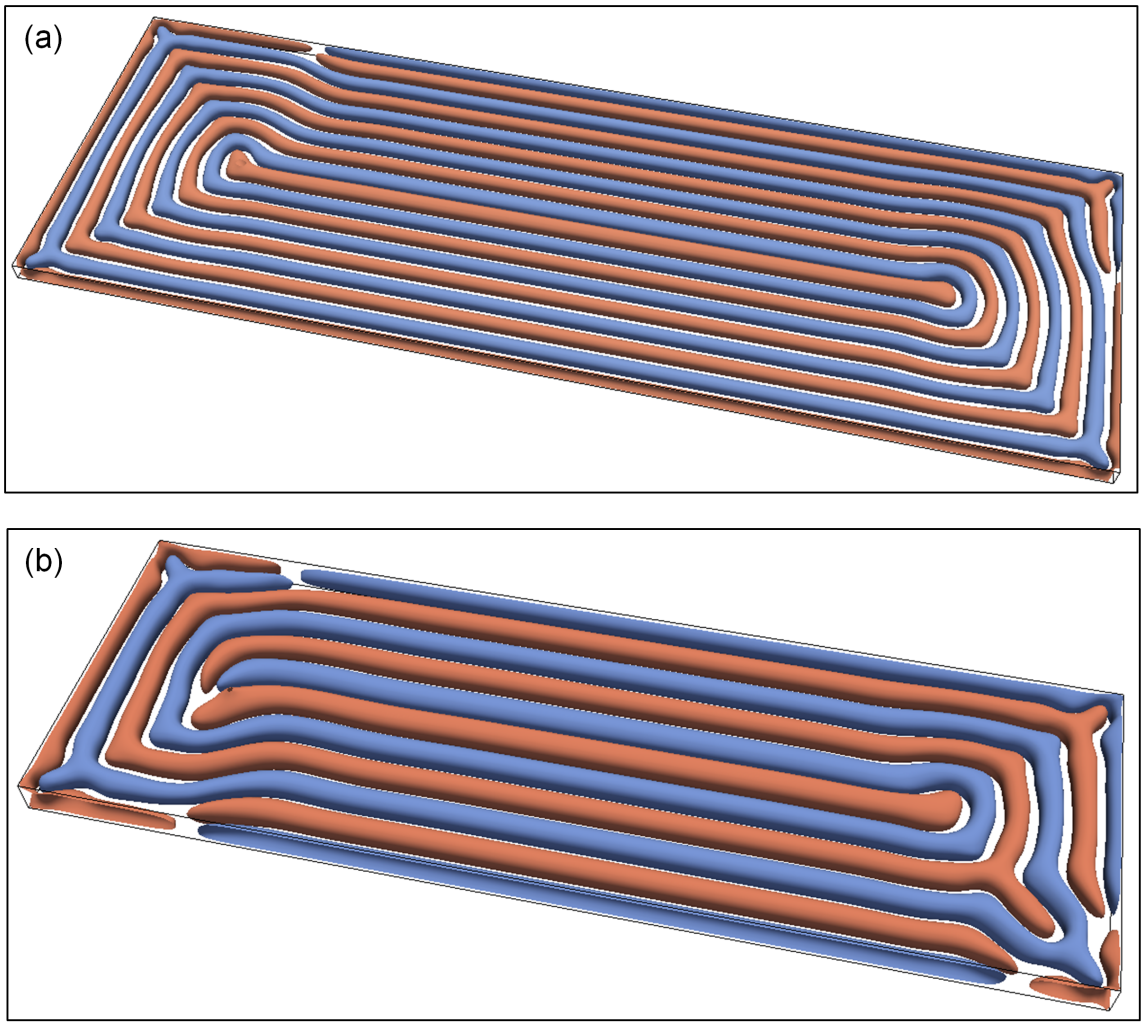

Figure A.2: OOMMF-simulated domain configurations in the 2.3×6.7 µm^2 Py sample for (a) a thickness of 140 nm with $K_{\mathrm{int}} = 40$ kJm^{-3} and (b) a thickness of 240 nm with $K_{\mathrm{int}} = 17$ kJm^{-3}, respectively. The blue and red-brown colors represent the out-of-plane magnetization iso-surfaces with a magnetization component of $M_{\mathrm{z}} = \pm 0.5 M_{\mathrm{s}}$, respectively.

demagnetizing factors along the orthogonal axes for a rectangular sample, shown in Fig. A.1(a), of lateral dimensions $2a = 6700$ nm, $2b = 2300$ nm and of two different thicknesses $2c = 140$ nm and 240 nm can be obtained from equation (A.1). The demagnetizing factors for the 140 nm thick sample are $N_{\mathrm{x}}^{140} = 0.026$, $N_{\mathrm{y}}^{140} = 0.077$ and $N_{\mathrm{z}}^{140} = 0.897$, respectively. With the increase of the thickness to 240 nm, the demagnetizing factors change to $N_{\mathrm{x}}^{240} = 0.038$, $N_{\mathrm{y}}^{240} = 0.115$ and $N_{\mathrm{z}}^{240} = 0.847$, respectively.

Considering the demagnetizing factors parallel to the easiest, i.e., the x axis and the hardest, i.e., the z axis of the rectangular sample, the shape anisotropy $K_{\mathrm{s}} = (1/2)\mu_0 M_{\mathrm{s}}^2 (N_{\mathrm{x}} - N_{\mathrm{z}})$ decreases from $K_{\mathrm{s}}^{140} = 404.8$ kJm^{-3} to $K_{\mathrm{s}}^{240} = 376.0$ kJm^{-3} with the increase of the thickness from 140 nm to 240 nm, respectively.

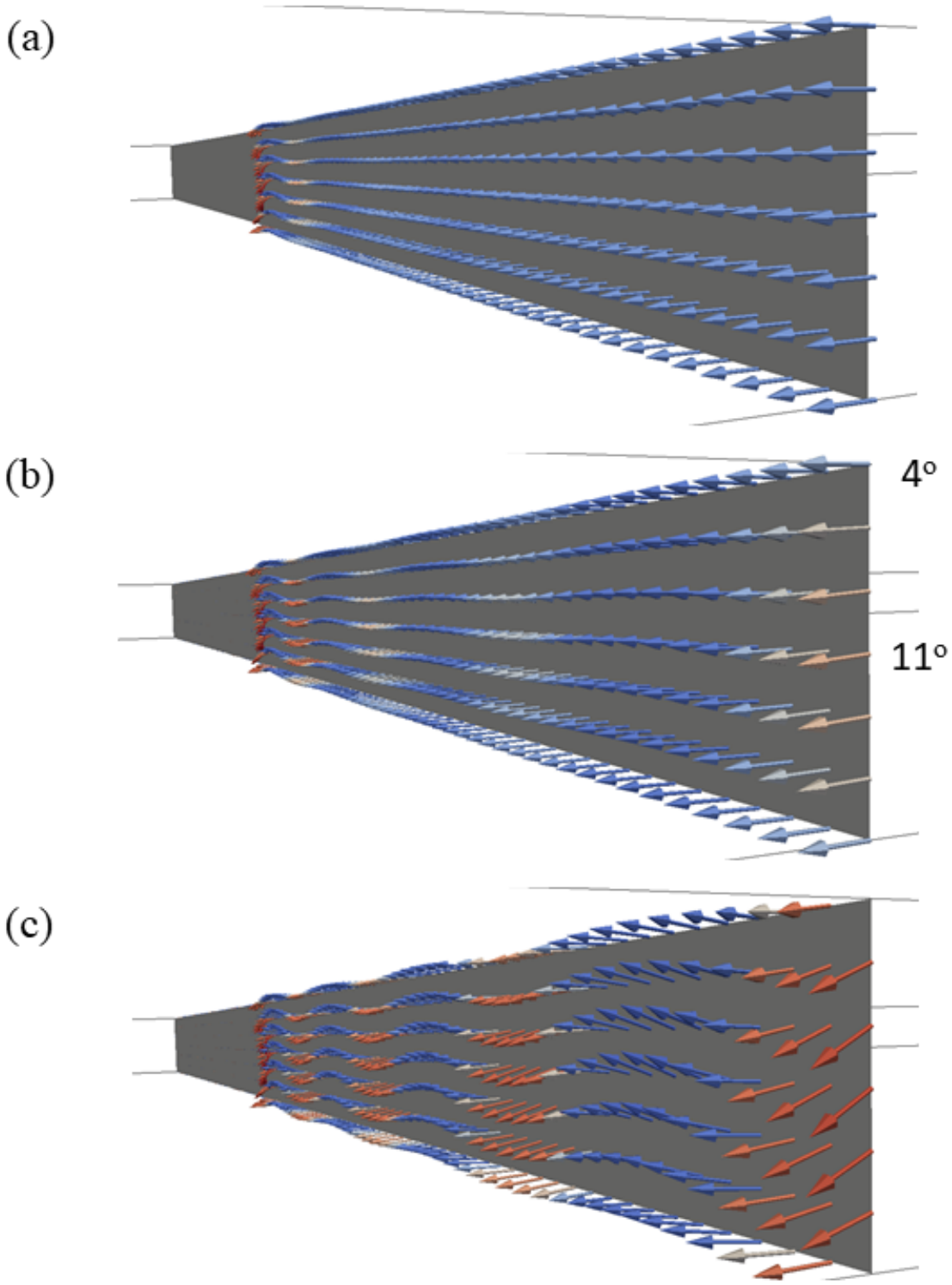

Figure A.3: Cross-sectional images (as described in Fig. 2.20) of the magnetization inside stripe domains in a 140 nm thick 2.3×6.7 µm^2 Py sample with (a) $K_{\mathrm{int}} = 32$ kJm^{-3}, (b) $K_{\mathrm{int}} = 34$ kJm^{-3}, and (c) $K_{\mathrm{int}} = 35$ kJm^{-3}, respectively. The angles of the magnetization with respect to the horizontal direction are shown in (b).

The interplay of the out-of-plane anisotropy K_{int} and the in-plane anisotropy K_{s} constitutes a resulting anisotropy K_{r} at an out-of-plane angle of $\theta = \arctan(K_{\mathrm{int}}/K_{\mathrm{s}})$ along which the magnetization aligns, as shown in Fig. A.1(b). As K_{s} decreases with the increase of the thickness, a smaller K_{int} is required to orient the magnetization at a critical angle θ_0 at which stripe domains are formed. Therefore, the K_{int} value obtained from the OOMMF simulations for the formation of stripe domains decreases from 40 $\mathrm{kJm^{-3}}$ to 17 $\mathrm{kJm^{-3}}$ with the increase of the thickness from 140 nm to 240 nm, as shown in Fig. A.2. The angle θ_0 calculated from the demagnetizing factors is a result of a simplified continuous approach assuming a purely uniform magnetization. It amounts to 5.6° for 140 nm thick sample with $K_{\mathrm{int}} = 40$ $\mathrm{kJm^{-3}}$ and $K_{\mathrm{s}}^{140} = 404.8$ $\mathrm{kJm^{-3}}$. However, from the OOMMF cross-sectional image for a 140 nm thick sample with $K_{\mathrm{int}} = 34$ $\mathrm{kJm^{-3}}$, the maximum angle of the magnetization of 11° and the minimum angle of 4° were observed at the middle-plane across the thickness and at the surfaces, respectively, as shown in Fig. A.3(b). For 140 nm thick sample, approximately above $K_{\mathrm{int}} = 34$ $\mathrm{kJm^{-3}}$ the stripe domains were found to start extending inside the domains, as seen in Fig. A.3. From this image, it can also be seen that the angle of the magnetization inside the stripe domains increases with increase of perpendicular anisotropy.

The perpendicular anisotropy constants K_{int} at the critical thickness are almost ten times smaller than the in-plane shape anisotropy constants K_{s}. As a result, the magnetization inside the stripe domains is not completely out-of-plane but tilted towards out-of-plane with a strong variation of the magnetization direction both across the film thickness as well as along the lateral directions as shown in Fig. 2.20 in chapter 2.

A.2 Cross-sectional images of Permalloy films prepared at different argon pressures

In Fig. A.4 TEM images of the cross-sectional grain morphology of the two Py films prepared at 1.5 and 30.0 µbar Ar pressures are shown, respectively. The Py film prepared at 1.5 µbar Ar pressure shows a dense morphology without visible columnar grains, whereas the Py film prepared at 30.0 µbar Ar pressure shows a porous morphology built up of columnar grains. From the comparison of Fig. A.4 with Fig. 4.3, it can be seen that the growth of two Py layers on top of each other did not alter the grain morphologies of the individual films.

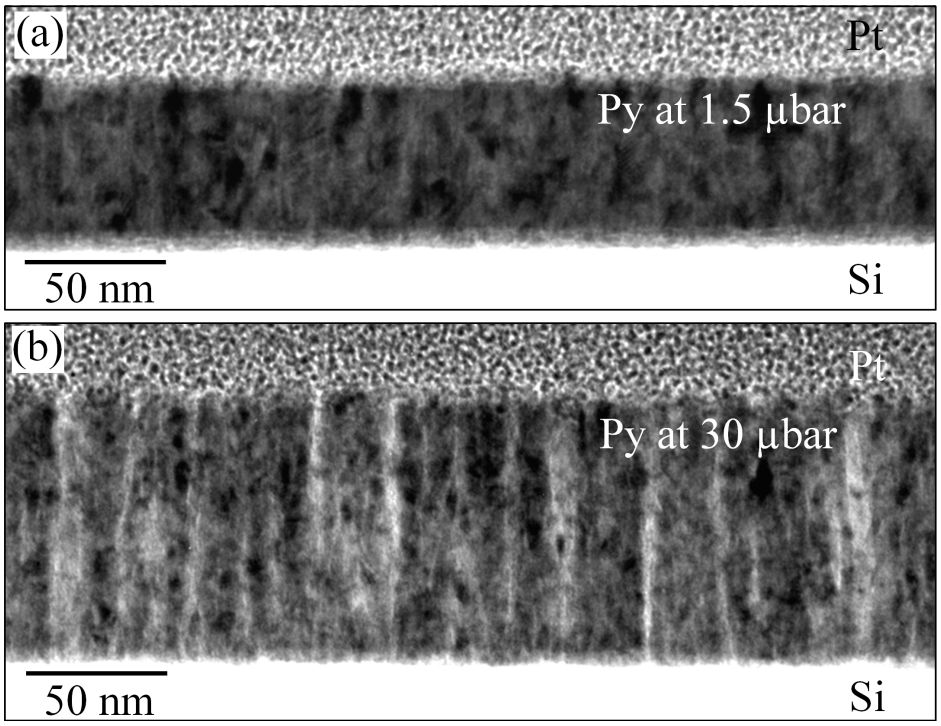

Figure A.4: Bright-field TEM images of the cross-sectional grain morphology of the Py films grown on Si substrates at (a) 1.5 µbar and (b) 30.0 µbar Ar pressures, respectively. Capping layers of Pt were deposited on the top to protect the Py films during the necessary FIB treatment.

A.3 Domain configurations of disk-shaped films as a function of the argon pressure

In Fig. A.5 remanent magnetic domain states inside two arrays of Py disks prepared at 1.5 and 5.0 µbar Ar pressures are shown, respectively. It is found that all Py disks prepared at 1.5 µbar Ar pressure show a single-vortex domain configuration as their remanent states, whereas very few Py disks prepared at 5.0 µbar show the single-vortex domain configuration as their remanent states. Most of the Py disks prepared at 5.0 µbar show either triangular domains or diamond configurations (see Fig. 4.1) as their remanent states. In this image, an information about the change of domain configurations as a function of Ar pressure in Py disks, in addition to the Py squares discussed in chapter 4, is provided.

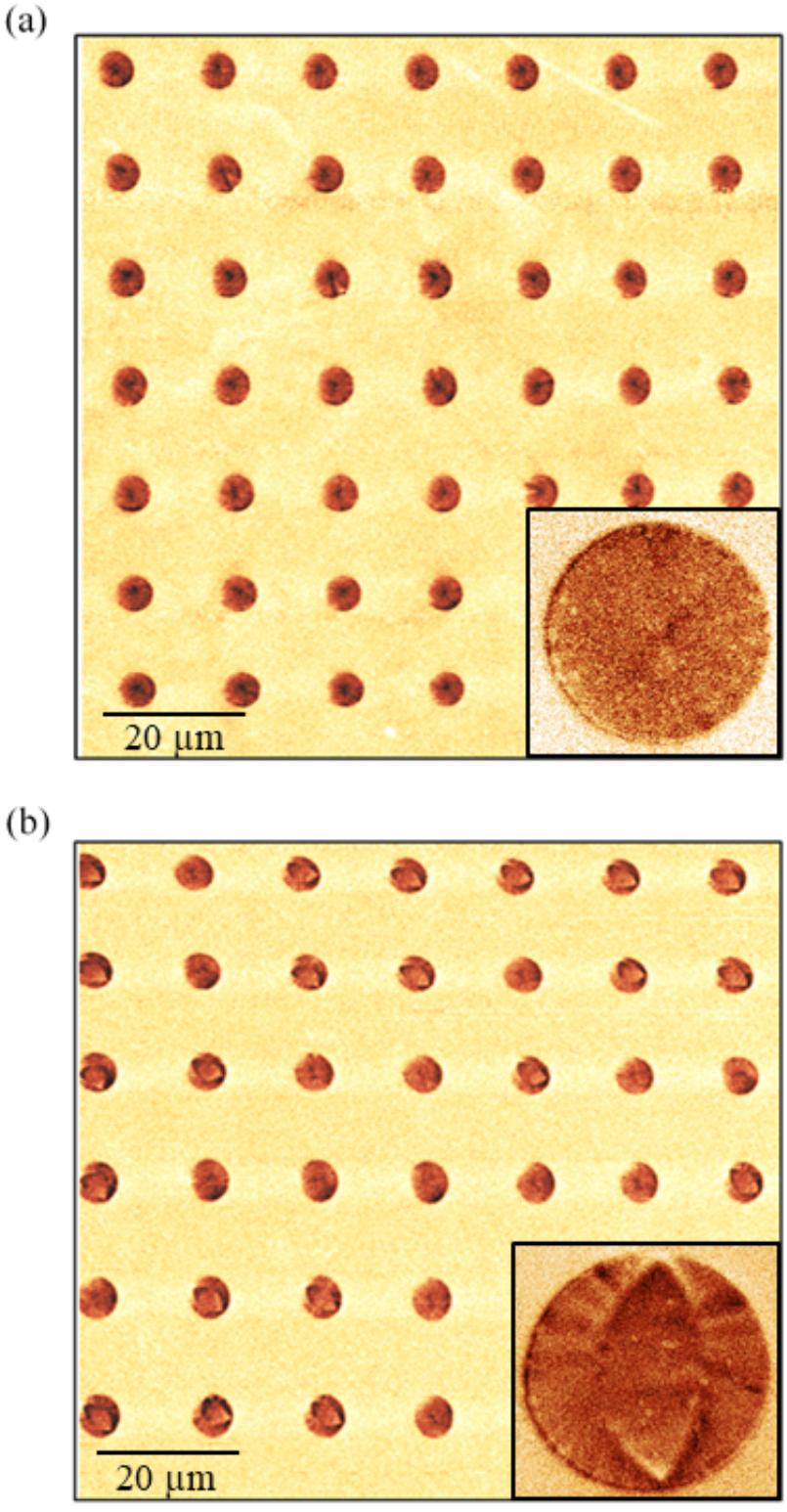

Figure A.5: MFM image of the remanent state of (a) 65 nm thick Py disks prepared at 1.5 µbar Ar pressure and (b) 50 nm thick Py disks prepared at 5.0 µbar Ar pressure. The disk diameter is 5.0 µm and the edge to edge inter-spacing is 10.0 µm. Inset images show (a) a single-vortex and (b) a diamond domain configurations.

Bibliography

[1] J. Coey, Scr. Mater. **67**, 524 (2012).

[2] A. Hubert and R. Schäfer, *Magnetic domains : the analysis of magnetic microstructures* (Springer, Berlin, 1998).

[3] M. J. Donahue, Adv. Cond. Matter Phys. **2012**, 1 (2012).

[4] N. Wiese, S. McVitie, J. N. Chapman, A. Capella-Kort, and F. Otto, EPL **80**, 57003 (2007).

[5] B. Filippov, M. Dubovik, and V. Zverev, J. Magn. Magn. Mater. **374**, 600 (2015).

[6] H. Asada, H. Kubo, J. Yamasaki, M. Takezawa, and T. Koyanagi, J. Phys.: Conf. Ser. **200**, 042003 (2010).

[7] M. Redjdal, A. Kakay, T. Trunk, M. F. Ruane, and F. B. Humphrey, J. Appl. Phys. **89**, 7609 (2001).

[8] M. Redjdal, A. Kakay, M. F. Ruane, and F. B. Humphrey, J. Appl. Phys. **91**, 8278 (2002).

[9] V. V. Zverev, B. N. Filippov, and M. N. Dubovik, Phys. Solid State **56**, 1785 (2014).

[10] B. D. Cullity and C. D. Graham, *Introduction to Magnetic Materials* (Wiley-IEEE Press, New York, 2008).

[11] N. Saito, H. Fujiwara, and Y. Sugita, J. Phys. Soc. Jpn. **19**, 1116 (1964).

[12] A. Holz and H. Kronmüller, Phys. Stat. Sol. **31**, 787 (1969).

[13] W. Karboul-Trojet, Y. Roussigné, D. Faurie, and S. M. Chérif, Eur. Phys. J. B **85**, 339 (2012).

[14] E. Feldtkeller, J. Phys. Colloques **32**, C1 (1971).

[15] A. V. Svalov, I. R. Aseguinolaza, A. Garcia-Arribas, I. Orue, J. M. Barandiaran, J. Alonso, M. L. FernÁndez-Gubieda, and G. V. Kurlyandskaya, IEEE Trans. Magn. **46**, 333 (2010).

[16] Y.-T. Chen, J.-Y. Tseng, T.-S. Sheu, Y. Lin, and S. Lin, Thin Solid Films **544**, 602 (2013).

[17] T. Schrefl, H. Schmidts, J. Fidler, and H. Kronmüller, J. Magn. Magn. Mater. **124**, 251 (1993).

[18] S. Konishi, IEEE Trans. Magn. **19**, 1838 (1983).

[19] R. J. Spain and H. W. Fuller, J. Appl. Phys. **37**, 953 (1966).

[20] S. Tacchi, S. Fin, G. Carlotti, G. Gubbiotti, M. Madami, M. Barturen, M. Marangolo, M. Eddrief, D. Bisero, A. Rettori, and M. G. Pini, Phys. Rev. B **89**, 024411 (2014).

[21] C. Banerjee, P. Gruszecki, J. W. Klos, O. Hellwig, M. Krawczyk, and A. Barman, Phys. Rev. B **96**, 024421 (2017).

[22] F. Cheynis, A. Masseboeuf, O. Fruchart, N. Rougemaille, J. C. Toussaint, R. Belkhou, P. Bayle-Guillemaud, and A. Marty, Phys. Rev. Lett. **102**, 107201 (2009).

[23] S. S. P. Parkin, M. Hayashi, and L. Thomas, Science **320**, 190 (2008).

[24] T. Shinjo, T. Okuno, R. Hassdorf, K. Shigeto, and T. Ono, Science **289**, 930 (2000).

[25] V. D. Nguyen, O. Fruchart, S. Pizzini, J. Vogel, J.-C. Toussaint, and N. Rougemaille, Sci. Rep. **5**, 12417 (2015).

[26] C. Zinoni, A. Vanhaverbeke, P. Eib, G. Salis, and R. Allenspach, Phys. Rev. Lett. **107**, 207204 (2011).

[27] A. Masseboeuf, O. Fruchart, J. C. Toussaint, E. Kritsikis, L. Buda-Prejbeanu, F. Cheynis, P. Bayle-Guillemaud, and A. Marty, Phys. Rev. Lett. **104**, 127204 (2010).

[28] M. Noske, H. Stoll, M. Fähnle, R. Hertel, and G. Schütz, Phys. Rev. B **91**,

014414 (2015).

[29] A. Thiaville, J. Garćia, and J. Miltat, J. Magn. Magn. Mater. **242-245**, 1061 (2002).

[30] D. Atkinson, D. A. Allwood, G. Xiong, M. D. Cooke, C. C. Faulkner, and R. P. Cowburn, Nat. Mater. **2**, 85 (2003).

[31] Y. Nakatani, A. Thiaville, and J. Miltat, Nat. Mater. **2**, 521 (2003).

[32] G. S. D. Beach, C. Nistor, C. Knutson, M. Tsoi, and J. L. Erskine, Nat. Mater. **4**, 741 (2005).

[33] L. Berger, J. Appl. Phys. **55**, 1954 (1984).

[34] J. Y. Lee, K. S. Lee, S. Choi, K. Y. Guslienko, and S. K. Kim, Phys. Rev. B **76**, 1 (2007).

[35] J. W. Lau, M. Beleggia, M. A. Schofield, G. F. Neumark, and Y. Zhu, J. Appl. Phys. **97**, 10E702 (2005).

[36] J. W. Lau, M. Beleggia, and Y. Zhu, J. Appl. Phys. **102**, 043906 (2007).

[37] F. Kloodt-Twesten, S. Kuhrau, P. Staeck, D. R. Cavicchia, F. Lofink, H. P. Oepen, and R. Frömter, Phys. Rev. B **97**, 024426 (2018).

[38] R. D. Gomez, J. S. Ma, A. Arkilic, S. H. Chung, and C. Krafft, J. Appl. Phys. **109**, 07D310 (2011).

[39] J. Shi, T. Zhu, S. Tehrani, Y. Zheng, and J.-G. Zhu, J. Magn. Magn. Mater. **198-199**, 251 (1999).

[40] J. Shi, S. Tehrani, and M. R. Scheinfein, Appl. Phys. Lett. **76**, 2588 (2000).

[41] M. Coïsson, F. Celegato, E. Olivetti, P. Tiberto, F. Vinai, and M. Baricco, J. Appl. Phys. **104**, 033902 (2008).

[42] C. C. Chang, Y. C. Chang, I. C. Lo, and J. C. Wu, J. Magn. Magn. Mater. **310**, 2612 (2007).

[43] Y. Chang, C. Chang, W. Hsieh, H. Lee, and J. Wu, IEEE Trans. Magn. **41**, 959 (2005).

[44] S. Voltan, C. Cirillo, H. J. Snijders, K. Lahabi, A. García-Santiago, J. M. Hernández, C. Attanasio, and J. Aarts, Phys. Rev. B **94**, 094406 (2016).

[45] M. Kamruzzaman, I. Rahman, and M. Rahman, J. Mater. Process. Tech. **119**, 312 (2001).

[46] M. Langosch, H. Gao, and U. Hartmann, J. Phys. D **45**, 085001 (2012).

[47] Y. Zheng and J.-G. Zhu, J. Appl. Phys. **81**, 5471 (1997).

[48] J. E. L. Bishop, Brit. J. Appl. Phys. **17**, 1451 (1966).

[49] 'Barkhausen noise as a magnetic nondestructive testing technique,' in *From Bulk to Nano: The Many Sides of Magnetism* (Springer Berlin Heidelberg, Berlin, Heidelberg, 2008) pp. 19–40.

[50] R. M. Bozorth, Rev. Mod. Phys. **25**, 42 (1953).

[51] B. Gehrmann, J. Magn. Magn. Mater. **290-291**, 1419 (2005).

[52] M. J. Donahue and D. G. Porter, *OOMMF User's Guide, Version 1.0* (NISTIR 6376, National Institute of Standards and Technology, Gaithersburg, MD, 1999).

[53] L. Landau and E. Lifshitz, Physik. Z. Sowjetunion **8**, 153 (1935).

[54] W. F. Brown, Jr., *Micromagnetics* (Intersceince, New York, 1963).

[55] W. F. Brown, J. Phys. Radium **20**, 101 (1959).

[56] F. Bloch, Zeitschrift für Physik **74**, 295 (1932).

[57] L. Nëel, *Theoretical remarks on ferromagnetism at low temperatures. In Progress in Low-Temperature Physics* (Gorter C.J. (Ed.), North Holland: Amsterdam pp. 347-350, 1955).

[58] C. Kittel, Phys. Rev. **70**, 965 (1946).

[59] C. Kittel, Rev. Mod. Phys. **21**, 541 (1949).

[60] N. S. Akulov, Zeitschrift für Physik **67**, 794 (1931).

[61] A. Aharoni and S. Shtrikman, Phys. Rev. **109**, 1522 (1958).

[62] R. Becker and W. Döring, 'Ferromagnetism,' (Springer: Berlin, 1939).

[63] E. C. Stoner and E. P. Wohlfarth, Philos. Trans. Royal Soc. A **240**, 594 (1948).

[64] H. Kronmüller, 'General micromagnetic theory,' in *Handbook of Magnetism and Advanced Magnetic Materials* (American Cancer Society, 2007).

[65] A. P. Guimarães, *Principles of Nanomagnetism*, NanoScience and Technology, Vol. (Springer International Publishing, Cham, 2017) p. 43.

[66] S. Chikazumi, *Physics of Ferromagnetism* (Oxford University Press, Oxford, 2005).

[67] J. Fidler, R. Chantrell, T. Schrefl, and M. Wongsam, in *Encyclopedia of Materials: Science and Technology*, edited by K. J. Buschow, R. W. Cahn, M. C. Flemings, B. Ilschner, E. J. Kramer, S. Mahajan, and P. Veyssière (Elsevier, Oxford, 2001) pp. 5642 – 5650.

[68] L. D. Buda-Prejbeanu, *Modelling of spintronic devices: from basic operation mechanisms toward optimization* , Habilitation à diriger des recherches, Communauté Université Grenoble Alpes (2017).

[69] T. L. Gilbert, IEEE Trans. Magn. **40**, 3443 (2004).

[70] J. Fidler and T. Schrefl, J. Phys. D **33**, R135 (2000).

[71] M. Oogane, T. Wakitani, S. Yakata, R. Yilgin, Y. Ando, A. Sakuma, and T. Miyazaki, Jpn. J. Appl. Phys **45**, 3889 (2006).

[72] H. Chang, P. Li, W. Zhang, T. Liu, A. Hoffmann, L. Deng, and M. Wu, IEEE Magn. Lett. **5**, 1 (2014).

[73] M. A. W. Schoen, D. Thonig, M. L. Schneider, T. J. Silva, H. T. Nembach, O. Eriksson, O. Karis, and J. M. Shaw, Nat. Phys. **12**, 839 (2016).

[74] A. Hubert and W. Rave, J. Magn. Magn. Mater. **196-197**, 325 (1999).

[75] L. Néel, Compt. Rend. **241**, 533 (1955).

[76] E. E. Huber, D. O. Smith, and J. B. Goodenough, J. Appl. Phys. **29**, 294 (1958).

[77] S. Middelhoek, J. Appl. Phys. **34**, 1054 (1963).

[78] M. Prutton, Phil. Mag. **5**, 625 (1960).

[79] A. Hubert, physica status solidi (b) **32**, 519 (1969).

[80] A. E. LaBonte, J. Appl. Phys. **40** (1969).

[81] I. L. Prejbeanu, L. D. Buda, U. Ebels, and K. Ounadjela, Appl. Phys. Lett. **77**, 3066 (2000).

[82] S. Foss, B. M. Moskowitz, R. Proksch, and E. D. Dahlberg, J. Geophys. Res. **103**, 30551 (1998).

[83] A. Hubert, J. Magn. Magn. Mater. **35**, 249 (1983).

[84] R. Schäfer, J. Magn. Magn. Mater. **215-216**, 652 (2000).

[85] W. Rave and A. Hubert, J. Magn. Magn. Mater. **184**, 179 (1998).

[86] A. Hubert, IEEE Trans. Magn. **11**, 1285 (1975).

[87] A. Hubert, J. Phys. Colloques **49**, C8 (1988).

[88] H. B. Braun, Advances in Physics **61**, 1 (2012).

[89] E. Feldtkeller, Angew. Phys. **19**, 530 (1965).

[90] P. R. Kotiuga, IEEE Trans. Magn. **25**, 3476 (1989).

[91] A. Thiaville, J. M. Garćia, R. Dittrich, J. Miltat, and T. Schrefl, Phys. Rev. B **67**, 094410 (2003).

[92] R. Hertel and C. Andreas, in *Magnetic Nano- and Microwires*, Woodhead Publishing Series in Electronic and Optical Materials, edited by M. Vázquez (Woodhead Publishing, 2015) pp. 653 – 677.

[93] A. P. Malozemoff and J. C. Slonczewski, *Magnetic Domain Walls in Bubble Material* (Academic Press, New York, 1979).

[94] R. D. Gomez, T. V. Luu, A. O. Pak, I. D. Mayergoyz, K. J. Kirk, and J. N. Chapman, J. Appl. Phys. **85**, 4598 (1999).

[95] V. V. Zverev and B. N. Filippov, J. Exp. Theor. Phys. **117**, 108 (2013).

[96] V. V. Zverev and B. N. Filippov, Phys. Met. Metall. **114**, 116 (2013).

[97] M. N. Dubovik, E. Z. Baykenov, V. V. Zverev, and B. N. Filippov, Phys. Met.

Metallogr. **119**, 203 (2018).

[98] R. Schafer, W. K. Ho, J. Yamasaki, A. Hubert, and F. B. Humphrey, IEEE Trans. Magn. **27**, 3678 (1991).

[99] M. Redjdal, A. Kákay, M. F. Ruane, and F. B. Humphrey, J. Appl. Phys. **91**, 8278 (2002).

[100] S. Huo, J. Bishop, J. Tucker, W. Rainforth, and H. Davies, J. Magn. Magn. Mater. **218**, 103 (2000).

[101] S. Huo, J. Bishop, J. Tucker, W. Rainforth, and H. Davies, J. Magn. Magn. Mater. **177-181**, 229 (1998).

[102] M. Seul and D. Andelman, Science **267**, 476 (1995).

[103] O. Perevertov, J. Thielsch, and R. Schäfer, J. Magn. Magn. Mater. **385**, 358 (2015).

[104] Y.-W. Lai, R. Schäfer, L. Schultz, and J. McCord, Appl. Phys. Lett. **96**, 022507 (2010).

[105] M. Wuttig, J. Li, and C. Craciunescu, Scr. Mater. **44**, 2393 (2001).

[106] R. Schäfer, N. Mattern, and G. Herzer, IEEE Trans. Magn. **32**, 4809 (1996).

[107] X. Z. Yu, Y. Onose, N. Kanazawa, J. H. Park, J. H. Han, Y. Matsui, N. Nagaosa, and Y. Tokura, Nature **465**, 901 (2010).

[108] O. Portmann, A. Vaterlaus, and D. Pescia, Nature **422**, 701 (2003).

[109] F. Virot, L. Favre, R. Hayn, and M. D. Kuz'min, J. Phys. D: Appl. Phys. **45**, 405003 (2012).

[110] D. S. Lo and M. M. Hanson, J. Appl. Phys. **38**, 1342 (1967).

[111] S. Min, J. A. Bain, and D. W. Greve, J. Appl. Phys. **91**, 6824 (2002).

[112] P. Zou, W. Yu, and J. A. Bain, J. Appl. Phys. **91**, 7830 (2002).

[113] P. Zou, W. Yu, and J. A. Bain, IEEE Trans. Magn. **38**, 3501 (2002).

[114] G. Chin, IEEE Trans. Magn. **7**, 102 (1971).

[115] H. D. Arnold and G. W. Elmen, Bell Syst. Tech. J. **2**, 101 (1923).

[116] R. M. Bozorth, Bell Syst. Tech. J. **29**, 251 (1950).

[117] https://archive.org/stream/PopularMechanics1925/Popular_Mechanics_12_1925#page/n3/mode/2up.

[118] J. M. D. Coey, *Magnetism and Magnetic Materials* (Cambridge University Press, Cambridge, 2009).

[119] J. Groenland, C. Eijkel, J. Fluitman, and R. de Ridder, Sens. Actuator A-Phys. **30**, 89 (1992).

[120] J. Daughton, J. Magn. Magn. Mater. **192**, 334 (1999).

[121] I. V. Vernyhora, V. A. Tatarenko, and S. M. Bokoch, ISRN Thermodynamics **2012**, 11 (2012).

[122] L. F. Yin, D. H. Wei, N. Lei, L. H. Zhou, C. S. Tian, G. S. Dong, X. F. Jin, L. P. Guo, Q. J. Jia, and R. Q. Wu, Phys. Rev. Lett. **97**, 067203 (2006).

[123] J. McCord, B. Erkartal, T. von Hofe, L. Kienle, E. Quandt, O. Roshchupkina, and J. Grenzer, J. Appl. Phys. **113**, 073903 (2013).

[124] E. Klokholm and J. A. Aboaf, J. Appl. Phys. **52**, 2474 (1981).

[125] E. B. Park, S.-U. Jang, J.-H. Kim, and S.-J. Kwon, Thin Solid Films **520**, 5981 (2012).

[126] A. Le Bail, I. Madsen, L. M. D. Cranswick, J. K. Cockcroft, P. Norby, A. D. Zuev, A. Fitch, J. Rodriguez-Carvajal, C. Giacovazzo, R. B. Von Dreele, P. Scardi, N. C. Popa, R. Allmann, L. A. Solovyov, B. Hinrichsen, U. Schwarz, A. Altomare, A. Moliterni, R. Caliandro, R. Rizzi, N. V. Y. Scarlett, and M. Jansen, *Powder Diffraction*, edited by R. E. Dinnebier and S. J. L. Billinge (The Royal Society of Chemistry, 2008) pp. p001–p582.

[127] Y. Masiyama, Sci. Repts. Tohoku Univ. **20**, 574 (1931).

[128] M. M. Yang and J. A. Aboaf, J. Appl. Phys. **66**, 3734 (1989).

[129] G. Janssen, Thin Solid Films **515**, 6654 (2007).

[130] M. Ohring, in *Materials Science of Thin Films (Second Edition)*, edited by M. Ohring (Academic Press, San Diego, 2002) second edition ed., pp. 95 – 144.

[131] J. Han, S. L. Thomas, and D. J. Srolovitz, Prog. Mater. Sci. **98**, 386 (2018).

[132] L. H. Lin and H. L. Beauchamp, J. Vac. Sci. Technol. **10**, 987 (1973).

[133] https://www.layouteditor.org/layout/basics.

[134] http://probe.olympus-global.com/en/product/omcl_ac240ts_r3/spec.html.

[135] B. Bhushan, *Nanotribology and Nanomechanics* (Springer Berlin Heidelberg, Berlin, Heidelberg, 2008).

[136] F. Ferri, M. P. da Silva, and E. M. Jr., in *Atomic Force Microscopy*, edited by V. Bellitto (IntechOpen, Rijeka, 2012) Chap. 3.

[137] L. Folks and R. Woodward, J. Magn. Magn. Mater. **190**, 28 (1998).

[138] M. Koblischka, M. Kirsch, R. Pfeifer, S. Getlawi, F. Rigato, J. Fontcuberta, T. Sulzbach, and U. Hartmann, J. Magn. Magn. Mater. **322**, 1697 (2010), proceedings of the Joint European Magnetic Symposia.

[139] S. Porthun, L. Abelmann, and C. Lodder, J. Magn. Magn. Mater. **182**, 238 (1998).

[140] M. Koblischka, U. Hartmann, and T. Sulzbach, J. Magn. Magn. Mater. **272-276**, 2138 (2004).

[141] L. Gao, L. Yue, T. Yokota, R. Skomski, S. Liou, H. Takahoshi, H. Saito, and S. Ishio, IEEE Trans. Magn. **40**, 2194 (2004).

[142] Y. Seo and W. Jhe, Rep. Prog. Phys. **71**, 016101 (2008).

[143] R. Garcıa and R. Pérez, Surf. Sci. Rep. **47**, 197 (2002).

[144] U. Hartmann (2000).

[145] N. Jalili and K. Laxminarayana, Mechatronics **14**, 907 (2004).

[146] R. Jagtap and A. Ambre, Indian J. Eng. Mater. Sci. **13**, 368 (2006).

[147] U. Hartmann, Ann. Rev. Mater. Sci. **29**, 53 (1999).

[148] U. Hartmann, Phys. Lett. A **137**, 475 (1989).

[149] D. V. Ovchinnikov and A. A. Bukharaev, Tech. Phys. **46**, 1014 (2001).

[150] H. J. Hug, B. Stiefel, P. J. A. van Schendel, A. Moser, R. Hofer, S. Martin, H.-J. Güntherodt, S. Porthun, L. Abelmann, J. C. Lodder, G. Bochi, and R. C. O'Handley, J. Appl. Phys. **83**, 5609 (1998).

[151] T. Häberle, F. Haering, H. Pfeifer, L. Han, B. Kuerbanjiang, U. Wiedwald, U. Herr, and B. Koslowski, New J. Phys. **14**, 043044 (2012).

[152] C. Rawlings and C. Durkan, Nanotechnology **24**, 305705 (2013).

[153] A. Hubert, W. Rave, and S. L. Tomlinson, Phys. Status Solidi B **204**, 817.

[154] M. M. Soares, E. de Biasi, L. N. Coelho, M. C. dos Santos, F. S. de Menezes, M. Knobel, L. C. Sampaio, and F. Garcia, Phys. Rev. B **77**, 224405 (2008).

[155] G. Csaba and W. Porod, J. Comput. Electron. **2**, 225 (2003).

[156] D. Rugar, H. J. Mamin, P. Guethner, S. E. Lambert, J. E. Stern, I. McFadyen, and T. Yogi, J. Appl. Phys. **68**, 1169 (1990).

[157] K. Babcock, V. Elings, M. Dugas, and S. Loper, IEEE Trans. Magn. **30**, 4503 (1994).

[158] S. Foner, Rev. Sci. Instrum. **30**, 548 (1959).

[159] S. Foner, J. Appl. Phys. **79**, 4740 (1996).

[160] J. Epp, in *Materials Characterization Using Nondestructive Evaluation (NDE) Methods* (Elsevier, 2016) pp. 81–124.

[161] R. Jenkins, 'X-ray techniques: Overview,' in *Encyclopedia of Analytical Chemistry* (American Cancer Society, 2006).

[162] Goerg H. Michler, *Electron Microscopy of Polymers* (Springer Berlin Heidelberg, Berlin, Heidelberg, 2008).

[163] D. J. Smith, Mater. Today **11**, 30 (2008).

[164] https://en.wikipedia.org/wiki/Transmission_electron_microscopy.

[165] D. Kumar and A. O. Adeyeye, J. Phys. D **50**, 343001 (2017).

[166] J. Leliaert and J. Mulkers, J. Appl. Phys. **125**, 180901 (2019).

[167] D. V. Berkov, K. Ramstöcck, and A. Hubert, Phys. Status Solidi A **137**, 207 (1993).

[168] L. Exl, S. Bance, F. Reichel, T. Schrefl, H. Peter Stimming, and N. J. Mauser, J. Appl. Phys. **115**, 17D118 (2014).

[169] J. E. Miltat and M. J. Donahue, in *Handbook of Magnetism and Advanced Magnetic Materials* (John Wiley & Sons, Ltd, Chichester, UK, 2007) pp. 1–23.

[170] T. Schrefl, G. Hrkac, S. Bance, D. Suess, O. Ertl, and J. Fidler, in *Handbook of Magnetism and Advanced Magnetic Materials* (John Wiley & Sons, Ltd, Chichester, UK, 2007) pp. 1–30.

[171] https://mumax.github.io/.

[172] A. Vansteenkiste, J. Leliaert, M. Dvornik, M. Helsen, F. Garcia-Sanchez, and B. Van Waeyenberge, AIP Advances **4**, 107133 (2014).

[173] http://www.micromagus.de/home.html ().

[174] http://nmag.soton.ac.uk/nmag/.

[175] http://micromagnum.informatik.uni-hamburg.de/ ().

[176] http://www.magpar.net/.

[177] https://www.fz-juelich.de/pgi/pgi-6/EN/Forschung/MagnetizationDynamics/Simulations/TetraMAG/_node.html.

[178] http://feellgood.neel.cnrs.fr/.

[179] B. Van de Wiele, A. Manzin, L. Dupre, F. Olyslager, O. Bottauscio, and M. Chiampi, IEEE Trans. Magn. **45**, 1614 (2009).

[180] S. Fu, W. Cui, M. Hu, R. Chang, M. J. Donahue, and V. Lomakin, IEEE Trans. Magn. **52**, 1 (2016).

[181] P. Pirro, T. Koyama, T. Brächer, T. Sebastian, B. Leven, and B. Hillebrands, Appl. Phys. Lett. **106**, 232405 (2015).

[182] B. Van Waeyenberge, A. Puzic, H. Stoll, K. W. Chou, T. Tyliszczak, R. Hertel, M. Fähnle, H. Brückl, K. Rott, G. Reiss, I. Neudecker, D. Weiss, C. H. Back, and G. Schütz, Nature **444**, 461 (2006).

[183] S. Goolaup, M. Ramu, C. Murapaka, and W. S. Lew, Sci. Rep. **5**, 9603 (2015).

[184] S. Cherifi, R. Hertel, J. Kirschner, H. Wang, R. Belkhou, A. Locatelli, S. Heun, A. Pavlovska, and E. Bauer, J. Appl. Phys. **98**, 043901 (2005).

[185] J. W. Lau, J. K. Bording, M. Beleggia, and Y. Zhu, Appl. Phys. Lett. **88**, 012508 (2006).

[186] W. E, W. Ren, and E. Vanden-Eijnden, J. Appl. Phys. **93**, 2275 (2003).

[187] J. McCord, J. Appl. Phys. **95**, 6855 (2004).

[188] S. Liou, R. Sabiryanov, S. Jaswal, J. Wu, and Y. Yao, J. Magn. Magn. Mater. **226-230**, 1270 (2001).

[189] I. Rissanen and L. Laurson, Phys. Rev. B **94**, 144428 (2016).

[190] G. Gubbiotti, L. Albini, G. Carlotti, M. De Crescenzi, E. Di Fabrizio, A. Gerardino, O. Donzelli, F. Nizzoli, H. Koo, and R. D. Gomez, J. Appl. Phys. **87**, 5633 (2000).

[191] D. Goll, G. Schütz, and H. Kronmüller, Phys. Rev. B **67**, 094414 (2003).

[192] C. Dietrich, R. Hertel, M. Huber, D. Weiss, R. Schäfer, and J. Zweck, Phys. Rev. B **77**, 174427 (2008).

[193] K. Yamada, S. Kasai, Y. Nakatani, K. Kobayashi, H. Kohno, A. Thiaville, and T. Ono, Nat. Mater. **6**, 270 (2007), 0702589 .

[194] A. Hubert and M. Rührig, J. Appl. Phys. **69**, 6072 (1991).

[195] L. J. Heyderman, S. Czekaj, F. Nolting, E. Müller, P. Fischer, P. Gasser, and L. López-Díaz, J. Appl. Phys. **99**, 063904 (2006).

[196] M. T. Bryan, D. Atkinson, and R. P. Cowburn, Appl. Phys. Lett. **85**, 3510 (2004).

[197] F. Liorzou, B. Phelps, and D. Atherton, IEEE Trans. Magn. **36**, 418 (2000).

[198] N. Amos, R. Fernandez, R. Ikkawi, B. Lee, A. Lavrenov, A. Krichevsky, D. Litvinov, and S. Khizroev, J. Appl. Phys. **103**, 07E732 (2008).

[199] J. McCord, B. Erkartal, T. von Hofe, L. Kienle, E. Quandt, O. Roshchupkina, and J. Grenzer, J. Appl. Phys. **113**, 073903 (2013).

[200] C. B. Hill, W. R. Hendren, R. M. Bowman, P. K. McGeehin, M. A. Gubbins, and V. A. Venugopal, Meas. Sci. Technol. **24**, 045601 (2013).

[201] U. Helmersson, M. Lattemann, J. Bohlmark, A. P. Ehiasarian, and J. T. Gudmundsson, Thin Solid Films **513**, 1 (2006).

[202] S. Min, J. A. Bain, and D. W. Greve, J. Appl. Phys. **91**, 6824 (2002).

[203] A. S. Dzhumaliev, Y. V. Nikulin, and Y. A. Filimonov, Phys. Solid State **58**, 1053 (2016).

[204] J. D. Freeman, J. Vac. Sci. Technol. A **9**, 421 (1991).

[205] A. Svalov, B. González Asensio, A. Chlenova, P. Savin, A. Larrañaga, J. Gonzalez, and G. Kurlyandskaya, Vacuum **119**, 245 (2015).

[206] A. Svalov, G. Kurlyandskaya, B. González Asensio, J. Collantes, and A. Larrañaga, Mater. Lett. **152**, 159 (2015).

[207] G. Nahrwold, J. M. Scholtyssek, S. Motl-Ziegler, O. Albrecht, U. Merkt, and G. Meier, J. Appl. Phys. **108**, 013907 (2010).

[208] X.-L. Tang, H. Su, H.-W. Zhang, Z.-Y. Zhong, and Y.-L. Jing, Thin Solid Films **550**, 616 (2014).

[209] K. Yamamoto and M. Kitada, J. Mater. Sci. Mater. Electron **7**, 455 (1996).

[210] S. Craig and G. L. Harding, J. Vac. Sci. Technol. **19**, 205 (1981).

[211] Y. Gan, Surf. Sci. Rep. **64**, 99 (2009).

[212] S. J. Fang, S. Haplepete, W. Chen, C. R. Helms, and H. Edwards, J. Appl. Phys. **82**, 5891 (1997).

[213] G. Williamson and W. Hall, Acta Metallurgica **1**, 22 (1953).

[214] M. Salou, B. Lescop, S. Rioual, A. Lebon, J. B. Youssef, and B. Rouvellou, Surf.

Sci. **602**, 2901 (2008).

[215] M. R. Fitzsimmons, T. J. Silva, and T. M. Crawford, Phys. Rev. B **73**, 014420 (2006).

[216] R. Hertel, Zeitschrift für Metallkunde **93**, 957 (2002).

[217] K. Müller, J. Appl. Phys. **58**, 2573 (1985).

[218] J. A. Thornton, Annu. Rev. Mater. Sci. **7**, 239 (1977).

[219] J. A. Thornton, in *Proc. SPIE 0821, Modeling of Optical Thin Films*, edited by M. R. Jacobson (1988) p. 95.

[220] N. Kaiser, Appl. Opt. **41**, 3053 (2002).

[221] W. Zhang, W. Zhang, L. Lin, B. Peng, H. Jiang, and S. Yang, J. Magn. Magn. Mater. **280**, 143 (2004).

[222] H. Fujiwara, J. Phys. Soc. Jpn. **20**, 2092 (1965).

[223] C. Ross, Annu. Rev. Mater. Res. **31**, 203 (2001).

[224] M. Foerster, O. Boulle, S. Esefelder, R. Mattheis, and M. Kläui, 'Handbook of spintronics,' (Springer Netherlands, Dordrecht, 2014) Chap. Domain Wall Memory Device, pp. 1–46.

[225] D. Givord, M. F. Rossignol, and D. W. Taylor, J. Phys. IV France **02**, C3 (1992).

[226] J. Steiner, R. Schäfer, H. Wieczoreck, J. McCord, and F. Otto, Phys. Rev. B **85**, 104407 (2012).

[227] H. A. M. Van Den Berg, J. Appl. Phys. **61**, 4194 (1987).

[228] H. A. M. Van Den Berg and D. K. Vatvani, IEEE Trans. Magn. **18**, 880 (1982).

[229] M. N. Dubovik, V. V. Zverev, and B. N. Filippov, J. Exp. Theor. Phys. **123**, 108 (2016).

[230] M. J. Donahue, Adv. Cond. Matter Phys. **2012**, 1 (2012).

[231] R. G. Elías and A. Verga, Eur. Phys. J. B **82**, 159 (2011).

[232] V. V. Zverev, B. N. Filippov, and M. N. Dubovik, Phys. Solid State **56**, 1785

(2014).

[233] J.-S. Gau, Mater. Sci. Eng. B **3**, 377 (1989).

[234] J. Lenz and S. Edelstein, IEEE Sens. J. **6**, 631 (2006).

[235] G. Scheunert, O. Heinonen, R. Hardeman, A. Lapicki, M. Gubbins, and R. M. Bowman, Appl. Phys. Rev. **3**, 011301 (2016).

[236] V. Vinnichenko, L. Fomin, I. Malikov, and G. Mikhailov, J. Magn. Magn. Mater. **385**, 451 (2015).

[237] W. Rave and A. Hubert, IEEE Trans. Magn. **36**, 3886 (2000).

[238] D. Chumakov, J. McCord, R. Schäfer, L. Schultz, H. Vinzelberg, R. Kaltofen, and I. Mönch, Phys. Rev. B **71**, 014410 (2005).

[239] R. Shull, Y. Kabanov, V. Gornakov, P. Chen, and V. Nikitenko, J. Magn. Magn. Mater. **400**, 191 (2016).

[240] B. R. Craig, S. McVitie, J. N. Chapman, D. O. O'Donnell, and A. B. Johnston, J. Appl. Phys. **102**, 013911 (2007).

[241] X. Fu, S. D. Pollard, B. Chen, B.-K. Yoo, H. Yang, and Y. Zhu, Sci. Adv. **4**, eaat3077 (2018).

[242] N. Wiese, S. McVitie, J. N. Chapman, A. Capella-Kort, and F. Otto, EPL **80**, 57003 (2007).

[243] S. Hankemeier, R. Frömter, N. Mikuszeit, D. Stickler, H. Stillrich, S. Pütter, E. Y. Vedmedenko, and H. P. Oepen, Phys. Rev. Lett. **103**, 147204 (2009).

[244] H. A. M. van den Berg and D. K. Vatvani, J. Appl. Phys. **52**, 6830 (1981).

[245] S. Middelhoek, J. Appl. Phys. **34**, 1054 (1963).

[246] A. Neudert, J. McCord, R. Schäfer, R. Kaltofen, I. Mönch, H. Vinzelberg, and L. Schultz, J. Appl. Phys. **99**, 08F302 (2006).

[247] D. A. Herman, B. E. Argyle, and B. Petek, J. Appl. Phys. **61**, 4200 (1987).

[248] M. Löhndorf, A. Wadas, H. A. Van Den Berg, and R. Wiesendanger, Appl. Phys. Lett. **68**, 3635 (1996).

[249] P. E. Roy, J. H. Lee, T. Trypiniotis, D. Anderson, G. A. Jones, D. Tse, and C. H. Barnes, Phys. Rev. B **79**, 3 (2009).

[250] C. A. Fowler, E. M. Fryer, and D. Treves, J. Appl. Phys. **31**, 2267 (1960).

[251] T. Kimura, F. Wakaya, and K. Gamo, Jpn. J. Appl. Phys. **40**, 6357 (2001).

[252] D. A. Garanin, Phys. Rev. B **55**, 3050 (1997).

[253] O. Fruchart, N. Rougemaille, A. Bendounan, J.-C. Toussaint, R. Belkhou, Yuan Tian, Hyeonseung Yu, F. Cheynis, A. Masseboeuf, P. Bayle-Guillemaud, and A. Marty, IEEE Trans. Magn. **46**, 1552 (2010).

[254] V. D. Nguyen, O. Fruchart, S. Pizzini, J. Vogel, J.-C. Toussaint, and N. Rougemaille, Sci. Rep. **5**, 12417 (2015).

[255] A. Arrott and R. Hertel, J. Magn. Magn. Mater. **322**, 1389 (2010).

[256] L. Huang and Y. Zhu, Appl. Phys. Lett. **95**, 10 (2009).

[257] P. Pirro, T. Koyama, T. Brächer, T. Sebastian, B. Leven, and B. Hillebrands, Appl. Phys. Lett. **106**, 232405 (2015).

[258] K. Wagner, A. Kákay, K. Schultheiss, A. Henschke, T. Sebastian, and H. Schultheiss, Nat. Nanotechnol. **11**, 432 (2016).

[259] F. Garcia-Sanchez, P. Borys, R. Soucaille, J.-p. Adam, R. L. Stamps, and J.-v. Kim, Phys. Rev. Lett. **114**, 247206 (2015).

[260] S. Huo, J. Bishop, J. Tucker, W. Rainforth, and H. Davies, IEEE Trans. Magn. **33**, 4056 (1997).

[261] S. Müller-Pfeiffer, M. Schneider, and W. Zinn, Phys. Rev. B **49**, 15745 (1994).

[262] M. Schneider, S. Muller-Pfeiffer, and W. Zinn, J. Appl. Phys. **79**, 8578 (1996).

[263] A. Masseboeuf, T. Jourdan, F. Lancon, P. Bayle-Guillemaud, and A. Marty, Appl. Phys. Lett. **95**, 212501 (2009).

[264] E. E. Huber and D. O. Smith, J. Appl. Phys. **30**, S267 (1959).

[265] R. J. Spain, Appl. Phys. Lett. **3**, 208 (1963).

[266] R. W. DeBlois, J. Appl. Phys. **40**, 1084 (1969).

[267] H. Fujiwara, J. Phys. Soc. Jpn. **20**, 2092 (1965).

[268] G. Karapetrov, A. Belkin, M. Iavarone, J. Fedor, V. Novosad, M. V. Milošević, and F. M. Peeters, J. Supercond. Nov. Magn. **24**, 905 (2011).

[269] B. Baek, W. H. Rippard, S. P. Benz, S. E. Russek, and P. D. Dresselhaus, Nat. Commun. **5**, 1 (2014).

[270] N. Nagaosa and Y. Tokura, Nat. Nanotechnol. **8**, 899 (2013).

[271] A. Fert, N. Reyren, and V. Cros, Nat. Rev. Mater. **2**, 17031 (2017).

[272] R. Hertel, Nat. Nanotechnol. **8**, 318 (2013).

[273] D. Navas, C. Redondo, G. A. Badini Confalonieri, F. Batallan, A. Devishvili, Ó. Iglesias-Freire, A. Asenjo, C. A. Ross, and B. P. Toperverg, Phys. Rev. B **90**, 054425 (2014).

[274] T. Herranen and L. Laurson, Phys. Rev. B **92**, 100405 (2015).

[275] D. Navas, C. Nam, D. Velazquez, and C. A. Ross, Phys. Rev. B **81**, 224439 (2010).

[276] S. H. Lee, F. Q. Zhu, C. L. Chien, and N. Marković, Phys. Rev. B **77**, 132408 (2008).

[277] C. Moutafis, S. Komineas, C. A. F. Vaz, J. A. C. Bland, and P. Eames, Phys. Rev. B **74**, 214406 (2006).

[278] K. Efthimiadis and N. Ntallis, J. Magn. Magn. Mater. **446**, 245 (2018).

[279] H. Niedoba and M. Labrune, J. Magn. Magn. Mater. **321**, 2178 (2009).

[280] A. Hierro-Rodriguez, R. Cid, M. Vélez, G. Rodriguez-Rodriguez, J. I. Martín, L. M. Álvarez-Prado, and J. M. Alameda, Phys. Rev. Lett. **109**, 117202 (2012).

[281] S. Zhang, A. K. Petford-Long, and C. Phatak, Sci. Rep. **6**, 31248 (2016).

[282] O. de Abril, M. d. C. Sánchez, and C. Aroca, J. Appl. Phys. **100**, 063904 (2006).

[283] W. Jiang, P. Upadhyaya, W. Zhang, G. Yu, M. B. Jungfleisch, F. Y. Fradin, J. E.

Pearson, Y. Tserkovnyak, K. L. Wang, O. Heinonen, S. G. E. te Velthuis, and A. Hoffmann, Science **349**, 283 (2015).

[284] E. R. P. Novais, P. Landeros, A. G. S. Barbosa, M. D. Martins, F. Garcia, and A. P. Guimarães, J. Appl. Phys. **110**, 053917 (2011).

[285] R. Novak, F. Garcia, E. Novais, J. Sinnecker, and A. Guimarães, J. Magn. Magn. Mater. **451**, 749 (2018).

[286] A. Hubert, Phys. Stat. Sol. **38**, 699 (1970).

[287] S. Singh, H. Gao, and U. Hartmann, Phys. Rev. B **98**, 060414 (2018).

[288] R. M. Vakhitov and E. B. Magadeev, Phys. Met. Metallogr. **115**, 849 (2014).

[289] G. Chen and A. K. Schmid, Adv. Mater. **27**, 5738 (2015).

[290] B. Dupé, M. Hoffmann, C. Paillard, and S. Heinze, Nat. Commun. **5**, 1 (2014).

[291] I. Manke, N. Kardjilov, R. Schäfer, A. Hilger, M. Strobl, M. Dawson, C. Grünzweig, G. Behr, M. Hentschel, C. David, A. Kupsch, A. Lange, and J. Banhart, Nat. Commun. **1**, 125 (2010).

[292] S. Jamet, S. Da Col, N. Rougemaille, A. Wartelle, A. Locatelli, T. O. Menteş, B. Santos Burgos, R. Afid, L. Cagnon, S. Bochmann, J. Bachmann, O. Fruchart, and J. C. Toussaint, Phys. Rev. B **92**, 144428 (2015).

[293] A. Masseboeuf, O. Fruchart, F. Cheynis, N. Rougemaille, J.-C. Toussaint, A. Marty, and P. Bayle-Guillemaud, Ultramicroscopy **115**, 26 (2012).

[294] A. Fernández-Pacheco, R. Streubel, O. Fruchart, R. Hertel, P. Fischer, and R. P. Cowburn, Nat. Commun. **8**, 15756 (2017).

[295] J. Vogel, W. Kuch, R. Hertel, J. Camarero, K. Fukumoto, F. Romanens, S. Pizzini, M. Bonfim, F. Petroff, A. Fontaine, and J. Kirschner, Phys. Rev. B **72**, 220402 (2005).

[296] L. Thomas, M. G. Samant, and S. S. P. Parkin, Phys. Rev. Lett. **84**, 1816 (2000).

[297] V. Bhavar, P. Kattire, S. Thakare, S. Patil, and R. Singh, IOP Conf. Ser. Mater. Sci. Eng. **229**, 012021 (2017).

[298] R. M. Mahamood and E. T. Akinlabi, 'Types of functionally graded materials and their areas of application,' in *Functionally Graded Materials* (Springer International Publishing, Cham, 2017) pp. 9–21.

[299] T. Hiratani, M. Namikawa, H. Ninomiya, Y. Oda, and H. Toda, Electr. Eng. Jpn. **193**, 18 (2015).

[300] Y. Watanabe, S. H. Kang, J. W. Chan, J. W. Morris, T. J. Shaw, and J. Clarke, J. Appl. Phys. **89**, 1977 (2001).

[301] R. I. Joseph and E. Schlömann, J. Appl. Phys. **36**, 1579 (1965).

[302] R. I. Joseph, Geophysics **41**, 1052 (1976).

[303] A. Aharoni, J. Appl. Phys. **83**, 3432 (1998).